TECHNISCHE
UNIVERSITÄT
WIEN
Vienna│Austria

DISSERTATION

Reconstruction of 3D wet refractivity fields in the lower atmosphere along bended GNSS signal paths

ausgeführt zum Zwecke der Erlangung des akademischen Grades eines Doktors der technischen Wissenschaften unter der Leitung von

Ao.Univ.Prof. Dipl.-Ing. Dr.techn. Robert Weber

E120-4

Department für Geodäsie und Geoinformation

Forschungsgruppe Höhere Geodäsie

eingereicht an der Technischen Universität Wien
Fakultät für Mathematik und Geoinformation

von

Dipl.-Ing. Gregor Möller BSc

Heinzelmanngasse 6/4

1200 Wien

Matr.-Nr.: 0526613

Wien, Juli 2017

BEGUTACHTER

Prof. Dr. Alain Geiger

Institut für Geodäsie und Photogrammetrie

Eidgenössische Technische Hochschule Zürich, Schweiz

Prof. Dr. rer. nat. Jens Wickert

Institut für Geodäsie und Geoinformationstechnik

Technische Universität Berlin, Deutschland

Acknowledgements

My decision to switch from TU Dresden to TU Wien for an Erasmus year has turned out to be a defining decision of my academic career. While I finished my Bachelor´s degree with focus on photogrammetry and laser scanning, the lectures of my supervisor Robert Weber drew my interest in the direction of GNSS as a new research focus. Throughout my years of research and during my position as university assistant, Robert supported me - and not only in scientific questions in the context of my doctoral thesis. I thank Robert for sharing his experience and for his competent guidance. It has kept me motivated during my studies.

I would also like to thank Johannes Böhm for his inspiring ideas. As an expert in atmospheric modelling, it was not possible to write this doctoral thesis without asking from time to time for his professional advice. Together with Robert Weber, he creates a great work environment in our research unit with space for personal research activities but also for joint activities like running, soccer or barbecue evenings.

Thanks also to all of my colleagues and former colleagues for the positive working atmosphere. I will especially remember the numerous active discussions during coffee and lunch breaks. Even though I - and probably those around me - am happy that the scientific studies of recent years have come to a preliminary end, I am thankful for everyday at the Department. In this sense: Thank you for the last seven years. I look forward to seeing you again! After my holidays.

I say thank you to my patient wife. I am sorry for the numerous stories about GNSS, though I am grateful for your willingness to listen. I love you. Special thanks goes also to my parents and family for their continued support. At this point I promise, I will not attempt to survey the moon, at least not on site.

Abstract

The present dissertation suggests an innovative reconstruction technique for estimating wet refractivity fields in the lower atmosphere from signals of the Global Navigation Satellite Systems (GNSS). Therewith the aim is to complement existing observing systems, in particular to capture the high temporal and spatial variability of water vapour in the lower atmosphere.

The invented technique is based on the tomography principle as commonly applied in medicine for diagnostic purposes. Major challenges to be solved relate to the unfavourable observation geometry defined by the number and distribution of ground stations and GNSS satellites in view. Moreover, for each GNSS observation the GNSS signal path and the tropospheric signal delay have to be determined; both serve as the principal input data for GNSS tomography.

By making use of dual-frequency GNSS observations and advanced processing strategies, tropospheric delay parameters are estimated with mm to cm-accuracy for a network of ground-based GNSS receivers. The individual components of the tropospheric delay are examined and evaluated. Thereby also the impact of rather small but important effects like hydrostatic gradients, remaining tropospheric signals in post-fit residuals as well as atmospheric bending is further investigated. If the bending is not considered, the tomography solution is deteriorated by misallocations during the reconstruction process of signal paths. Ray-tracing through a priori refractivity fields helps to minimise these effects and allows for the reconstruction of signal paths more accurately than the common straight-line approach.

Further attention is also given to the mathematical formulation of ill-conditioned, inverse problems. In this respect optimisation strategies are devised which allow for minimisation of artefacts introduced by the reconstruction process itself. In addition quality parameters are described for evaluating the accuracy of the reconstructed wet refractivity fields using weighted least squares methods.

With the newly defined approach, wet refractivity fields are generated that coincide with radiometer and radiosonde measurements in an alpine environment significantly better than operational weather models. This makes GNSS tomography interesting for meteorological applications. Furthermore, other disciplines, which relay on accurate modelling of the signal delay in the lower atmosphere, can benefit from improved refractivity fields.

Kurzfassung

Im Rahmen dieser Dissertation wurde eine Rekonstruktionstechnik entwickelt, die es erlaubt auf Basis von Signalen der globalen Satellitennavigationssysteme (GNSS) atmosphärische Refraktivitätsfelder mit zeitlich hoher Auflösung zu bestimmen. Der Fokus liegt dabei auf einer verbesserten Modellierung des zeitlich und räumlich variablen Wasserdampfgehaltes in den unteren Schichten der Atmosphäre.

Der entwickelte Rekonstruktionsansatz basiert auf dem Prinzip der Tomographie welches heutzutage vor allem in der diagnostischen Medizin eingesetzt wird. Die größten Herausforderungen in der Anwendung auf GNSS Signale liegen in der ungünstigen Beobachtungsgeometrie begründet. Darüber hinaus muss für jede Beobachtung mit hoher Präzision die Laufzeitverzögerung bestimmt und der Signalweg durch die neutrale Atmosphäre rekonstruiert werden. Beides sind die wesentlichen Eingangsdaten für GNSS Tomographie.

Auf Basis von Zweifrequenz-GNSS Beobachtungen und erweiterten Auswertestrategien wird die troposphärische Laufzeitverzögerung mit mm bis cm-Genauigkeit geschätzt. Des Weiteren werden die individuellen Bestandteile, aus denen sich die Laufzeitverzögerung zusammensetzt, näher untersucht. Dabei wird auch auf kleinere Effekte, wie hydrostatische Gradienten, den verbleibenden Informationsgehalt in den Beobachtungsverbesserungen, sowie auf die Signalablenkung in der Atmosphäre näher eingegangen. Bleibt die Signalablenkung bei der Rekonstruktion der Signalwege unberücksichtigt können Fehlzuordnungen auftreten, die sich direkt auf die Qualität der Refraktivitätsfelder auswirken. Aus diesem Grund werden verschiedene Strahlenverfolgungsansätze untersucht und ihr Einfluss auf die Rekonstruktion der Signalwege abgeschätzt.

Darüber hinaus werden mathematische Verfahren getestet, die bei schlecht konditionierten, inversen Problemen helfen Artefakte zu minimieren, die durch den Rekonstruktionsansatz selbst hervorgerufen werden. Zusätzlich werden Genauigkeitsparameter beschrieben, die es erlauben die Qualität der geschätzten Refraktivitätsfelder zu bewerten.

Mit dem entwickelten Rekonstruktionsansatz können feuchte Refraktivitätsfelder bestimmt werden, die im Vergleich zu Wettermodellen eine deutlich bessere Übereinstimmung mit Radiometer- und Radiosondenprofilen zeigen. Dies macht GNSS Tomographie für meteorologische Anwendungen interessant. Auch andere Disziplinen können von den verbesserten Refraktivitätsfeldern profitieren welche eine genaue Beschreibung der Signalverzögerung in den unteren Schichten der Atmosphäre benötigen.

Contents

Chapter 1

Introduction

Earth´s atmosphere is a thermo-hydrodynamical system. Its forcing is dominated by solar radiation but is also affected by very local effects such as the topography or vegetation cover. Due to its complexity we must keep in mind that a "growth in understanding strongly depends on the improvement of the measurements and observing systems" (Peixoto & Oort, 1992). Future evolution of atmospheric science leans on densified classical observing systems and new, more complex observation technologies like radar, lidar or infrared radiometers (Bauer *et al.*, 2015).

Since the early 1990s also microwave signals of the Global Navigation Satellite Systems have also been utilised to derive information about the atmospheric constituents and their thermo-dynamical state, see Bevis *et al.* (1992). Procedures have been developed to estimate the general slowing of the microwave signals in the atmosphere, and in particular due to water vapour in the troposphere. Since this time the GNSS technique has become more and more important as an observation technique for atmosphere research. Nowadays GNSS derived tropospheric solutions, from ground-based or space-based GPS measurements as obtained from satellite missions like COSMIC (http://www.cosmic.ucar.edu/), contribute routinely to weather forecast systems, e.g. for evaluation, inter-comparison purposes or for direct assimilation into operational numerical weather forecast models (Andrews, 2000).

In the last two decades the GNSS observing networks have been continuously densified; e.g. the GNSS network of the European Meteorological Services consists of about 2200 GNSS sites in Europe, as of October 2015 (see http://egvap.dmi.dk). Besides, existing GNSS systems are being further enhanced, new regional and global systems are being built-up and the quality of the observations is increasing continuously. By 2020 about 120 navigation satellites are expected to be observable on three frequencies (Moran, 2014). Simulations of future constellations reveal a more favourable satellite geometry which

admits a more homogeneous scanning of the atmosphere above a ground network of GNSS receivers. Fostered by these developments, advanced processing strategies and evaluation methods are necessary to exploit the full potential of future GNSS systems for describing the physical state of the neutral atmosphere and the dynamic of its constituents.

1.1 Thesis contribution

This dissertation conveys the knowledge and understanding of GNSS as an observation technique for sensing the state and the dynamics of atmospheric water vapour. Therefore the lower atmosphere is approached in an observant way.

An overview about major developments within this field of research since Flores (1999) is provided by Manning (2013). Further honour is given to recent works from Adavi & Mashhadi-Hossainali (2014); Benevides *et al.* (2017); Brenot *et al.* (2017); Yao *et al.* (2016) and Xia *et al.* (2013).

By taking current developments into account, the innovative character of this dissertation and main contribution to the state of knowledge is summarised as follows:

- Deployment of reconstruction tools and routines for retrieving structural information about water vapour in the lower atmosphere from GNSS signal delays.

- Minimisation of artefacts introduced by the reconstruction process itself using mathematical optimisation and regularisation methods.

- Determination of enhanced wet refractivity fields considering atmospheric bending effects, hydrostatic gradients and observation weighting methods.

- Introduction of the inter-satellite ranging technique as a new observation technique for water vapour distribution in the lower atmosphere.

The proposed approach, based on the principle of tomography, is applicable at various time scales. Dependent on how fast the GNSS observations of a ground network of GNSS stations can be made available, wet refractivity fields can be provided for post-processing or now-casting applications within a couple of minutes. Therewith it has great potential to fill in the gaps of current meteorological observing systems.

In case of a stable observation geometry, the wet refractivity fields can be derived from GNSS signals more accurately than from operational weather models. This makes GNSS tomography interesting for meteorological applications, e.g. for improving the short-term

weather forecast, but also for various other disciplines which rely on accurate wet refractivities or derived products like tropospheric signal delays.

1.2 Thesis outline

Following the preface,

Chapter 2 provides an inside into the object of investigation, the structure of the atmosphere, the parameters to describe its thermo-dynamical state and its global distribution.

Chapter 3 highlights the principles of atmospheric physics, the relation between electromagnetic waves in the microwave frequency band and the neutral atmosphere, which can be utilised to derive information about its composition.

Chapter 4 introduces the Global Navigation Satellite Systems (GNSS) and highlights processing strategies for differenced and undifferenced dual-frequency GNSS observations, with focus on the estimation of tropospheric parameters, using a least squares approach.

Chapter 5 gives an overview of meteorological sensors for atmospheric pressure, temperature and humidity and provides insight into pressure extrapolation methods and related errors, required for the determination and reduction of hydrostatic effects in GNSS tropospheric parameters.

Chapter 6 is dedicated to the reconstruction of Slant Wet Delays (SWD) from GNSS tropospheric parameters with special focus on wet mapping functions, post-fit observation residuals and remaining hydrostatic effects in the gradient parameters.

Chapter 7 describes the principles of GNSS tomography with all relevant components. A linear and an iterative non-linear resolution strategy for inverse tomography is presented and tested against synthetic GNSS slant wet delays.

Chapter 8 is dedicated to an alpine tomography test case. The methods and models invented in Chapter 7 are applied to real observations. The reconstructed wet refractivity fields are validated against radiometer and radiosonde data in the Inn valley, Austria.

Chapter 9 summarises the major findings and gives recommendations on how to use GNSS tomography products in GNSS positioning and atmosphere research.

Chapter 10 provides an outlook on inter-satellite-ranging which can be a useful complement to existing observation techniques for describing the distribution of water vapour and temperature in the lower atmosphere.

Chapter 2

Earth's atmosphere

Atmosphere [atmos, greek: 'vapour' and sphaira, greek: 'sphere'] refers to the gaseous envelope of the Earth or in general of a celestial body. The prevailing belief is that the Earth´s atmosphere came into existence as a result of volcanic fumigation around 4 billion years ago with steam (H_2O), carbon dioxide (CO_2) and trace gases[1] like hydrogen (H_2) or methane (CH_4) as the dominant constituents (Wallace & Hobbs, 2006). The Miller-Urey experiment (Miller, 1953) demonstrates how this composition allowed for the formation of the chemical building elements of life. Fostered by several advantageous conditions the evolutionary atmosphere converted into a living atmosphere. The Earth´s gravity was strong enough to hold heavier elements like nitrogen (N_2), oxygen (O_2) and therewith most of the water vapour in the atmosphere. The opportune distance to the sun allowed the Earth´s surface to cool down so that most of the water vapour started to precipitate around 3.6 billion years ago. Rising oceans absorbed most of the atmospheric carbon dioxide, and sedimented it into carbon rocks. Solar ultra-violet radiation stimulated photochemical reaction: water vapour and carbon dioxide were split into their components, hydrogen escaped into space, and the concentration of oxygen and ozone (O_3) increased. The ozone shield reduced high energy radiation at the surface and supported therewith the grow of vegetation. While oxygen and carbon (C) formed broader chemical bonds, non-reactive gases like nitrogen and argon (Ar) remained and accumulated in the atmosphere. Today´s concentration of oxygen and ozone was achieved around 500 million years ago (Spektrum, 2016). Since this time significant changes in global temperature and other climate related parameters have been highly related to variations in the concentration of carbon dioxide

---

[1]A trace gas is defined by its relative concentration. It contributes with less than 1% to the total atmospheric volume.

and methane in the atmosphere, with water vapour as a key amplifier of global warming (Dessler *et al.*, 2008).

2.1 Atmospheric constituents

Earth´s atmosphere is almost in a state of hydrostatic equilibrium. Turbulent mixing keeps the relative concentrations of long-lived constituents like nitrogen, oxygen, argon or carbon dioxide nearly constant in the lower $100\,km$ of the atmosphere.

Constituent	Molecular weight	Content
Nitrogen (N_2)	28.01	$78.08\,\%$
Oxygen (O_2)	32.00	$20.95\,\%$
Argon (Ar)	39.94	$0.93\,\%$
Carbon dioxide (CO_2)	44.01	$380\,ppm$
Neon (Ne)	20.18	$18\,ppm$
Helium (He)	4.00	$5\,ppm$
Methane (CH_4)	16.04	$1.75\,ppm$
Ozone (O_3)	48.00	$0 - 0.1\,ppm$
Water vapour (H_2O)	18.02	$0 - 5\,\%^*$

Table 2.1: Present composition of Earth´s atmosphere. The fractional concentration by volume of each constituent has been computed in relation to dry air.*The fractional content of water vapour is counted additively. Source: Wallace & Hobbs (2006)

Above, the density of molecules is so low that each gas behaves as if it alone were present. As a consequence the concentration of heavier gases decreases more than those of lighter constituents. In contrast, water vapour exhibits a heterogeneous distribution because it condenses and precipitates out when air is lifted. Thus, it is concentrated only in the lower few kilometres of the atmosphere (see Section 2.3.2). Further, the residence time[2] influences the mixing-ratio. Short-lived constituents like ozone "do not remain in the atmosphere long enough to become well mixed" (Wallace & Hobbs, 2006, p. 27).

According to Table 2.1 nitrogen and oxygen make up $99.03\,\%$ of total atmospheric content. Although the fractional concentration of all other constituents of the total atmospheric volume does not exceed $1\,\%$, specific gases play a dominant role in the global climate and weather system. Essentially water vapour, carbon dioxide and ozone but also methane,

---

[2]Residence time is the time a substance remains within a specified reservoir.

nitrous oxide, carbon monoxide and chlorofluorocarbons (CFCs) absorb and re-emit incoming solar radiation or outgoing terrestrial radiation emitted from the Earth´s surface and therewith contribute significantly to the radiation budget.

2.2 Earth´s net radiation

Net radiation describes the balance between incoming and outgoing energy at the top of the atmosphere. The solar constant $S_c = 1365\,W/m^2 \pm 0.3\,\%$ (Li *et al.*, 2011) defines the amount of incoming radiation at a distance of one astronomical unit from the sun. Due to Earth´s rotation, the effective incoming solar radiation is $\frac{1}{4}S_c = 341.3\,W/m^2$. The variation of $\pm 0.3\,\%$[3] is widely explained by the 11-year periodic solar cycle (Gray *et al.*, 2010). However, the resulting amount of irradiation S_0 received on Earth per unit area depends also on the actual distance to the sun[4], the angle of insolation, the path length through the atmosphere and the atmospheric conditions. In Vienna [lat: 48.21°, lon: 16.37°] S_0 varies with the angle of incidence within the annual cycle between $150\,W/m^2$ and $460\,W/m^2$, the global mean is $\sim 161\,W/m^2$ (Trenberth *et al.*, 2009).

The thermal emission P (λ_{max}[5]$= 10\,\mu m$) emitted by Earth´s surface is determined by Stefan-Boltzmann law

$$P = \varepsilon_s \cdot \sigma \cdot T_{bb}^4 \tag{2.1}$$

where ε_s is emissivity, $\sigma = 5.670373 \cdot 10^{-8}\,Wm^{-2}K^{-4}$ is the Stefan-Bolzmann constant and T_{bb} is the black body temperature of Earth´s surface. Assuming an emissivity of $\varepsilon_s = 1$ (Earth´s surface is very close to a blackbody in the bandwidth of thermal radiation) and a mean surface temperature of $T_s \sim 289.1\,K$, derived from the reanalysis of the National Centers for Atmospheric Prediction and Research (NCEP-NCAR), Earth´s thermal emission follows to $396\,W/m^2$. Trace gases like water vapour, carbon dioxide, ozone, nitrous oxide or methane absorb certain wavelengths of the outgoing radiation and scatter it back to the surface. The long-wave downward radiation leads to a warming of Earth´s surface. The so-called greenhouse effect results in a temperature increase of around $33\,K$, whereby water vapour ($20.6\,K \triangleq 62\,\%$) and carbon dioxide ($7.2\,K \triangleq 22\,\%$)

---

[3]A variation of 0.3 % sounds small but equates to about ten times the world energy consumption of humans per year.

[4]Variations are caused by the eccentricity of the Earth orbit of currently 0.0167 (yearly cycle) and changes in Earth´s orbit parameters (Milankovitch cycles).

[5]The dominant wavelength λ_{max} of emitted radiation results from Wien's displacement law assuming a temperature of $288\,K$.

are the dominant greenhouse gases. The resulting total net radiation is summarised in Table 2.2.

Solar irradiation absorbed at the surface	$+161\,W/m^2$
Thermal emission by the Earth´s surface	$-396\,W/m^2$
Long-wave downward radiation	$+333\,W/m^2$
Net radiation	$+98\,W/m^2$

Table 2.2: Earth´s net radiation budget

The remaining excess in net radiation of $98\,W/m^2$ is compensated by non-radiative processes which allow for the storing and transporting of energy for some time before being emitted as long-wave radiant energy back into space (Trenberth *et al.*, 2009). The most prominent non-radiative processes are latent heat flux (evapotranspiration of water, melting of ice) - which counts for $80\,W/m^2$ - and sensible heat in the form of conduction and convection of about $17\,W/m^2$. These processes induce heating, oceanic currents, atmospheric circulation, turbulences and a wide variety of weather effects.

The resulting net absorption of around $1\,W/m^2$ in the global-mean energy budget is currently explained by changes in albedo from reduced snow and ice cover and to changes in atmospheric composition, circulation and clouds (Trenberth *et al.*, 2009).
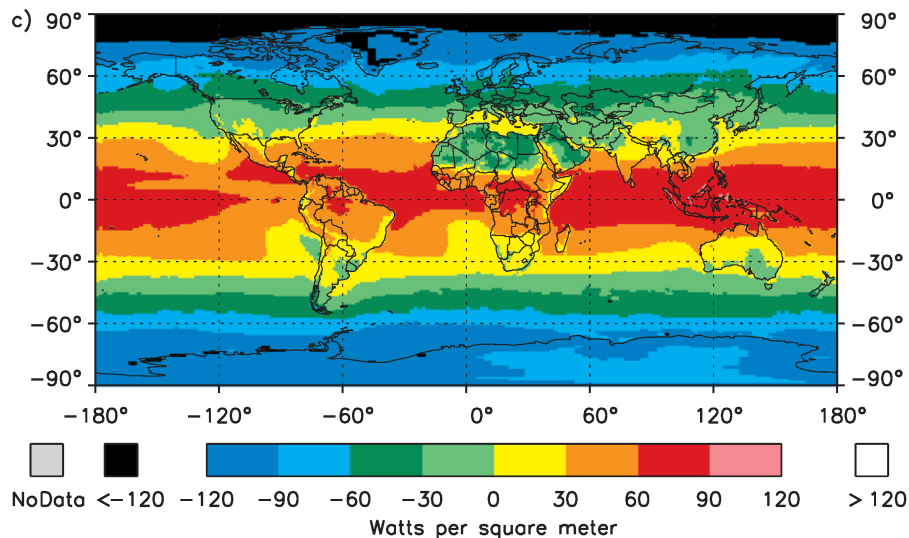
Figure 2.1: Geographical distribution of annual-mean net radiation in W/m^2. Source: Mlynczak *et al.* (2011)

In contrast the geographical differences of heat transfer are much more distinct. Figure 2.1 highlights a strong latitude dependency which results in an excess of radiation in the tropics and a deficit poleward 40° latitude on both hemispheres. Longitudinal differences are related to the surface specific albedo, the water vapour distribution in the atmosphere and the resulting cloud coverage, e.g. the dry conditions and the high albedo of sand results in a negative net radiation over North Africa. Due to the low albedo of water, oceans absorb more radiation than land surfaces. Fostered by the distribution of land areas at high latitudes the resulting net radiation difference of $22.5\,W/m^2$ is carried by the atmosphere from ocean to land by sensible heat or latent heat (Mlynczak *et al.*, 2011). Latter goes along with a net atmospheric moisture transport from ocean to land of $40 \cdot 10^3\,km^3/yr$ which corresponds to around $3.2\,PW$ of latent heat transfer. The distinct global differences in net radiation are the main driver of atmospheric dynamics. Other effects like geothermal heat flux ($\sim 0.027\,\%$), interplanetary dust, solar wind, and thermal radiation from space have minor impact and are therewith neglected in the global radiation budget.

2.3 State of the atmosphere

To approach the atmosphere in an observant way, measurands have to be found which allow for description of the state of the atmosphere. Gibb´s rule defines the degree of freedom f_n of gases in thermodynamic equilibrium as a function of involved gas components N and phases P (liquids, solids, gases) according to the following:

$$f_n = N - P + 2 \tag{2.2}$$

Since the atmosphere is well approximated by a two-component ($N = 2$), gaseous system ($P = 1$, no clouds) formed by dry air and water vapour, three independent variables (e.g. pressure p, temperature T and specific humidity q) are sufficient to define its thermodynamic state. The relation between pressure and temperature is given by the general gas equation. Assuming ideal gases, i.e. no interaction between the gas molecules, it follows to

$$p = \rho \cdot R_M \cdot T \tag{2.3}$$

with ρ as the density of air. The term R_M, the specific gas constant, is the quotient of the ideal gas constant $R = 8314.459\,J/(kmol\,K)$ and the molar mass of the gaseous system. The molar mass for dry air is defined as the weighted mean of the molecular weights of the

dry atmospheric gases, see Table 2.1 and follows to $M_d = 28.9645\,kg/kmol$. The molar mass M_w of water vapour is $18.0153\,kg/kmol = 0.622 \cdot M_d$ and the specific gas constant of water vapour follows to $R_w = 461.5221\,J/(kg\,K)$.

According to Dalton´s law, a gas mixture is defined by the partial pressures p_i of the component gases, assuming constant temperature.

$$p = \sum_i p_i = \sum_i \rho_i \cdot R_{M,i} \cdot T \tag{2.4}$$

According to previous assumptions, the pressure of moist air is the sum of the pressure p_d of dry air and the pressure p_w of water vapour, better known as water vapour pressure e.

$$p = p_d + e \tag{2.5}$$

In the form of the ideal gas law, the equation of moist air also reads

$$p = \rho \cdot R_d \cdot T_v \tag{2.6}$$

where
$$T_v = \frac{T}{(1 + 0.378 \cdot e/p)} \tag{2.7}$$

is the virtual temperature that dry air would have assuming the same pressure and density as moist air. It allows for use of the dry-air equation of state for moist air (with $T \geqq T_v$). The amount of water vapour in a given volume of air is defined by the specific humidity q [g/kg] as the ratio of the density ρ_w of water vapour and ρ the density of moist air.

$$q = \frac{\rho_w}{\rho} = \frac{0.622 \cdot e}{p - 0.378 \cdot e} \tag{2.8}$$

Moreover, humidity is expressed in several different ways. The most common measure is relative humidity rh [%]
$$rh = \frac{e}{E} \tag{2.9}$$

where E is the saturation vapour pressure in hPa. According to WMO (2008) E is the pressure of water vapour in a state of neutral equilibrium with a plane surface of pure water and is well approximated by an empirical function of temperature

$$E = 6.112 \cdot e^{\frac{17.62 \cdot t}{243.12 + t}} \tag{2.10}$$

with temperature t in °C. Eq.2.9 and Eq.2.10 can be combined to compute water vapour pressue from relative humidity. Also commonly used is absolute humidity $ah\,[g/m^3]$. In the form of the ideal gas law it reads:

$$ah = \frac{e}{R_w \cdot T_v} \tag{2.11}$$

In Chapter 5 techniques are described which allow for measuring of pressure, temperature and relative humidity and therewith of the state of the atmosphere.

However, "a complete specification of the state of the atmosphere should also include the global distribution of other variables, such as cloudiness, aerosols, and so on, because they influence the large-scale behaviour of the atmosphere. Although precipitation, evaporation, and runoff are fluxes and not state variables, they are intimately connected with the state of the atmosphere ..." (Peixoto & Oort, 1992, p. 131).

2.3.1 Pressure and temperature distribution

Assuming hydrostatic equilibrium ($\partial p = -g\rho\partial h$) air pressure p is determined by the weight $g\rho dh$ (gravity acceleration g times mass ρdh) of the overlaying column of air. For practical reasons the density ρ is replaced using Eq.2.6 to obtain the basic equation for barometric height measurements.

$$\partial p = -\frac{p \cdot g}{R_d \cdot T_v} \cdot \partial h \tag{2.12}$$

Since air is very compressible, the density of air varies with pressure and temperature. In order to solve Eq.2.12 for pressure, further assumptions are necessary. First, gravity changes only slightly with height, hence it is assumed to be constant within a certain height interval. According to Kraus (2001) g can be described as a function of latitude φ and ellipsoidal height h

$$g = g_{eq} \cdot (1 + 0.00530244 \cdot sin^2\varphi + 0.00000582 \cdot sin^2 2\varphi) \cdot (1/(1 + h/R_E)^2) \tag{2.13}$$

where $g_{eq} = 9.78032677\,m/s^2$ is the normal gravity at the equator. A detailed derivation of Eq.2.13 is provided in Appendix A.2.

Besides, the virtual temperature T_v in Eq.2.12 is assumed as constant, which is reasonable for height differences up to $200\,m$ with a maximum pressure error of $10\,Pa$. Therewith Eq.2.12 can be defined as the integral between pressure p_0 at any level zero, e.g. at Earth´s

surface, and any other pressure level p_1 according to the following:

$$\frac{R_d \cdot T_v}{g} \cdot \int_{p_0}^{p_1} \partial(\ln p) = \int_{p_0}^{p_1} \partial h \tag{2.14}$$

After integration and combination of the natural logarithms the hypsometric equation reads

$$\frac{R_d \cdot T_v}{g} \ln\left(\frac{p_0}{p_1}\right) = h_1 - h_0 \tag{2.15}$$

with $h_1 - h_0$ as the height difference (exactly determined as the difference in geopotential height), the thickness of the intervening layer. The hypsometric equation describes the change in pressure with height which is proportional to the mean virtual temperature between both levels. If the pressure and temperature is known at surface level, Eq.2.15 can be solved for pressure p_1.

$$p_1 = p_0 \cdot e^{\frac{-g}{R_d \cdot T_v} \cdot (h_1 - h_0)} \tag{2.16}$$

In synoptic meteorology Eq.2.16 is used to compute pressure values for different levels, e.g. to create sea-level pressure maps. For height differences up to $50\,m$ Eq.2.16 can be further simplified, see WMO (2008).

$$p_1 = p_0 \cdot \left(1 + \frac{(h_1 - h_0)}{29.2 \cdot T_v}\right) \tag{2.17}$$

For larger height differences the virtual temperature T_v in Eq.2.16 should be reduced to mean height using lapse rate Γ.

$$\bar{T}_v = T_v + \Gamma \cdot \frac{(h_1 - h_0)}{2} \tag{2.18}$$

From observations, a standard atmosphere lapse rate Γ of $-6.5\,K/km$ has been defined, valid from sea level up to $11\,km$ altitude. In contrast the adiabatic lapse rate Γ_d, i.e. the temperature gradient of dry air without any transfer of heat is $-9.8\,K/km$. It results from the first law of thermodynamics and the assumption of hydrostatic equilibrium

$$\Gamma_d = \frac{g}{c_p} \tag{2.19}$$

with gravity $g = 9.80665\,m/s^2$ and the specific heat capacity $c_p = 1003.5\,kg\,m^2/(s^2\,kg\,K)$ of dry air at 0 °C assuming constant pressure. The difference between environmental lapse

rate Γ and adiabitic lapse rate is caused by the release of latent heat and heat transfer, which varies significantly in time and space.

2.3.1.1 Global pressure and temperature model (GPT2w)

The empirical model GPT2w (Böhm *et al.*, 2015) provides the meteorological parameters pressure, temperature, mean temperature, lapse rate, specific humidity and water vapour decrease factor for any user position and time. Its parameters were derived from ten years of monthly mean pressure reanalysis data (ERA-Interim) of the European Centre for Medium-Range Weather Forecasts (ECMWF) and are stored on global 1° x 1° grids as mean, annual and semi-annual variations. The GPT2w model is a good alternative if e.g. no actual information about the vertical temperature distribution is available. In the following GPT2w is used to create global pressure, temperature and water vapour pressure maps and to evaluate different approximation methods using Eq.2.16. The results of the evaluation are summarised in Table 5.4.

2.3.1.2 Global pressure maps

The weighted Global Mean Surface Pressure (GMSP) derived from GPT2w pressure values is $985.2\,hPa$. Figure 2.2 shows its distribution on a global grid. For the computation of GMSP the gridded pressure values were weighted by the cosine of the latitude of the grid points.
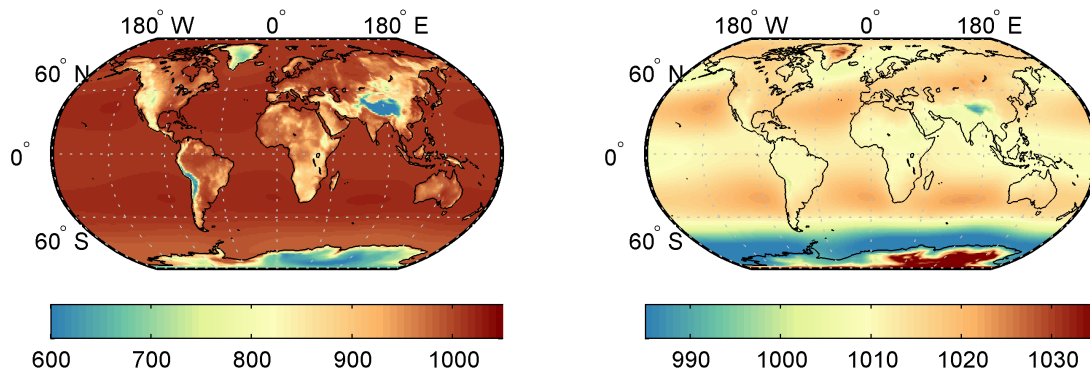
Figure 2.2: Global mean pressure in hPa as provided with GPT2w at the surface (left) and reduced to sea level (right)

At the surface, pressure variations are strongly related to the elevation of the surface. In order to also highlight zonal variations, pressure was reduced to sea level by means of Eq.2.16 and Eq.2.18 using surface temperature and lapse rate from GPT2w.

At sea level, mean pressure variations appear in the range of $980\,hPa$ to $1050\,hPa$. The Southern Ocean pressure low centred at around 60° south is related to large temperature and humidity gradients between the Antarctic and the subtropical latitudes (see Figure 2.3 and Figure 2.5). The high pressure over the Antarctic is caused by sinking of cold air which goes along with persistent high pressure, especially in local winter. Further visible pressure zones are, e.g. the intertropical convergence zone (low pressure), subtropical highs, the Iclandic low or the Azores high. However, not all pressure anomalies in Figure 2.2 are related to observable phenomena. The reduced pressure over highlands and over the Antarctic is prone to larger systematic effects induced by small deviations in lapse rate. A mean pressure value of more than $1050\,hPa$ seems to be rather unrealistic, albeit larger instantaneous pressure variations have already been observed. From the historical weather records an all-time minimum of $890\,hPa$ at sea level appeared on the 12th of November 1971 in Taifun Irma East on the Philippines with a decrease in pressure of $97\,hPa$ in $24.5\,h$ (Kraus, 2001). In contrast, a maximum of $1085\,hPa$ at sea level was observed on the 31st of December 1968 resulting in a cold high in Central Asia.
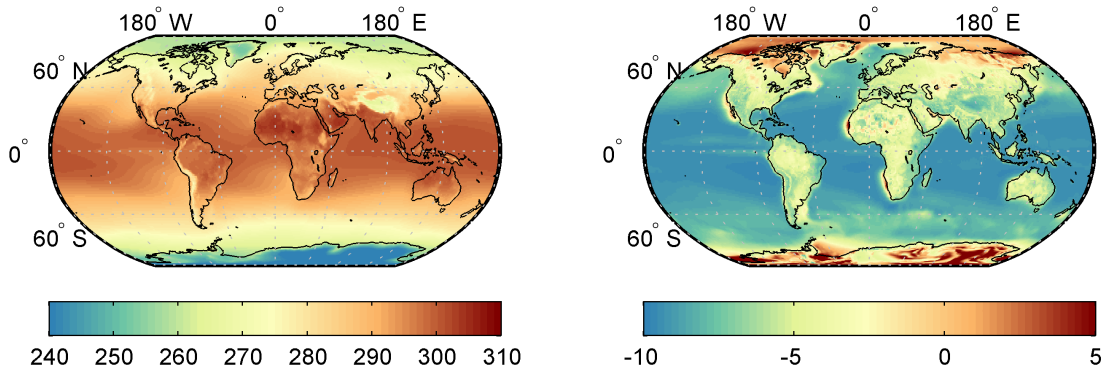
Figure 2.3: Global mean temperature in K (left) and lapse rate in K/km (right) as provided with GPT2w at the surface

2.3.1.3 Surface temperature and lapse rate

The global temperature in the lower atmosphere is a result of incoming solar radiation (see Figure 2.1) and convection influenced e.g. by clouds, turbulences, terrain (mountains, coastlines) or surface type (sea, snow, ice, ...). Figure 2.3 left shows the resulting mean temperature [K] as provided with GPT2w at the surface with a weighted Global Mean Surface Temperature (GMST) of $287.8\,K$ (14.6 °C). For the computation of GMST the

gridded temperature values were weighted by the cosine of the latitude of the grid points. The agreement between GMST derived from GPT2w and other datasets like from NASA (2016) is quite remarkable ($<$ 0.05 °C).

Highest temperatures are observed within the intertropical region and lowest over the polar regions, especially over the Antarctic. Large temperature horizontal gradients are visible in the mid-latitudes (meridional), and along coasts and mountains. Larger fluctuations (daily and annual) are mainly dedicated to land surfaces since oceans are much more thermal inert[6]. However, the land-sea contrast pronounced at the surface diminishes with height. Strong variations are smoothed out by atmospheric motions.

Figure 2.3 right shows the lapse rate [K/km] as derived for GPT2w from the temperature difference between the lowest levels of ERA-Interim with a global mean of $-5.3\,K/km$, valid near the surface. Under special circumstances a positive lapse rate (temperature inversion) is possible and common during night, over continents, sea ice and snow during winter; see Ramaswamy *et al.* (2006). However, a nominal lapse rate of $-4\,K/km$ in moist tropical areas and of -8 to $-9\,K/km$ in the drier subtropics as stated by Ramaswamy *et al.* (2006) is only partly confirmed, since the method applied to obtain lapse rates for GPT2w was tuned for use near the surface. Significant variation from nominal lapse rate in the planetary boundary layer (the lowest $2-3\,km$) is well known and documented (Wallace & Hobbs, 2006). Hence a single temperature gradient does not represent the entire vertical temperature variation in the lower atmosphere. Nevertheless, it is a good approximation of the temperature distribution up to around $9\,km$ at the poles and around $12\,km$ at the equator (Ramaswamy *et al.*, 2006).

Figure 2.4 separately shows the vertical mean temperature distribution up to $30\,km$ altitude for winter and summer months on both hemispheres. Significant lapse rate anomalies are visible near the surface and particularly in higher layers. According to the lapse rate criteria, the coldest layer in the lower atmosphere is defined as tropopause (see Section 2.4); highlighted in Figure 2.4 as a solid line between $9\,km$ at the poles and $16\,km$ at the equator. Above the tropopause, the temperature becomes isothermal, especially over the poles in local winter, or increases slightly, as visible over the tropics, low and middle latitudes.

Deviations from the nominal lapse rate define the stability of the atmosphere. A large negative lapse rate is related to stronger instability. The upper air is "too cold" and warmer air keeps rising, leading to convection and transport of humidity into higher atmospheric layers which is the precondition e.g. for cloud forming and precipitation.

---

[6]The thermal inertia of oceans is related to the higher specific heat capacity than air. In addition, the mixing in water bodies has a strong impact on the temperature variation.
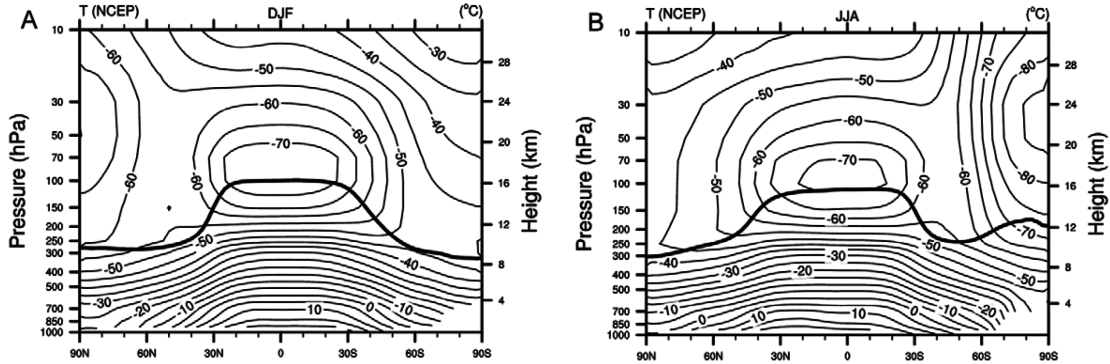
Figure 2.4: Global vertical temperature profiles as obtained from NCEP-NCAR reanalyses for December-January-February (left) and June-July-August (right). The solid line denotes the tropopause which separates the lower atmosphere from upper layers. Source: Ramaswamy *et al.* (2006)

For the characterisation of stability, a quantity, i.e. the so-called potential temperature T_Θ, was defined as the fictitious temperature a parcel of air would have at surface level assuming dry adiabatic conditions

$$T_\Theta = T \cdot \left(\frac{p}{p_s} \right)^{\frac{R_d}{c_p}} \tag{2.20}$$

where p_s is the pressure at surface level and c_p is the specific heat capacity as already introduced for the definition of lapse rate (see Eq.2.19). A constant potential temperature or an increase of potential temperature with height defines the status of a neutral or stable atmosphere, unlike a decrease of potential temperature which is related to static instability (Channon, 2016).

2.3.2 Water vapour distribution

Water remains in the atmosphere only 8-10 days[7], thus it tends to be rather locally concentrated. Since the water vapour in the atmosphere is closely linked to temperature distribution, the Clausius-Clapeyron relation allows for description of the water-holding

---

[7]The computation of residence time of water vapour in the atmosphere is based on the total mass of water in the atmosphere (around 30 kg/m² which corresponds to a global water layer of around 3 cm) and a mean rainfall rate of roughly 0.3 cm/day (Wallace & Hobbs, 2006).

capacity of the atmosphere as a function of temperature.

$$\ln\left(\frac{e_{s2}}{e_{s1}}\right) = \frac{\triangle H_{m,v}}{R}\left[\frac{1}{T_1} - \frac{1}{T_2}\right] \tag{2.21}$$

With temperature $T_1 = 287.8\,K$, $T_2 = T_1 + 1\,K$, ideal gas constant $R = 8.314459\,J/(mol\,K)$ and enthalpy of vaporisation of water $\triangle H_{m,v} = 45054\,J/mol$ (Marsh, 1987) an increase in temperature of $1\,K$ is related to an increase of saturation water vapour of $6.7\,\%$. Consequently, warmer air tends to be moister because it can hold more water vapour.

Figure 2.5 left shows the mean water vapour pressure in hPa, computed from the specific humidity grid provided by GPT2w using Eq.2.8.
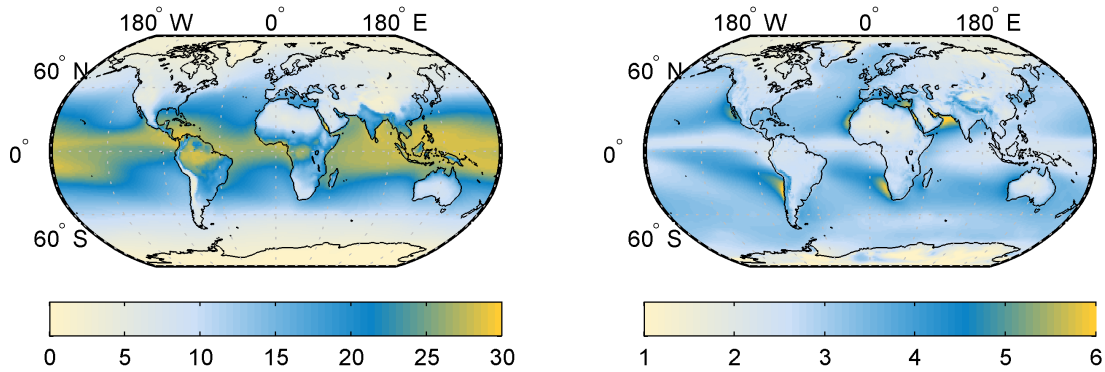
Figure 2.5: Global mean water vapour pressure in hPa (left) and decrease factor dimensionless (right) as provided with GPT2w at the surface

The global distribution of water vapour at the surface resembles the temperature distribution as shown in Figure 2.3, albeit larger regional deviations are visible e.g. over the Sahara or Australia. These deviations are related to the physiography of Earth´s surface, warm and cold ocean currents, and the ocean-land distribution because the air over the oceans contains in general more water vapour than over continents.

Figure 2.5 right shows the mean water vapour decrease factor λ_e which describes the decrease of water vapour with height as a function of partial pressures (dry air pressure p and water vapour pressure e) on two distinct levels.

$$e_1 = e_0 \cdot (p_1/p_0)^{\lambda_e+1} \tag{2.22}$$

The retrieval of λ_e is tricky because the distribution of water vapour with height is rather irregular (much more than the temperature lapse rate). Taking only layers near ground into account is yielding to unrealistic or at least to not practical values. Hence, for GPT2w a kind of vertical average value has been defined for each grid point without loosing information about its local characteristic (for further details see Böhm *et al.* 2015). On a regional scale λ_e reflects atmospheric circulations. In the intertropical convergence zone, upwelling moisture produces lower decrease factors than in the downwelling horse latitudes (30° north and south). High regional evaporation over the ocean causes a maximum decrease factor of up to 6.8 (the weighted mean is 2.96), which is related to a rapid decrease of water vapour with height.
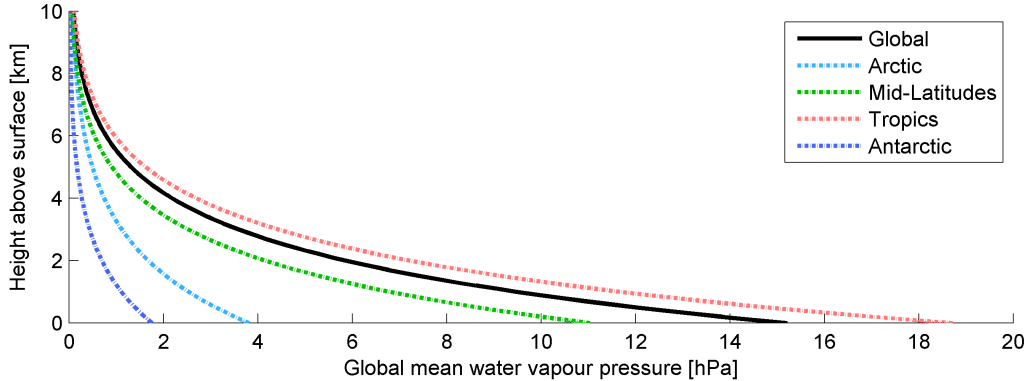
Figure 2.6: Global vertical mean water vapour pressure distribution

Figure 2.6 shows the vertical trend in water vapour decrease with height for specific latitude bands. Although large zonal variations are visible near the surface, only a very small amount of water vapour remains in higher atmospheric layers, above $10\,km$ altitude. Just a very small amount of water vapour breaks through into higher layers and affects to a certain extent the radiative balance which causes higher temperatures in lower atmosphere and cooling above (Schiller *et al.*, 2009).

Measurements of the vertical humidity distribution, e.g. from radiometers, radiosounders, microwave or infrared satellite systems (see Chapter 5), confirm these processes but show also significant short-term deviation from climatological maps in lower layers. Thus, in contrast to the dry components of air, water vapour is more variable (temporally and spatially) and therewith much more difficult to predict.

2.4 The atmospheric layers

The vertical distribution of temperature is widely used for dividing the atmosphere into different layers. Figure 2.7 shows the four distinct layers (troposphere, stratosphere, mesosphere and thermosphere) related to the mean temperature distribution in mid latitudes up to $100\,km$ above the surface. Two adjacent layers are separated by a transition layer called pause [pauein, greek: 'to stop'] which is characterised by a rather constant temperature distribution and therefore acts as a barrier between distinct layers.
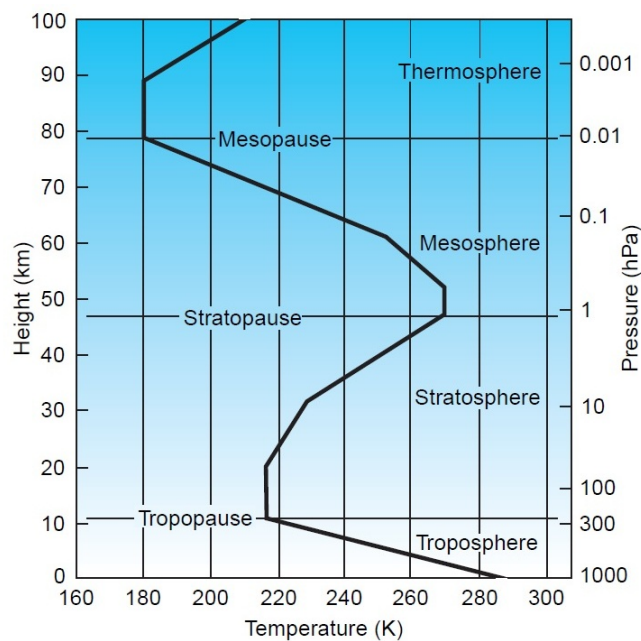
Figure 2.7: U.S. Standard Atmosphere 1976: Annual mean temperature in mid latitudes. Source: Wallace & Hobbs (2006)

The **troposphere** is characterised by an average temperature lapse rate of ~ 6.5 °C/km and encompasses the lower $7\,km$ to $20\,km$ of the atmosphere, thus it is also called the lower atmosphere. Within this layer about $90\,\%$ of total atmospheric mass and about $99\,\%$ of the water vapour and aerosols are concentrated (Wallace & Hobbs, 2006). The troposphere is emphasised since most of the weather phenomena like clouds, rain, snow, hurricanes or thunderstorms occur in the lower atmosphere. Strong vertical winds and the relatively high mean water vapour content of $30\,kg$ per $1\,m^2$ surface area determine the fundament of clouding and precipitation formation. The vertical movements are widely

induced by differential heating of the surface with larger variations between low and high latitudes.

The cold **tropopause** delimits the troposphere from the overlying stratosphere and is defined by an abrupt change in temperature lapse rate. The WMO (1957) described the tropopause as "the lowest level above $450\,hPa$ at which the lapse rate decreases to 2 °C/km or less, provided that the average lapse rate between this level and all higher levels within $2\,km$ does not exceed 2 °C/km". Since temperature decrease is a precondition for convective heat transfer - the dominant heat transfer in liquids and gases - the tropopause acts as a barrier between troposphere and stratosphere. Thus almost no water vapour is observed above the tropopause. Reichler *et al.* (2003) used the definition of the World Meteorological Organization (WMO) to compute tropopause heights and extracted the corresponding pressure values from ECMWF level III data (January and July 1992 - 1994). The tropopause pressure values were compared with observed tropopause pressure values at 340 global radiosonde stations. Largest deviations of up to $60\,hPa$ were found in the subtropics and mid-latitudes of both hemispheres which are "most likely associated with strong meridional gradients in tropopause height". Rieckh *et al.* (2014) analysed radio occultation data from 2001 to 2013 and confirmed the height variability at northern hemispheric mid latitudes and in the Asian monsoon region. Santer *et al.* (2003) found recent changes of tropopause heights to be the result of anthropogenic and natural external forces and further detected a global-mean tropopause pressure decrease by $2.16\,hPa$/decade. This goes along with an increase in tropical tropopause height and a cooling of the tropopause.

The second lowest layer, the **stratosphere**, contains about $10\,\%$ of total atmospheric mass and is governed by an increase of temperature with height up to $\sim 50\,km$ which causes strong stratification. The stratosphere is dynamically stable, dry and ozone rich[8]. Vertical mixing is much more inhibited and particles tend to remain longer in the stratosphere than in the troposphere. The temperature increase is caused by absorption of high energy radiation and breaking of ozone into atomic (O_1) and molecular oxygen (O_2). An interesting feature of stratospheric circulation is gravity wave[9] induced quasi-biennial oscillations (QBO) (Baldwin *et al.*, 2001) which induce global mass transport of tracers like ozone or water vapour. The conditions in the stratosphere have a significant impact on weather condition and processes, like the forming of low-pressure areas in the troposphere.

---

[8]300 times higher concentration than at Earth´s surface
[9]Gravity waves are sinusoidal vertical density and temperature variations in the atmosphere.

The **mesosphere** is defined by a strong negative temperature gradient between $50\,km$ and $80\,km$ (up to $100\,km$, dependent on latitude and season) above the surface. Strong zonal East-West winds dominate the dynamic in this part of the middle atmosphere, and gravity wave amplitudes can become so large that they dissipate and drive global circulation. The degree of ionisation increases with height and ends up in the D-layer at $60\,km$ to $80\,km$, visible at daytime. Since the mesosphere lies above maximum altitudes for aircrafts and balloons and below the lowest altitude for orbital spacecrafts it is so far poorly understood.

The **thermosphere** is defined by an increase of mean temperature with height due to absorption of solar radiation which goes along with photodissociation and photoionisation. Dependent on solar activity the degree of photoionisation and temperature varies significantly and therewith the concentration of free electrons and ions in the atmosphere. The layer with highest concentration of free electrons and ions (F-layer) defines the upper layer of the thermosphere at around $500\,km$ to $800\,km$ altitude. Beyond, the term exosphere [ἔξω éxō, ancient greek: 'outside'] is used to characterise the outer upper part of the atmosphere. Molecules are gravitationally and magnetically bound but the density is too low, thus this part is not further considered herein.

Apart from a separation based on the vertical distribution of temperature, also other criteria for differentiation can be applied. Widely used is a separation based on the degree of ionisation. The **neutral atmosphere** describes the non-ionised component of the atmosphere. It comprises the troposphere, stratosphere and dependent on the solar activity also parts of the mesosphere up to $70-80\,km$ above the surface. The atmospheric component above is called the **ionosphere** and encompasses the upper mesosphere and thermosphere. The outer ionosphere also forms part of the magnetosphere.

Chapter 3

Electromagnetic wave propagation in the neutral atmosphere

Electromagnetic wave propagation defines how energy is transferred through a medium. A closer examination of this phenomenon was carried out and is described in the following to reveal the basic relations between electromagnetic waves and the refractive and reflective properties of the traversed medium, in particular the neutral atmosphere. Thereby the index of refraction is of special significance since it connects the properties of electromagnetic waves with the atmospheric state variables (pressure, temperature, humidity, ...). This allows the usage of electromagnetic signals for sensing the neutral atmosphere. In this respect, the global horizontal and vertical distribution of refractivity is reviewed to obtain a first impression about the related information content in electromagnetic, especially in microwave signals.

3.1   Maxwell´s equations

The basic equations which describe signal propagation were formed in 1862 by J. C. Maxwell, known as the four Maxwell's equations (Jackson, 1998).

$$\nabla \cdot E = \frac{\varrho}{\epsilon}, \quad \nabla \times E = -\frac{\partial B}{\partial t}$$

$$\nabla \cdot B = 0, \quad \nabla \times B = \mu J + \mu\epsilon\frac{\partial E}{\partial t}$$

(3.1)

According to Eq.3.1 a electric field E is either caused by electric charges or by a varying magnetic field. The nabla-operator ∇ describes the divergence of E. The strength of the

electric field is determined by the total charge ϱ and the electric permittivity ϵ of the propagation medium.

In turn, the magnetic flux density B is a function of the change in the electric field E (i.e. E and B are coupled). B can be described by the magnetic permeability μ of the propagation medium and the change in the electric current density $J = \kappa \cdot E$, with κ as the electric conductivity of the propagation medium. In free space, i.e. in a non-conducting media like the neutral atmosphere, the total charge ϱ and the electric conductivity κ are well approximated by zero.

Assuming little spatial and temporal variation of ϵ and μ, Eq.3.1 can be decoupled. By following (Thide, 2011) two equivalent second-order partial differential equations for the electric and the magnetic field are obtained, describing how the fields propagate as vector waves through free space.

$$\nabla^2 E = \mu\epsilon\frac{\partial^2 E}{\partial t^2}$$

$$\nabla^2 B = \mu\epsilon\frac{\partial^2 B}{\partial t^2}$$
(3.2)

The resulting phase velocity v_p of the electromagnetic wave is determined by the medium-dependent constants ϵ and μ.

$$v_p = \frac{1}{\sqrt{\epsilon \cdot \mu}}$$
(3.3)

In vacuum, where $\epsilon_0 = 8.854187817 \cdot 10^{-12}\,F/m$ and $\mu_0 = 4\pi \times 10^{-7}\,H/m$, the phase velocity follows to $v_p = 299792458\,m/s$, i.e. the electromagnetic wave propagates with the speed of light. According to Jackson (1998) the phase velocity is also defined as the ratio between the constant speed of light c and a quantity n which is called the index of refraction. It expresses the refractive and reflective properties of the traversed medium

$$v_p = \frac{\nu}{k} = \frac{c}{n}$$
(3.4)

where ν is the frequency and k is the wave number. In vacuum is $n = 1$, in matter is $n \neq 1$, i.e. the signal is slower or faster than the speed of light, dependent on the electric and magnetic properties of the medium. In the neutral atmosphere is $1 < n < 1.0004$, hence the index of refraction is often replaced by refractivity N which scales n up according to:

$$N = (n - 1) \cdot 10^6$$
(3.5)

whereby N is expressed in mm/km (ppm).

3.2 Frequency dependency

In quantum optics electromagnetic fields are considered as quantum objects, characterized by its elementary energy parcels, called photons. The Planck constant $\hbar = 6.626 \cdot 10^{-34}\,J \cdot s$ relates the energy of a single photon E_h to the frequency ν according to:

$$E_\hbar = \hbar \cdot \nu \tag{3.6}$$

where the frequency describes the number of repeating cycles per second and is usually given in Hz (hertz) according to Heinrich Rudolf Hertz who provided 1887 first evidence of electromagnetic waves (Hertz, 1887). The whole electromagnetic spectra encompasses more than 24 orders of magnitude, ranging from $1\,Hz$ to $10^{24}\,Hz$, see Figure 3.1.
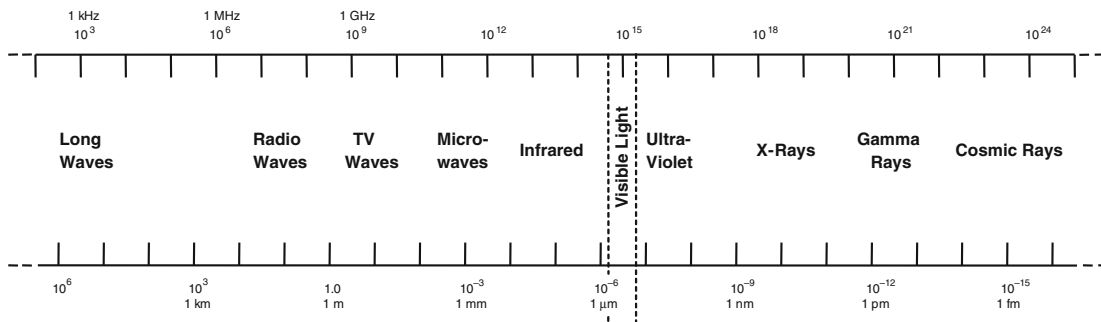
Figure 3.1: Electromagnetic spectrum. Source: Halliday *et al.* (1981)

According to standards of the Institute for Electrical and Electronic Engineers (IEEE, 2003) the microwave frequency spectra is further proratable into various frequency bands. Table 3.1 gives an overview about the frequency bands defined between $1\,GHz$ and $110\,GHz$, whereby the L-band is of greatest interest for navigation applications, in particular for GNSS (see Section 4.1).

Band designation	L	S	C	X	Ku	K	Ka	V	W
Frequency range [GHz]	1-2	2-4	4-8	8-12	12-18	18-27	27-40	40-75	75-110

Table 3.1: Standard microwave-frequency bands

The relation between frequency and wavelength λ is given by Eq.3.7:

$$\lambda = \frac{v_p}{\nu} = \frac{n}{k} \tag{3.7}$$

23

where v_p is the phase velocity, k is the wave number and n is the index of refraction. Latter is therewith related to the propagation velocity but also to the frequency of the electromagnetic wave.

For a more detailed description Liebe (1985) split the refractivity $N = (n-1) \cdot 10^6$ into three components.

$$N = N_0 + N^{'}(\nu) + i\, N^{''}(\nu) \tag{3.8}$$

The real part $N_0 + N^{'}(\nu)$ consists of a frequency-independent term N_0 plus a dispersive refraction term $N^{'}(\nu)$ and describes the refraction and the change in speed of the radio wave. If the medium has no optical loss or gain, the imaginary part is zero, otherwise the refractivity N becomes complex. The imaginary part describes the absorption by atmospheric constituents, whereby the specific attenuation γ is computed according to:

$$\gamma = K(\lambda) \cdot N^{''} \tag{3.9}$$

where $K(\lambda)$ is a wavelength dependent constant and $N^{''}$ describes the oxygen and water vapour distribution at their specific resonant lines, see Liebe (1985). Figure 3.2 shows the specific attenuation for the microwave frequency band (1 - 1000 GHz).
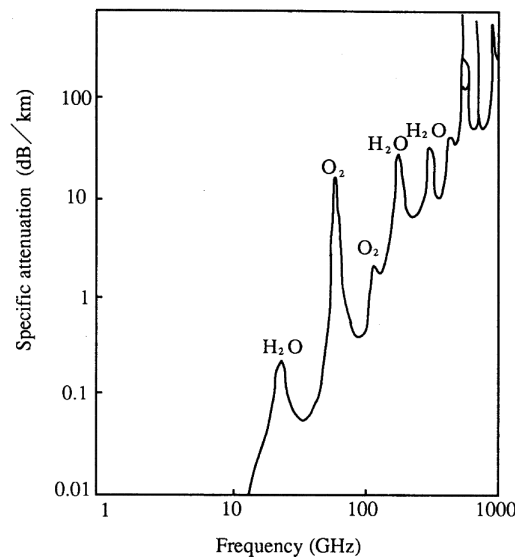
Figure 3.2: Microwave absorption due to atmospheric gases. Source: Kraus (2001)

Attenuation of microwaves mainly due to water and oxygen begins to matter above $20\,GHz$. Thus for atmospheric research by means of satellite techniques the frequency

range is limited to so-called atmospheric windows. The radiation in other frequency bands is mainly absorbed by trace gases like CO_2, H_2O, OH or CH_4. Since clouds and rain are not penetrated by infrared and optical frequencies only the radio signals ($3\,Hz$ - $3\,THz$), especially the microwave signals ($0.3\,GHz$ to $100\,GHz$) are of particular interest for continuous space-based applications (see Marzano & Visconti, 2003 for further details).

3.3   Atmospheric refraction

In Section 2.3 the atmosphere was specified as a two-component, gaseous system formed by dry air and water vapour and is therewith well described by three independent variables, e.g. pressure p, temperature T and specific humidity q. In order to connect the index of refraction n with these state parameters, the Clausius-Mossotti equation is introduced

$$\frac{\epsilon - 1}{\epsilon + 2} \cdot \frac{M}{\rho} = \frac{N_a \cdot \alpha_e}{3 \cdot \epsilon_0} \tag{3.10}$$

where:

ϵ	is the electric permittivity with ϵ_0 as the vacuum permittivity
M	is the molar mass
ρ	is the air density
N_a	is the Avogadro constant and
α_e	is the electronic polarisability.

According to Lorenz (1880) the electric permittivity ϵ can be replaced by $n = \sqrt{\epsilon}$. For cases in which the index of refraction is around one (like in air) Eq.3.10 can be further simplified to:

$$n - 1 = \frac{N_a \cdot \alpha_e}{2 \cdot \varepsilon_0} \cdot \frac{\rho}{M} = \frac{2}{3}\alpha_m \cdot \frac{\rho}{M} \tag{3.11}$$

The index of refraction is consequently proportional to the density of air, whereby the term α_m describes the molar polarisability. Further, Eq.3.11 can be combined with the ideal gas equation (Eq.2.3) to connect the index of refraction with the state parameters pressure and temperature

$$n - 1 = K_1' \cdot \frac{p}{T} \tag{3.12}$$

where the proportionality factor K_1' is a constant.

However, for polar gases like water vapour, which possess a permanent dipole, the dipole moment d cannot be neglected anymore. Thus, in 1929 P. J. W. Debye added an additional term to the Clausius-Mossotti equation which describes the polarisation of the dielectric

$$\frac{n^2 - 1}{n^2 + 2} \cdot \frac{M}{\rho} = \frac{N_a}{3 \cdot \varepsilon_0} \cdot \left(\alpha_e + \frac{d^2}{3 \cdot k_B \cdot T} \right) \tag{3.13}$$

where $k_B = 1.381 \cdot 10^{-23} J/K$ is the Boltzmann constant and T is temperature in K. Therewith the relation between index of refraction, pressure and temperature concludes to

$$n - 1 = \frac{p}{T} \cdot \left(A + \frac{B}{T} \right) \tag{3.14}$$

where "the A term represents the contribution to the dielectric constant of the atomic and electronic polarisation, and the B term the contribution of the dipole moment" (Essen & Froome, 1951, p. 871). Since water vapour is the only major gas in the atmosphere that has a permanent dipole moment, the B term is directly related to water vapour in the atmosphere.

According to Dalton´s law and analogous to Eq.2.5, the refractivity of moist air[1] is obtained by combination of Eq.3.12 and Eq.3.14

$$N = K_1 \cdot \frac{p_d}{T} + K_2 \cdot \frac{e}{T} + K_3 \cdot \frac{e}{T^2} \tag{3.15}$$

where p_d is the partial pressure of dry air. The index of refraction was replaced by the refractivity N, expressed in ppm. Further, the pressure of the polar gases was replaced by water vapour pressure e. The factor K_1 accounts for the dry air contribution to the total refractivity, K_2 and K_3 are the factors for water vapour. For a specific frequency these factors are constants. Thereby it is assumed that the air is an ideal gas. The deviation from an ideal gas can be described by compressibility factors, separately for dry air (Z_d) and water vapour (Z_w). Therefore Eq.3.15 has to be extended:

$$N = K_1 \cdot \frac{p_d}{T} \cdot Z_d^{-1} + K_2 \cdot \frac{e}{T} \cdot Z_w^{-1} + K_3 \cdot \frac{e}{T^2} \cdot Z_w^{-1} \tag{3.16}$$

A number of expressions exist for estimating the compressibility factors. In literature widely the empirical expressions from Owens (1967) are used. For a more detailed description the reader is referred to Aparicio *et al.* (2009).

---

[1]Moist air is described by a two-component, gaseous system formed by dry air and water vapour.

3.3.1 Refractivity constants

Over the last decades the refractivity constants were re-calculated for specific frequency bands. Table 3.2 provides an overview about the most common sets of constants, valid for microwaves (see Section 3.2).

Author	$K_1 \left[\frac{K}{hPa}\right]$	$K_2 \left[\frac{K}{hPa}\right]$	$K_3 \left[\frac{K^2}{hPa}\right]$
Essen & Froome (1951)	77.636 ± 0.027	64.695 ± 0.198	371800 ± 400
Smith & Weintraub (1953)	77.607 ± 0.013	71.6 ± 8.5	374700 ± 3100
Thayer (1974)	77.604 ± 0.014	64.79 ± 0.08	377600 ± 400
Bevis *et al.* (1994, unweighted)	77.6 ± 0.05	70.4 ± 2.2	373900 ± 1200
Rüeger (2002, best average)	$77.689^2 \pm 0.0094$	71.2952 ± 1.3	375463 ± 760

Table 3.2: Review of refractivity coefficients

In order to obtain these constants, the index of refraction $(n - 1)$ was either measured precisely using e.g. microwave cavity methods (Essen & Froome, 1951) or extrapolated from available optical measurements (Thayer, 1974) to the microwave frequency band. Almost all coefficients listed in Table 3.2 are based on measurements which were conducted before the 1960´s and differ mainly due to selection and averaging strategies. Smith & Weintraub and Thayer´s coefficients were the first relative reliable sets with a high nominal precision (see Bevis *et al.*, 1994). Later studies, e.g. by Hill *et al.* (1982), revealed that the standard deviation of these coefficients and of several measurements are too optimistic and further, that the extrapolated values of Thayer, especially K_2 does not fit to measurements in the microwave frequency band. Bevis *et al.* (1994) combined 17 (7) available measurements to compute unweighted mean values for K_1 (K_2 and K_2), i.e. without taking their "unknown" precision into account. Since the fundamental relations are still not fully understood, the combination of available measurements seems to be the most appropriate and the most robust method. This was presumably the thought of Rüeger (2002) who took the largest available set of measurements into account and computed therefore a "best average" and a "best available" set but unfortunately without giving any recommendation on which set should be finally used. Hence, today a variety of coefficients is in common use. Until new findings or rather more accurate measurement are available, the "best average" values as provided by Rüeger (2002) are used in further analysis.

---

[2]assuming a carbon dioxide concentration of 375 ppm

Essen & Froome (1951) introduced also a fourth constant (K_c) for carbon dioxide since it is not as constant as the other dry gases[3]. Although a certain carbon dioxide concentration was already considered for the computation of K_1, it should be updated from time to time taking the actual CO_2 concentration into account. For practical purposes the annual variation can be neglected so far, hence K_c is treated as optional.

Further, additional terms were added to take the contribution of hydrometeors (cloud water, ice or snow) into account. The extended refractivity equation without compressibility factors then reads:

$$N = K_1 \cdot \frac{p_d}{T} + K_2 \cdot \frac{e}{T} + K_3 \cdot \frac{e}{T^2} + K_{lw} \cdot M_{lw} + K_{ice} \cdot M_{ice} \qquad (3.17)$$

where M_{lw} is the liquid water content and M_{ice} is the amount of ice water in the atmosphere. Liebe et $al.$ (1991) proposed a method which allows to compute the refractivity constants (K_{lw} and K_{ice}) from the density of liquid water and ice, temperature and frequency. For frequencies less than $100\,GHz$ is $K_{lw} \sim 1.45$ and $K_{ice} \sim 0.69$. Under certain (severe weather) conditions hydrometeors cause a delay of GNSS signals of up to several centimetre (Douša et $al.$, 2016). However, in most cases the additional terms are negligible.

For most GNSS applications it might be useful to replace the pressure of dry air p_d by the total mass density $\rho = \rho_d + \rho_w$. Therewith a hydrostatic component (N_h) and a non-hydrostatic component (N_{nh}) is obtained

$$N = N_h + N_{nh} = K_1 \cdot \frac{R}{M_d}\rho + K_2' \cdot \frac{e}{T} + K_3 \cdot \frac{e}{T^2} \qquad (3.18)$$

where the new constant K_2' is given by

$$K_2' = K_2 - K_1 \cdot \frac{M_w}{M_d}. \qquad (3.19)$$

The hydrostatic component is slightly larger[4] than the dry component but nearly independent from the highly variable mixing ratio (mass of water vapour to mass of dry air), which can be of practical relevance.

---

[3] The carbon dioxide concentration increases by 1 to $1.5\,ppm/year$ with an annual variation of about $6\,ppm$ due to photosynthesis (Peixoto & Oort, 1992).

[4] The difference between hydrostatic and dry refractivity is always positive and can be up to $10\,ppm$ under very warm and humid conditions (T = 40 °C and rh = 100 %), see Mendes (1999).

3.3.2 Uncertainty of refractivity

Assuming that Eq.3.15 is exact, the uncertainty of N can be evaluated by means of the law of error propagation (assuming that the parameters are uncorrelated) according to:

$$N = \frac{\partial N}{\partial T}dT + \frac{\partial N}{\partial p}dp + \frac{\partial N}{\partial e}de + \frac{\partial N}{\partial K_1}dK_1 + \frac{\partial N}{\partial K_2}dK_2 + \frac{\partial N}{\partial K_3}dK_3 \qquad (3.20)$$

In consequence the uncertainty of refractivity (σ_N) is determined by the standard deviations of the individual components.

$$\sigma_N = \left[\left(\frac{\partial N}{\partial T} \cdot \sigma_T \right)^2 + \left(\frac{\partial N}{\partial p} \cdot \sigma_p \right)^2 + \left(\frac{\partial N}{\partial e} \cdot \sigma_e \right)^2 + \left(\frac{\partial N}{\partial K_1} \cdot \sigma_{K_1} \right)^2 + ... \right]^{\frac{1}{2}} \qquad (3.21)$$

In order to solve Eq.3.21, the theoretical standard deviation σ for pressure, temperature and relative humidity was taken over from WMO (2008), which provides realistic margins for a wide range of meteorological parameters (assuming sensor performance under nominal and recommended exposure). The uncertainty of the constants were set according to Rüeger (2002, best average coefficients) and are summarised in Table 3.3 together with the used standard deviations for the other relevant parameters.

σ_p	σ_T	σ_{rh}	σ_e	σ_{K1}	σ_{K2}	σ_{K3}
$\pm 0.3\,hPa$	$\pm 0.2\,K$	$\pm 3\,\%$	$\pm 0.52\,hPa$	$\pm 0.0094\,K/hPa$	$\pm 1.3\,K/hPa$	$\pm 760\,K^2/hPa$

Table 3.3: Standard deviations, i.e. the achievable measurement uncertainty of relevant meteorological parameters and constants

The standard deviation σ_e of water vapour was computed by applying the law of error propagation to Eq.2.9 by taking σ_T and σ_{rh} into account. Subsequently, the values in Table 3.3 were used for the calculation of the theoretical standard devition of refractivity. The results, assuming standard atmospheric conditions at sea-level, are listed in Table 3.4.

$\frac{\partial N}{\partial T}\sigma_T$	$\frac{\partial N}{\partial p}\sigma_p$	$\frac{\partial N}{\partial e}\sigma_e$	$\frac{\partial N}{\partial K_1}\sigma_{K1}$	$\frac{\partial N}{\partial K_2}\sigma_{K2}$	$\frac{\partial N}{\partial K_3}\sigma_{K3}$	σ_N
$\pm 0.25\,ppm$	$\pm 0.08\,ppm$	$\pm 2.37\,ppm$	$\pm 0.03\,ppm$	$\pm 0.05\,ppm$	$\pm 0.09\,ppm$	$\pm 2.39\,ppm$

Table 3.4: Uncertainty of refractivity and its components assuming standard atmospheric conditions ($p = 1013\,hPa$, $T = 15\,°C$, $rh = 60\,\%$)

The standard deviation of refractivity is $\pm 2.39\,ppm$ which equates to an percentage uncertainty of about $\pm 0.75\,\%$. By far the largest impact ($\pm 2.37\,ppm$) is related to the uncertainty of water vapour. The refractivity constants alone have only a minor impact on the refractivity. Under standard atmospheric conditions their uncertainties sum up to $\pm 0.11\,ppm$ ($\pm 0.03\,\%$) which is rather negligible.

In order to determine the refractivity with an uncertainty of $\pm 1.0\,ppm$, the temperature must be measured with an standard deviation of $\pm 1.0\,K$, which corresponds to an standard deviation in pressure of around $\pm 13\,hPa$, or $\pm 5\,\%$ in relative humidity. Thereby it is assumed that the respective other parameters are determined error-free. Consequently, utmost care has to be taken when measuring humidity and temperature.

3.4 Global and local refractivity distribution

The refractivity expresses the state of atmosphere and varies like its describing parameters in time and space. Fabry (2006) found, that the distribution of refractivity on mesoscale is widely related to variability in humidity (75 % of the total contribution) and temperature (24 %) and only slightly affected by pressure variations. The horizontal and vertical distribution of these meteorological parameters is discussed in Section 2.3.

The refractivity is of special interest because it highlights the interaction between the meteorological parameters and is therewith a valuable parameter for the analysis of the current weather situation and climate. In order to highlight the horizontal distribution near ground the empirical model GPT2w was used to compute mean refractivity values at the surface, separately for the dry and wet component. For the description of the vertical distribution, the most prominent models are highlighted and compared to the radiosonde observations which allows to compute vertical profiles, reflecting the current state of the atmosphere.

3.4.1 Horizontal distribution near ground

For analysis of the horizontal refractivity distribution, gridded mean pressure, temperature and specific humidity values provided by GPT2w at the surface were converted to dry and wet refractivity using Eq.2.8 and Eq.3.15. Its global distribution is shown in Figure 3.3.

The weighted sum of the gridded values yields to a Global Mean Surface Refractivity (GMSR) of $332\,ppm$, whereby the largest part ($262\,ppm$) is caused by the dry atmospheric constituents and $70\,ppm$ by water vapour.
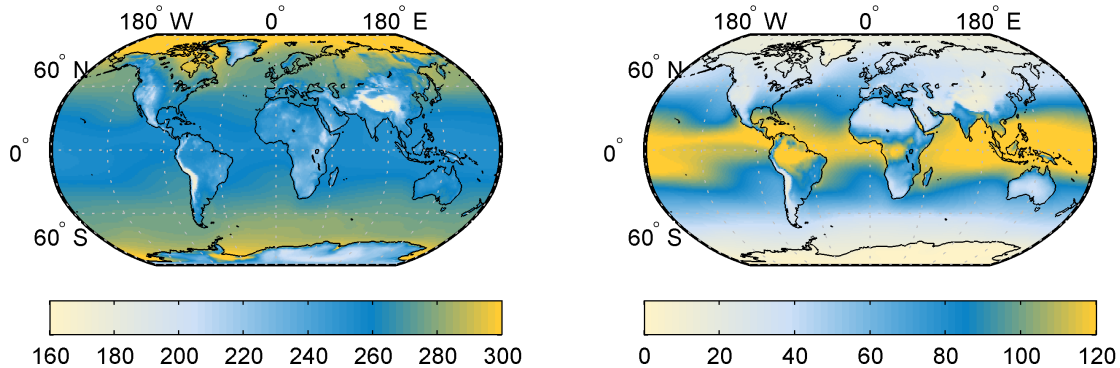
Figure 3.3: Global mean dry refractivity in ppm (left) and wet refractivity in ppm (right) derived from GPT2w pressure, temperature and specific humidity values at the surface

Local deviations from GMSR are primarily latitude- and altitude-dependent. Lower temperatures at higher latitudes induce largest dry refractivities (of around $300\,ppm$), especially over the Arctic. Lowest refractivities (around $180\,ppm$) are related to low pressure values over the mountain ranges in Asia, South America and the Antarctic.

Although water vapour contributes only by around $20\,\%$ to refractivity, the induced wet refractivity variations on global scale are almost as large as for the dry constituents, namely $120\,ppm$. The largest wet refractivities of more than $130\,ppm$ are observed at low latitudes, especially over oceans, in the tropics and subtropics. In contrast almost no wet refractivity exists over the poles and highlands.

Maps of annual refractivity variations (not shown here), e.g. as computed by Bean & Dutton (1966), reveal that the refractivity distribution widely reflects global climate differences. The prevailing transport of moist maritime air inland e.g. over Europe induces relatively small annual variations of 20 to $30\,ppm$. In contrast annual changes of up to $90\,ppm$ are observed south of the sahel zone over Africa or over the Indian monsoon region. In general large continental cells with moderate variation stand out from ocean cells, characterised by rather small variability.

Figure 3.4 shows the course of refractivity for Innsbruck, Austria over a period of two weeks in May 2013. The time series were derived from meteorological measurements of pressure, temperature and relative humidity, observed at the airport of Innsbruck (lat: 47.26°, lon: 11.36°, H: 578 m). More details about the measurement sensors and their uncertainty are provided in Section 5.1.
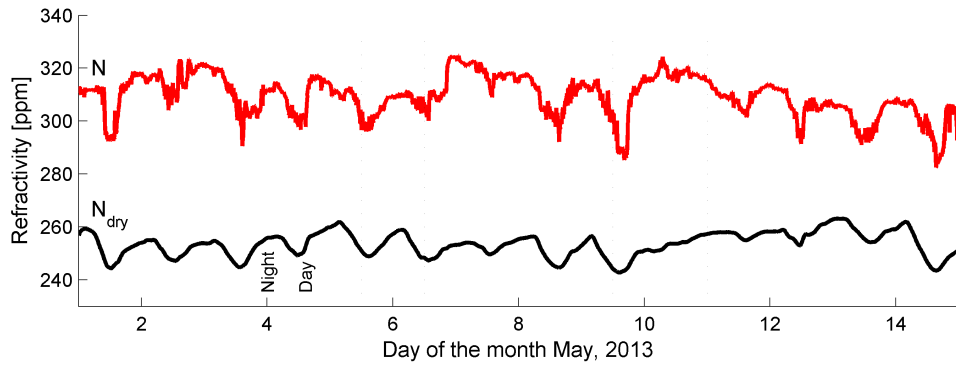
Figure 3.4: Refractivity variations as observed in Innsbruck, Austria in May 2013

Largest refractivity variations in Figure 3.4 are related to the daily cycle of temperature and water vapour pressure, overlaid by small-scale fluctuations of humidity. A small negative peak like during the 3rd of May, 12 UTC is most likely related to a cold front passing which caused a decrease in temperature and relative humidity. Larger variations in refractivity are also related to storm events and stronger vertical winds like it was observed in the evening of the 3rd of May. In general, strong short-term variations during the day were observed around sunset and smallest around sunrise. Fabry (2006) explained this effect by variations of surface winds, which are mostly stronger in the afternoon than in the morning.
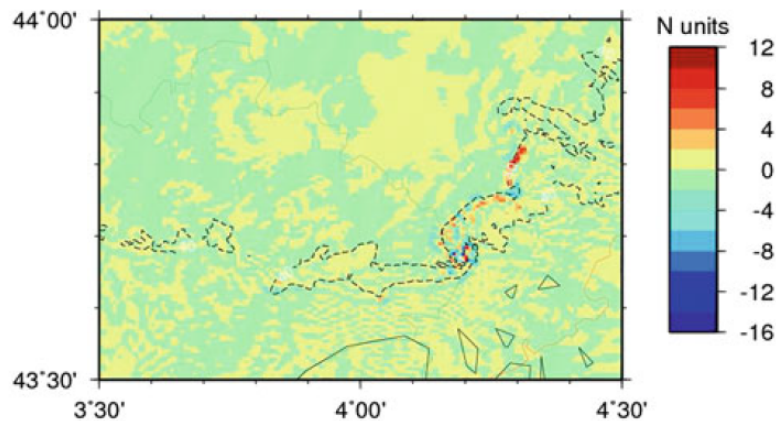
Figure 3.5: Possible near-ground refractivity change within a mesoscale convective system, derived from the high-resolution Meso-NH model for the 20th October 2008, 15:49 UTC. Source: Besson *et al.* (2012)

Peixoto & Oort (1992) analysed the spectrum of kinetic energy and confirmed the daily cycle but found also large energy variations in the annual cycle and in the periods of days to weeks, which are related to large-scale transient disturbances in mid-latitudes along the polar front. An additional peak in the sub-daily spectrum of kinetic energy was detected and is allocated to small-scale turbulent motions with a maximum at the $1\,min$ period.

Figure 3.5 shows possible changes in refractivity within one minute near surface as generated by Besson *et al.* (2012) from simulations of a mesoscale convective system formed at the 20th of October 2008 over the Hérault plains in South France. The highest changes of up to $12\,ppm/min$ are colocated with the most intense activity in the quasi-stationary convective band caused by the rapid evolution of the storm at that time.

Houze (2004) stated that convective activity generates large spatial and temporal variability in temperature and humidity, through evaporation and condensation processes involved in the upward motion of moist air and during precipitation events. Besson *et al.* (2012) analysed the dynamic and thermodynamic fields of a mesoscale convective system and found that a cold and dry pool is generated by evaporation at middle and high levels just ahead of the convection, which can be observed as sharp changes in refractivity. A change in refractivity of about $20\,ppm$ or more within a distance of about $20\,km$ is highly connected to strong vertical winds and severe weather. This specific variability leads to refractivity variations that can be used to characterise these phenomena. A deeper inside is expected from the analysis of vertical refractivity profiles.

3.4.2 Vertical distribution

Vertical profiles of refractivity can be reconstructed from surface measurements using models like the standard atmosphere model for refraction (IEEE, 1990), which is based on the exponential function:

$$N(H) = N_s \cdot \exp\left[\lambda_h \cdot (H - H_s)\right] \tag{3.22}$$

where N_s is the refractivity at surface, $\lambda_h = -0.136\,km^{-1}$ is the decrease factor, H_s is the surface height and H the height of interest.

Another, more sophisticated model was proposed by Hopfield (1969) which describes the refractivity profile as a polynomial function of height, separately for the dry and the wet component.

$$N_d = N_{ds} \cdot \left(\frac{H_d^e - H}{H_d^e}\right)^\mu \tag{3.23}$$

$$N_w = N_{ws} \cdot \left(\frac{H_w^e - H}{H_w^e} \right)^{\mu} \tag{3.24}$$

with

$$\mu = \frac{g}{R_d \Gamma} - 1. \tag{3.25}$$

Assuming that $g = 9.80665 \, m/s^2$, $R_d = 287.0569 \, J/(kg \, K)$ and temperature lapse rate $\Gamma = 0.0068 \, K/m$, μ is around 4. Both terms, H_d^e and H_w^e express the height above surface at which N_d and N_w are zero. They can be computed from surface temperature (t_s) in °C by the following empirical equations of Hopfield (1969), see Mendes (1999).

$$H_d^e = 40.136 + 0.14872 \cdot t_s \tag{3.26}$$

$$H_w^e = 13.268 - 0.09796 \cdot t_s \tag{3.27}$$

Figure 3.6 left of centre shows dry and wet refractivity profiles derived from radiosonde observations in Vienna, Austria. Background information to the radiosonde data are provided in Section 5.4.
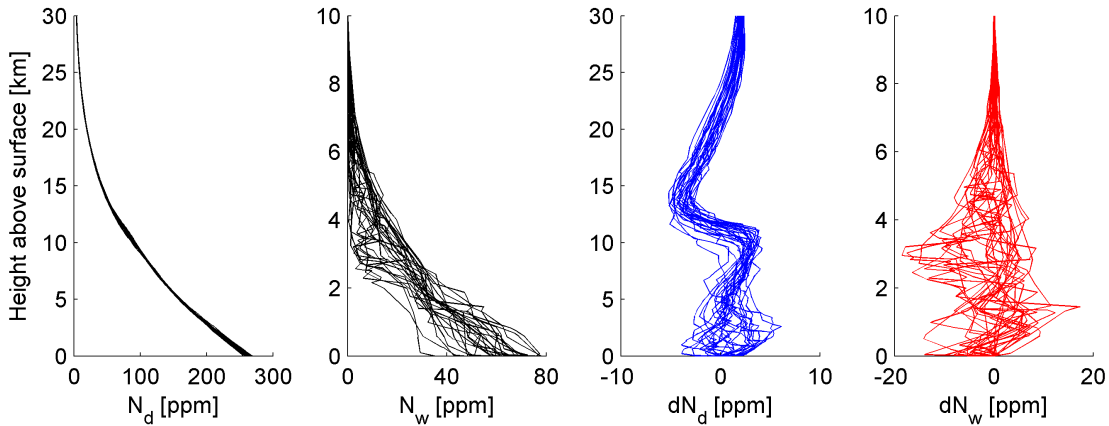
Figure 3.6: Refractivity profiles at radiosonde site Vienna during the first two weeks in May 2013. The blue and red curves represent the differences between Hopfield (1969) model and radiosonde profiles, respectively for dry and wet refractivity

The profiles, as observed twice a day (00:00 UTC and 12:00 UTC) during May 2013, were stacked separately for the dry and the wet component to highlight their temporal variations. While the dry refractivity profile remains rather stable over time and decreases almost exponentially with height (as expected from an atmosphere in hydrostatic equilibrium) the wet profiles are much more scattered. Already at surface it varies about three

34

times more then their dry counterparts. Further, divers wet profiles can be identified which have an inverse character, i.e. wet refractivity increases with height. However, the vertical extension is limited to about $10\,km$ height above surface, which widely reflects the vertical distribution of water vapour as shown in Figure 2.6.

In order to validate the performance of the Hopfield refractivity model, radiosonde measurements at surface (i.e. at the beginning of their flight) were used for the computation of the initial values (N_{ds} and N_{ws}). Then, the initial refractivities were extrapolated to the fulcrums of the radiosonde profile using Eq.3.23 and Eq.3.24 and subtracted from the radiosonde profiles to determine differences with respect to the Hopfield model. The blue and red curves in Figure 3.6 show the differences for the dry and wet component, respectively. Although the same surface values were used, large deviations from the radiosonde profiles are already visible within the lowest layers of the atmosphere. The error in dry refractivity is dominated by random errors until $5\,km$ above the surface and systematic effects above with largest deviation of around $\pm 5 - 7\,ppm$. These upper air deviations are caused by temperature variations near the tropopause which cannot be described well by a constant lapse rate Γ.

Nevertheless, the error in the wet component is about three times larger (around $\pm 15 - 18\,ppm$) than that of the dry counterpart. Thus, the Hopfield model, fed with surface measurements, is less suited for the analyses of most weather phenomena as broached in Section 3.4.1. Their refractivity variation is mainly below the model accuracy.

In general, the high variable distribution of wet refractivity is very difficult to capture within an empirical model. As shown in Figure 3.6 surface measurements alone provide mostly insufficient information about the vertical distribution of wet refractivity. Hence 3D observation methods, like radio occultation (Beyerle *et al.*, 2006) or the innovative GNSS tomography technique can be a valuable source of information for the analysis of current weather situations and weather forecast. More details are provided in Chapter 7.

3.5   Anomalies in wave propagation

The path of a signal through the atmosphere is affected by variations in index of refraction (n). The component of the gradient n perpendicular to the path causes the signal to be bent. Assuming a spherically stratified atmosphere n is connected with the Earth´s radius r and elevation angle ε as follows:

$$n_1 \cdot r_1 \cdot cos\left(\varepsilon_1\right) = n_2 \cdot r_2 \cdot cos\left(\varepsilon_2\right) \tag{3.28}$$

According to Bean & Dutton (1966) the resulting bending angle τ reads:

$$\tau_{1,2} = - \int\limits_{n_1, \varepsilon_1}^{n_2, \varepsilon_2} cot\left(\varepsilon\right) \frac{dn}{n} \tag{3.29}$$

Dependent on the actual weather conditions the change in index of refraction with height can be either positive, zero or negative.

$$\frac{dn}{dr} > 0, \qquad \frac{dn}{dr} = 0, \qquad \frac{dn}{dr} < 0 \tag{3.30}$$

A positive gradient leads to a negative curvature of the ray path, i.e. the ray is curved upwards, 'away' from Earth´s surface. However, due to the stratification of the atmosphere this case seldomly occurs (Ghosh, 2002).

In most cases the gradient is either zero (this appears often in the boundary layer of the atmosphere) or negative (standard case). In the standard troposphere is $dn/dr = -40\,ppm/km$.

Special attention has to be paid to anomalies in wave propagation, caused by large negative gradients. If the curvature of the signal equals the curvature of the Earth $(1/a)$, where a is the radius of the Earth, a ray gets "trapped" in the atmosphere. Then the following relation is fulfilled

$$\frac{n_2 \cdot r_2 \cdot cos\left(\varepsilon_2\right)}{n_1 \cdot r_1} \geq 1 \tag{3.31}$$

where the term ε_2 reflects the angle of penetration. The resulting ray paths is shown in Bean & Dutton (1966, p. 149). By rewriting of Snell´s law the associated gradient of refractivity is obtained by

$$\frac{dn}{dr} = -n_2 \cdot \left[\frac{1}{r_2} + \frac{\varepsilon_2^2}{2 \cdot h} \right] \tag{3.32}$$

where h is the top height of the trapping layer. If $\varepsilon_2 = 0$, the gradient dn/dr follows to $-n/r_2$ which is about $-157\,ppm/km$ near surface.

In order to identify trapping events more easily a modified refractivity M was defined. It is the hypothetical refractivity assuming a flat Earth. In case the gradient of M (dM/dr) becomes negative, the signal is bended toward Earth´s surface.

$$M(h) = N(h) + \left(\frac{h}{r-h} \right) \cdot 10^6. \tag{3.33}$$

Since the effect is frequency dependent, a longest wavelength λ_{max} trapped is computed by

$$\lambda_{max} = 251.4 \cdot \left(\frac{N_2 - N_1}{h} - 0.157 \right)^{\frac{1}{2}} \cdot 10^{-3} \cdot h^{\frac{3}{2}} \qquad (3.34)$$

Bean & Dutton (1966) analysed the occurrence of ground-based ducts for radiosonde sites in US and found a maximum wavelength trapped of $\lambda_{max} = 30\,cm$. Although the distribution of events is very local, a refractivity gradient of $-157\,ppm/km$ up to $-420\,ppm/km$ was observed at every station. The resulting maximum frequency of occurrence follows to $13\,\%$. However, the number of events decreases rapidly with elevation angle ε_2. Above $2°$ almost no events where detected anymore, thus only observations at very low elevation angles near $0°$ are affected by this phenomenon.

3.5.1 Multiple ray-paths

In general the wavelength of microwave signals is small compared to the scale of atmospheric phenomena. In consequence the principle of geometric optics is valid, i.e. the signal trajectory is well described as line by the Eikonal equation (see Section 7.2.3).

However, large gradients in refractivity might lead to multiple rays or diffraction, especially when refractivity differences are sharply distinct. In such cases geometric approaches are limited. Wave-theoretic approaches like the radio-holographic method (Jin *et al.*, 2014) or the Mie scattering theory (Melbourne, 2004) help to overcome these limitations. Phenomena like caustic rays or trapped rays as described in previous section are better resolvable. Thus, wave-theoretic approaches attract more and more attention in GNSS signal processing, especially for Radio Occultation (RO). A detailed overview about wave-theoretic approaches for RO is given by Melbourne (2004).

Chapter 4

GNSS data processing

Global Navigation Satellite Systems provide continuous and instantaneous positioning and timing services. This can be guaranteed by a multi-satellite constellation (of 24 or more satellites), whereby each satellite transmits two or more carrier signals in the microwave frequency L-band ($1-2\,GHz$). When a GNSS signal passes the atmosphere its propagation is affected by the atmospheric constituents as described in Chapter 3. Bevis *et al.* (1992) demonstrates that the resulting excess path lengths can be estimated precisely from GNSS phase observations. Since then GNSS is widely recognised as observing technique for remotely sensing the atmosphere.

In the following basic information about the GNSS signal structure, the observation equations and the relation between signal delay and tropospheric parameters are provided which justifies the use of GNSS as remote sensing technique. Further the principles of tropospheric parameter estimation are presented, necessary for the analysis of dual-frequency GNSS pseudorange and phase measurements in batch processing using linear least squares methods. Thereby a special focus is laid on the handling of differenced and undifferenced ground-based and satellite-based observations. Further, the post-fit residuals are analysed, to identify remaining tropospheric effects which are insufficiently modelled or not covered by the functional model.

4.1   Global Navigation Satellite Systems

As of the 10th of October 2016 the Global Positioning System (GPS) encompasses 31 (12 IIR, 7 IIR-M and 12 IIF) operational satellites and its Russian counterpart GLONASS incorporates 24 (22 M, 1 M+ and 1 K1) operational satellites, which is sufficient to guar-

antee full operational capability. The GNSS signal plan as shown in Table 4.1 summarises the available signals as transmitted by each satellite.

System	L-Band	Centre frequency	Modulated codes	Transmitting satellites
GPS	L1	$1575.42\,MHz$	C/A, P, (M)	all, (IIR-M and IIF)
GPS	L2	$1227.60\,MHz$	(C), P, (M)	all, (IIR-M and IIF)
GPS	L5	$1176.45\,MHz$	C, M	IIF
GLO	L1	$1602 + 0.5625 \cdot k\,MHz$	C/A, P	all
GLO	L2	$1246 + 0.4375 \cdot k\,MHz$	C/A, P	all
GLO	L3	$1207.14\,MHz$	C/A, P	M+ and K1

Table 4.1: GPS and GLONASS signal plan

In contrast to other GNSS systems GLONASS makes use of the Frequency Division Multiple Access (FDMA) technique whereby each satellite (identified by its channel number $k = -7, ... + 6$) transmits on a slightly different frequency. The two modern GLONASS satellite types (M+ and K1) support both, the FDMA and the widely common Code Division Multiple Access (CDMA) technique. Latter is currently available for the L3 signals but will be extended to the other frequency bands with the next generation of GLONASS satellites (Urlichich *et al.*, 2011).

The L-band was selected for GNSS because it penetrates atmospheric trace gases, is rain-fade resistant and therewith well suited for continuous operations. Further it is relatively easy tracked (less pointing of antenna) and better processed than high frequency data (Ogaja, 2011). On top of the carrier signal (L1, L2, ...) codes are modulated which allow for signal acquisition. The Coarse/Acquisition code (C/A) on L1 is still the most important signal for mass market applications. On L2 only the encrypted P-code (Y-code) was available until GPS satellite type IIR. All users without knowledge of this code had no direct access to the L2 signal. To overcome this problem codeless and semi-codeless tracking techniques or hybrid versions (squaring, cross-correlation, Z-tracking) were developed, see Woo (2000). These techniques allow the tracking of GPS L2 but only with some limitations (e.g. lower signal-to-noise ratio) but will become less important in future when the remaining 12 GPS IIR satellites are replaced by more modern satellites which provide a new civil code on L2. Furthermore, the IIF generation transmits already a civil signal on L5 which allows the acquisition of a third frequency.

The GNSS receiver has the main task to differentiate between the different transmitters, to compute pseudoranges (i.e. biased estimates of the true distance between satellite

and receiver) and to use the pseudorange and carrier phase measurements to solve the navigation equations for the parameters of interest or to store the observations in files[1] for post-processing applications. In addition to the observation type (C, L, ...) and frequency (1, 2, 3, 5) each observation is further characterised by an attribute (C, S, L, X, P, W, Y, M, N, ...) to inform about the tracking method and therewith about the origin of the measurement (Gurtner & Estey, 2007).

For geodetic applications basically the carrier measurements (L1, L2, L5) are relevant because they are less noisy and less prone to multipath than pseudorange measurements. Nevertheless, the pseudorange measurements are helpful for data pre-processing or ambiguity fixing, see Section 4.6. Unfortunately both, pseudorange and carrier phase measurements are affected by many systematic errors like clock errors, propagation effects or noise. Hence the observation equations are introduced to describe the functional relation between the measurements and the relevant error sources.

4.2 Observation equations

The observation equation is defined separately for pseudorange observations $C_{r,\nu}^s$

$$C_{r,\nu}^s = \varrho_r^s + c \cdot \delta t_r - c \cdot \delta t^s + \Delta \varrho_{r,\nu}^s \tag{4.1}$$

with

$C_{r,\nu}^s$	... pseudorange between satellite s and receiver r at frequency ν
ϱ_r^s	... geometric distance between satellite s and receiver r
$c \cdot \delta t_r$	... correction of receiver clock at signal reception time t converted to meters
$c \cdot \delta t^s$	... correction of satellite clock at transmission time $t - \tau_r^s$ converted to meters
τ_r^s	... signal travelling time (from satellite to receiver)
$\Delta \varrho_{r,\nu}^s$	... further propagation delays and site-specific effects

and phase observations $L_{r,\nu}^s$

$$L_{r,\nu}^s = \varrho_r^s + c \cdot \delta_r - c \cdot \delta^s + \Delta \varrho_{r,\nu}^s + \nu \cdot n_{r,\nu}^s \tag{4.2}$$

---

[1]GNSS observations are usually stored in RINEX format (Gurtner & Estey, 2007).

with

$L_{r,\nu}^s$ ... phase observation for the satellite-receiver pair (s-r) at frequency ν

$n_{r,\nu}^s$ ... unknown number of cycles (carrier phase ambiguity).

The pseudorange observation $C_{r,\nu}^s$ results from the signal travelling time, clock errors, propagation delays and further site-specific effects as summarised by the parameter $\Delta\varrho_{r,\nu}^s$. The user position is covered by the geometric distance term $\varrho_r^s = |x^s - x_r|$ where x_r denotes the user position and x^s the satellite position.

The phase observation equation contains an additional parameter, namely the phase ambiguity, i.e. the unknown number of cycles $(n_{r,\nu}^s)$. Fortunately this parameter remains constant as long as the signal is tracked continuously and can be estimated together with the other parameters. In case of signal interruption a jump in cycles appears which can be corrected in some cases by applying a cycle slip detection method (Dach *et al.*, 2015). Otherwise a new ambiguity parameter has to be set up for the remaining observation arc.

Highest accuracy can be obtained if the phase ambiguity can be fixed to its integer number. Therefore all systematic effects have to be carefully modelled or eliminated by differencing techniques (see Section 4.3.2). Special attention has to be given to the unknown hardware delays, also known as uncalibrated phase delays. In the phase observation equation they are comprised by the clock parameters δ_r and δ^s which reflect not only the instantaneous offset to system time but also hardware delays and the so-called inter-frequency and inter-system biases (Dach *et al.*, 2015)[2]. Without knowledge of theses phase biases a carrier phase ambiguity solution is not possible for undifferenced observations. Even by double-differencing (see Section 4.3.2) not necessarily all biases are cancelled (Håkansson *et al.*, 2017). Hence a successful multi-GNSS ambiguity solution can only by guaranteed when these biases are determined or introduced into the observation equation as known (Hinterberger, 2016).

Beside the clock parameters further effects $(\Delta\varrho_{r,\nu}^s)$ have also a significant impact on the observations. Eq.4.3 highlights the most prominent ones:

$$\Delta\varrho_{r,\nu}^s = TRO_r^s + ION_{r,\nu}^s + MP_{r,\nu} + APC_r + REL + \varepsilon_r^s \tag{4.3}$$

with

---

[2]Thus strictly speaking, the clock terms should be defined as frequency dependent ($\delta_{r,v}$ and δ_v^s).

TRO_r^s ... tropospheric delay along the signal path from satellite s to receiver r

$ION_{r,\nu}^s$ ... frequency dependent ionospheric delay along the signal path

$MP_{r,\nu}$ ... frequency and station specific multipath effects

APC_r ... antenna specific phase centre corrections

REL ... relativistic effects

ε_r^s ... remaining errors and noise affecting pseudorange and phase observations.

A detailed description of the individual systematic effects can be found in Xu (2007). In the following special attention is given to the modelling and estimation of tropospheric delays (TRO_r^s). Their impact is similar on both, pseudorange and phase observations. Other effects like the ionospheric delay ($ION_{r,\nu}^s$), multipath (MP_r) and some effects in ϵ_r^s like the phase wind up[3] or receiver noise have to be treated differently for pseudorange and phase measurements.

4.3 Combination of observations

Common systematic effects appear not exclusively between pseudorange and phase observations but also between same observation types, stations or subsequent epochs. This correlation in time and space is utilised in GNSS data processing to remove common systematic effects between observations and therewith to reduce the number of unknown parameters in the observation equation. Dependent on the number of receivers involved, it is distinguished between the forming of linear combinations (single receiver technique) and the forming of differences (between two or more receivers).

4.3.1 Linear combinations

Simultaneous observations recorded at one station on two frequencies can be combined to

$$\phi_{LC} = i \cdot \phi_1 + j \cdot \phi_j \tag{4.4}$$

where ϕ_{LC} is the so-called general linear combination which results from measurements ϕ_1 and ϕ_2, observed on frequency ν_1 and ν_2 in cycles. The coefficients i and j determine the

---

[3]A rotation of the satellite antenna results in a change in phase of the right-hand polarised carrier phase signal which is interpreted by the receiver as a change in distance of up to one wavelength. The effect is not visible in pseudorange observations.

characteristic of ϕ_{LC}. The resulting wavelength of the linear combination is

$$\lambda_{LC} = \frac{c}{i \cdot \nu_1 + j \cdot \nu_2} \tag{4.5}$$

where c is the speed of light. In terms of metres, the general linear combination reads:

$$L_{LC} = \alpha \cdot L_1 + \beta \cdot L_2 \tag{4.6}$$

The coefficients $\alpha + \beta = 1$ are related to i and j as follows:

$$\alpha = \frac{i \cdot \lambda_1}{\lambda_{LC}}, \quad \beta = \frac{j \cdot \lambda_2}{\lambda_{LC}} \tag{4.7}$$

Assuming uncorrelated observations the noise σ_{LC} of the combination can be computed by means of the law of error propagation from the noise $\sigma_{1,2}$ of the original measurements on ν_1 and ν_2.

$$\sigma_{LC} = \sqrt{\alpha^2 \cdot \sigma_1^2 + \beta^2 \cdot \sigma_2^2} \tag{4.8}$$

The effect of multipath mp_{LC} on the linear combination is defined as the sum of the individual components

$$mp_{LC} = |\alpha \cdot mp_1| + |\beta \cdot mp_2| \tag{4.9}$$

The first order ionospheric delay I_{LC}^{1st} in terms of the delay at frequency ν_1 reads:

$$I_{LC}^{1st} = I_{L1}^{1st} \cdot \left(\alpha + \beta \cdot \frac{\nu_1^2}{\nu_2^2} \right) \tag{4.10}$$

According to their characteristics with respect to wavelength, noise, multipath and remaining ionospheric delay a set of linear combinations based on dual-frequency observations is defined and commonly used in GNSS data processing.

The **ionosphere-free linear combination** for instance removes the first-order (up to 99.9 %) ionospheric effect. Therefore the dispersive character of the ionosphere is utilised, i.e. the ionospheric delay is widely removed due to its dependency on the inverse square of the frequency. The resulting ionospheric-free phase observation L_{IF} reads:

$$L_{IF} = \frac{f_1^2 \cdot L_1 - f_2^2 \cdot L_2}{f_1^2 - f_2^2} \tag{4.11}$$

where the nominal frequency f_1 and f_2 is defined by the satellite system frequency plan, see Table 4.1. It is the common observation used in GNSS data processing.

43

The **geometry-free or ionospheric combination** L_I is defined by:

$$L_I = L_1 - L_2 \tag{4.12}$$

It cancels out the geometric part and leaves all frequency dependent effects, mainly the ionospheric delay, hardware delays and phase wind up (Springer, 2009). The ionospheric combination is used to estimate the ionospheric electron content or to detect cycle slips. For pseudorange observations it is defined vice versa $(C_2 - C_1)$ since the ionospheric effect enters into the pseudorange observation equation with opposite sign.

The aim of the **wide-lane linear combination** L_{WL} is primarily to generate an observation with wider wavelength. It is used for cycle slip detection and aids in integer ambiguity resolution.

$$L_{WL} = \frac{f_1 \cdot L_1 - f_2 \cdot L_2}{f_1 - f_2} \tag{4.13}$$

The **narrow-lane linear combination** creates a low-noise signal (lower than each seperate component) with narrow wavelength. It allows to increase the precision in fixed ambiguity mode.

$$L_{NL} = \frac{f_1 \cdot L_1 + f_2 \cdot L_2}{f_1 + f_2} \tag{4.14}$$

The **Melbourne-Wübbena linear combination** combines the two linear combinations L_{WL} and C_{NL} and eliminates therewith all effects except ambiguities and noise (Springer, 2009). Thus it its suited for outlier detection, cycle slip detection and ambiguity estimation. The Melbourne-Wübbena linear combination has the same wavelength as the wide-lane linear combination. However, its noise and multipath error depends widely on the quality of the pseudorange observations.

$$L_{MW} = \frac{1}{f_1 - f_2} \cdot (f_1 \cdot L_1 - f_2 \cdot L_2) - \frac{1}{f_1 + f_2} \cdot (f_1 \cdot C_1 + f_2 \cdot C_2) \tag{4.15}$$

Table 4.2 lists the main characteristic of each carrier phase linear combination. The wavelength λ_{LC}, the noise σ_{LC}, the ionospheric I_{LC}^{1st} and multipath effects mp_{LC} were calculated by means of Eq.4.5 to 4.10. The latter three parameters are given by its amplitude factors, relative to the L_1 phase observation.

Further useful combinations exist (Glaner, 2017) but are not mentioned here since they were not considered in the data analysis. Nevertheless, in GNSS data processing usually more than one linear combination is used together, e.g. wide lane ambiguities are commonly fixed and introduced into the narrow-lane ambiguity solution to decorrelate the

ambiguities and to reduce the necessary ambiguity search space (Richert & El-Sheimy, 2007). Consequently the motivation for using linear combinations is not only to eliminate or to mitigate unwanted terms but also to reduce the computing effort.

LC	Coefficients		λ_{LC}	σ_{LC}/σ_{L1}	$I_{LC}^{1st}/I_{L1}^{1st}$	mp_{LC}/mp_{L1}
L_1	i = 1	j = 0	$19.0\,cm$	1	1	1
L_2	i = 0	j = 1	$24.2\,cm$	1.3	1.6	1.3
L_{IF}	i = 77	j = -60	$0.6\,cm$	3.2	0	4.5
L_I	i = 60	j = -77	∞	1.6	-0.6	2.3
L_{WL}	i = 1	j = -1	$86.2\,cm$	6.4	-1.3	9.1
L_{NL}	i = 1	j = 1	$10.7\,cm$	0.8	1.3	1.1

Table 4.2: Characteristic of common GNSS linear combinations based on dual-frequency observations at $v_1 = 1575.42\,MHz$ and $v_2 = 1227.60\,MHz$. The amplitude factors for noise, ionospheric delay and maximum multipath effect were computed relative to the L_1 observation

4.3.2 Forming observation differences

The main motivation for forming differences between GNSS observations is to eliminate nuisance parameters. The simplest form, the so-called single-difference, is defined as the difference between simultaneous measurements at two receivers to one satellite. For phase measurements it reads[4]:

$$L_{r12,\nu}^{s1} = L_{r2,\nu}^{s1} - L_{r1,\nu}^{s1} \tag{4.16}$$

Two single-differences to two satellites (s_1 and s_2) can be combined to one double-difference observation

$$L_{r12,\nu}^{s12} = L_{r12,\nu}^{s2} - L_{r12,\nu}^{s1} \tag{4.17}$$

whereby the receiver and satellite clock corrections including identical hardware delays are eliminated. Further, common propagation delays observed at two stations to two satellites are mitigated and therewith most of the systematic effects are removed. The remaining systematic effects are highly correlated with baseline length. By increasing receiver distance especially atmospheric errors remain in the double-difference observation equation. Thus, dependent on the baseline length, slightly different processing strategies for ambiguity fixing are defined, see Section 4.6. Since the difference is a special form

---

[4]Analogous is the forming of single-differences between pseudorange measurements.

of the linear combination with $\alpha = 1$ and $\beta = -1$, Eq.4.8 and 4.9 can be applied to compute the observation noise and the maximum multipath error of the double-difference observation, separately for each frequency ν. With respect to the basic zero-difference observations the noise is amplified by the factor of two and the maximum multipath even by a factor of four, i.e. the multipath error can be up to one phase cycle, in worst case. Typically, carrier phase multipath is in the order of a few cm.

In addition, two double-difference observations between two different epochs can be combined to a triple difference. This combination is widely used in GNSS data pre-processing to detect and to correct cycle slips (Dach *et al.*, 2015).

4.3.3 Impact of linear combinations on the covariance matrix

The mathematical correlations introduced by linear combinations depend primarily on the involved observations but also on the baseline strategy. Latter defines which observations are processed together.

To show the principal relation two double-difference observations from two receivers (r_1 and r_2) to three satellites (s_1, s_2, s_3) are formed, whereby satellite s_1 is used as reference satellite.

$$L_{r12,v}^{s12} = L_{r12,v}^{s2} - L_{r12,v}^{s1} = L_{r2,v}^{s2} - L_{r1,v}^{s2} - L_{r2,v}^{s1} + L_{r1,v}^{s1}$$

$$L_{r12,v}^{s13} = L_{r12,v}^{s3} - L_{r12,v}^{s1} = L_{r2,v}^{s3} - L_{r1,v}^{s3} - L_{r2,v}^{s1} + L_{r1,v}^{s1} \tag{4.18}$$

In matrix notation Eq.4.18 reads:

$$\begin{bmatrix} L_{r12,v}^{s12} \\ L_{r12,v}^{s13} \end{bmatrix} = A \cdot L = \begin{bmatrix} 1 & -1 & -1 & 1 & 0 & 0 \\ 1 & -1 & 0 & 0 & -1 & 1 \end{bmatrix} \cdot \begin{bmatrix} L_{r1,v}^{s1} \\ L_{r2,v}^{s1} \\ L_{r1,v}^{s2} \\ L_{r2,v}^{s2} \\ L_{r1,v}^{s3} \\ L_{r2,v}^{s3} \end{bmatrix} \tag{4.19}$$

From design matrix (A) the variance-covariance matrix (Cov) can be build according to

$$Cov = 2 \cdot \sigma_0^2 \cdot A \cdot A^T = 2 \cdot \sigma_0^2 \cdot \begin{bmatrix} 4 & 2 \\ 2 & 4 \end{bmatrix} \tag{4.20}$$

where σ_0^2 is the variance of unit weight and reflects the observation noise. The covariances in Cov are not zero, i.e. a correlation is introduced by differencing. Only if all correlations in the double-difference observations are considered correctly, i.e. the functional model is completely known and the stochastic model is perfectly accurate, the forming of linear combinations would have no impact on the parameter estimation (Richert & El-Sheimy, 2007). Consequently, in double difference processing for every epoch the correlation matrix has to be recomputed which can be very time consuming.

4.4 Functional description of the tropospheric delay

The tropospheric delay, also known as Slant Total Delay (STD), is related to the index of refraction n (see Section 3.3) by the following equation:

$$TRO_r^s = STD = \int_S n \cdot ds - \int_{S_0} ds \qquad (4.21)$$

where S is the 'true' signal path and S_0 is the theoretical straight line signal path in vacuum between satellite and receiver. Taking Eq.3.5 and 3.18 into account, the slant total delay can be rewritten as the sum of three components, namely the hydrostatic delay, the wet delay and the geometric bending.

$$STD = SHD + SWD = 10^{-6} \int_S N_h \cdot ds + 10^{-6} \int_S N_w \cdot ds + \left[\int_S ds - \int_{S_0} ds \right] \qquad (4.22)$$

The hydrostatic delay is caused by the dry atmospheric gases, the wet delay results from the contribution of water vapour[5], the bending is a consequence of Snell´s law (see Eq.3.28).

The STD as well as its hydrostatic and wet components cannot be estimated directly since the total number of unknown parameters in the GNSS solution would be higher than the number of observations. Instead, the STD is split into an isotropic and an azimuth-dependent term.

$$STD = ZHD \cdot mf_h(\varepsilon) + ZWD \cdot mf_w(\varepsilon) + G(\varepsilon, \alpha) \qquad (4.23)$$

---

[5]and to a small extent of condensed water in form of clouds and ice, see Section 3.3.1.

The isotropic slant delay is described by the delay in zenith direction ($ZHD + ZWD$) and the corresponding mapping functions (mf_h, mf_w) which absorb the elevation (ε) dependency of the signal delay, separately for hydrostatic and wet delay. By definition, the hydrostatic mapping function includes also the bending effect. Nowadays, the Vienna Mapping Function (VMF1, see Böhm *et al.*, 2006a) or VMF1 like concepts are commonly used in GNSS data processing. Empirical mapping functions like the Global Mapping Function (GMF, see Böhm *et al.*, 2006b) or the improved GPT2w mapping function (Böhm *et al.*, 2015) are also used since they are widely consistent with VMF1 but easier to implement (do not depend on external input). The possible loss of accuracy by empirical mapping functions, as analysed in Section 6.2 for selected wet mapping functions, is known but not critical for the estimation of tropospheric parameters. Hence, both types of mapping functions are common in GNSS data analysis and are applicable down to an elevation angle of 3°.

The hydrostatic zenith delay can be determined properly from surface pressure values. Hence usually an accurate model, like the one given by Saastamoinen (1972) is used to describe the hydrostatic delay

$$ZHD = 10^{-6} \cdot \frac{K_1 \cdot R_d \cdot p_s}{g_m \cdot (1 - 0.00266 \cdot cos(2\varphi) - 0.28 \cdot 10^{-6} H)} \tag{4.24}$$

where K_1 is the refractivity constant of dry air, R_d is the specific gas constant of dry air and p_s is the surface pressure which is corrected for local gravity effects by taking mean gravity $g_m = 9.784 \, m/s^2$, station latitude φ and station height above the geoid H into account. Only in very rare cases (e.g. during strong upwinds) a deviation from hydrostatic equilibrium causes ZHD errors of up to $20 \, mm$ (Davis *et al.*, 1985). However, in general cases Eq.4.24 allows a very correct modelling of the hydrostatic delay and is only limited by the accuracy of surface pressure. Accurate pressure values can be obtained from meteorological sensors or numerical weather models (see Section 5.6.2). In GNSS analysis it is also common to use empirical models like GPT (Böhm *et al.*, 2007) or GPT2w (Böhm *et al.*, 2015) to derive pressure values for each GNSS site. The ZHD mapped to the elevation angle of the satellite is usually subtracted from the measurements and only the ZWD and the asymmetric term is estimated in GNSS analysis.

The first-order horizontally asymmetric term $G(\varepsilon, \alpha)$ in Eq.4.23 reflects local changes in temperature and particularly in water vapour but contains also to some extent hydrostatic effects (see Section 6.3). MacMillan (1995) proposed a gradient model which describes the

gradient delay as a function of elevation and azimuth angle

$$G(\varepsilon, \alpha) = mf_g(\varepsilon) \cdot [G_N \cdot cos(\alpha) + G_E \cdot sin(\alpha)] \tag{4.25}$$

where $mf_g(\varepsilon) = mf_h(\varepsilon) \cdot cot(\varepsilon)$. Chen & Herring (1997) replaced the elevation dependent term $mf_h(\varepsilon) \cdot cot(\varepsilon)$ by the gradient mapping function $mf_g = 1/(sin(\varepsilon) \cdot tan(\varepsilon) + C)$, with $C = 0.0032$, nowadays used as standard in GNSS data processing (Herring, 1992). Typical ranges for $|G_N|$ and $|G_E|$ are $0 - 2\,mm$. A gradient of $1\,mm$ corresponds to a delay of about $55\,mm$ when projected to $7°$ elevation angle using the gradient mapping function.

Further, more extended gradient models, like the one proposed by Masoumi *et al.* (2016) or second order gradients (Landskron, 2017) are already in use in the analysis of numerical weather model data but only partially in GNSS data analysis. This might change in a couple of years since the number of GNSS satellites and signals increases continuously which will allow a reliable estimation of additional tropospheric parameters.

4.5 Parametrisation of the tropospheric delay

In GNSS software packages like Bernese v5.2 (Dach *et al.*, 2015) or Napeos v3.3.1 (Springer, 2009) the concept of continuous piece-wise linear offsets (Teke, 2011) is used for tropospheric parameter estimation. Therefore the parameter of interest x at observation time t is replaced by the parameters x_i and x_{i+1} at two equidistant nodal points (t_i, t_{i+1}) using a piece-wise linear offset function.

$$x = x_i + \frac{t - t_i}{t_{i+1} - t_i} \cdot (x_{i+1} - x_i) \tag{4.26}$$

In tropospheric analysis a temporal spacing $\Delta t = t_{i+1} - t_i$ of one hour or a multiple thereof is generally used to define the nodal points, whereby the following relation has to be fulfilled $t_i < t < t_{i+1}$. This strict timing reveals some benefits in case different time series should be further analysed or combined. Consequently each unknown parameter in Eq.4.23 has to be replaced by a piece-wise linear offset function. Typically the elevation angle (ε), the azimuth angle (α), the hydrostatic and wet mapping function (mf_h, mf_w) as well as the zenith hydrostatic delay are known or modelled adequately. Thus only the parameters ZWD, G_E and G_N are usually parameterised. The piece-wise linear offset function for ZWD (and analogue for the two other parameters) reads:

$$zwd = zwd_i + \frac{t - t_i}{t_{i+1} - t_i} \cdot (zwd_{i+1} - zwd_i) \tag{4.27}$$

For parameter estimation also the partial derivatives of the piece-wise linear offset function with respect to the unknowns (x_i and x_{i+1}) are needed. For zwd (and analogue for the two other parameters) they are:

$$\frac{\partial zwd}{\partial zwd_i} = 1 - \frac{t - t_i}{\Delta t} \tag{4.28}$$

$$\frac{\partial zwd}{\partial zwd_{i+1}} = \frac{t - t_i}{\Delta t} \tag{4.29}$$

These two partial derivatives are applied in Section 4.6.1 to set up the functional model A for parameter estimation. Further details are provided in Appendix A.4.

4.6 Processing strategy for ground-based observations

The estimation of tropospheric parameters from ground-based GNSS phase observations is usually summarised under the expression 'GNSS meteorology' (Bevis *et al.*, 1992). Highest accuracy can be obtained when a geodetic GNSS antenna is mounted on a stable reference site. Then the station position can be estimated in static mode (usually once per day) or introduced as known into the observation equation. This allows to reduce the number of unknowns and to decorrelate the station height from the tropospheric parameters (Ahn, 2016).

For the definition of the basic processing strategy for ground-based observations it is assumed that dual-frequency phase and pseudorange observations are available, with a sample rate of $30\,sec$ for static receivers or $1\,sec$ for moving receivers[6]. Further, it is presumed that the tropospheric estimates are not required in real time. Hence only post-processing strategies are presented. Details to the near real-time processing are also provided in Karabatic *et al.* (2011).

---

[6]Schüler (2006) or Vyas *et al.* (2011) showed that tropospheric parameters can also be estimated with reasonable accuracy under kinematic conditions, when the receiver is installed on moving platforms like on ships, cars or airplanes.

4.6.1 Least squares adjustment

The near real-time condition allows to process the observations in batch mode. A batch filter waits until all observations within a pre-defined estimation arc are available and processes them at once. Since several parameters like ambiguity parameters remain constant over a longer time period, therewith the redundancy (number of observations n_{obs} minus unknowns u) can be increased.

A redundancy larger than zero defines an over-determined problem. A least squares adjustment considers these redundant measurements to determine reliable estimates together with accuracy parameters for observations and unknowns. Further, it allows to handle accuracy information and to take possible correlations between the observations into account. In GNSS data analyses usually the least squares estimator as derived in Appendix A.4 for uncorrelated and equally weighted observations is applied. In matrix notation it reads:

$$\hat{X} = X_0 + \delta\hat{X} = X_0 + \left(A^T \cdot A\right)^{-1} \cdot A^T \cdot l \tag{4.30}$$

see Koch (1996) or Niemeier (2002) for a more detailed description.

4.6.1.1 Correlation and weighting

According to Section 4.3.3 observations, especially double-differenced observations, cannot be treated as uncorrelated. Further, the observations should also not be considered as equally accurate since:

- Pseudorange observations are noisier than phase observations.

- Each frequency, each receiver and each linear combination (see Table 4.2) has its specific noise characteristic.

- Observations at low elevations are generally more exposed to atmospheric effects and multipath then observations at higher elevations.

So far these effects were neglected in the definition of the least squares approach. However, Rothacher *et al.* (1998) showed that the accuracy of the estimated tropospheric parameters can be significantly improved when a sophisticated stochastic model is introduced into the adjustment process.

A stochastic model based on the variance-covariance matrix Cov_{ll} reflects the precision of observations on its diagonal elements (σ_n^2) and the correlation between observations (σ_{nm})

on the non-diagonal elements. In case of uncorrelated observations and unit-variances, matrix Cov_{ll} is an identity matrix of size (n_{obs}, n_{obs}). Then Eq.4.30 can be applied for parameter estimation.

However, in general the relative accuracy between observations is known and can be introduced into the equation system. Therefore a weighting function P is defined as follows:

$$P = \sigma_0^2 \cdot Cov_{ll}^{-1} \tag{4.31}$$

where σ_0^2 is the a priori variance of the unit weight. Its impact is further explained in Section 7.2.4.7 where the method of variance component analysis is introduced.

It is recommended to define different weights w at least for pseudorange and phase observations. A typical ratio between these two types of observation is: $w_c/w_p = 10^{-2}$. Further, a downweighting of observations below 10° elevation is useful to reduce the impact of unmodelled systematic errors (e.g. multipath) on the solution. A typical elevation-dependent weighting function $w(\varepsilon)$ reads:

$$w(\varepsilon) = sin^2(\varepsilon) \tag{4.32}$$

Luo *et al.* (2009) showed that weights based on the signal-to-noise ratio can further improve the accuracy of estimated tropospheric parameters.

However, in order to introduce the stochastic model into the adjustment process, the optimisation strategy has to be redefined as follows

$$\left[Res^T \cdot P \cdot Res\right] \rightarrow min \tag{4.33}$$

where the squared sum of the weighted residuals (Res) has to be minimised. This leads to the following solution (compare to Eq.4.30):

$$\hat{X} = X_0 + \delta\hat{X} = X_0 + \left(A^T \cdot P \cdot A\right)^{-1} \cdot A^T \cdot P \cdot l \tag{4.34}$$

The term $A^T \cdot P \cdot A = N$ can be summarised as normal equation matrix. The variance-covariance matrix of the estimated parameters ($Cov_{\hat{X}\hat{X}}$) reads

$$Cov_{\hat{X}\hat{X}} = s_0^2 \cdot N^{-1} \tag{4.35}$$

where the standard deviation s_0 of the unit weights a posteriori is defined by

$$s_0 = \sqrt{\frac{Res^T \cdot P \cdot Res}{n_{obs} - u}}. \tag{4.36}$$

The correlation between observations is usually not known a priori but can be computed from the variance-covariance matrix of the adjusted observations

$$C_{\hat{l}l} = A \cdot Cov_{\hat{X}X} \cdot A^T \tag{4.37}$$

and introduced into the equation system by recomputation of the weighting matrix.

$$P = s_0^2 \cdot Cov_{\hat{l}l}^{-1} \tag{4.38}$$

If double-difference observations of more than 30 to 40 stations are processed in once, the computation of correlations might become critical due to computational resources. Hence less correct approaches have been developed which allow for taking at least the correlation between baselines or frequencies into account (Dach *et al.*, 2015). Temporal correlations are usually not considered although they are significant up to several minutes temporal spacing (Miller, 2010).

4.6.1.2 Constraints

In case good a priori values (e.g. station coordinates) are known, absolute constraints help to restrict the variability of the estimates with respect to the preferred values. The extended normal equation system reads:

$$\hat{X} = X_0 + \delta\hat{X} = X_0 + \left(A^T \cdot P \cdot A + A_c^T \cdot P_c \cdot A_c\right)^{-1} \cdot A^T \cdot P \cdot l + A_c^T \cdot P_c \cdot l_c \tag{4.39}$$

where A_c is the design matrix for the pseudo-observations, l_c is the reduced observation vector for the constraints and P_c denotes the weighting matrix for the pseudo-observations. The resulting standard deviation of the unit weights a posteriori follows to:

$$s_0 = \sqrt{\frac{Res^T \cdot P \cdot Res + Res_c^T \cdot P_c \cdot Res_c}{n_{obs} + n_c - u}} \tag{4.40}$$

where n_c and Res_c are the number of pseudo-observations and the pseudo-observation residuals, respectively. In case of absolute constraints A_c becomes an identity matrix of

size (n_c, n_c). Loose absolute constraints are often defined to avoid numerical instability in the normal equation system, e.g. due to observations gaps.

Relative constraints allow for controlling the behaviour between subsequent two parameters. In case of tropospheric parameters they are usually applied between two consecutive nodal points. If the temporal spacing of the estimated parameters is low, or if too few observations are available within a certain period, relative constraints can help to reduce the noise in the estimated time series. Too tight relative constraints can be identified by analysis of the loss function $\Omega = \delta \hat{X}^T \cdot P \cdot \delta \hat{X}$ of the estimated parameters, see Section 7.2.4.7.

4.6.2 Strategy for undifferenced observations

Undifferenced processing is the station-wise processing of pseudorange and carrier phase measurements by introducing fixed satellite orbit and clock parameters. This concept, also known as Precise Point Positioning technique (PPP) was firstly introduced by Anderle (1970) and became important after precise satellite orbit and high-rate satellite clock products were made available (Kouba, 2015). For cm-level accuracy the following input data is required:

- Series of dual-frequency phase and code observations, e.g. in RINEX format (Gurtner & Estey, 2007)

- Precise satellite orbits and high rate satellite clock corrections, e.g. from the International GNSS service (IGS) or any other analysis centre, see Kouba (2015).

- Earth rotation parameters (corrections to universal time and coordinates of the pole), consistent with the set used to generate the satellite orbits and clock corrections.

- A phase centre model for each transmitting and receiving antenna (e.g. igs08.atx, see Schmid *et al.*, 2015).

- A priori station coordinates (preferably in the reference frame of the orbits, valid for the epoch of interest).

- Differential code biases to correct for time delays between GNSS signals transmitted from one satellite.

- Site-specific loading constituents for the computation of ocean tidal loading corrections (e.g. using FES2012 model, Bos & Scherneck, 2017).

Further input model data for highest accuracy (not considered herein):

- Ionospheric files to correct higher order ionospheric effects (not necessary in times of low solar activity)

- Site information for non-tidal loading corrections (for atmosphere, ocean and hydrosphere)

- Atmospheric tidal loading corrections

- Uncalibrated phase delays for undifferenced ambiguity fixing

- Pressure values at site and updated mapping coefficients, e.g. from VMF1 troposphere model (Böhm *et al.*, 2006a).

The introduced information and models should be as good as possible since in undifferenced processing all errors propagate directly into the GNSS solution.

4.6.2.1 Orbit fitting

Precise satellite orbits are usually provided every $15\,min$ in form of tabulated coordinates realised in the International Terrestrial Reference System (ITRS). To determine satellite positions for each data point the orbits have to be interpolated. A polynomial fit is usually not accurate enough, thus for best fit a reduced-dynamic orbit determination approach (Tapley, 1973) is applied to solve for the equations of motion in the inertial reference system. This approach is based on precise models describing the gravitational and non-gravitational forces which act on the satellite. Additional unmodelled forces are estimated as radiation pressure coefficients and stochastic pulses.

Transformation of the ITRF satellite coordinates into the inertial Geocentric Celestial Reference Frame (GCRF) is described in the IERS Conventions 2010 (Petit & Luzum, 2010) by three rotation matrices

$$[ITRF] = Q(t) \cdot R(t) \cdot W(t) \cdot [GCRF] \tag{4.41}$$

where $Q(t)$, $R(t)$ and $W(t)$ rise from the motion of the celestial pole, Earth rotation and polar motion, respectively. The motion of the celestial pole is well approximated over decades by nutation and precession models. In contrast, corrections to universal time and pole offsets have to be updated regularly, e.g. by implementation of subdaily corrections as provided together with the orbit and clock products or by the International Earth Rotation and Reference System Service (IERS).

4.6.2.2 Data pre-processing

For tropospheric parameter estimation observations at low elevations are favorably for the de-correlation of tropospheric parameters from receiver height and receiver clock biases. Further, the gradient mapping function (see Eq.4.25) is almost equivalent to $1/sin(\varepsilon)$ for elevation angles larger than 20°, thus only observations at lower elevations can contribute to the estimation of gradient parameters. Nevertheless, observations at very low elevations are strongly affected by unmodelled systematic effects like multipath or deficiencies in the mapping function. Consequently, observations below 3° elevation angle are generally eliminated and the remaining observations have to be carefully checked for noticeable problems. This includes:

- A check for outliers using the reduced observation vectors, the Melbourne-Wübbena linear combination (L_{MW}) and differences between ionosphere-free linear combinations (L_{IF}) of pseudorange and phase observations.

- Correction of cycle slips using the Melbourne-Wübbena linear combination (L_{MW}), the differences between the ionosphere free linear combinations (L_{IF}) of pseudorange and phase observations and the differences between geometry-free linear combinations (L_I).

- Removal of unpaired phase observations ($L1$ without $L2$ or vice versa) and short observation arcs, e.g.< 10 data points.

If a cycle slip cannot be corrected an ambiguity is initialised. Usually small cycle slips and outliers remain undetected in the data pre-processing and have to be removed iteratively during parameter estimation by analysis of the post-fit residual vector. Nevertheless the quality of the cleaned pseudorange observations is good enough to estimate receiver clock corrections which are commonly introduced as initial values into the parameter estimation process. Replacing the pseudorange observations by smoothed pseudorange observations can have a positive impact on the accuracy and convergence of the adjustment process (Dach *et al.*, 2015). However, this approach was not further pursued.

4.6.2.3 Parameter estimation based on phase observations

For standard parameter estimation the ionosphere-free linear combination (L_{IF}) is generated to eliminate first order ionospheric effects. The reduced phase observation vector (o-c) results from introducing a priori values into the L_{IF} observation equation for the parameters of interest. Further, the satellite position and clock corrections are fixed to their

given values and for the other nuisance parameters (relativistic effects, antenna phase centre offsets, phase-wind up effect, hydrostatic tropospheric delay, ...) model corrections are applied. It is assumed that these corrections are accurate enough so that the corresponding parameters can be removed from the equation system. Consequently the functional model is generated for the remaining unknowns: ambiguities, station coordinates, receiver clock corrections, tropospheric parameters and inter-frequency biases (if GLONASS data is processed). Inter-system biases are usually absorbed by the ambiguity term. Since only a float ambiguity solution is foreseen, the inter-system bias is neglected.

The least squares adjustment is repeated until the stop criteria (e.g. the convergence of the Root Mean Square (RMS) of the weighted residuals) is reached. In each iteration the post-fit residual vector is checked and outliers are eliminated. For the first few iterations usually a wider selection criteria is set than for the last iterations. Under normal conditions up to 5 % of observations are rejected, a higher loss rate indicates bad observation data or a too tight threshold for outlier rejection.

After the final iteration the normal equation matrix is stored together with the estimated parameters and the post-fit residuals in files. For further processing of the tropospheric parameters the SINEX TRO format is used (International GNSS Service, 2017).

4.6.2.4 Comments to ambiguity fixing

To overcome the ambiguity fixing problem in PPP a multi-station PPP solution can be set up. Thereby ambiguities are fixed on double difference level and introduced as constraints into the adjustment process (Springer, 2009). The technique is promising in case of global networks but limited applicable in small ones.

A direct ambiguity fixing on undifferenced level is also possible by introducing uncalibrated phase delays into the PPP solution (Hinterberger, 2016). Since this approach is not supported by the available software packages Napeos and Bernese, no ambiguity fixing to integer was carried out in the analysis of undifferenced observations.

4.6.3 Strategy for differenced observations

In principal PPP and the DD approach are equivalent with respect to redundancy and also with respect to the estimates in case a correct stochastic model is introduced. Practically the DD approach has some advantages in data processing since the satellite and receiver clock errors and therewith the hardware biases are cancelled out which allows the fixing of

integer ambiguities. Further also the pre-processing is less critical since the receiver clock error has to be known only with μs-accuracy (Dach *et al.*, 2015).

Unfortunately the greatest strength of double-difference (DD) processing, the elimination of common effects, is also a shortcoming at the same time in small networks ($< 500 \, km$). In such networks tropospheric parameters cannot be estimated in an absolute sense but rather with respect to a reference station. Therefore reference values (station coordinates and *ZTD*) have to be introduced, at least for one station, and constrained to their given values. Then the tropospheric parameters can be estimated like in PPP processing, except for the reference station.

In contrast to the described PPP solution (Section 4.6.2) two further processing steps have to be added for the DD solution. The first one is related to the definition of baselines, the second step is added for the ambiguity resolution. The baselines are selected with respect to baseline length, the number of simultaneous observations or more advanced strategies (Dach *et al.*, 2015). The right choice of baselines is important since the distance between stations and the distribution of reference stations have a strong impact on the GNSS solution. Further, the baseline length is used to define the ambiguity fixing strategy:

- direct resolution of L1 and L2 ambiguities (on short baselines)

- aided L1 and L2 ambiguities solution by introducing an ionosphere model (on long baselines)

- step-wise ambiguity solution: wide-lane ambiguities are resolved, using the wide-lane or the Melbourne-Wübbena linear combination, and introduced into the ionosphere-free linear combination to solve the narrow-lane ambiguities (medium or long baselines).

Before the ambiguity parameters can be resolved float ambiguities have to be estimated together with the other parameters using L1 and L2 or ionosphere-free double-difference observations (dependent on the baseline). The resulting double-difference residuals (*DDR*) are used to detect and to remove outliers until a convergence is reached. The integer ambiguities are resolved by applying statistical tests like the sigma strategy, QIF or the lambda method (Teunissen, 1994) on the estimated ambiguities to resolve the most likely integer number of cycles (relative to the reference station). Therewith the parameter estimation process can be carried out by introducing the fixed L1 and L2 ambiguities and reference values into the adjustment process. Reference values can be obtained from the IGS or any analysis centre since station coordinates and tropospheric parameters are usually estimated together with satellite orbits and clock corrections.

The final results have to be carefully checked since in DD processing a misbehaving station can downgrade the whole network solution. In case of noticeable problems (e.g. wrong reference coordinates) the parameter estimation has to be repeated by correcting or excluding the misbehaving stations. If the ambiguity fixing rate and the precision of the estimated parameters are reasonable, the estimated parameters and the post-fit residuals can be stored like in the PPP solution in common data format.

4.6.4   Reconstruction of zero-difference residuals

The post-fit residuals in DD processing are also differenced. In order to analyse satellite or station specific effects the double-difference residuals (DDR) have to be converted into zero-difference residuals (ZDR), also known as pseudo-ZDR since certain conditions have to be applied for the reconstruction. (Alber *et al.*, 2000) suggested an approach in which the DDR vector is replaced by the product of a matrix A_1 and a vector of single-difference residuals (SDR).

$$DDR = A_1 \cdot SDR \tag{4.42}$$

Each column of matrix A_1 refers to a satellite, the number of rows is similar to the number of double-difference residuals available for a specific epoch and baseline. The first satellite of each double-difference residual is defined as reference satellite. Each reference satellite is considered in matrix A_1 with '1'; the corresponding satellite with '-1'. In this way the functional model is setup and solved epoch-wise. Unfortunately the resulting equation system contains only $n-1$ observations for n unknows, i.e. matrix A_1 cannot be inverted. However, this problem can be solved by additional constraints.

In the following it is assumed that the residuals are normal distributed, i.e. that the sum of the residuals is zero.

$$\sum_s sdr_s = 0 \tag{4.43}$$

In consequence the observation vector DDR can be extended by '0' and an additional row with ones can be added to matrix A_1 which makes the equation system solvable. However, a more realistic result is obtained when each satellite is weighted individually. Therefore the zero-mean condition was extended as follows

$$\sum_s w_s \cdot sdr_s = 0 \tag{4.44}$$

where w_s defines the weight for each satellite s. According to the weights used in data processing (see Eq.4.32) w_s was defined as follows

$$w_s = sin^2(\bar{\varepsilon}_s) \tag{4.45}$$

where the elevation angle $\bar{\varepsilon}_s$ was computed as mean elevation angle between the two involved stations. The resulting *SDR* vector reads:

$$SDR = A_1^{-1} \cdot DDR \tag{4.46}$$

The procedure is carried out for all baselines and all epochs to obtain a full set of *SDR*s. Afterwards the same approach is repeated to recover the zero-difference residuals.

$$ZDR = A_2^+ \cdot SDR \tag{4.47}$$

Dependent on the baseline strategy it may happen that A_2 is not of full rank. Thus the general inverse (Penrose, 1955), also called the Moore and Penrose inverse ($+$) was applied for solving the equation system.

The processing is carried out for all satellites and for all epochs to obtain *ZDR* for each station-satellite pair. In order to validate the reconstructed pseudo-*ZDR* a comparison between undifferenced post-fit residuals and reconstructed pseudo-*ZDR* based on simulated observations was carried out.
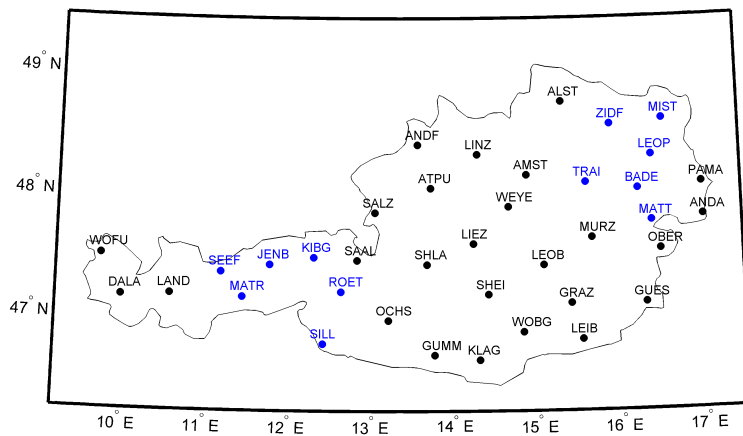

Figure 4.1: Distribution of GNSS reference sites in Austria. GPS observations were generated for the 12 stations highlighted in blue

4.6.5 Comparison of undifferenced ZDR and pseudo-ZDR

The following study on post-fit residuals is based on simulated dual-frequency GPS observations. Two $24\,h$ sets of observations were generated for 12 stations in Austria (see Figure 4.1). Both sets differ only with respect to the applied troposphere model. While no troposphere model was applied to the first set of observations, ZTDs and East-West gradients were simulated for the second set, see Appendix A.3 for details about the data generation. Figure 4.2 shows the resulting L1 phase difference between the two sets. The phase difference was multiplied with the wavelength of L1 $(299,792,458\,m/1575.42\,MHz)$ to obtain dL1 in metre.
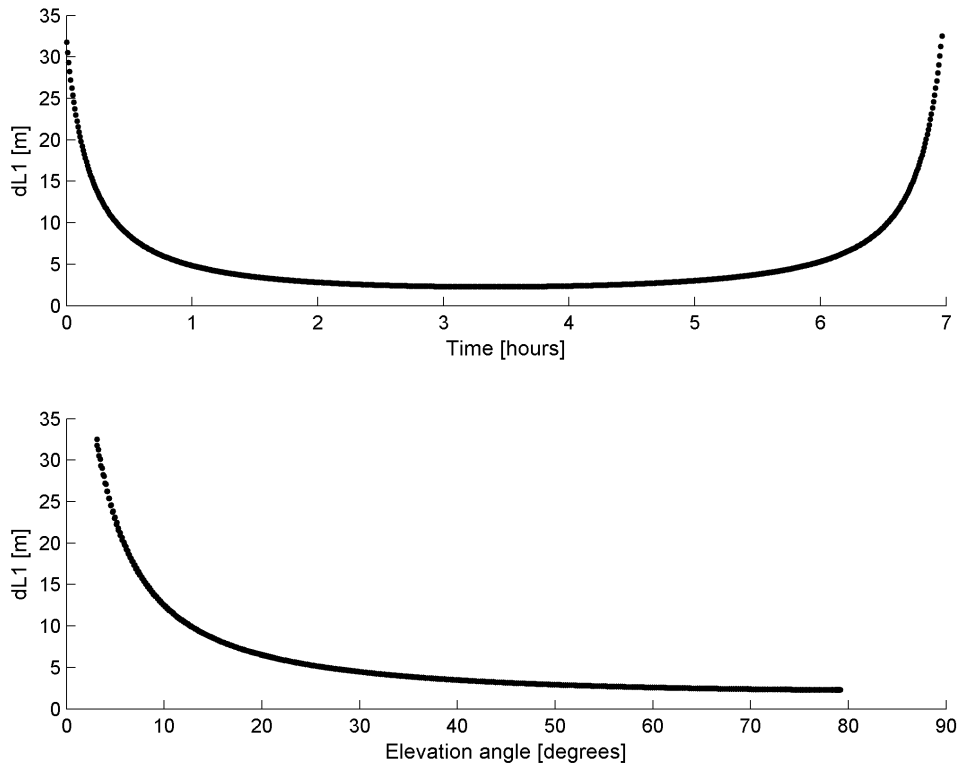

Figure 4.2: L1 phase differences which reflect the tropospheric delay applied to the synthetic GPS observations, exemplary for station Baden and GPS satellite PRN12

Since no troposphere was modelled for the first set of observations the difference in L1 can be interpreted as anisotropic STD applied to the second set of observations. At very low elevation angles small variations in STD appear between rising and setting satellite. This is caused by the azimuth-dependent East-West gradient of 2 mm which was added to the

observations of station Baden (BADE) and the other five stations in the surrounding in order to simulate a weather front coming from Eastern Europe.

The observations of all 12 stations were processed undifferenced in PPP mode and differenced in double-difference approach to estimate tropospheric parameters with 30 min temporal resolution. In order to review the quality of the estimated parameters, the *ZTD* and gradients were mapped to the elevation and azimuth angle of the satellite (according to Eq.4.23 and Eq.4.25) and compared with the dL1 phase differences. The resulting *STD* error (dL1 minus computed *STD*) is smaller than $1\,mm \pm 0.1mm$ (not shown here) if both *ZTD* and gradient parameters are estimated, since neither observation noise nor multipath was added to the observations. Thereby no differences could be identified between PPP and the DD approach. Small deviations from zero are mainly caused by rounding errors. The post-fit observation residuals (*DDR* and *ZDR*) are zero ($<1\,\mu m \pm 0.1\mu m$) since no further systematic effects were simulated.
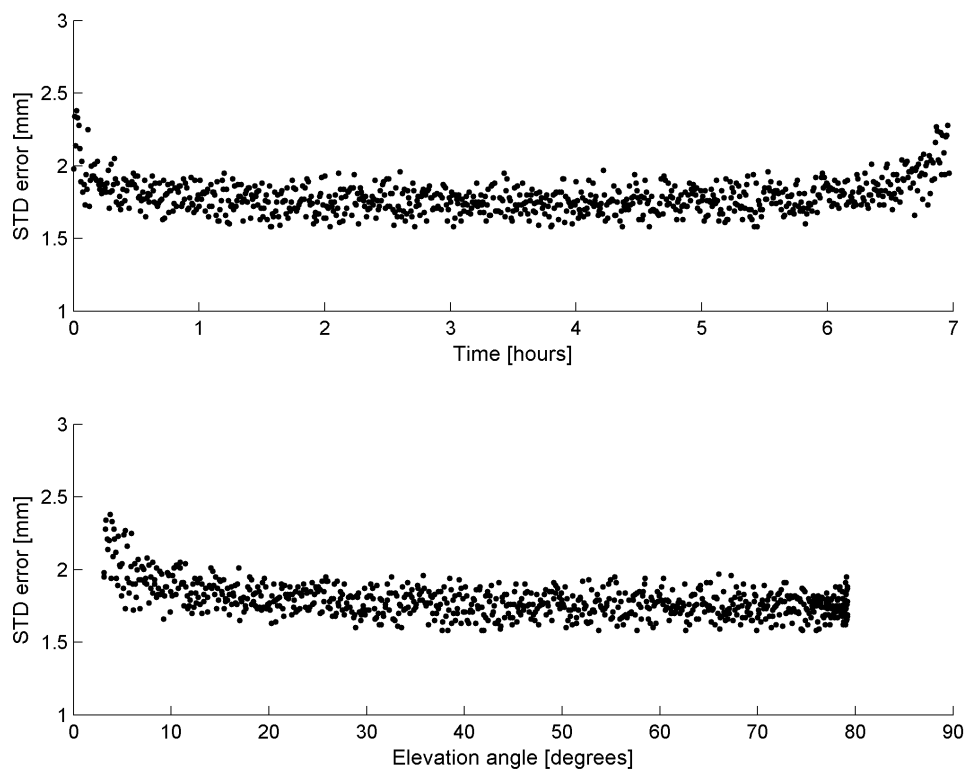

Figure 4.3: *STD* error [mm] for station Baden and GPS satellite PRN12 using undifferenced post-fit residuals (*ZDR*)

In order to evaluate the information content in the post-fit residuals, the processing was repeated but without estimating gradient parameters. The *ZTD* and station coordinates were heavily constrained to their initial values to guarantee that the post-fit residuals contain only unmodelled anisotropic effects.

For the reconstruction the *ZTD* was mapped to the elevation angle of the satellite to obtain isotropic *STD*. Then the post-fit residuals (*ZDR* or pseudo-*ZDR*) were added to the isotropic *STD* to obtain anisotropic delays. For evaluation, the anisotropic *STD* was compared with the *STD* used to simulate the observations.

Figure 4.3 shows the resulting *STD* error for the PPP solution. For station BADE and GPS satellite PRN12 it is around $2\,mm \pm 0.1mm$, i.e. the anisotropic part was recovered almost entirely from the zero-difference residuals except for a small offset. Latter appears since a constant term of the unmodelled tropospheric delay was absorbed by the ambiguity parameter.
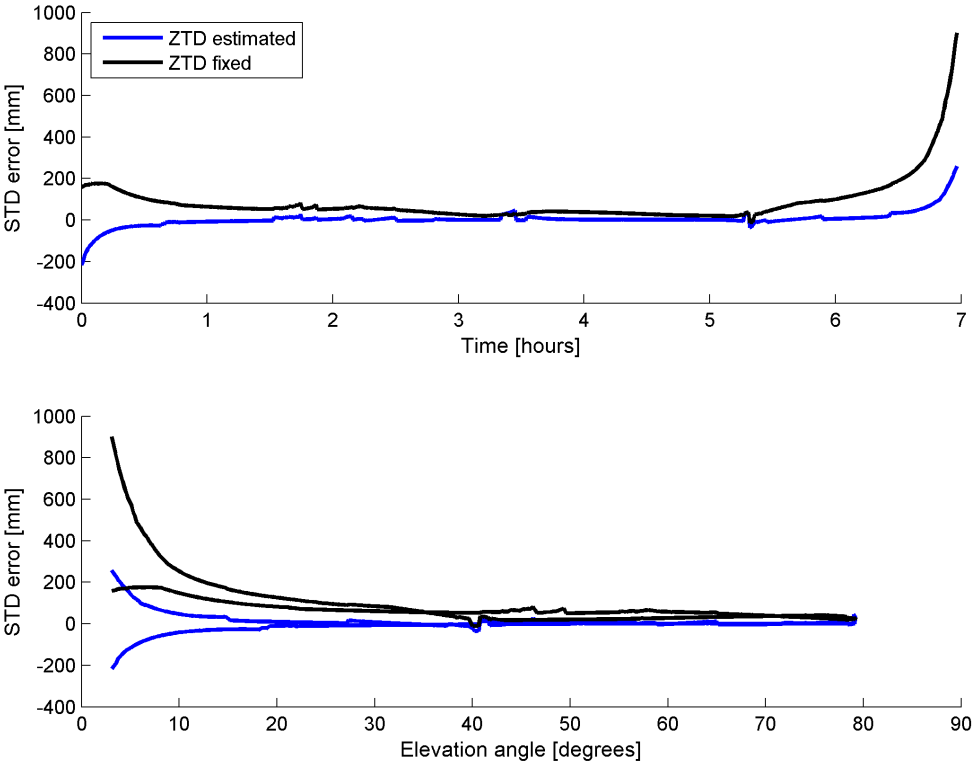

Figure 4.4: *STD* error [mm] for station Baden and GPS satellite PRN12 using reconstructed post-fit residuals (pseudo-*ZDR*)

Figure 4.4 shows the resulting *STD* error for the DD solution. Independent from the number of stations involved and the baseline strategy, the anisotropic delay could not be sufficiently reconstructed from pseudo-*ZDR*s. If only one baseline (BADE-TRAI) is processed, the *DDR* and also the reconstructed pseudo-*ZDR* are almost zero since the anisotropic effects were differenced out in data processing. In best case the resulting *STD* error for station BADE and satellite PRN12 is $-1\,mm \pm 37\,mm$. This was obtained by fixing the *ZTD* and by taking all possible baselines between the 12 stations into account for the reconstruction of pseudo-*ZDR* using the method proposed by (Alber *et al.*, 2000) (blue curve in Figure 4.4). However, a comparable result ($0\,mm \pm 38\,mm$) is obtained if no residuals are added to the isotropic *STD*.

In practice the *ZTD* is not known and therewith cannot be fixed to their given values. Thus an additional solution was created whereby *ZTD* but no gradient parameters were estimated (black curve in Figure 4.4). This results in an increase of bias and standard deviation ($84\,mm \pm 105\,mm$). The example underscores the importance to estimate gradient parameters in addition to *ZTD*s. An unmodelled East-West gradient of $2\,mm$ introduced an *ZTD* error of $35\,mm \pm 13\,mm$.

It turned out that the applied reconstruction method proposed by (Alber *et al.*, 2000) is less suited for the reconstruction of pseudo-*ZDR* in the given scenario. The reconstructed values are mostly to small. In addition jumps appear in the time series every time a satellite rises or sets (visible in Figure 4.4). The magnitude of the jumps can be reduced by downweighting of low elevation satellites, however the reconstruction process cannot be significantly improved therewith. Therefore in further chapters only the undifferenced PPP processing technique is used for the analysis of the tropospheric information content in post-fit residuals.

4.7   Processing strategy for satellite-based observations

In case of satellites-based GNSS receivers tropospheric effects are usually of minor importance since most GNSS signals are received before they enter the atmosphere. However special satellite missions like METOP (von Engeln *et al.*, 2009) are dedicated to operational meteorology. Specifically designed GNSS receivers onboard of LEO (Low Earth Orbit) satellites allow for measuring the bended and delayed signal after travelling through Earth´s limb. "The change of the signal can then be used to infer the atmospheric structure of the celestial body of interest" (Jin *et al.*, 2014, p. 93). The applied technique is widely known as Radio Occultation (RO) technique [occultus, latin: 'hide']. In the

following the principle of RO data processing is briefly introduced. For more details the reader is referred to Beyerle *et al.* (2006) or Kursinski *et al.* (1997).

The basic observables are amplitude and phase measurements transmitted by the GNSS satellite. The raw phase measurements are modelled as follows:

$$L_{r,\nu}^s = \varrho_r^s + c \cdot \delta_r - c \cdot \delta^s + TRO_r^s + ION_{r,\nu}^s + \varepsilon_r^s \qquad (4.48)$$

Thereby it is assumed that antenna specific phase centre corrections and relativistic effects are already corrected.

In contrast to Eq.4.2 the ambiguity term $n_{r,\nu}^s$ is not relevant since the derivative of the phase but not the absolute phase is of interest. In order to retrieve the total atmospheric excess phase delay $(TRO_r^s + ION_{r,\nu}^s)$ both, the geometrical distance term ϱ_r^s and the clock terms have to determined or eliminated in data processing. The geometric distance is usually determined by precise orbit determination methods (see Section 4.6.2.1) and the clock term is mitigated e.g. by applying single differencing techniques, see Wickert *et al.* (2002).

In order to retrieve more information about the atmospheric properties, profiles of refractivity or electron density are derived from the time series of atmospheric excess phase delays. For more details to the conversion assuming spherical symmetry, geometric optics and wave optics methods or Abel transform, the reader is refered to Phinney & Anderson (1968) and Melbourne (2004).

Chapter 5

Meteorological data sources

In the following meteorological sensors and models for atmospheric pressure, temperature or humidity are introduced. Not all are regularly used in GNSS data processing, some of them can be treated as complementary, others are used for evaluation of GNSS slant wet delays or derived products in the following chapters.

5.1   Weather stations

Most land-based weather stations worldwide are designed to fulfil the WMO (2008) requirements, describing the atmospheric conditions at site or for specific needs (e.g. to serve aviation needs at airports or to fulfil synoptic requirements). Therefore each station is equipped with various meteorological instruments to take in-situ measurements in a widely automated way. For long-term applications it is important that the meteorological sensors are calibrated and that they maintain the known uncertainty over longer time periods, ideally over one or more years without recalibration.

For **temperature** the sensor has to be in thermal equilibrium with the environment (except for radiometers, see Section 5.3) and sensitive to thermal expansion or change in electrical resistance. In meteorological networks like in the Austrian TAWES network (Pevny & Mair, 2008) each station is equipped with a thermistor (Logotronic, 2016) which allows measuring the temperature in the measuring range from-50 °C to 60 °C with an uncertainty of $\pm 0.1\,K$. In order to obtain representative measurements at site, the sensor is typically installed at a height of $\sim 1.5\,m$ above ground level. The thermistor provides measure of resistance (R_T) which can be converted to temperature (T) according to

$$R_T = a \cdot exp(b/T) \tag{5.1}$$

where a and b are sensor dependent constants.

The atmospheric **pressure** is recorded prevalent with electronic barometers. The BM35 barometer (Meteolabor AG, 2005) or its precursor BG1 (Pevny & Mair, 2008) contain a resonator pressure sensor as measuring unit. It detects variations in resonance frequency of a vibrating mechanical system caused by changes in air pressure. Precise barometers like the BM35 can therewith 'measure' air pressure in the temperature range from $-25\,°C$ to $60\,°C$ with an accuracy of about $\pm 0.05\,hPa$ and a drift $< 100\,ppm/year$. Pressure values usually refer to the orthometric height of the pressure sensor rounded to the nearest metre, also known as pressure height or barometric height. Air pressure is also often reduced to mean sea level or an agreed datum. Common methods for reduction are described in Section 2.3.1. Such values have to be handled with care if no information about the reduction method is provided (Boisits, 2014).

The atmospheric **humidity** is measured with hygrometers. Modern humidity sensors are sensitive either to changes in temperature of condensation, resistance or electrical capacitance. The most widely used method is the psychrometric method. A psychrometer like the EE33 (E+E Elektronik, 2016) consists of two thermometers. One thermometer is covered with a thin water film. The less humid the air the larger is the temperature difference $(T - T_E)$ between both thermometers. With the psychrometer formula the temperature difference can be converted to water vapour pressure e

$$e = E(p,\,T_E) - A_P \cdot p \cdot (T - T_E) \tag{5.2}$$

where E is the saturation water vapour pressure at temperature T_E, p is the air pressure at the wet thermometer and A_P is the psychrometer coefficient (WMO, 2008). The approach is very well applicable for temperatures above $0\,°C$. Hence psychrometers are usually equipped with a heater to guarantee continuous operation also around the freezing point. The EE33 as widely in use in the TAWES network is working in the temperature range from $-15\,°C$ to $40\,°C$ with an accuracy of $\pm 1.3\,\%$ in relative humidity if $rh < 90\,\%$ and $\pm 2.3\,\%$ if $rh > 90\,\%$.

5.2 Numerical weather models

Numerical Weather Models (NWM) combine observations which describe the current state of the atmosphere with numerical computer models based on classical laws of physics to predict the atmospheric state at any future epoch and to assess its degree of confidence

(Bauer *et al.*, 2015). Operational weather centres provide nowadays predictions from the very short range at kilometre scale up to global seasonal forecasts at the scale of tens of kilometres. A comprehensive overview about NWM is given in Stensrud (2009).

The basic equations in NWM, either diagnostic or prognostic, have to be solved numerically using spatial and temporal discretisation. Thus the NWM is usually characterised by its **spatial resolution**. The smallest atmospheric features resolved have usually wavelengths four to five times the numerical resolution. "The higher the resolution, the more accurate the calculations become (better representation of mountains, coastlines and their effect on large-scale flow and more accurate description of horizontal and vertical structure)." (Andersson, 2015, p. 11).

The lowest model level, the **orography**, is usually derived from high resolution surface models like ETOPO1 (NOAA, 2017) rescaled to the NWM grid. It approximates the topography by a mean elevation above geoid. In mountainous areas the orography is often complemented by sub-grid orographic fields to capture the terrain related impact in more detail. Further parameters like land-sea-mask, albedo, soil temperature and soil moisture, snow coverage depth, see surface temperature are also very important aspects of the NWM to capture the complex atmospheric processes. Small-scale processes like vertical turbulence or convection are still unresolved and therefore described in a statistical way as parameterisation processes. For example convective clouds are not predicted individually but rather their physical effect on the surrounding atmosphere, in terms of latent heat, precipitation, moisture transport and momentum. In this context convection schemes allow to differentiate between deep, shallow and mid-level convection, see Andersson (2015).

Another important part of NWM is **data assimilation**. The forecast skill on the Southern Hemisphere was improved significantly when satellite data were exploited and assimilated into NWM after 1999, see Bauer *et al.* (2015). The observations used can be categorised roughly into in-situ observations and remote-sensing observations. Halloran (2014) gives an overview about the datasets assimilated at United Kingdom´s Meteorological Office. Besides, traditional observations like synoptic data, temperature or wind profiles also ground-based GPS derived zenith delays enter more and more into the forecast system. For assimilation 3D- or 4D-Var analysis tools (Bannister, 2007) are used to create a sequence of model states that fits the available observations and background model. Further it compares the observations with the forecast and computes physically and dynamically consistent corrections for all variables connected to the observations. The impact on the forecast field is thereby driven by the assumed accuracy (for observations and background-errors) and the observation density. The densification of classical networks and the ex-

ploration of new, more complex observations help to further improve the quality of the NWM analysis and to increase the forecast skill (Peixoto & Oort, 1992).

5.2.1 Operational analysis data from ECMWF

The European Centre for Medium Range Weather Forecasts (ECMWF) provides a broad range of model products like forecasts, climate reanalyses or further specific datasets, mostly free of charge to ECMWF members and co-operating states. All products are generated with the ECMWF Integrated Forecast System (IFS) whereby the High RESolution atmospheric forecast model (HRES) is of particular interest for GNSS applications. It describes the static relation between pressure, density, temperature and height and the time evolution of wind, surface pressure, temperature and water vapour. Additional equations characterise the changes in the hydrometeors (rain, snow, liquid water, cloud ice content, etc.) or tracers such as ozone (Haiden *et al.*, 2015).

The HRES atmospheric fields are currently provided on 137 model levels or 25 pressure levels (ECMWF, 2017). Analysis data are available with a temporal resolution of 6 hours at 0, 6, 12 or 18 UTC. Forecast data are available with a 3 hours forecast time step for the next six days and a 6 hours forecast time step for the next ten days. Further specifications of the HRES model are summarised in Table 5.1.

Parameter	Setting
Model	Meso-scale atmospheric forecast model (HRES)
Output	Analysis: 6 h, forecast: 3 h for 6 days and 6 h for 10 days
Domain	-90° to 90° lat, 0° to 359.5° lon
Resolution	0.5° lat x 0.5° lon, 361 x 720 grid points
Pressure levels	25 (1000, 950, 925, 900, 850, 800, 700, 600, 500, 400, 300, 250, 200, 150, 100, 70, 50, 30, 20, 10, 7, 5, 3, 2, 1 hPa)
Parameters	geopotential $[m^2/s^2]$, temperature [K], specific humidity [kg/kg]
Format	grib1

Table 5.1: Main specifications of the operational ECMWF analysis data

5.2.2 ALARO model data for Austria

The deterministic forecast model ALARO is a further development of the ALADIN model (Wang *et al.*, 2006) for resolutions around five km. ALARO was developed within the

international numerical weather prediction project ALADIN, a cooperation of 13 European and three North African national weather services. The ALARO5-Austria configuration as used at the Zentralanstalt für Meteorologie und Geodynamik (ZAMG) in Austria is coupled to the global IFS forecasting system at ECMWF, i.e. the initial state of the free atmosphere is derived from the ECMWF IFS system by interpolation to the ALARO grid. In addition TAWES data is assimilated to improve the initial state of the surface field. Further details about the model characteristics are summarised in Table 5.2.

Parameter	Setting
Model	ALARO, version CY35T1/CY36T1
Output	Analysis: 3 h, forecast: 1 h for 3 days
Domain	44.99° to 49.99° lat ; 6.98° to 18.98° lon
Resolution	0.04° lat x 0.06° lon ($\sim$4.8 km), 126 x 201 grid points
Pressure levels	18 (1000, 950, 925, 900, 875, 850, 825, 800, 750, 700, 650, 600, 500, 400, 300, 200, 150, 100 hPa)
Parameters	geopotential [m^2/s^2], temperature [K], specific humidity [kg/kg]
Format	grib1

Table 5.2: Main specifications of provided operational ALARO analysis data

5.3 Passive microwave radiometers

Profiles of temperature and humidity can be derived from multi-spectral analysis of the radiation emitted by atmospheric constituents. Passive microwave radiometers measure the signal intensity in units of brightness temperature T_b. The brightness temperature is related to atmospheric temperature $T(s)$ and attenuation $\gamma(s)$

$$T_b = T_{bg} \cdot e^{-op(\infty)} + \int\limits_0^\infty T(s) \cdot \gamma(s) \cdot e^{-op(s)} ds \qquad (5.3)$$

where T_{bg} is the background radiation and $op(s)$ is the opacity from ground to point s in the atmosphere (Elgered *et al.*, 1991). Both, attenuation $\gamma(s)$ and opacity $op(s)$ are frequency-dependent which allows the separation of the individual contributions from oxygen, water vapour and liquid water. Therefore passive radiometers are operated on selected frequency bands. Observations near the water vapour absorption line ($22.235\,GHz$ or $183.31\,GHz$) are linked to absolute humidity. Frequencies near the oxygen absorption line ($60\,GHz$ or

118.75 GHz) provide information about the temperature distribution. Often an additional channel, e.g. the so-called cloud correction channel at 31.4 GHz, is used to correct for liquid water droplets.

The frequency-dependency is valid as long as the drop size is significantly smaller than the observed wavelength. During snow or rain rates $< 5\,mm/h$ the humidity profile accuracy is reduced by around 20 %. At larger rain rates the profile is distorted, thus radiometers are often equipped with external sensors to flag rain events (Rose, 2011a).

The Humidity And Temperature PROfiling microwave radiometer (HATPRO, see Rose, 2011b) as in use at University of Innsbruck (Massaro *et al.*, 2015) or at GFZ Potsdam (Shangguan *et al.*, 2015) is operating in different scanning modes. In zenith observation mode (Z-mode) the radiometer measures in vertical direction in order to derive vertical profiles of temperature and humidity. In the boundary layer scanning mode (BL-mode) the resolution of the temperature profile in the lowest layers ($< 1000\,m$) can be further increased by scanning the atmosphere at certain elevation angles towards 5°. Unfortunately the BL-mode is not operable at $22\,GHz$ since no saturation of the brightness temperature occurs in this frequency band, consequently the radiometer cannot provide more information about the humidity distribution than in Z-mode.

Nevertheless, HATPRO provides profiles of temperature and humidity with an vertical resolution of

- 100 m in the lower atmospheric layers from 0 - 2000 m

- 200 - 250 m in the range from 2000 - 5000 m and

- 400 m in the layers above 5000 m, up to 10000 m.

In BL-mode the vertical resolution of the temperature profile in the lower 1.2 km of the atmosphere can be increased to 30 m. New devices also support a satellite tracking mode. Therefore the radiometer is equipped with a GNSS receiver which allows the determination of wet and dry atmospheric delays along the line-of-sight.

The absolute brightness temperature accuracy of the HATPRO can be specified with 0.5 K in the measurement range from $0 - 800\,K$ whereby the antenna thermal stability is the limiting factor. The HATPRO guarantees a stability of $\pm 0.03\,K$ over the full operating temperature range which allows to derive humidity and temperature profiles with an accuracy of $\pm 0.4\,g/m^3$ and $\pm 0.25\,K\,RMS$, respectively, with a temporal resolution of 1 min or less. In order to guarantee absolute accuracy, radiometers have to be permanently calibrated, either with internal references, e.g. in the so-called tipping curve method (Han

& Westwater, 2000) or with external cold loads. Therewith it can be assured that the provided profiles are stable over time and comparable with other measuring techniques. Unfortunately these devices are relative expensives and due to the large operating expense are only in use at selected locations.

5.4 Radiosondes

Radiosounding is one of the most accurate technique for measuring of vertical pressure, temperature, humidity or wind profiles, using instruments carried by a balloon through the atmosphere. For about 80 years radiosondes were the primary source of information for upper-air measurements up to heights of about $35\,km$ (Smit *et al.*, 2013; WMO, 2008). Radiosondes of the RSxx series produced by Vaisala are nowadays operational standard in upper-air sounding networks. The latest type RS92 (Vaisala, 2010) is equipped with a capacitive wire sensor for temperature, two thin-film capacitor sensors with integrated heating element for relative humidity and a silicon sensor for air pressure. In contrast to weather stations (see Section 5.1) radiosounding sensors are exposed to a much wider range of meteorological conditions. Hence high demands are made concerning accuracy and stability. Most modern systems are able to provide temperature within the measurement range from -90 °C to 60 °C with a standard error of $\pm 0.1\,K$ up to $\pm 0.5\,K$ at $3\,hPa$. The total uncertainty in relative humidity can be specified by about $\pm 5\,\%$, whereby the error increases with decreasing temperature. The air pressure is usually provided with $\pm 1\,hPa$ accuracy (2σ) between $1080\,hPa$ and $100\,hPa$ and $\pm 0.6\,hPa$ above up to $3\,hPa$. All measurements are usually provided high rate, i.e. once per seconds which corresponds to a vertical resolution of about $5\,m$.

For data transmission the radiosonde is equipped with a telemetry system which allows for continously transmission of the measurements to a ground station. Further, a modern radiosonde consists also of a single-frequency GPS receiver for in-flight determination of the sensor position with about $10\,m$ horizontal and $20\,m$ vertical position accuracy or m-accuracy in post-processing using differential GPS techniques (Vaisala, 2013).

Radiosondes are usually launched at specific sites, once or twice a day (at noon and midnight). International databases like the one produced by ESRL (NOAA's Earth System Research Laboratory) provide radiosonde measurements for about 1000 global sites, including also four active sites in Austria (Linz, Wien, Innsbruck, Graz), with data since 1992.

5.5 Empirical models

In contrast to meteorological measurements describing the current state of the atmosphere, empirical models are an adequate source of information if meteorological parameters are required but not with highest accuracy. An empirical tropospheric model usually consists of all required components (primarily a climatological background dataset and its describing functions, either physics-based or of empirical nature) for the computation of meteorological parameters. The empirical model GPT2w (Böhm *et al.*, 2015) as already introduced in Section 2.3.1.1 provides the meteorological parameters pressure, temperature, mean temperature, lapse rate, specific humidity and water vapour decrease factor for any user position and time. Its performance in contrast to other empirical models is described in Möller *et al.* (2014). Beside Table 5.3 gives an overview about existing tropospheric blind models, currently in use in GNSS data processing.

Model	Resolution	Parameters	References
RTCA MOPS	15°, mean and annual terms	$p, T, \Gamma, e, \lambda_e$	RTCA (1999)
GPT	Spherical harmonics up to degree and order nine, mean	p, T	Böhm *et al.* (2007)
GPT2w	1°, mean, annual and semi-annual terms	$p, T, T_m, \Gamma, e, \lambda_e$	Böhm *et al.* (2015); Möller *et al.* (2014)
GPT2w ALARO	0.2° x 0.3°, mean, annual and semi-annual terms	$p, T, T_m, \Gamma, e, \lambda_e$	Sammer (2017)
ESA model	1.5°, mean, annual and daily terms	$p, T_m, \Gamma_m, e, \lambda_e$	ESA (2012)
TropGrid	1°, mean, annual and daily terms	$T, T_m, \Gamma_m, p, e, \lambda_e$	Schüler (2001)

Table 5.3: Overview about tropospheric blind models used in GNSS data processing

5.6 Pressure extrapolation

Most GNSS sites are not equipped with meteorological sensors and even though, pressure sensors are most often not installed at the height of the GNSS antenna reference point. Also NWM data and climatological data as used in empirical models are provided usually

73

on grids or predefined levels. Thus an extrapolation method has to be applied for obtaining atmospheric pressure at GNSS site.

5.6.1   The hypsometric equation and related extrapolation errors

In Section 2.3.1 the hypsometric equation (Eq.2.16) was introduced for the extrapolation of atmospheric pressure to mean sea level. In order to evaluate its range of application the resulting pressure extrapolation error was computed, exemplary for the Austria network of weather stations[1]. Therefore the pressure measured at one site was extrapolated to all other weather stations. The resulting differences between observed and extrapolated pressure were analysed with respect to station distance and station height difference.

As input for the hypsometric equation the virtual temperature T_v was computed from measured temperature at site using Eq.2.7 and afterwards reduced to mean height using Eq.2.18. Therefore a constant temperature lapse rate of $-6.5\,K/km$ was assumed. The gravity g at mean height and mean latitude was derived from Eq.2.13.

In total 223 TAWES sites and around 9000 epochs in May and June 2013 were analysed. Figure 5.1 shows the differences in pressure (measured minus extrapolated) for selected station pairs, over the first ten days in May 2013.
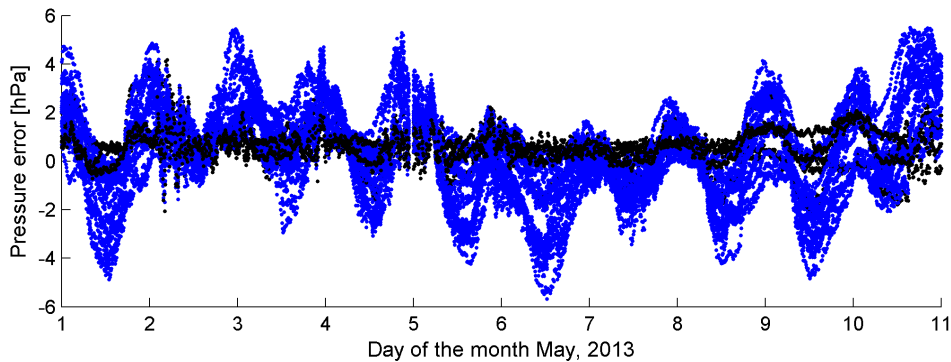
Figure 5.1: Pressure extrapolation error derived from measurements at TAWES station 11190 in Eisenstadt, Burgenland

For distances smaller than $100\,km$ (black dots) the variations are around $1\,hPa$ but can be up to $6\,hPa$ for more distant stations (blue dots). During night-time the extrapolated pressure values are systematical smaller than the measured values and vice versa during

---

[1]See Appendix B.1 for more details about the Austrian network of weather stations, called TAWES.

daytime. This semi-diurnal pressure waves are not an artefact of the extrapolation method but rather related to local pressure variations whose effect on the pressure error increase with station distance and height difference. The effect is commonly known as 'Alpine Pumping', see Winkler *et al.* (2006).

For further analysis the bias and standard deviation was computed for each station pair, taking the period of two months into account. Figure 5.2 highlights the bias and standard deviation as functions of the geometric station distance. Each dot represents one station pair.
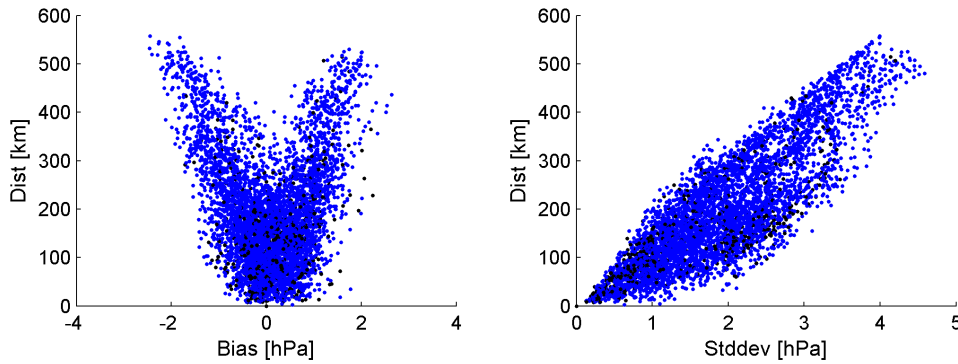
Figure 5.2: Pressure extrapolation error as function of station distance. A dot drawn in black indicates that both stations are located on the same height level $\pm 100\,m$

The bias varies between $-2\,hPa$ and $+2\,hPa$, whereby the station distance has only minor impact on the bias for stations closer than $250\,km$. Above $250\,km$ station distance, the bias is either distinct positive or negative, dependent on the stations involved[2].

A slightly different picture is drawn for the standard deviation which increases almost linearly with station distance. Thereby sub-diurnal pressure waves as visible in Figure 5.1 have a significant impact if the station distance is larger than $100\,km$. From the analysed pressure values a regression line was computed which describes the increase in standard deviation as follows:

$$stddev(p)\,[hPa] = 0.60\,[hPa] + 0.0068 \cdot dist\,[km] \tag{5.4}$$

By means of Eq.5.4 the expected pressure extrapolation error can be assessed. In order to keep the extrapolation error smaller than $\pm 2\,hPa$ in $95\,\%$ of the cases, the extrapolation

---

[2]Pressure values measured at sites in Eastern Austria and extrapolated to sites in Western Austria are mostly smaller than the measurements at the Western sites.

distance should be smaller than $60\,km$. If the sub-daily pressure waves (see Figure 5.1) are modelled, the standard deviation could be further reduced. Latter is recommended especially on longer distances.

In addition to the station distance also the difference in station height and its effect on bias and standard deviation was studied. For a more detailed analysis Figure 5.3 highlights the bias and standard deviation as function of the station height difference.
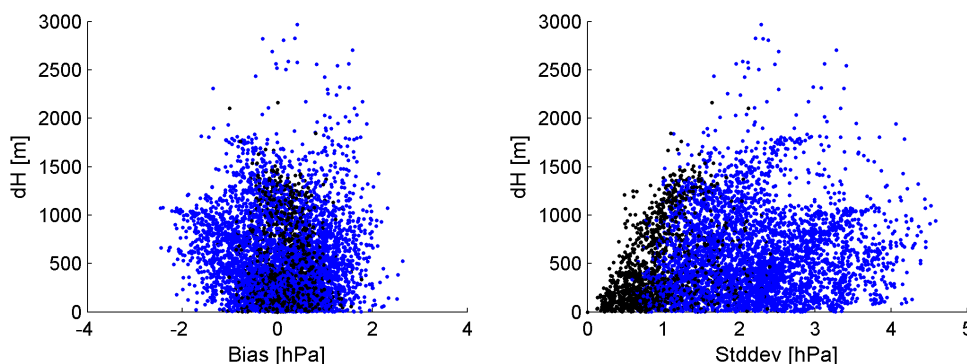

Figure 5.3: Pressure extrapolation error as function of height difference. The black dots highlight station pairs closer than $100\,km$

The bias is widely unaffected by the station height. Based on the analysed network the pressure at GNSS site can be determined with a mean bias of $0.1\,hPa \pm 0.8\,hPa$. Thereby neither the station distance nor the station height difference has a significant impact on the accuracy.

For the standard deviation a dependency on height difference is only little-noticed. For all height differences a standard deviation between $\pm 1\,hPa$ and $\pm 5\,hPa$ was observed, only for close-by stations ($<100\,km$) also standard deviations smaller than $\pm 1\,hPa$ appear.

Approximation method	Impact on pressure reduction
$1/(1+h/R_E)^2$ in Eq.2.13 is replaced by $(1-3.14 \cdot 10^{-7}h)$	$< 0.3\,Pa$
Normal gravity g_n instead of Eq.2.13	$1-2\,hPa$
Temperature instead of virtual temperature	$0.5-2\,hPa$ in the Tropics
Constant temperature	$0-60\,hPa$ over the Antarctic

Table 5.4: Impact of the strategy on pressure reduction from surface to mean sea level

If not the suggested approach, i.e. the hypsometric equation with further simplifications would be used, the resulting extrapolation errors would further increase. Table 5.4 summarises the impact for most relevant simplifications. Therefore not only the Austrian stations but a global network of stations was analysed.

In fact not only the extrapolation error but also the sensor uncertainty has an impact on how accurate the pressure can be determined at GNSS site. However, if calibrated sensors as described in Section 5.1 are used, the impact of the sensor uncertainty can be minimised to less than $\pm 0.1\,hPa$. Thereby it is assumed that the station height is precisely known, otherwise an additional bias in pressure of about $\pm 0.1\,hPa/m$ is introduced.

5.6.2   NWM data versus weather stations

From data provided by the TAWES network, HRES and ALARO time series of air pressure were computed for 38 GNSS reference sites in Austria (see Figure 4.1 and Appendix B.2 for station coordinates) whereat May and June 2013 were selected as test period.

For each GNSS station a close-by TAWES station was found within the distance of $80\,km$ and a maximum height difference of $250\,m$. On average a TAWES station exist within the radius of $13\,km$, with a mean height distance of around $50\,m$. The TAWES pressure values were extrapolation to GNSS site using the hypsometric equation (see Section 5.6.1). Beforehand the data was cleaned, i.e. unrealistic values and observations larger than three times the standard deviation were removed, and thinned out, i.e. only data at 0, 6, 12 and 18 h UTC were considered for further analysis since the HRES analysis data are available only at these epochs. If no TAWES data was available exactly at epoch, a linear interpolation method was applied to the measurements near in time (maximum $30\,min$). Larger time gaps were not refilled by interpolation in order to reduce interpolation errors.

The hypsometric equation was also used for reduction of the NWM pressure values (from HRES and ALARO) to the GNSS site. Therefore geopotential Φ, temperature T and specific humidity q was read in for each grid point. The geopotential was divided by normal gravity $g_n = 9.80665\,m/s^2$ to obtain geopotential height Z_g.

$$Z_g = \frac{\Phi}{g_n} \tag{5.5}$$

Further Z_g was converted to orthometric height H using Eq.5.6 as given in Kačmařík *et al.* (2017)

$$H = \frac{g_n \cdot R_E \cdot Z_g}{g \cdot R_E - g_n \cdot R_E} \tag{5.6}$$

where R_E is the effective Earth radius (see Appendix A.2) and g is the gravity acceleration (see Eq.2.13). The EGG97 geoid model (Denker & Torge, 1998) was exploited to convert orthometric heights (H) to ellipsoidal heights (h). Specific humidity was converted to water vapour pressure e using Eq.2.8.

For each GNSS site the adjacent four grid points of the NWM grid were selected and the pressure values from the closest pressure level were reduced for the four points to GNSS height using the hypsometric equation. Afterwards a bilinear interpolation method was applied for horizontal interpolation from grid to GNSS site.
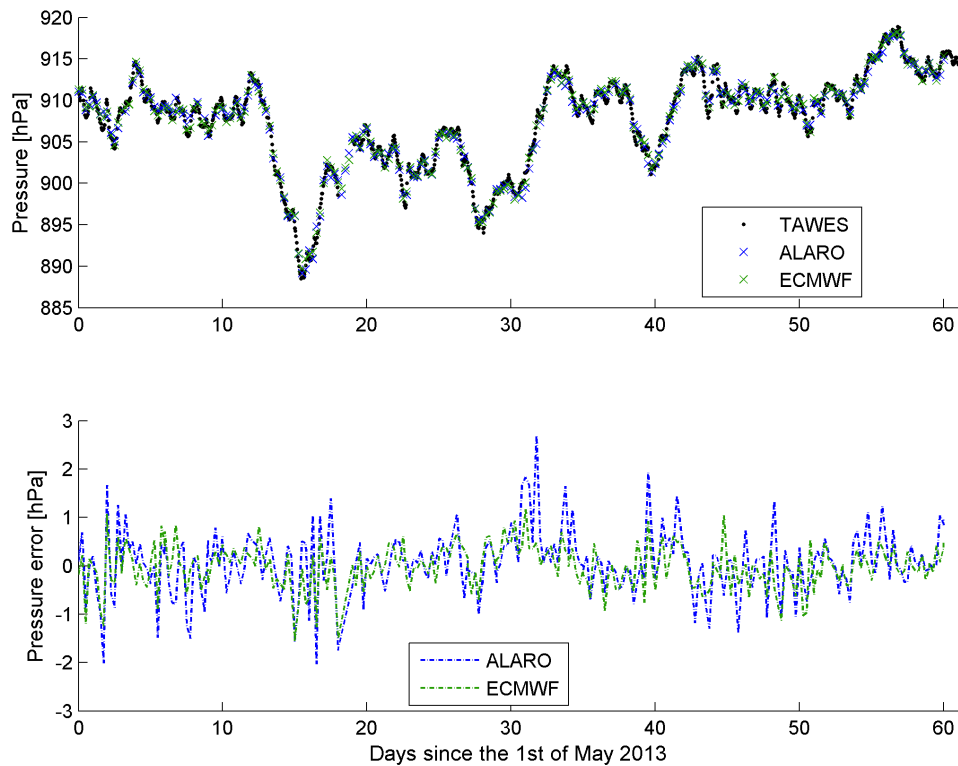
Figure 5.4: Top: Pressure values at GNSS site Dalaas in Western Austria, extrapolated from various pressure sources. Bottom: Differences in pressure between in-situ (TAWES) and NWM (ECMWF and ALARO) data

Figure 5.4 shows the obtained pressure values, exemplarily for GNSS site Dalaas (DALA), located in Western Austria, submontane at a height of about $950\,m$. The consistency of the different data sources is remarkable. Both, the extrapolated in-situ data and the NWM data describe the pressure distribution over the period of two month very precisely. Table 5.5 provides the statistic for Dalaas but also in summary for all other GNSS sites.

Station	$\bar{dp}(T-H)$	$\bar{dp}(T-A)$	$max(T-H)$	$max(T-A)$	$s_{dp}(T-H)$	$s_{dp}(T-A)$
Dalaas	-0.01 hPa	0.08 hPa	1.55 hPa	2.69 hPa	0.44 hPa	0.64 hPa
All (average)	-0.06 hPa	0.09 hPa	1.70 hPa	2.75 hPa	0.42 hPa	0.67 hPa
All (min)	-0.58 hPa	-0.40 hPa	0.86 hPa	1.60 hPa	0.21 hPa	0.44 hPa
All (max)	0.47 hPa	0.49 hPa	3.39 hPa	5.15 hPa	0.98 hPa	1.01 hPa

Table 5.5: Results from evaluation of NWM as data source for atmospheric pressure. H stands for ECMWF HRES model and A for ALARO model. The pressure values from the TAWES network (T) were used as reference, the columns "max(T-H)" and "max(T-A)" describe the largest absolute differences in pressure occurring, $\bar{dp}$ is the bias and s_{dp} the resulting standard deviation obtained for May and June 2013

The bias between TAWES (T) and HRES (H) as well as between TAWES and ALARO (A) at station Dalaas is smaller than $0.1\,hPa$ with a standard deviation of $\pm0.44\,hPa$ and $\pm0.64\,hPa$, respectively. Since the ALARO model is based on the ECMWF forecast system but with higher spatial resolution and more local data assimilated, it was expected that it can provide pressure values more accurately than the operational HRES data. However, Figure 5.4 and Table 5.5 show the opposite for station Dalaas but also for the other sites. Whereas the bias is comparable for both NWMs, their deviation from the TAWES data is considerably. The standard deviation of the ALARO data is on average $0.25\,hPa$ ($60\,\%$) larger than for the HRES data. Further analysis revealed that the difference in standard deviations increases with latitude and decreases with height.

Nevertheless, in $95\,\%$ of the cases the absolute pressure error does not exceed $0.8\,hPa$ for HRES data and $1.3\,hPa$ in case of ALARO data. Therewith both NWMs are well suited for the computation of pressure values at GNSS site, in the best case with a standard deviation smaller than $\pm0.5\,hPa$ with respect to in-situ measurements.

5.6.3   NWM data versus radiosondes

Due to the low number of launches radiosondes are not an ideal source for air pressure in GNSS applications but their high accuracy allows to use them for evaluation of other techniques at common sites. In the following pressure profiles derived from radiosonde measurements are compared twice a day (at 00 and 12 UTC) with pressure profiles derived from HRES and ALARO data. Therefore the pressure data was interpolated in $200\,m$ steps to common height levels from surface up to the top level of the ALARO model, which corresponds to an height of about $17\,km$.

Figure 5.5 shows the results for radiosonde site Vienna (lat: 48.25°, lon: 16.36°, H: 200 m) derived from data of the first two weeks in May 2013. The solid line represents the mean bias $\bar{dp}(H)$ between both techniques, separately for HRES and ALARO data. The dotted lines define the 95 % confidence interval of the pressure error, computed according to

$$\bar{dp}(H) \pm t(0.975; n) \cdot \frac{s_{dp}(H)}{\sqrt{n_t}} \tag{5.7}$$

where $s_{dp}(H)$ is the standard deviation at height H and $n_t = 28$ the number of epochs. Parameter $t(0.95; 28) = 2.048$ is the factor with which the standard deviation was multiplied for obtaining the boarders of the 95 % confidence interval.
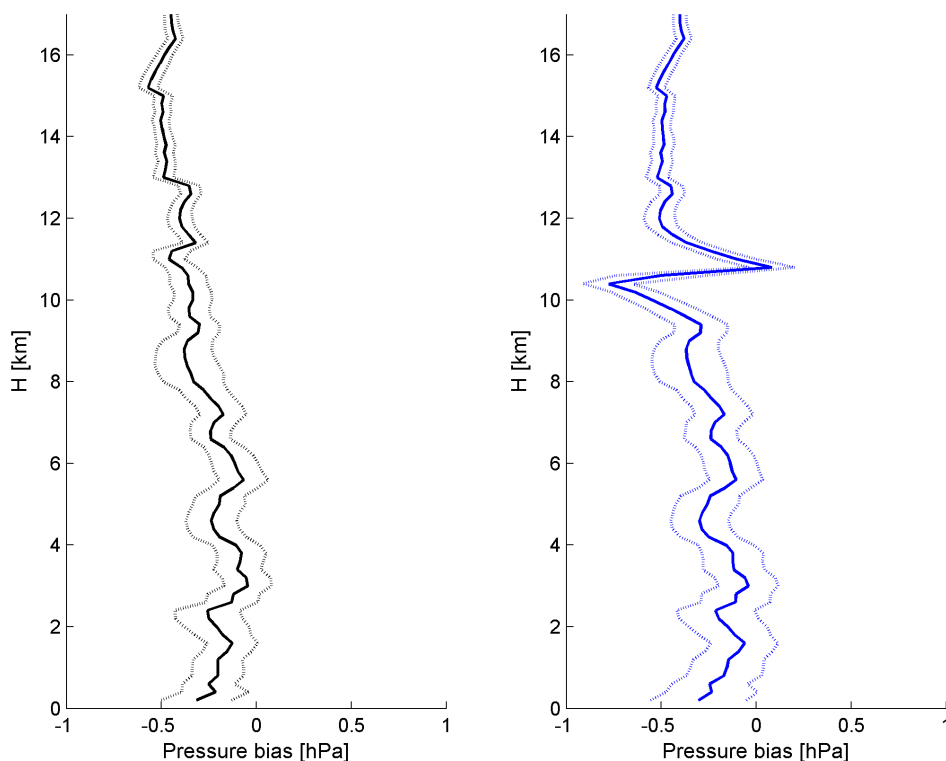
Figure 5.5: Comparison of pressure profiles derived from radiosonde (RS) and NWM data at station Vienna (lat: 48.25°, lon: 16.36°) for the first two weeks in May 2013. (Left) RS minus HRES data, (Right) RS minus ALARO data

Both, HRES and ALARO data are in good agreement with the radionsonde data, the resulting bias is smaller than $0.8\,hPa$.

Largest differences between HRES and ALARO are visible between 10 and 12 km altitude, which represents, the tropopause. A more detailed analysis revealed that this is related to the absence of the 250 hPa pressure level in the ALARO dataset. Since the temperature distribution in this part of the atmosphere is not linear, errors in temperature lead to larger pressure interpolation errors. A spline interpolation of temperature would help to reduce the pressure error in this part of the atmosphere but would increase the error in all other parts, hence it was not generally applied.

Furthermore, the range of the confidence interval shows that NWM and radiosonde data agree also well in time. Largest variations of about $\pm 0.5\,hPa$ were observed near surface, but decreases continuously with height to about $\pm 0.1\,hPa$ at 12 km altitude. In total, HRES shows a slightly better agreement to radionsonde data than ALARO. Hence TAWES pressure data and HRES data are used for reduction of hydrostatic effects in GNSS tropospheric parameters.

Chapter 6

Reconstruction of slant wet delays

In general Slant Wet Delays (SWD) cannot be estimated directly from GNSS measurements (see Section 4.4) but rather its components (ZWD, G_N and G_E) when air pressure at the GNSS site and adequate mapping functions (mf_h, mf_w, mf_g) are introduced. By taking Eq.4.23 and 4.25 into account the SWD is defined as follows:

$$SWD = ZWD \cdot mf_w(\varepsilon) + mf_g(\varepsilon) \cdot [G_N \cdot cos(\alpha) + G_E \cdot sin(\alpha)] \qquad (6.1)$$

Thereby it is assumed that the isotropic hydrostatic part and hydrostatic gradients were already removed. However, most GNSS processing software packages do only allow for considering empirical blind models like GPT or standard atmosphere for the determination of isotropic hydrostatic delays. Further, in GNSS data processing it cannot be distinguished between hydrostatic and wet gradients. Thus SWD should be corrected subsequently, if more precise pressure values can be made available.

In the following the reconstruction of slant wet delays from GNSS tropospheric estimates and the impact of its individual components is highlighted. For completeness also the post-fit observation residuals are evaluated since they may contain unmodelled tropospheric effects, not covered by the estimated tropospheric parameters.

6.1 Hydrostatic model

Saastamoinen (1972) proposed a hydrostatic model which allows the computation of Zenith Hydrostatic Delays (ZHD) from atmospheric pressure values p_s at GNSS site. Usually the coefficients in the hydrostatic model are replaced by the values suggested by Davis *et al.* (1985). Therewith and under the assumption of hydrostatic equilibrium Eq.4.24 can be

rewritten as follows

$$ZHD = \frac{0.0022768 \cdot p_s}{1 - 0.00266 \cdot cos(2\varphi) - 0.28 \cdot 10^{-6}H_s} \tag{6.2}$$

where p_s is surface pressure, φ is latitude and H_s is the orthometric height of the GNSS site. In case of NWM data, atmospheric pressure is not only provided on surface level but also on model levels. Thus also a second approach for the determination of ZHD is supposable. Thereby the pressure values are evaluated together with temperature and humidity profiles using the first term of Eq.3.18 for computation of vertical hydrostatic refractivity (N_h) profiles

$$N_h = K_1 \cdot \frac{R}{M_d}\rho \tag{6.3}$$

whereby density ρ results from Eq.2.6 to:

$$\rho = \rho_d + \rho_w = \frac{M_d}{R} \cdot \left[\frac{p}{T} - \left(1 - \frac{M_w}{M_d}\right) \cdot \frac{e}{T}\right] \tag{6.4}$$

By vertical integration or summation in case of discrete levels, Eq.4.22 can be rewritten for ZHD as follows

$$ZHD = 10^{-6} \int_{H_0}^{\infty} N_h \cdot dH = 10^{-6} \sum_{H=0}^{\infty} N_h \cdot dH \tag{6.5}$$

where dH results from the height difference between the model levels, for which N_h was computed. In order to make both approaches comparable, the coefficients $R = 8314.34\,J/kmol/K$, $M_d = 28.9644\,kg/kmol$, $M_w = 18.0152\,kg/kmol$ and $K_1 = 77.604$ K/hPa as suggested by Thayer (1974) were introduced into Eq.6.3 and Eq.6.4.

To avoid a positive bias in ZHD (of about $1\,cm$), the vertical resolution of the HRES data (see Section 5.2.1) has to be further increased. In the following a vertical resolution (dh) of $100\,m$ is proposed. A finer resolution, e.g. as suggested by Rocken *et al.* (2001) was tested but is not required since the difference in ZHD between $5\,m$ and $100\,m$ vertical resolution is smaller than $0.1\,mm$ and therewith negligible.

The vertical interpolation was carried out individually for each meteorological parameter. For air pressure the hypsometric equation was exploited with pressure values from the closest pressure level. Temperature was computed for each height level by linear interpolation between the temperature values given at adjacent pressure levels. For water vapour Eq.2.22 was used whereby the water vapour decrease factor λ_e was computed from water

vapour pressure values given at adjacent pressure levels i and $i+1$.

$$\lambda_{e,i} = (H_{i+1} - H_i)/log\left(\frac{e_i}{e_{i+1}}\right) \tag{6.6}$$

Under hydrostatic equilibrium assuming error free pressure values both approaches, the model of Saastamoinen (1972) and the vertical integration through hydrostatic refractivity profiles should be consistent.
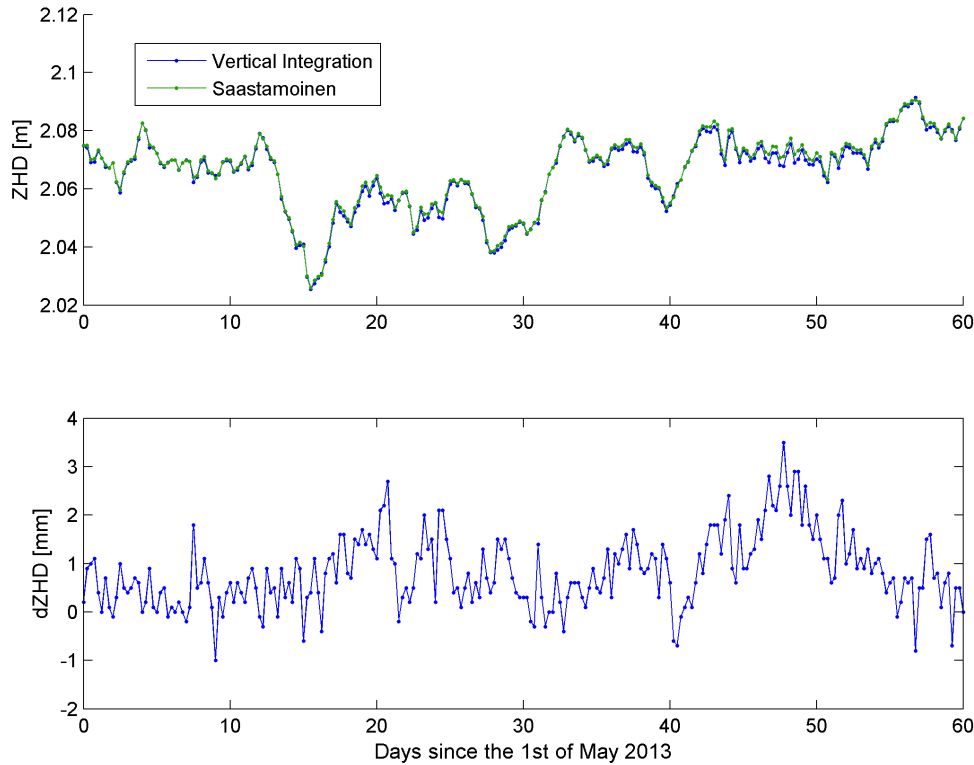

Figure 6.1: *ZHD* times series for station Dalaas as derived from ECMWF weather model data using two different approaches, the model of Saastamoinen (1972) and vertical integration

At station Dalaas (see Figure 6.1) the bias and standard deviation in *ZHD* between both approaches is $0.84\,mm \pm 0.74\,mm$, with a maximum offset observed of $3.5\,mm$ in mid of June 2013. Similar results were found for 13 other stations in Austria with a bias and standard deviation of $0.48\,mm \pm 0.71\,mm$ and a maximum offset of $3.6\,mm$.

Further analysis of the differences between both approaches revealed that mainly the bias but also the standard deviation is location-dependent. Smallest bias was obtained for stations in North-East Austria and the largest for stations in South-West Austria at higher

altitudes. It is assumed that these variations are mainly related to interpolation errors in pressure and temperature but also to deviations of the atmosphere from hydrostatic equilibrium[1].

However, since the differences are mostly smaller than $1\,mm$ both approaches can be treated as widely consistent. The benefit of the Saastamoinen (1972) model is that it is applicable to NWM data but also to site-specific pressure values. For further analysis the *ZHD* derived from accurate pressure data using Eq.6.2 was subtracted from GNSS derived *ZTD*s to correct for a priori hydrostatic model errors. The resulting *ZWD* is considered as widely free of hydrostatic effects.

6.2 Wet mapping function

According to Eq.6.1 the dominant (isotropic) part of *SWD* is obtained by multiplying the *ZWD* with mapping factors $mf_w(\varepsilon)$ which describe the elevation-dependency of the wet delay.

$$SWD \approx ZWD \cdot mf_w(\varepsilon) \tag{6.7}$$

Mapping functions like GMF (Böhm *et al.*, 2006b), GPT2w (Böhm *et al.*, 2015) or VMF1 (Böhm *et al.*, 2006a) allow for the computation of these factors for any specific site, epoch or elevation angle of interest. In the following the performance quality of the three mapping functions at low elevation angles and selected stations in Austria is analysed. As reference 2D ray-tracing through HRES pressure level data was carried out for computation of reference slant wet delays at distinct elevation and azimuth angles. The applied ray-tracer is an enhancement of the Nafisi *et al.* (2012) 2D ray-tracer taking spatial refractivity variations into account. Details and comparisons with the Hofmeister (2016) ray-tracer are provided in Section 7.2.3.

Deng *et al.* (2011) showed that the fractional error of ray-traced slant total delays is about $0.2\,\%$ in bias and $0.6\,\%$, in standard deviation, respectively. No comparable evaluation was found for *SWD*. Hence in Section 6.5 a comparison between GNSS derived and ray-traced *SWD*s was carried out.

The approach for determining mapping function errors using ray-traced delays is taken from Möller *et al.* (2014). Since only the wet mapping function is evaluated, the approach was adapted as follows:

---

[1]Compare to Hauser (1989) who integrated the equations of motion for the atmosphere and computed deviations from hydrostatic equilibrium for different sites in mountainous areas.

$$dSWD(\varepsilon) = SWD_R(\varepsilon) - ZWD_R \cdot mf_w(\varepsilon) \tag{6.8}$$

where $dSWD$ is the resulting slant wet delay error caused by insufficient mapping, ZWD_R is the zenith wet delay and SWD_R the slant wet delay derived by ray-tracing, ε is the outgoing (vacuum) elevation angle, $mf_w(\varepsilon)$ is the wet mapping factor - calculated from GMF, GPT2w and VMF1 respectively.

In contrast to Möller *et al.* (2014), where no azimuthal refractivity variations were considered for the computation of ray-traced delays (1D ray-tracing), the present reference dataset had to be corrected first for azimuth-dependent variations which are not described by the analysed mapping functions. Otherwise an offset of about $1\,cm$ at 15° elevation angle and of up to $3\,dm$ at 2° would be introduced (see Figure 6.3). These are the maximum azimuth-dependent variations observed within the analysed period.

In order to reduce the azimuth-dependent variations a mean SWD_R was computed for each elevation angle by averaging the ray-traced delays of all azimuth directions (from 0° to 330° in 30°-steps). These mean SWD_R were introduced in Eq.6.8 together with the station- and epoch-dependent mapping factors $mf_w(\varepsilon)$ for the computation of slant wet delay differences $dSWD(\varepsilon)$, caused by insufficient mapping. Figure 6.2 shows the resulting mean bias and standard deviation of all $dSWD$s, for distinct elevation angles between 2° and 15°.
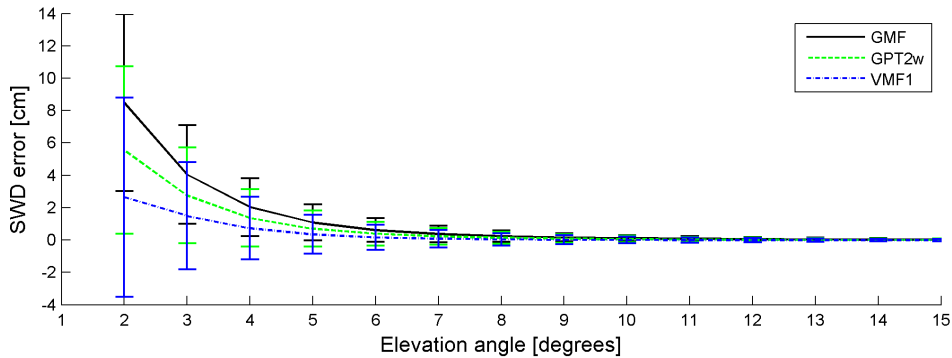
Figure 6.2: Mean bias and standard deviation of the differences in SWD [cm] between ray-tracing and GMF (black), GPT2w (green) and VMF1 (blue), calculated for 13 selected GNSS stations in Austria for the 1st of May 2013, 0, 6, 12 and 18 UTC

All mapping functions perform well for elevation angles above 10° with a corresponding bias and standard deviation $< 1\,mm$. Below 10° station-dependent variations become

more dominant. In consequence the standard deviation increases with decreasing elevation angle, almost similar for all analysed mapping functions.

Furthermore, not only the standard deviation but also the bias increases with decreasing elevation angle. On average each mapping function under-determines the elevation-dependency during the test period, whereby VMF1 shows the smallest bias. The resulting bias and standard deviation at 5° is $1.1 \pm 1.1\,cm$ for GMF, $0.7 \pm 1.1\,cm$ for GPT2w and $0.3 \pm 1.2\,cm$ for VMF1, respectively.

In comparison to Urquhart (2011) who also analysed the performance of GMF ($0.7 \pm 2.4\,cm$ at 5°) and VMF1 ($0.3 \pm 2.0\,cm$ at 5°) at global sites a similar performance with respect to bias but a smaller standard deviation was found although gridded VMF1 coefficients were used and interpolated from a global 2.0° x 2.5° grid to the GNSS sites in Austria.

Kačmařík et $al.$ (2017) analysed the impact of the mapping functions on the STD (i.e. the combined effect of hydrostatic and wet delay) at selected GNSS sites in Austria, Czech Republic and Germany. Over a period of two months (May and June 2013) GMF induced a ZTD bias of $1.2 \pm 0.2\,mm$ and a standard deviation of $1.9 \pm 0.3\,mm$ with respect to a VMF1 based ZTD.

Both, bias and standard deviation are smaller than expected from the comparison in Figure 6.2. The reason is that most GNSS satellites are visible at higher elevation angles, on average at around 35° at mid latitudes. Since the differences between the mapping functions are only significant below 10°, only around 20 % of the observations are affected by mapping function differences. In consequence the empirical mapping function GMF provides similar results as VMF1 for the analysed stations in Central Europe.

6.3   Azimuthal asymmetry

With a correlation length $< 60\,km$ (Shoji et $al.$, 2004) is azimuthal asymmetry a rather local effect. This is quite comprehensible since the largest part of azimuthal asymmetry is caused by local variations in water vapour pressure and air temperature. Further variations on larger scale are related to differences in tropospheric height (the troposphere is thicker at the equator and thinner at the poles) and variations in air pressure. Further site-specific characteristic can also be related to topography-induced effects. Morel et $al.$ (2015) showed that gradients tend to point in opposite direction to the largest terrain downslopes, whether these slopes are well defined.

The horizontal gradient model as proposed by Chen & Herring (1997) and commonly used in GNSS data processing compensates for the major parts of azimuthal asymmetry. The

analysis of the tropospheric parameters for 380 GNSS stations, provided by the International GNSS Service (IGS) for the year 2013, revealed that in 97 % of the cases gradients are smaller than $2\,mm$ and thus have to be modelled with care.

Unfortunately in GNSS analysis a discrimination between hydrostatic and wet contribution is not possible. Hence the estimated gradient parameters are usually treated as wet gradients. In consequence a small hydrostatic delay is introduced in Eq.6.1.

In order to compensate for hydrostatic effects in gradients, ray-traced hydrostatic delays can be a promising source of information. In Section 5.6.2 and 6.1 it was pointed out that HRES data are a precise source of atmospheric pressure. Douša *et al.* (2016) illustrates that tropospheric horizontal gradients estimated from GNSS data and derived from NWM data are in good agreement, especially if high resolution NWM data is used. Landskron (2017) estimated gradient parameters for a global network of VLBI stations using ray-traced delays through global operational ECMWF data with 1° spatial resolution and $6\,h$ temporal resolution. For the year 2013 absolute mean hydrostatic gradients of $0.22\,mm$ (max $0.86\,mm$) in North-South direction and $0.12\,mm$ (max $1.18\,mm$) in East-West direction were obtained. In consequence the effect of hydrostatic gradients cannot be neglected.
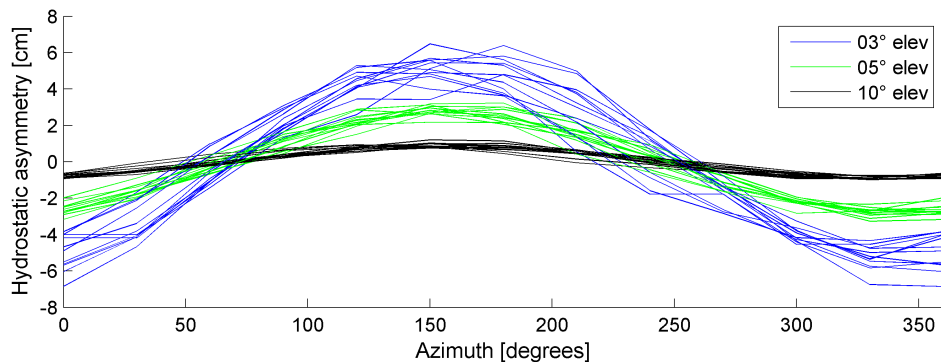
Figure 6.3: Hydrostatic component of azimuthal asymmetry as obtained by ray-tracing through ECMWF data for selected elevation and azimuth angles and 13 Austrian GNSS reference sites. Epoch: 1st of May 2013, 00 UTC

For the Austrian GNSS network ray-tracing through HRES pressure level data was carried out to determine hydrostatic delays for selected elevation and azimuth angles. Figure 6.3 shows the resulting hydrostatic azimuthal asymmetry for 13 Austrian GNSS stations and selected elevation angles whereby a mean hydrostatic delay for each elevation angle and epoch was previously removed. The hydrostatic asymmetry on May 1st, 2013 is dominated

by a distinct North-South gradient which causes delay variations of up to $7\,cm$ at 3° elevation angle.

In order to remove hydrostatic gradients from all slant delays, first for each GNSS satellite in view the ray-traced hydrostatic delay was computed. Afterwards, for compensation of the isotropic part additional ray-traced delays were determined for the same elevation angle but equidistant azimuth angles (separated by 30°). From all resulting ray-traced delays the mean hydrostatic delay was computed by averaging and further removed from the ray-traced hydrostatic delays in direction of the satellite. In contrast to the methods proposed by Chen & Herring (1997) or Brenot (2006) hereby not the mean value over a range of elevation angles is derived but rather for the single observation.

Fortunately the hydrostatic asymmetry is not as temporally variable as its wet counterpart. Thus a linear interpolation method was applied for the description of temporal variations between the epochs (0, 6, 12, 18 UTC) at which the NWM data is provided.

6.4 Tropospheric effects in zero-difference residuals

In Section 3.4.1 it was highlighted that under certain conditions, especially in convective systems variations in refractivity of up to $12\,ppm/min$ can be observed. These short-term variations but also further small-scale effects like turbulences in the troposphere cannot be described with the tropospheric parameters ZWD, G_N and G_E. These unmodelled tropospheric effects remain entirely in the post-fit observation residuals whether GNSS observations are processed undifferenced and if they are not absorbed by other parameters (e.g. station clock). Shoji *et al.* (2004) showed that post-fit residuals are correlated only up to $2\,km$ in distance. Hence, beside satellite clock errors mainly site-effects like tropospheric effects, multipath and unmodelled antenna phase variations characterise the post-fit residuals.

Station-wise residual stacking

Processing strategies like spectral analysis (Axelrad *et al.*, 1996) or residual stacking methods (Knöpfler, 2015) allow for identification and mitigation of signals in the post-fit residuals. Kačmařík *et al.* (2017) computed systematic effects by stacking of post-fit residuals in 1° x 1° bins over a period of two months (May and June 2013), residuals larger than three sigma were removed beforehand although its effect is not significant (Kaplon, 2017).

Figure 6.4 shows the distribution of the raw and of the cleaned residuals (after systematic effects were removed) for station Kirchberg (KIBG) in Tirol, Austria.
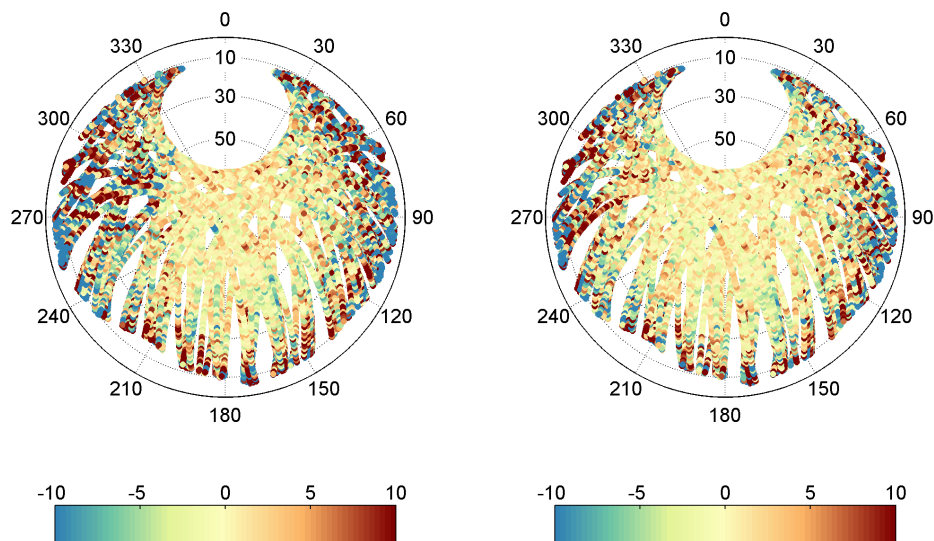

Figure 6.4: Phase residual pattern for GNSS station Kirchberg [mm]. (Left) raw post-fit residuals and (right) cleaned post-fit residuals. Period 5th to 12th of May 2013

Almost no residuals appear at higher elevation angles above 60°. Below 60° the magnitude of the residuals but also its variation increases. At station Kirchberg a specific residual pattern in North-West direction is visible which is probably related to multipath. After residual cleaning the upper part of this pattern (between 15° and 50° elevation angle) widely vanishes. In consequence also the standard deviations improve, see Table 6.1.

Station	$\overline{Res}(raw)$	$\overline{Res}(cln)$	$s_{Res(raw)}$	$s_{Res(cln)}$
KIBG	-0.12 mm	-0.09 mm	10.29 mm	8.85 mm
SAAL	-0.01 mm	-0.03 mm	9.44 mm	8.62 mm
POTS	0.01 mm	0.23 mm	15.31 mm	14.39 mm
WTZR	-0.19 mm	0.04 mm	15.64 mm	14.17 mm

Table 6.1: Statistic of raw and cleaned post-fit residuals for selected stations in Austria and Germany for GPS and GLONASS satellites observed above 5° elevation angle between the 5th and 12th of May 2013

While the bias is almost zero, larger differences between the analysed stations are visible with respect to standard deviation. This has several reasons. First, individual antenna

phase corrections were applied for the stations in Austria but only type corrections for the German stations. The resulting effect, in the order of a few millimetres, causes a noisier behaviour in the residual pattern of the two German stations.

However, largest differences are related to obstructions at low elevation angles. For all sites a cut-off angle of 3° was preset but for some stations, especially at the Austrian stations further obstructions affect signal reception. Compared to station Potsdam (POTS) on average 20 % fewer observations, especially at lower elevation angles, were received at station Saalfelden.

Further differences in the distribution of residuals are related to multipath effects as already shown in Figure 6.4 but also to antenna and receiver specifications. A comparison of eight geodetic antenna and receiver configurations (Möller, 2015) revealed significant differences with respect to multipath susceptibility, cycle slips and carrier-to noise-ratio.

However, due to cleaning it is expected that the post-fit residuals are mainly free of multipath, unmodelled antenna phase variations and other long term systematic effects. The question is if and when these cleaned residuals should be added to the *SWD* for reconstruction of unmodelled tropospheric delays. Well, this is rather difficult to answer since a clear reference for evaluation is missing. Comparisons with radiometer data at GFZ Potsdam (Kačmařík *et al.*, 2017) showed that the differences in *STD* between both techniques increase after post-fit residuals were added. Even after the post-fit residuals were cleaned, i.e. multipath effects were removed by stacking methods, no better agreement was observed. However, this is not a clear argument but up to now no study confirms that cleaned post-fit residuals improve the *SWD* solution.
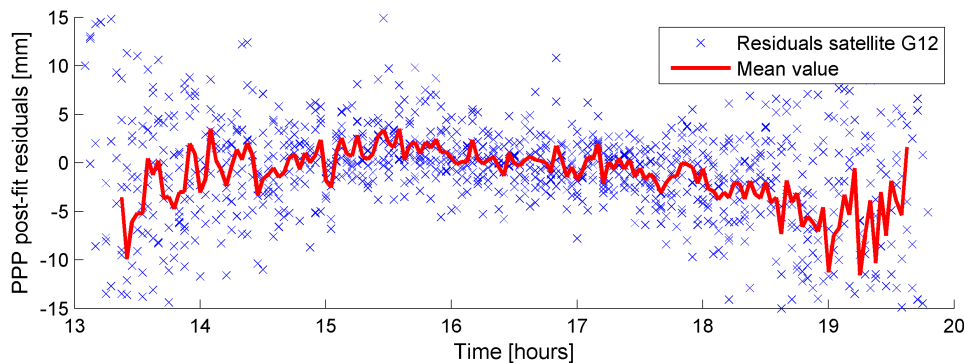
Figure 6.5: Stacked post-fit residuals for satellite G12 and seven GNSS sites in Austria, Germany and Czech Republic as obtained on the 5th of May 2013

Satellite-wise stacking of post-fit residuals

Further improvement in post-fit residual processing is expected by satellite-wise stacking of post-fit residuals at common epochs. Taking a larger number of stations into account, it is assumed that thereby site-specific tropospheric effects are averaged out and that common errors like satellite clock errors can be identified. For testing of this approach the cleaned post-fit residuals were plotted satellite-wise, see Figure 6.5 and for each epoch a mean value was computed by taking at least five non co-located GNSS sites into account.

In GNSS data processing final satellite clock products as provided by ESOC with $30\,sec$ temporal resolution and an accuracy of about $20\,ps$ (ESOC, 2017) were fixed to their given value. In consequence satellite clock errors of $6\,mm$ are introduced in the GNSS solution. A standard deviation of the stacked residuals of about $3\,mm$ indicates that about half of the satellite clock error could be identified and in further consequence removed from the post-fit residuals. Figure 6.6 shows the resulting residuals for station Saalfelden.
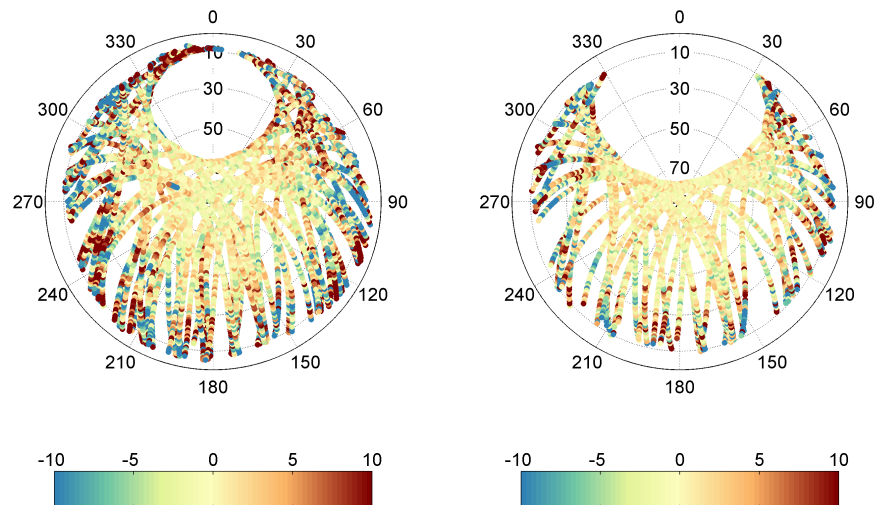
Figure 6.6: Residual pattern for GNSS station Saalfelden as obtained on the 31st of May 2013 [mm]. (Left) raw post-fit residuals and (right) post-fit residuals after cleaning of satellite-clock errors; residuals which could not be cleaned from satellite-clock errors (stacking requires at least five non co-located sites) are not shown

The last day in May (DoY 151) was selected since during this day a cyclone was passing over station Saalfelden (see Section 8.1). In consequence the residual pattern of station Saalfelden became more noisier than on the rather calm days before. Such an increase is not visible at other stations (e.g. station Potsdam) which was affected by the cyclone one day before, see Figure 6.7.
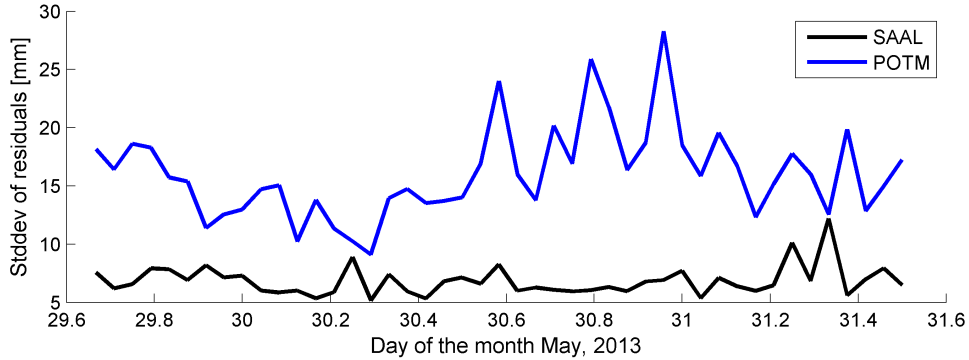
Figure 6.7: Standard deviation of the undifferenced GNSS post-fit residuals, computed in hourly batches for the last three days in May 2013

Nevertheless, satellite-wise stacking is appropriate for visual analysis of specific events but if not a larger network of stations is processed this technique generates gaps or higher variations in the residual time series, especially at low elevation angles. Re-introduced into GNSS data processing or applied to slant wet delays for GNSS tomography these gaps would degrade the solution. Hence in Section 8.2.4.4 the stacking technique was not applied for analysis of the impact of post-fit residuals on the tomography solution.

6.5 Comparison of GNSS with ray-traced SWDs

Comparison of GNSS slant wet delays with ray-traced delays was carried out to identify systematic effects between both techniques. Thereby all GPS and GLONASS satellites in view above 5° elevation angle as observed at station Saalfelden on the 30th of May 2013 were analysed (in total about 45,000 observations).

From the estimated *ZTD* the hydrostatic delay was removed using the Saastamoinen (1972) model and local pressure values extrapolated from TAWES station 11137 (see Appendix B.1) to GNSS site Saalfelden using the hypsometric equation. The resulting *ZWD* and the two gradient parameters (G_N and G_E) were interpolated linearly to the epoch of interest and afterwards mapped to the elevation and azimuth angle of the satellite using GMF for *ZWD* and the gradient mapping function for the gradient parameters. In addition a second solution was generated whereby GMF was replaced by VMF1. The largest *SWD* offset between GMF and VMF1 is $7\,mm$ at 5° elevation angle. Over all elevation angles a bias and standard deviation of $-0.1\,mm \pm 0.4\,mm$ was obtained.

The ray-traced slant wet delays were computed by means of the ray-tracer as already applied in Section 6.2 for evaluation of the wet mapping functions. The required background refractivity field was derived from HRES data, provided every 6 hours at 0, 6, 12, 18 UTC. Between the nodal points a linear interpolation method was applied to the refractivity fields in order to increase the temporal resolution to $30\,sec$ (the sampling rate of the GNSS observations).

Figure 6.8 shows the differences between GNSS and ray-traced slant wet delays. In addition to the linear temporal interpolation a second solution based on spline interpolation was computed. The spline solution is not shown since it provided slightly worse results (bias between ray-traced and GNSS derived SWDs increased slightly from $11.5\,mm$ to $12.1\,mm$).
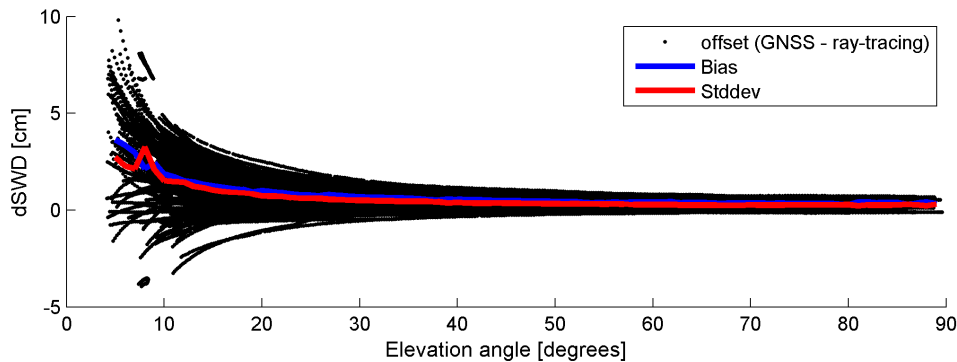
Figure 6.8: Differences in SWD between GNSS and ray-tracing through ECMWF data, exemplary for station Saalfelden and the 30th of May 2013

Both, bias and standard deviation of the differences in SWD increase proportional with decreasing elevation angle. They are $-3\,mm \pm 3\,mm$ in zenith direction and $-36\,mm \pm 27\,mm$ at 5° elevation angle, which corresponds to a relative bias of about $3.5\,\%$ and a relative standard deviation of about $2.5\,\%$. A similar characteristic but a smaller relative bias was found by Deng *et al.* (2011) for STDs. Kačmařík *et al.* (2017) explains the larger bias at station Saalfelden by the submontane location, South-West of Salzburg, which is not represented well by the HRES data. In consequence a larger bias than on other stations is introduced.

Finally, from the comparison of ray-traced and GNSS derived SWDs it can be concluded that both techniques are sensitive to the current water vapour and temperature distribution in the atmosphere but that their systematic differences are still significant which makes GNSS derived slant wet delays interesting for atmospheric studies.

Chapter 7

GNSS tomography of the lower atmosphere

For conversion of precise integral measurements (like $SWDs$) into two-dimensional structures, a technique called tomography [tomo, greek: 'slice'] has been invented. The basic mathematics behind were established by Radon (1917), also known as Radon transform. The first practical scanner based on this technique was built by Cormack (1963) and Hounsfield (1973), who were therefore awarded with the Nobel prize for medicine in 1979. Introduced in diagnostic radiology it allows the reconstruction of cross-sections of human body from X-ray scans.

Almost in parallel the tomography concept was developed and applied in geosciences. First results were published by Aki *et al.* (1977) who describe a three-dimensional inversion method for simultaneous reconstruction of seismic body wave velocities and epicentre coordinates.

According to Iyer & Hirahara (1993) the general principle of tomography is described as follows:

$$f_S = \int\limits_S g(s) \cdot ds \tag{7.1}$$

where f_S is the projection function, $g(s)$ is the object property function and ds is a small element of the ray path S along which the integration takes place. In geosciences $g(s)$ is usually replaced by signal velocity, slowness or refractivity; latter is related to velocity by Eq.3.4. The integral measure (f_S) is signal travel time or phase excess which can be converted to signal travel time.

One difficulty in performing the integral is that the ray path is not a straight line but rather dependent on the object properties along the signal path. A change in $g(s)$ leads to a change in S and f_S.

Another challenge is related to the limited number of radio sources and detectors with respect to the size of the object of interest. The resulting number and distribution of integral measurements are usually not sufficient for reconstruction of two or three-dimensional models in an analytical way using Radon transform. Hence in geosciences, the Abel tranform, a further simplification of the Radon transform is more popular. It allows for determination of one-dimensional profiles from integral measurements of excess phase delay, assuming spherical symmetry. Due to the unique observation geometry it is usually applied to GNSS phase measurements provided by radio occultation missions (see Section 4.7).

The conditions for the Abel transform (spherical symmetry and parallel observation paths) are not fulfilled for ground-based GNSS observation techniques. In addition the Abel transform does not allow for determination of two- or even three-dimensional refractivity fields. Therefore the inverse problem is either solved linearly or iterative non-linearly (Iyer & Hirahara, 1993). A full non-linear solution is not of practical relevance since it can be shown that the travel path is not significantly perturbed by linearisation assumptions (Rawlinson & Sambridge, 2003). In the following common solving techniques (linear and iterative non-linear) are presented and it is analysed whether they can be applied for reconstruction of refractivity fields in the lower atmosphere from ground-based GNSS observations.

7.1 Solving techniques

If f_s in Eq.7.1 is replaced by the Slant Total Delay (STD) and $g(s)$ by the index of refraction $(n - 1)$, the basic function of GNSS tomography is obtained as follows:

$$STD = \int_S n \cdot ds - \int_{S_0} ds \qquad (7.2)$$

where S is the 'true' signal path and S_0 is the theoretical straight line signal path in vacuum. The second term in Eq.7.2 stems from the definition of STD as described in Section 4.4. Strictly speaking also the limits of the integral have to be adapted. Since STD reflects the signal delay in the neutral atmosphere, also S should be limited to this part of the atmosphere (from surface up to about $80\,km$ altitude).

From the **Fermat´s principle** it can be assumed that first order changes of the ray path lead to second order changes in travel time, i.e. for small perturbation of the path, the travel-time is stationary. This principle is utilised for setting up the tomography approach.

In linear tomography S is replaced by S_0 and corrections to n are made under the assumption of straight lines. The iterative non-linear approach also ignores the path dependency in the inversion of n along ds but takes the signal bending into account by the definition of the ray paths. In consequence after each processing step the ray paths are re-computed by solving the Eikonal equation using e.g. ray-tracing shooting techniques (see Section 7.2.3).

In order to find a numerical solution for Eq.7.2 the object of interest, e.g. the neutral atmosphere is discretised in area elements (in two-dimensions) or volume elements (in three-dimensions) in which the index of refraction is assumed as constant. Consequently and by replacing the index of refraction with refractivity, Eq.7.2 reads:

$$std = \sum_{k=1}^{m} N_k \cdot d_k \tag{7.3}$$

where N_k is the constant refractivity and d_k is the ray length in volume element k. For the conversion of n into N usually a factor of 10^{-6} is introduced. However, this can be avoided if the length of the ray path is introduced in km and the slant total delay in mm.

Suppose that there are l observations (std), indexed by $j = 1, 2, ..., l$ and m volume elements (short: voxels) indexed by $k = 1, 2, ..., m$, a linear equation system can be set up. In matrix notation it reads:

$$STD = A \cdot N \tag{7.4}$$

where STD is the observation vector of size $(l, 1)$, N is the vector of unknowns of size $(m, 1)$ and A is a matrix of size (l, m) which contains the spatial derivatives of the slant total delays with respect to the unknowns.

$$\underline{A} = \begin{bmatrix} \frac{\partial std_1}{\partial N_1} & \frac{\partial std_1}{\partial N_2} & \cdots & \frac{\partial std_1}{\partial N_m} \\ \frac{\partial std_2}{\partial N_1} & \frac{\partial std_2}{\partial N_2} & \cdots & \frac{\partial std_2}{\partial N_m} \\ \vdots & \vdots & \vdots & \vdots \\ \frac{\partial std_l}{\partial N_1} & \frac{\partial std_l}{\partial N_2} & \cdots & \frac{\partial std_l}{\partial N_m} \end{bmatrix} \tag{7.5}$$

Since Eq.7.3 is linear, the partial derivatives of STD are the ray lengths (d_k) in each voxel. Analogue to Eq.7.4 the linear equation system is defined for slant wet delays

$$SWD = A \cdot N_w \tag{7.6}$$

whereby N is replaced by wet refractivity vector N_w. For linear tomography this has no further consequence. For the non-linear approach the hydrostatic component cannot be simply ignored since it has also an impact on the path geometry. Hence for each iteration the hydrostatic refractivity should be known with adequate accuracy for the determination of the path geometry.

7.1.1   The inverse problem

From Eq.7.6 a solution for N_w is obtained by inversion of matrix A.

$$N_w = A^{-1} \cdot SWD \tag{7.7}$$

The inverse A^{-1} exists if A is squared ($l = m$) and if the determinant of A is non-zero, otherwise matrix A is called singular. Unfortunately singularity appears in GNSS tomography since the observation data is incomplete and matrix A is not of full rank (i.e. has zero singular values). In consequence Eq.7.7 is ill-posed, i.e. not uniquely solvable. In order to find a solution anyway and to remove the deficiencies of the ill-posed problem several strategies have been developed for solving or avoiding the inverse problem. The most prominent are:

- Iterative algebraic reconstruction techniques

- Truncated singular value decomposition

- Tikhonov regularization

- others (bordering method, best linear mean square estimates, ...)

In the following the first three techniques, which were proven in practice as promising, are described more in detail.

7.1.2   Algebraic reconstruction techniques

Kaczmarz (1937) suggested an iterative Algebraic Reconstruction Technique (ART) for linear systems of equations. It allows for avoiding the inversion problem, further matrix A has not to be initialised entirely but rather row-wise, which can be a benefit in large equation systems. ART applied to Eq.7.6 reads:

$$N_w^{i+1} = N_w^i + \frac{\omega}{\langle A_j,\, A_j \rangle} \cdot \left(swd_j - \left\langle A_j^T,\, N_w^i \right\rangle \right) \cdot A_j \tag{7.8}$$

where A_j indicates the jth row of matrix A, $\langle A_j, A_j \rangle$ is the resulting inner product of the row vector and the difference $swd_j - \langle A_j^T, N_w^i \rangle$ is the corresponding residual. Dependent on the ray length and the relaxation factor ω the residual is fragmented and applied to N_w^i in order to obtain the improved refractivity field N_w^{i+1}, which is again input for the next iteration. Eq.7.8 converges to the solution of Eq.7.6 with minimal norm if $0 < \omega < 2$. However, Bender *et al.* (2011) showed that a relaxation parameter of ~ 0.175 provides best results in terms of convergence and stability, assuming regular gridded station networks of the size of Germany.

In practice ART has the advantage that it can be applied to any observation geometry, even to incomplete data problems like in GNSS tomography but in case of non-linearity in addition also matrix A has to be initialised iteratively.

7.1.2.1 Multiplicative algebraic reconstruction technique

Dependend on how the discretisation is done, different versions of ART exist. The Multiplicative Algebraic Reconstruction Technique (MART, see Bender *et al.* 2011) leads in general to a faster convergence than the additive ART technique.

$$N_{w,k}^{i+1} = N_{w,k}^i \cdot \left(\frac{swd_j}{\left\langle A_j^T, N_w^i \right\rangle} \right)^{\frac{\omega \cdot A_{j,k}}{\left\langle A_j, A_j \right\rangle}} \tag{7.9}$$

By using MART each refractivity is improved individually by multiplication with a correction term. A modification of the exponent of Eq.7.9 provides different subversions of MART as further described by Bender *et al.* (2011).

7.1.3 Truncated singular value decomposition

Moore (1920) and Penrose (1955) invented a general solution for singular and non-squared matrices, widely known as pseudo inverse or Moore-Penrose inverse A^+. A numerical solution for the pseudo inverse can be obtained by singular value decomposition (Strang & Borre, 1997). Thereby matrix A is split into three components

$$A = U \cdot S \cdot V^T \tag{7.10}$$

where U (l, l) and $V^T(m, m)$ are orthogonal matrices. The columns of U and V^T are the normalised left and right singular vectors of A, respectively. Matrix S (l, m) is a diagonal

matrix, the first m diagonal elements are the singular values $s_{k,k}$, all other elements are zero. From Eq.7.10 the pseudo inverse is obtained as follows

$$A^+ = V \cdot S^{-1} \cdot U^T \tag{7.11}$$

whereby only the non-zero diagonal elements of S are used. The ratio between the largest and the smallest singular value defines the condition number $\kappa(A)$.

$$\kappa(A) = \frac{|s_{max}|}{|s_{min}|} \tag{7.12}$$

A value of $\kappa(A)$ near 1 indicates a well-conditioned matrix, i.e. the solution is rather insensitive to measurements errors. A large condition number indicates an ill-conditioned problem. The condition number of A can be improved by neglecting tiny singular values. This technique is widely known as Truncated Singular Value Decomposition (TSVD) technique (Hansen, 2000).

Thereby the ill-conditioned matrix A is approximated by a better conditioned matrix $\tilde{A}$ of lower rank. Flores (1999) suggested $s_{lim} = 2.8\,km$ as threshold for $s_{k,k}$, i.e. all singular values smaller than s_{slim} are set to zero.
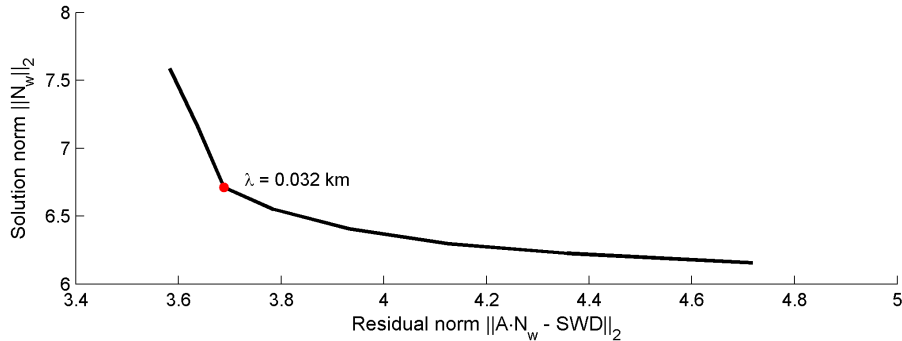
Figure 7.1: Representative L-curve for GNSS tomography settings, obtained by truncated singular value decomposition

7.1.3.1   L-curve technique

In practice an optimal threshold for s_{lim} can be determined using the L-curve technique (Hansen, 2000). Therefore a set of solutions is determined with varying s_{lim}-values. For each solution the norm of the regularised solution ($log\,\|N_w\|_2$) is plotted against the norm

of the residuals $(log \, \|A \cdot N_w - SWD\|_2)$. By connecting all points a concave L-shaped curve is obtained, whereby the corner of the curve, i.e. the point of maximum curvature, defines the optimal solution.

Figure 7.1 shows a L-curve for a typical GNSS tomography setting (more details about the data used is given in Section 8.2). The red dot indicates the corner point of the L-curve and therewith the optimal solution is obtained by setting $s_{lim} = 0.032 \, km$ as threshold for singular values. This point was found by analysis of the consecutive vectors and angles between the nodal points as described in Rodriquez (2005). The L-curve technique is applied in further chapters to find the optimal singular value threshold.

7.1.4 Tikhonov regularisation

A more generalised solution of the regularisation problem can be found in (Tikhonov, 1963) which gives a possible solution for the minimisation problem

$$N_{w,\eta} = arg \, min \left\{ \|A \cdot N_w - SWD\|_2^2 + \eta^2 \, \|L(N_{w0} - N_w)\|_2^2 \right\} \tag{7.13}$$

where η is called regularisation parameter or Tikhonov factor and N_{w0} is an a priori estimate of N_w. The 'size' of the solution is defined by the norm $\|L(N_{w0} - N_w)\|_2$ and the 'fit' by the norm of the residual vector $\|A \cdot N_w - SWD\|_2$. The best way for solving Eq.7.13 is to treat it as least squares problem (see Section 7.2.4.1). Elden (1977) showed that matrix L can be replaced by identity matrix I, i.e. in consequence the condition number of A is improved by adding a small multiple of the identity to matrix A.

$$\tilde{A} = A^T A + \eta \cdot I \tag{7.14}$$

A possible solution for η can be obtained by means of SVD (see previous section). Thereby the elements of diagonal matrix S are replaced by the coefficients $r_{k.k}$.

$$r_{k,k} = \frac{s_{k,k}^2}{s_{k,k}^2 + \eta} \tag{7.15}$$

If the Tikhonov factor is defined as sharp filter

$$\eta = \begin{cases} 1 \, for \, s_{k,k} \geq s_{lim} \\ 0 \, for \, s_{k,k} < s_{lim} \end{cases} \tag{7.16}$$

the resulting solution can be interpreted as smoothed TSVD solution.

7.2 Tomography model, data and algorithms

As consequence of the ill-posedness the tomography solution is sensitive to observation errors, changes in the observation geometry but also to the solving strategy and its parameters defined within the analysis. Hence GNSS tomography is in principle a complex optimisation problem. Its individual components and their contribution to the tomography solution have to be understood, otherwise the information content of the integral measurements is misallocated or superimposed by artefacts of the processing strategy.

In the following a set of synthetic slant wet delays is generated (forward operation) and processed using a tomography approach for the estimation of wet refractivity fields (backward operation). Based on the results specific tomography settings are evaluated in order to find an optimal processing strategy.
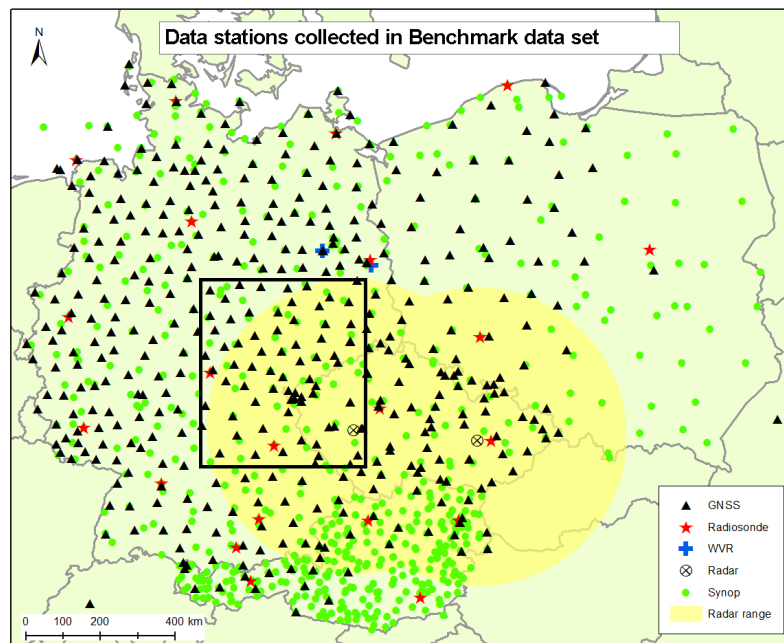
Figure 7.2: Distribution of GNSS sites in Central Europe. Source: Douša *et al.* 2016

7.2.1 Synthetic (ray-traced) slant wet delays

For a network of 72 GNSS stations located in Central Europe (see Figure 7.2, black rectangle) a set of slant wet delays was generated by 2D ray-tracing (see Section 7.2.3)

through operational ALARO weather model data. The mean station distance is about $50\,km$, the station height varies between $70\,m$ and $885\,m$. In order to simulate a realistic scenario the 'outgoing' elevation and azimuth angles were computed for the GPS and GLONASS satellites in view above 3° elevation angle using satellite broadcast ephemerides (see Appendix A.5).

7.2.2 Block parameterisation of the refractivity field

For solving the GNSS tomography problem for wet refractivity first the lower atmosphere has to be parameterised either using block parameterisation (voxels) or a grid parameterisation together with an adequate interpolation function (Perler, 2011; Manning, 2013). Also a discretisation in the wavenumber domain (Wang & Pratt, 1997) is possible but so far not common in GNSS tomography.

In the following the block parameterisation is used, i.e. the space above the ellipsoid is divided into curved volume elements, their centre points are defined by ellipsoidal coordinates. For the synthetic test case each voxel within the black rectangle in Figure 7.2 [lat: 48.75° - 52.25°, lon: 9.75° - 14.25°] was defined with a footprint of 0.5° x 0.5° which reflects approximately the mean GNSS station distance. Bender & Raabe (2007) defined this as the optimal horizontal resolution.

In vertical direction (Manning, 2013) found that 15 layers separated by exponential spacing provide best results compared to a lower number of levels and also compared to equidistant spacing. Thus, the exponential spacing between two consecutive levels was computed as follows

$$dh(i) = dh(0) \cdot q_h^i \tag{7.17}$$

where q_h is the so-called growth factor (Perler, 2011), $dh(0)$ is the height difference between the lowest two layers and $dh(i)$ is the height difference of the consecutive ones.

Vertical model	Resulting vertical voxel boundaries [m]
$15\,layers$, $dh(0) = 100$, $q_h = 1.3$, $layer1 = 50\,m$	0, 100, 200, 360, 538, 800, 1108, 1544, 2072, 2800, 3702, 4922, 6460, 8506, 11120, 14562
$15\,layers$, $dh(0) = 450$, $q_h = 1.1$, $layer1 = 225\,m$	0, 450, 900, 1440, 1990, 2636, 3308, 4086, 4902, 5840, 6832, 7962, 9166, 10530, 11990, 13638

Table 7.1: Selected vertical tomography models and corresponding vertical voxel boundaries

For further analysis two different settings were tested assuming a) an exponential vertical spacing with $q_h = 1.3$ and $dh(0) = 100\,m$ and b) an alternative 15-layer-solution with $q_h = 1.1$ and $dh(0) = 450\,m$. The resulting voxel model boundaries (bottom and top layers) are summarised in Table 7.1.

The larger q_h the higher the resolution at lower altitudes. A value of $q_h = 1.3$ as used for model a) and proposed by (Perler, 2011; Manning, 2013) was used in order to obtain a higher resolution at levels where a higher variation in water vapour is expected. Model b) is also defined by exponential spacing but with larger spacing between the lower layers which provides consequently a better observation geometry (see Section 7.2.3.4).

7.2.3 Reconstruction of signal paths (ray-tracing)

For the tomographic equation system (see Eq.7.7) the observation geometry has to be introduced. Thus in the following for each *SWD* the corresponding ray paths and the ray length in each voxel are determined using ray-tracing techniques. Input for the ray-tracer is at least the position of the transmitter at time of transmission and of the receiver at time of reception. Nevertheless for most applications it is sufficient to disregard the time offset between transmission and reception since the corresponding change in geometry is negligible.

In case of synthetic slant wet delays the station position is introduced as known and the GNSS satellite positions were determined at receiving time using satellite ephemerides as broadcasted on the 1st of May 2013 00:00 GPS-time. The corresponding formulas are provided in Appendix A.5.

Assuming that the geometric optics approximation is valid and that the microwave wave propagation is considered as ray (see Section 3.5.1) the ray path between transmitter and receiver can be determined by solving the Eikonal equation

$$\|\nabla L\|^2 = n\left(\overrightarrow{r}\right)^2 \tag{7.18}$$

where n is the index of refraction, described as function of the position vector $\overrightarrow{r}$, and L is the optical path length. Hofmeister (2016) provides a strict solution for Eq.7.18 for the 3D case but formulates also possible approaches for the 2D case. Latter is of major interest for ray propagation in the atmosphere since the computational burden can be significantly reduced while the error induced by limiting the ray to a vertical plane is small in comparison to a full 3D solution, see Nafisi *et al.* (2012).

In the following two common solving strategies for reconstruction of ray lengths are presented and compared to each other. Both are based on the piece-wise linear ray-tracing approach (Hofmeister, 2016) using shooting techniques (Rawlinson & Sambridge, 2003). Within the first strategy the ray path is assumed as straight line, the second strategy takes also the atmospheric bending into account.
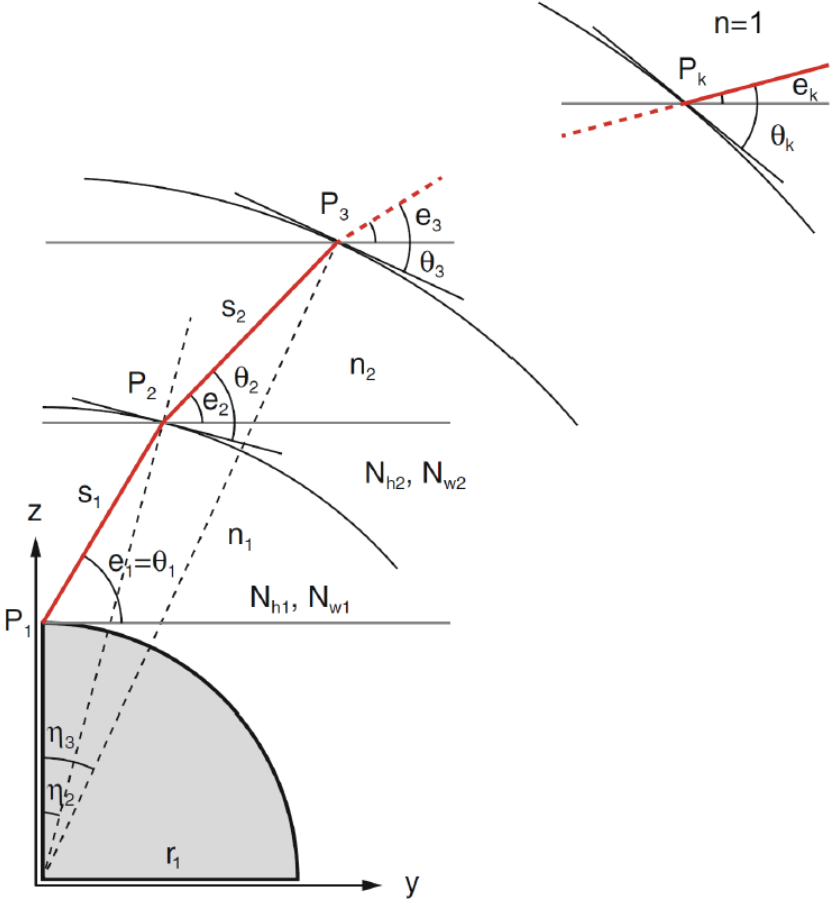

Figure 7.3: Geometry of the ray-tracing approach with the geocentric coordinates (y, z), the geocentric angles (θ, η), elevation angle e and s as the distance between two ray points. Source: Hofmeister (2016, Figure 4.1)

7.2.3.1   Straight line ray-tracing

Starting point for the ray-tracer is the receiver position, i.e. the ellipsoidal coordinates $(\varphi_1, \lambda_1, h_1)$ of the GNSS antenna, and the 'outgoing' elevation angle (ε) and azimuth (α) under which the satellite is observed (see formulas in Appendix A.5).

Therefore the initial parameters for ray-tracing, i.e. the geocentric coordinates (y, z) and the corresponding angles (Θ, η) can be derived

$$y_1 = 0 \tag{7.19}$$

$$z_1 = R_G + h_1 \tag{7.20}$$

$$\eta_1 = 0 \tag{7.21}$$

$$\theta_1 = \varepsilon \tag{7.22}$$

where R_G is the Gaussian radius, an adequate approximation of the Earth radius

$$R_G = \frac{a^2 \cdot b}{(a \cdot cos\varphi_1)^2 + (b \cdot sin\varphi_1)^2} \tag{7.23}$$

with a and b as the semi-axes of the reference ellipsoid (e.g. WGS84).

For applying the ray-tracing shooting technique the heights of the next points (P_i) on the ray path have to be defined. In GNSS tomography these are the intersection points between ray and voxel surfaces. This can be either a top layer or any of the lateral surfaces of the voxel model. In case of top layers Eq.7.24 to 7.27 can be directly applied for computation of the coordinates and angles of the corresponding ray points since the ellipsoidal heights of these layers are known.

$$y_2 = y_1 + d_1 \cdot cos(\varepsilon) \tag{7.24}$$

$$z_2 = z_1 + d_1 \cdot sin(\varepsilon) \tag{7.25}$$

$$\eta_2 = atan\left(\frac{y_2}{z_2}\right) \tag{7.26}$$

$$\theta_2 = acos\left(\frac{n_1}{n_2} \cdot cos\left(\Theta_1 + (\eta_2 - \eta_1)\right)\right) \tag{7.27}$$

$$d_1 = -\left(R_G + h_1\right) \cdot sin(\theta_1) + \sqrt{\left(R_G + h_2\right)^2 - \left(R_G + h_1\right)^2 \cdot cos(\theta_1)^2} \tag{7.28}$$

Height h_2 is the height of the top layer, n_1 and n_2 are the index of refraction at height h_1 and h_2, respectively and d_1 is distance between the two ray points. In case of a straight line the term $\frac{n_1}{n_2}$ can be set to '1', i.e. the ray-path is described independent from current atmospheric conditions.
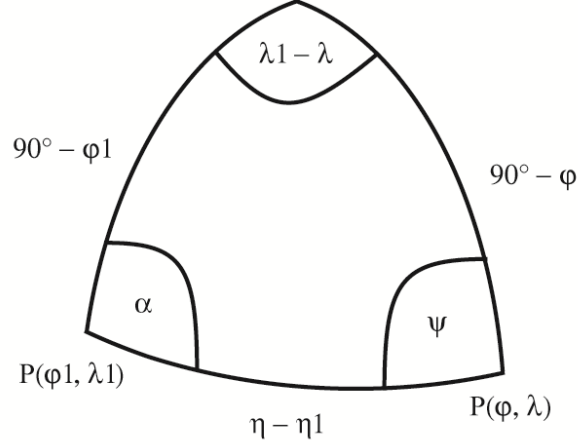
Figure 7.4: Spherical geometric relation used for the calculation of geocentric angle η

In contrast to the top layer, the heights of the intersection points with the other surfaces are unknown and have to be computed first. Figure 7.4 highlights the underlying observation geometry. Assuming spherical trigonometry the following relation is obtained

$$tan(\lambda - \lambda_1) = \frac{sin(\alpha)}{cos(\varphi_1) \cdot cot(\eta - \eta_1) - sin(\varphi_1) \cdot cos(\alpha)} \tag{7.29}$$

where λ is the longitude of the voxel surface. Assuming $\eta_1 = 0$ the geocentric angle η follows to:

$$\eta = acot\left(\frac{sin(\alpha)}{tan(\lambda - \lambda_1) \cdot cos(\varphi_1)} + tan(\varphi_1) \cdot cos(\alpha)\right) \tag{7.30}$$

In case of latitude φ the formula for η reads:

$$\eta = atan\left(\frac{tan\left(\frac{\varphi_1 - \varphi}{2}\right) \cdot sin\left(\frac{(\alpha + \psi)}{2}\right)}{sin\left(\frac{(\alpha - \psi)}{2}\right)}\right) \tag{7.31}$$

where ψ is the complement angle of the great circle arc, see Figure 7.4. Applying the law of sines it follows to:

$$\psi = asin\left(sin(\alpha) \cdot \frac{cos(\varphi_1)}{cos(\varphi)}\right) \tag{7.32}$$

107

The resulting angle ψ lies within the range $\left[-\frac{\pi}{2}, \frac{\pi}{2}\right]$. However, a second possible solution can be found within the range $[-\pi, \pi]$ by subtracting ψ from π. Introduced into Eq.7.31 it provides the geocentric angle(s). Finally the heights h of the intersection points are received by the following equation:

$$h = \left(\frac{cos(\varepsilon)}{cos(\varepsilon + \eta)} - 1\right) \cdot R_G + h_1 \qquad (7.33)$$

For further analysis only the heights within the range $0 < h < h_t$ are used, where h_t defines the upper voxel model boundary (see Table 7.1).

The benefit of this approach is that the number of iterations can be limited to the number of intersection points between ray and voxel model. This makes the algorithm fast and efficient. However a drawback is that the straight line approach provides still an approximation of the ray path since current atmospheric conditions and therewith the atmospheric bending is neglected. Moreover, a small systematic effect is introduced by spherical approximation. It results mainly from latitude-dependent variations in Earth´s curvature. Fortunately, the largest part can be compensated by setting the spherical radius to R_G, respectively for each receiver position. The remaining distance-dependent part can be widely neglected, especially for satellites observed at higher elevation angles.

7.2.3.2   Bended ray-tracing

The mathematical background for bended ray-tracing was already provided in the previous section but so far the impact of refractivity has been ignored by setting the term $\frac{n_1}{n_2}$ in Eq.7.27 to '1'. For taking the index of refraction and its variation into account first a data source has to be found which provides refractivities along the ray path with adequate accuracy. Another problem which arises is that in contrast to the straight line ray-tracing approach the 'true' ray path is not previously known but rather dependent on the refractivity distribution along the ray path. In consequence the 'true' ray path has to be computed iteratively within two nested loops.

In the **outer loop** meteorological parameters or if provided total refractivity fields are read in and preprocessed for the inner loop. Hereby the input data are converted into index of refraction and the vertical resolution is further increased by applying interpolation methods, e.g. as described in Section 6.1. For the reconstruction of the path lengths a vertical increment of $5\,m$ is proposed for the entire vertical range of the voxel model. Therewith the error in path length, especially for low elevation angles (down to three degrees) can be limited to $100\,m$ $\left(\frac{5\,m}{sin(3°)}\right)$.

Dependent on the quality of the refractivity fields the outer loop has to be repeated. In the optimal case it is operated after each inversion of the tomography model by re-initialisation of the improved refractivity field. Since this is very time consuming a reconstruction once in the beginning might be also of practical relevance.

In the **inner loop** the coordinates (φ_i, λ_i) of the ray path are computed for each height layer i using Eq.7.24 to 7.27 and the following formulas for latitude φ_i and longitude λ_i

$$\varphi_i = asin \left(sin \left(\varphi_1 \right) \cdot cos \left(\eta_i - \eta_1 \right) + cos \left(\varphi_1 \right) \cdot sin \left(\eta_i - \eta_1 \right) \cdot cos \left(\alpha \right) \right) \tag{7.34}$$

$$\lambda_i = \lambda_1 + atan \left(\frac{sin \left(\alpha \right)}{cot \left(\eta_i - \eta_1 \right) \cdot cos \left(\varphi_1 \right) - sin \left(\varphi_1 \right) \cdot cos \left(\alpha \right)} \right) \tag{7.35}$$

whereby φ_i and λ_i are defined in the range $\left[-\frac{\pi}{2}, \frac{\pi}{2} \right]$ and $[-\pi, \pi]$, respectively. The distances d_i between two consecutive layers follow from Eq.7.28.

Starting from the receiver position the processing is done in $5\,m$ steps until the ray reaches the top layer (h_t). Above the top layer the signal path is not of interest any more, in consequence the ray-tracer can be stopped. The elevation angle ε_t of the ray at the top layer is computed from the last set of geocentric angles θ_t and η_t by

$$\varepsilon_t = \theta_t + \eta_t. \tag{7.36}$$

The inner processing loop is repeated until $\varepsilon_t - \varepsilon + g_{bend}$ is smaller than a predefined threshold (e.g. 0.0001°), where g_{bend} is a correction term which takes the bending in the upper part of the atmosphere above the top layer into account. It can be computed by continuing ray-tracing or to a good approximation also by means of a bending model, e.g. as described by Hobiger *et al.* (2008a)

$$g_{bend} = \frac{0.02 \cdot exp \left(\frac{-h}{6000} \right)}{tan(\varepsilon)} \tag{7.37}$$

where h is the height of interest (e.g. height h_t of the top layer) and ε is the 'outgoing' elevation angle under which the satellite is observed.

After convergence of the inner loop the path length in each voxel is obtained by summing up the distances d_i of all ray parts within the voxel. The allocation of the ray parts is carried out by comparison of the ray coordinates $(\varphi_i, \lambda_i, h_i)$ with the coordinates of the voxel model. Therewith, the indices of the intersection points and of all ray parts between are determined.

The performance of the developed bended ray-tracer (Möller, 2016), which is an extension of the Vienna ray-tracer (Nafisi *et al.*, 2012), was validated against the ray-tracer developed within the RADIATE project[1] by Hofmeister (2016). Therefore operational ECMWF data were utilised (see Section 5.2.1) and for one station in Austria [lat: 47.799°, lon: 15.638°, h: $350\,m$] *SWD* time series were computed for selected elevation angles and azimuth angles using the following relation

$$swd = \sum_{i=1}^{t} N_i \cdot d_i \tag{7.38}$$

where $d_i\ [km]$ is the distance and $N_i\ [ppm]$ is the mean refractivity between two ray points. Figure 7.5 shows the *SWD* obtained on the 5th of December 2015 at 06 UTC for 3° elevation angle. The differences in *SWD* between both ray-tracers are in the mm range, hence it can be concluded that the distances but also of the refractivities seems to be correctly implemented.
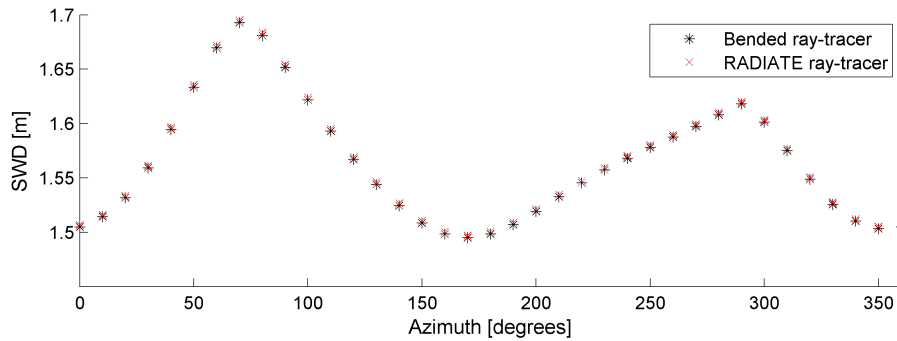
Figure 7.5: Slant wet delays as obtained for 3° elevation angle by ray-tracing through operational ECMWF data using the bended and the RADIATE ray-tracer

7.2.3.3 Impact on path length

In the following the differences between straight line and bended ray-tracing are further analysed. For both methods the ray positions (φ_i, λ_i) along the ray path were computed. Figure 7.6 shows the resulting path geometry for satellite 'G24' as observed at station '0145' (see coordinates in Appendix B.2) under an elevation angle of 3.7° and an azimuth angle of 26.1°.

---

[1]The RADIATE VLBI project was funded by Austrian Science Fund (FWF). Project number: P25320

The refractivity field required for bended ray-tracing was derived from the ALARO model (see Section 5.2.2) as already used for generation of the synthetic observations, i.e. the bended ray describes the 'true' path of the synthetic slant wet delays and the straight ray is its approximation.
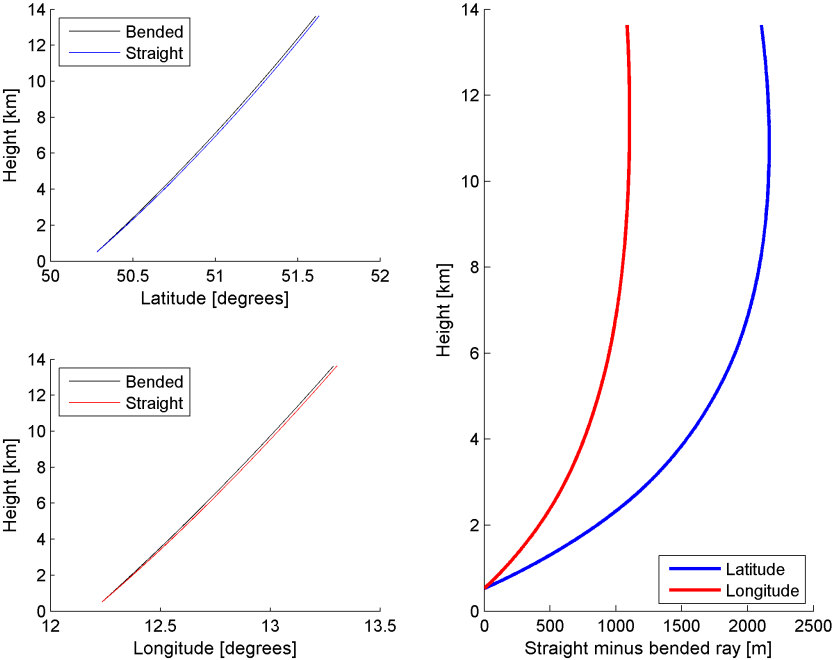
Figure 7.6: Differences in path geometry within the voxel model as derived from straight line and bended ray-tracing approach

In the beginning the ray position is equal for both methods but diverges with increasing height. The bended ray is travelling in most cases 'above' the straight ray (see Section 3.5 for exception), i.e. the straight ray enters the voxel model 'earlier' than the bended ray. In Figure 7.6 the effect is shown separately for latitude and longitude. In total the straight ray travels $2.4\,km$ 'further' within the voxel model. In consequence, using the straigth line approach the total ray length is determined systematically too large. Since this effect is highly correlated with the elevation angle further synthetic observations were processed. The resulting additional ray paths are plotted in Figure 7.7 as function of elevation angle.

The additional ray path decreases rapidly with increasing elevation angle. Already at about 15° it is below $0.1\,km$, thus it is concluded that the straight line ray-tracer approximates the ray length well for elevation angles above 15°. At lower elevation angles the bended ray-tracer should be applied.

111
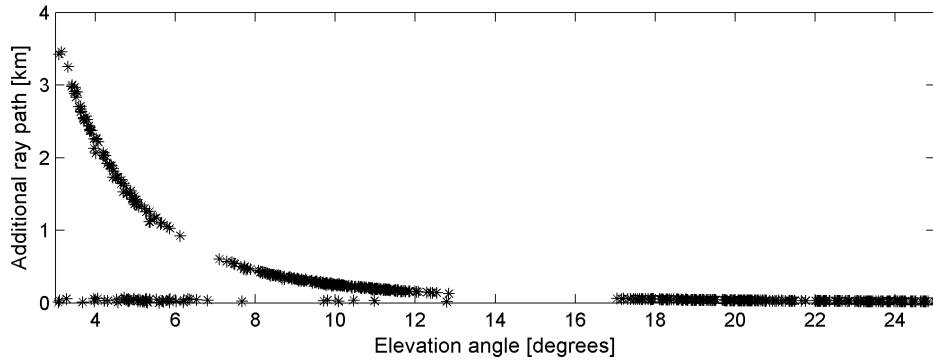
Figure 7.7: Additional ray path using the straight line ray-tracer

Further, Figure 7.7 shows that in some cases even for low elevation angles the difference in path length is small $(< 0.1\, km)$. Further analysis revealed that this appears when the ray leaves the voxel model through a lateral surface and not through the top layer. Then the difference in path length between both ray-tracing methods is in any case negligible.

7.2.3.4   Impact of vertical model on the observation geometry

Since the bended ray describes a different path than the straight ray it is also expected that different voxels are traversed. For further analysis of the observation geometry the two vertical models as described in Section 7.2.2 were applied to define the voxel boundaries. The horizontal resolution was set to 0.5° x 0.5°.

At first for each observation the traversed voxels were analysed. Assuming vertical model a) the straight ray traverses in $98.3\,\%$ the same voxels as the bended ray. For vertical model b) with $98.7\,\%$ a similar result was obtained. The $1-2\,\%$ in which different voxels are traversed are mainly caused by observations at low elevation angles $<$ 15°. These observations traverse in general more voxels before they reach the top layer, i.e. there is a higher chance to hit other voxels. In addition observations at low elevation angles are much more affected by atmospheric bending which leads to larger deviations in ray geometry as already shown in Figure 7.6.

For each voxel the number of traversing rays was computed using the synthetic dataset. In addition for each ray the receiving GNSS site was extraced. Figure 7.8 shows the number of rays per voxel and the number of GNSS sites involved as function of height layer.

Differences between both vertical models are clearly visible. Especially at lower layers the voxels of model b) are much more populated by rays than in model a) but also the

112

number of GNSS sites involved is in model b) mostly higher (except for the upper two layers) than in model a). Also visible for vertical model b) is that except for the lower layer the number of rays per voxel remains rather stable over the entire height range. In consequence and according to Bender & Raabe (2007) it is expected that vertical model b) provides a solution which is in fact more smoothed in the lower layers but in general more stable than model a), see Section 7.2.4.3 for more details.
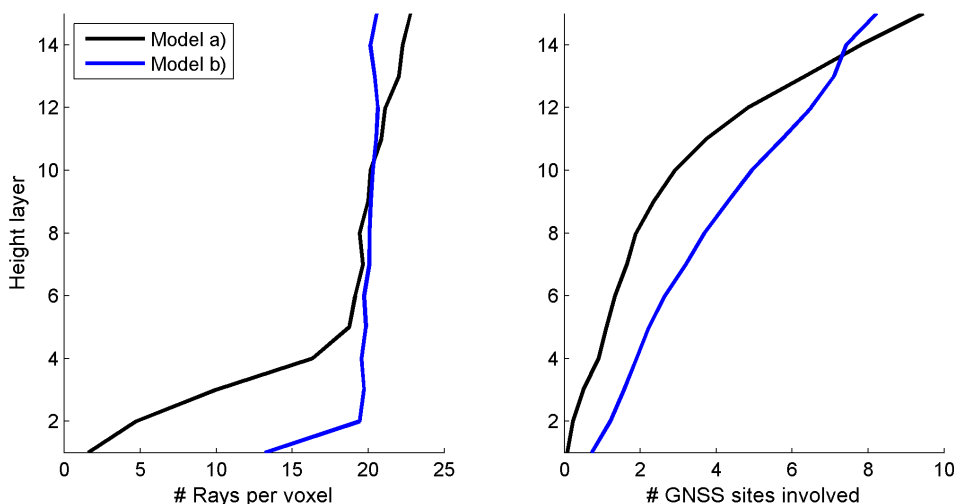
Figure 7.8: Observation geometry with the average number of rays per voxel (left) and the average number of GNSS sites involved (right)

7.2.3.5 Impact of ray-tracer on observation geometry

Even if the number of traversed voxels is in about 98% of the cases identical for both ray-tracers, it cannot be neglected that different parts of the voxel are traversed which leads to variations in path length and therewith to misallocations of the slant wet delays. In the following the path length in each voxel is further analysed.

For each ray and for each voxel the path length was computed, separately for straight and bended rays. From the differences in path length bias and standard deviation was derived, individually for each height layer. While the individual differences in path length vary between $\pm 3\,km$, the bias is at most layers negligible. The standard deviation of the differences increases from $0\,m$ near ground to $500\,m$ at $h = 14.6\,km$ since the voxel size but also the impact of the atmospheric bending increase with height (see Figure 7.6).

Further analysis revealed that the magnitude of the individual differences are highly correlated with elevation angle, hence different thresholds for elevation angle were tested. The results are summarised in Figure 7.9.
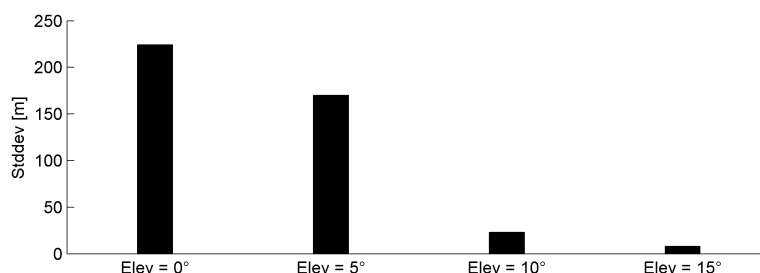
Figure 7.9: Standard deviation of the differences in path length caused by a mixed ray-tracing approach which uses the elevation angle as selection criteria. The path lengths obtained from the bended ray-tracer were used as referenced

In total four test solutions with different thresholds were computed and for each ray and for each voxel the path lengths were compared with the reference solution. In case of 'Elev=15°' observations below 15° elevation angle were processed using the bended ray-tracer and all other observations above with the fast straight line ray-tracer, the procedure was also repeated for the other elevation angles. Figure 7.9 shows that with increasing threshold the standard deviation decreases significantly. A good trade-off between processing time and accuracy was found by setting the threshold to 10°. In case of the synthetic dataset with this approach 84 % of the observations could be processed with the faster straight line ray-tracer without serious distortion of the observation geometry.

7.2.4 Synthetic tomography solution based on LSQ

Taking the synthetic observations and previous findings into account a tomography solution is obtained by solving Eq.7.39 for wet refractivity (N_w).

$$N_w = A^{-1} \cdot SWD \tag{7.39}$$

Observation vector SWD contains the 1502 synthetic slant wet delays and matrix A the corresponding path lengths in each voxel, determined with the ray-tracing approach defined in the previous section[2].

---

[2]Combined straight line and bended ray-tracing approach using an elevation angle of 10° as selection criteria.

7.2.4.1 Least squares adjustment

The synthetic observations are free of gross errors or systematic effects and the linear relation between the unknowns and the observations is correctly known, thus the preconditions are fulfilled for solving Eq.7.39 within a Least Squares Adjustment (LSQ). The basic equations and a derivation of the weighted least squares estimator are given in Section 4.6 and Appendix A.4. For the synthetic tomography solution Eq.4.34 is rewritten as follows

$$\hat{N}_w = \left(A^T \cdot P \cdot A\right)^{-1} \cdot A^T \cdot P \cdot SWD \tag{7.40}$$

where P is a weighting matrix which allows to take into account the relative accuracy between the observations (see Section 7.2.4.5), however for now the observations are treated as uncorrelated and equally accurate ($P = I$). Since matrix A is not invertible Eq.7.40 has to be solved by singular value decomposition. By combining Eq.7.11 with Eq.7.40 the tomography solution reads

$$\hat{N}_w = V \cdot S^{-1} \cdot U^T \cdot A^T \cdot P \cdot SWD \tag{7.41}$$

where the columns of U and V^T are the normalised left and right singular vectors of $A^T \cdot P \cdot A$, respectively. Matrix $S\left(l, m\right)$ is a diagonal matrix, the first m diagonal elements are the **eigenvalues** $eig = s_{k,k}^2$, all other elements are zero. The smaller the eigenvalue the poorer the corresponding linear combination of refractivities is resolved by the observations.

7.2.4.2 Regularisation

In Section 7.1 two regularisation methods, TSVD and Tikhonov regularisation are presented. Varah (1979) showed that in general both methods produce very similar results. Thus for the synthetic tomography solution only the TSVD technique was used because it could be implemented in a simple manner.

Based on the L-curve technique (see Section 7.1.3) an 'optimal' eigenvalue threshold of $0.01\,km^2$ was found. However, to highlight the impact of the threshold on the tomography result, two different solutions were computed, one using the 'optimal' threshold of $0.01\,km^2$ and an alternative solution using a ten times smaller threshold of $0.001\,km^2$. For both cases refractivity fields were estimated and compared with the reference refractivity field used to derive the synthetic observations. Figure 7.10 shows the results (reference minus estimated) for vertical model a), whereby voxel number '1' is dedicated to the South-West corner and '80' to the North-East corner of the voxel model.
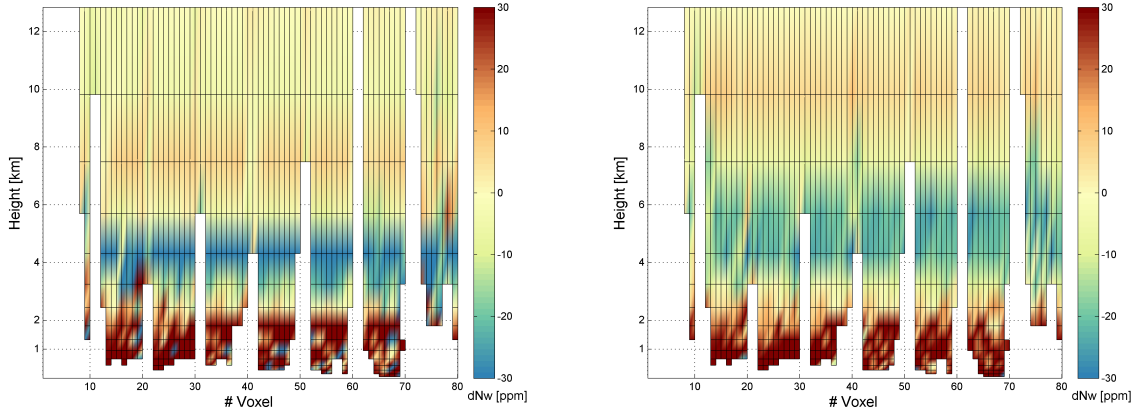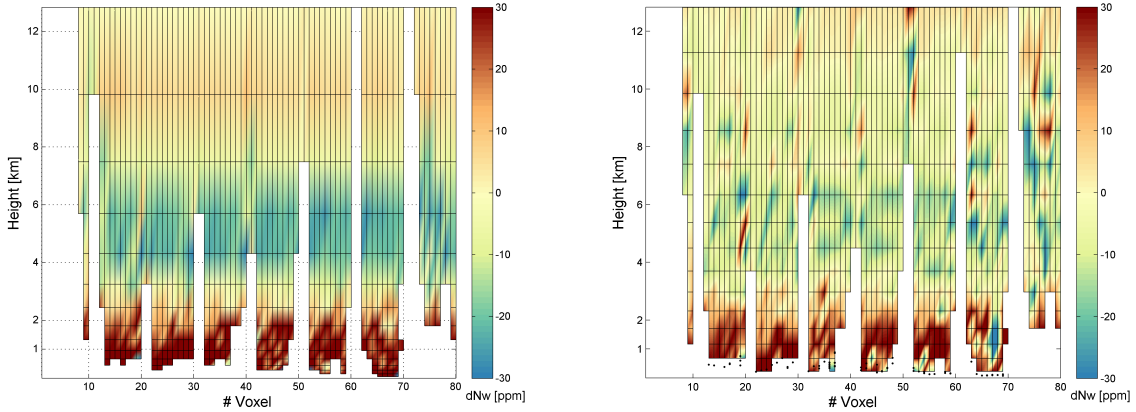
Figure 7.10: Differences in N_w [ppm] between reference field and synthetic tomography solution. Values larger than $0\,ppm$ indicate tomography reconstruction errors. Relative differences between both plots are caused by different eigenvalue thresholds of $s_{lim} = 0.001\,km^2$ (left) and $s_{lim} = 0.01\,km^2$ (right)

In general the optimal solution provides a smoother refractivity field than the alternative solution. The difference between both solutions is linked to 20 eigenvalues which are zero in the optimal but non-zero in the alternative solution. Related to the entire number this corresponds to a change in rank of about $3\,\%$. This highlights how sensitive the tomography solution is with respect to the eigenvalue threshold.

Beside, in both solutions the refractivity is underestimated in the lower atmosphere and overestimated in the middle atmosphere. The extension of this effect correlates with the number of non-zero eigenvalues. The lower the number the more the effect is 'smeared over' the entire voxel model. Hence the eigenvalue selection is a trade-off between ill-conditioning and 'over-smoothing'. In consequence regularisation techniques like the L-curve technique help to minimise these artefacts. In literature (Vasin, 2011; Tarantola, 2005) more advanced regularisation techniques are described. However at least one optimisation technique should be applied in GNSS tomography, otherwise the solution can become meaningless.

7.2.4.3   Impact of vertical model

An eigenvalue threshold of $0.01\,km^2$ as defined in the previous section was applied for deriving tomography solutions for the two different vertical models defined in Section 7.2.2. Figure 7.11 highlights that the vertical model, i.e. the selection of the voxel boundaries, has a significant impact on the tomography solution.

Figure 7.11: Differences in N_w [ppm] between reference field and synthetic tomography solution. Values larger than $0\,ppm$ indicate tomography reconstruction errors. Relative differences between both plots are caused by different vertical models used for the tomography solution. The model boundaries are listed in Table 7.1. In both cases s_{lim} was set to $0.01\,km^2$

In both models the refractivity is underestimated within the lower $2\,km$ of the atmosphere, whereby model b) tends to be slightly closer to the reference field. However, largest differences between the vertical models appear in the middle atmosphere ($4\,km < h < 7\,km$). While in vertical model a) the refractivity is systematically overestimated, model b) tends to provide more realistic results. Even if some more artefacts are visible since the eigenvalue threshold of $0.01\,km^2$ is not optimal for model b), on average the tomography solution is closer to the reference field.

The overall impression is that model b) fits much better the underlying observation geometry and allows better allocations of the slant wet delays than model a). Therewith the expectation expressed in Section 7.2.3.4, that model b) provides a more stable tomography result, is widely confirmed. Hence it was selected for the alpine test cases in Chapter 8.

7.2.4.4   A priori information

For the iterative non-linear approach, in particularly for the determination of bended ray paths, an a priori refractivity field is introduced, e.g. derived from standard atmosphere or NWM data. This information might be also of interest as a priori information for solving the equation system. Besides, if additional observations like ground-based observations or vertical refractivity profiles, e.g. derived from radiometer (Section 5.3) or radiosonde observations (Section 5.4) can be made available, they have to be introduced in any form

into the equation system. One possibility is to treat the additional observations (N_{w0}) as absolute constraints. Taking Eq.7.40 and Eq.4.39 into account the resulting refractivity estimator reads:

$$\hat{N}_w = N_{w0} + V \cdot S^{-1} \cdot U^T \cdot A^T \cdot P \cdot (SWD - A \cdot N_{w0}) \tag{7.42}$$

Matrix U, V and S are obtained by singular value decomposition of matrix $A^T \cdot P \cdot A + P_c$, where P_c containts the weights for vector N_{w0}. In the following this solution is called the **constrained solution.**

Another possibility to handle the extended equation system is to treat it as system of subsets with

$$A_{ext} = \begin{bmatrix} A \\ A_c \end{bmatrix} \tag{7.43}$$

$$SWD_{ext} = \begin{bmatrix} SWD \\ N_{w0} \end{bmatrix} \tag{7.44}$$

$$P_{ext} = \begin{bmatrix} P \\ P_c \end{bmatrix} \tag{7.45}$$

where A_c is the design matrix for N_{w0}. The extended equation system can be solved in the same manner as described in Section 7.2.4.1 using Eq.7.41, whereby A, SWD and P are replaced by its extended complements A_{ext}, SWD_{ext} and P_{ext}. In principle it provides the same results as the constrained solution.

A third possibility would be to solve the previously defined subsets iteratively by using the estimates ($\hat{X}$) and the variance-covariance matrix of the estimates ($Cov_{\hat{X}X}$) from the initial solution as a priori information for the next iteration. In case of two subsets the corresponding tomography solution reads:

$$\hat{N}_{w1} = V \cdot S^{-1} \cdot U^T \cdot A^T \cdot P \cdot SWD \tag{7.46}$$

$$Cov_{\hat{X}X} = V \cdot S^{-1} \cdot U^T \tag{7.47}$$

where U, V and S are obtained by singular value decomposition of matrix $A^T \cdot P \cdot A$. For the second (final) solution both, $\hat{N}_{w1}$ and $Cov_{\hat{X}X}$ are introduced into the equation system as follows

$$\hat{N}_w = \hat{N}_{w1} + V \cdot S^{-1} \cdot U^T \cdot A_c^T \cdot P_c \cdot \left(N_{w0} - A_0 \cdot \hat{N}_{w1} \right) \tag{7.48}$$

where U, V and S are obtained by singular value decomposition of matrix $A_0^T \cdot P_0 \cdot A_0 + Cov_{\hat{X}X}^{-1}$. This solution is called in the following the **partial solution**. A comparison of the constrained with the partial solution revealed that both provide identical results in case of full rank or if only one set of observations is available. Nevertheless, a benefit of the partial solution is that for each subset the eigenvalues can be treated separately. This allows to remove artefacts introduced by the linear combination of specific observations before the second set of observations, e.g. a priori information is applied. Further, in large equation systems it allows for reducing computational load since matrix A is divided into several parts.

In order to show the impact of a priori information or additional observations on the tomography solution in the following three scenarios are further analysed. In the **first scenario** it is assumed that each GNSS station is equipped with meteorological instruments for measuring temperature and water vapour pressure. Therefore wet refractivity is derived using Eq.3.18 and introduced into the equation system as absolute constraints[3].
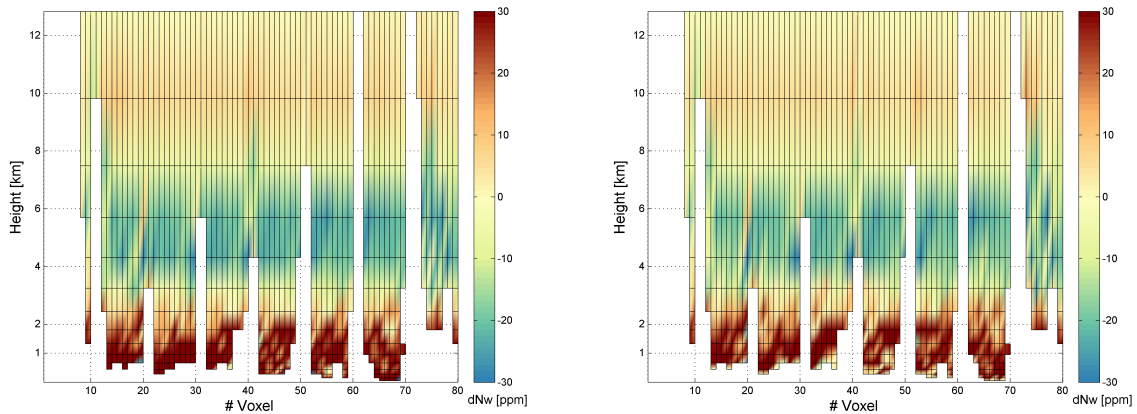
Figure 7.12: Comparison of tomography solution without (left) and with additional ground-based observations (right)

Figure 7.12 shows how this additional information influences the tomography solution. Improvements are observed particularly near ground but unfortunately the positive impact vanishes relative fast with increasing distance, especially in vertical direction. Tests with different weighting (higher weights on the ground observations) provided similar results. Therefore it is concluded that in-situ measurements help to stabilise the refractivity field near ground but have in general less impact on the tomography solution.

---

[3]In the synthetic case wet refractivity was derived from the ALARO data and extrapolated to GNSS site.

In a **second scenario** a vertical profile of wet refractivity is observed in the centre of the voxel model, e.g. by radiosondes[4]. These observations are introduced into the equation system as constraints, similar to the ground-based observations.

Figure 7.13 shows that the additional 'radiosonde observations' have a significant impact on the tomography solution. The negative bias in the middle atmosphere widely vanishes in all voxels although only one vertical profile in the centre of the voxel model was added and equally weighted like the other observations. This highlights how much the tomography solution would benefit from additional vertical information, especially for correction of misallocation in the lower and middle atmosphere.
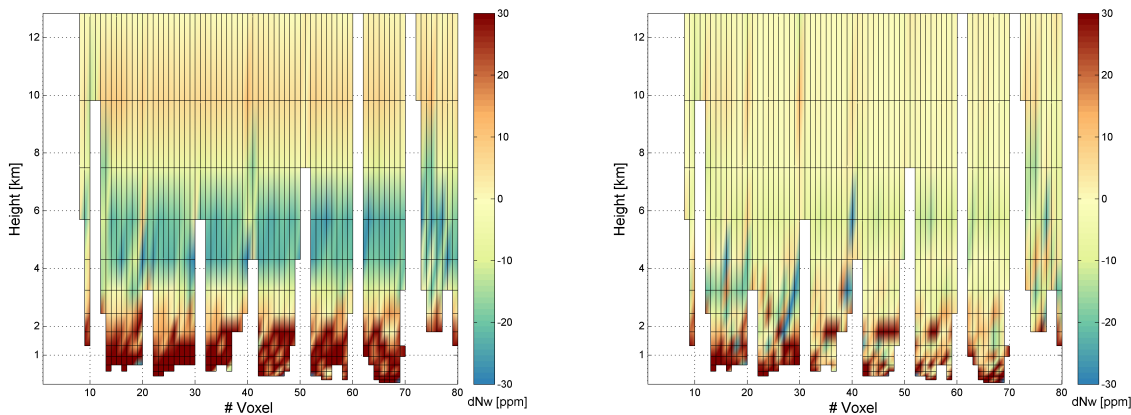
Figure 7.13: Impact of a single vertical profile of wet refractivity on the tomography solution

In a **third scenario** the entire a priori refractivity field was added to the equation system as absolute constraints with equal weights. Figure 7.14 shows that the estimated refractivity field benefits from the a priori information in several ways. First, refractivities are obtained for voxels which are not traversed by any observation. Second, the a priori information helps to reduce artefacts caused by ill-posedness. Deviations from the reference field still appear but large systematics as visible in the solution without a priori information (Figure 7.14 left) are not observed any more. The misallocations are widely removed, mainly due to the vertical information in the a priori refractivity field.

Based on this scenario also a partial solution was computed using Eq.7.48 and compared to the constraint solution. In both solutions the condition $P = I$ gives strong weight to the a priori information. This makes the tomography solution less sensitive to changes

---

[4]Similar as for the first scenario a profile of wet refractivity was derived from the ALARO data for all layers of voxel column 34.

in the equation system. Thus, the resulting differences between both solutions are rather small ($< 1\,ppm$) if an eigenvalue threshold of $0.01\,km^2$ is used for the partial solution[5]. Larger variations can be observed if the eigenvalue threshold is further increased or if more realistic weighting is applied.
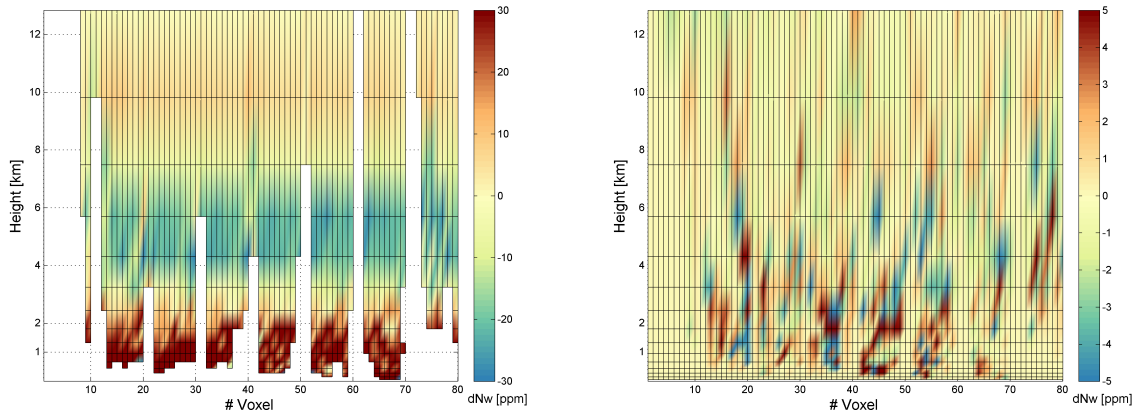
Figure 7.14: Impact of the a priori refractivity field on the tomography solution

7.2.4.5 Observation weights

Up to now observations were equally weighted. However, observation-dependent weighting might be beneficial for reduction of the impact of less accurate observations on the tomography solution. Especially at low elevation angles slant wet delays can be much more affected by mapping errors or unmodelled hydrostatic effects. Thus, in the following an elevation-dependent weighting model was tested and applied to the synthetic dataset.

First, the synthetic slant wet delays were modified by adding white noise of $-65\,dBW$, mapped by $sin(\varepsilon)$ to the elevation angle of the satellite. Figure 7.15 shows the resulting noise distribution.

After applying the noise to the observations the tomography solution was recomputed with the same settings as used in Section 7.2.4.2. The effects observed in the solution without noise (see Figure 7.14 left) are also visible in the noisy solution but further amplified. Especially in the middle atmosphere the refractivity is further overestimated, the standard deviation of the N_w-residuals increases slightly from $25.17\,ppm$ to $25.20\,ppm$.

---

[5]The eigenvalue threshold has no impact on the constrained solution since due to the a priori refractivities no eigenvalues below $1.0\,km^2$ are obtained.
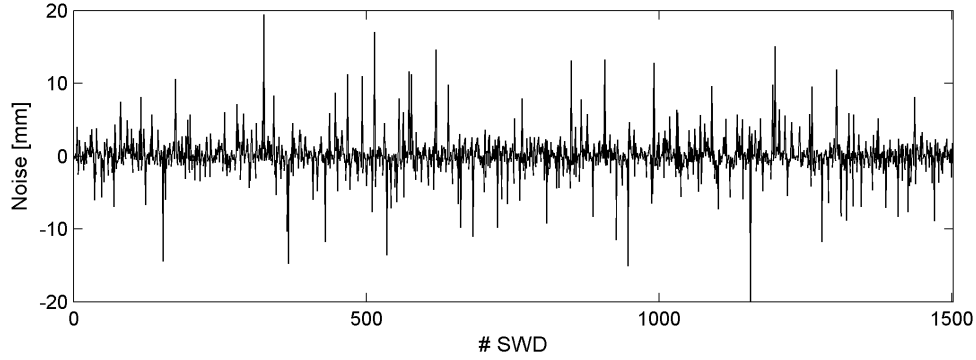
Figure 7.15: Simulated elevation-dependent noise

In a second run elevation-dependent weights were introduced. According to Eq.4.31 the weighting matrix P is defined as follows

$$P = \sigma_0^2 \cdot Cov_{ll}^{-1} \tag{7.49}$$

where σ_0^2 is the a priori variance of the unit weight and Cov_{ll} is the variance-covariance matrix a priori. The diagonal elements of Cov_{ll} are the variances σ_n^2 of the observations

$$\sigma_n^2 = sin^2\varepsilon \cdot \sigma_{ZTD}^2 \tag{7.50}$$

where σ_{ZTD}^2 is the variance of the observations in zenith direction. In case of real observations usually values between $1\,mm^2$ and $100\,mm^2$ are selected. For further testing the σ_{ZTD}^2 was set to $100\,mm^2$ and for each observation σ_{ZTD}^2 was mapped by $sin(\varepsilon)$ into the direction of the satellite.

By comparison of the two solutions (not shown here) significant differences could be observed. The largest impact is related to the eigenvalues, since singular value decomposition is applied to matrix $A^T \cdot P \cdot A$. In consequence, if the same eigenvalue threshold is used for both solutions, not the same number of eigenvalues is considered for the solution.

In order to assess solely the impact of the weighting (and not the influence of the eigenvalue threshold) first the eigenvalue threshold was adapted. Therefore the rank of the solution was used as selection criteria. In case of unit weighting the rank is 579. After elevation-dependent weights were applied the rank decreases to 369. In order to obtain the same rank as for the unweighted solution an eigenvalue threshold of $0.0000055\,km^2$ had to be used. After reprocessing with the newly defined threshold the impact caused by elevation-dependent weighting could be analysed.
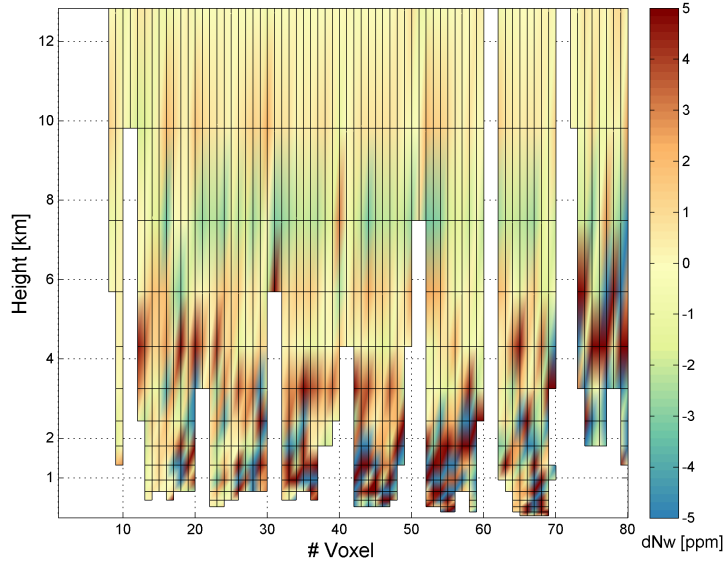
Figure 7.16: Impact of elevation-dependent weighting on the tomography solution

Figure 7.16 shows the resulting differences between weighted and unweighted solution. In some areas differences of up to $10\,ppm$ are observed which cannot always be interpreted as corrections, in some cases also a downgrade of the solution was observed. Nevertheless, since the standard deviation of the differences between estimated and reference refractivities decreases slightly by $1\,\%$, elevation-dependent weighting is applied in further analysis.

7.2.4.6   A priori refractivity weights

Already in Section 7.2.4.4 a solution with a priori refractivities was computed. Now the solution is recomputed by introducing individual weights for the a priori refractivity field. Since no accuracy information for the ALARO model parameters was available, a weighting model had to be defined. Steiner *et al.* (2006) provides height-dependent error curves for pressure, temperature and specific humidity in form of standard deviations. By error propagation (see Section 3.3.2) the standard deviation of wet refractivity is obtained as follows:

$$\sigma_{Nw} = \left[\left(\frac{\partial N_w}{\partial T} \cdot \sigma_T \right)^2 + \left(\frac{\partial N}{\partial q} \cdot \sigma_q \right)^2 + \left(\frac{\partial N}{\partial p} \cdot \sigma_p \right)^2 \right]^{\frac{1}{2}} \tag{7.51}$$

In addition a second weighting model was tested which assumes that standard deviation increases linearly with refractivity.

$$\sigma_{Nw} = 0.10 \cdot N_w \tag{7.52}$$

Figure 7.17 shows the resulting standard deviations as function of height. The model by Steiner *et al.* (2006) yields to standard deviations which remain constant for each height level, with largest values at $h = 1\,km$ (voxel 400 - 480). Introduced into the tomography solution it gives more weight to the a priori refractivities in the lower atmosphere than the refractivity-dependent model. In contrast the refractivity-dependent model introduces more variation between neighbouring voxels, especially in the lower $3\,km$ of the atmosphere but gives probably too much weight on the a priori refractivities in the middle and upper atmosphere. In Section 8.2.4.3 both models are further tested and compared using 'real' observations.
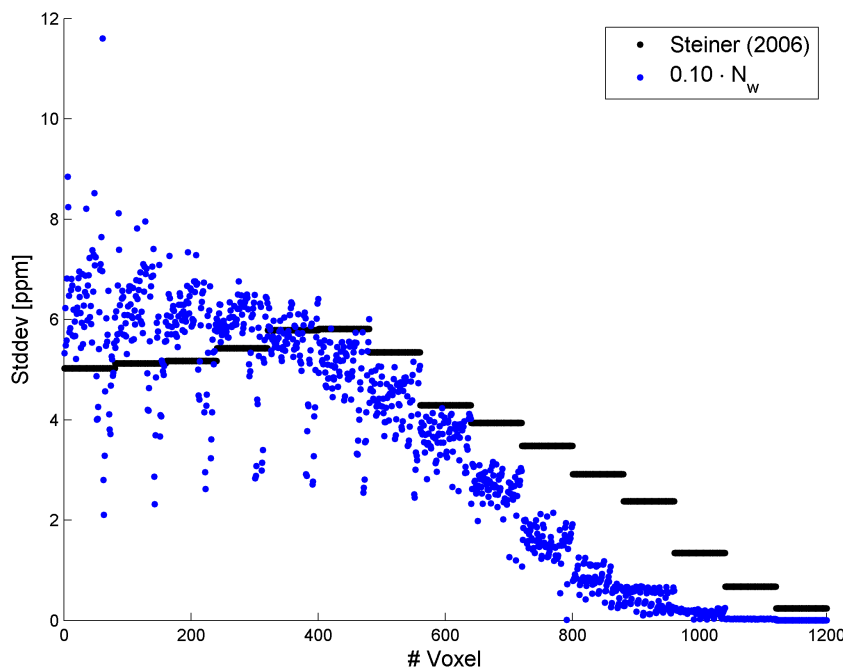
Figure 7.17: Standard deviation of the a priori refractivity field derived from two different weighting models

7.2.4.7 Quality indicators

From the least squares solution measures can be derived which give information about the resolved parameters but also about the observations, e.g. how well they fit the functional model. For example the **linearised resolution operator** (R) of the model space provides information about the number of resolved parameters and how well they are determined (Rawlinson & Sambridge, 2003; Tarantola, 2005). In case of singular value decomposition

R reads

$$R = V \cdot V^T \tag{7.53}$$

where V is obtained by singular value decomposition of matrix $A^T \cdot P \cdot A + P_c$ within the constrained solution (see Section 7.2.4.4). First, the trace of R yields the rank of the equation system; second if R is close to identity the parameters are well resolved, otherwise if any diagonal element of R is close to zero, the corresponding parameter is poorly resolved. In case of the synthetic dataset the diagonal elements of R are '1' or very close to '1'. Therewith and in this specific case R does not explain the differences between reference and estimated refractivity field as obtained in previous sections.

A second measure of quality, the **normalised misfit function** χ^2 is used to evaluate the a priori variance-covariance information

$$\chi^2 = \frac{(A \cdot N_w - SWD)^T \cdot Cov_{ll}^{-1} \cdot (A \cdot N_w - SWD)}{n_{obs}} + \frac{(N_w - N_{w0})^T \cdot Cov_c^{-1} \cdot (N_w - N_{w0})}{n_c} \tag{7.54}$$

whereby n_{obs} and n_c are the number of slant wet delays and a priori refractivities, respectively. A value of $\chi^2 \sim 1$ is obtained when the inverse solution fits the data to the level of noise, otherwise the applied weights are not set properly (Tarantola, 2005).

In the following χ^2 is computed for the synthetic dataset and it is further tested whether an insufficient weighting can be corrected by **variance component analysis** (Niemeier, 2002). Therefore a priori variances σ_0^2 of the unit weight are defined and corrected after each iteration, individually for each observation type i

$$\hat{\sigma}_{0,i}^2 = \frac{res_i^T \cdot p_i \cdot res_i}{sum(r_i)} \tag{7.55}$$

whereby the redundance vector (r_i) is derived from the variance-covariance matrix $Cov_{\hat{l}\hat{l}}$ of the adjusted observations.

$$r_i = diag(1 - Cov_{\hat{l}\hat{l}} \cdot p_i) \tag{7.56}$$

The variances of the unit weight are used to correct the weighting matrices for the next run, the processing is repeated until $\hat{\sigma}_{0,i}^2$ converges to one.

$$p_i = \frac{p_i}{\hat{\sigma}_{0,i}^2} \tag{7.57}$$

125

The method was applied to the synthetic dataset, thereby elevation-dependent weights with $\sigma_{ZTD} = 10\,mm$ were defined for the observations and the error model presented by Steiner *et al.* (2006) was applied to the a priori refractivities. The processing started with $\sigma^2_{0,i} = 1$ for both observation types, the results obtained for iteration 1, 5 and 10 are summarised in Table 7.2.

	χ^2	$\sigma^2_{0,1}\,[mm^2]$	$\sigma^2_{0,2}\,[mm^2]$	$\|res\|_2\,[ppm]$	$Res_{RMS}\,[ppm]$
Iteration 1	0.79	0.51	1.62	149.7	0.63
Iteration 5	1.06	0.88	1.22	126.7	0.74
Iteration 10	1.08	0.98	1.04	135.9	0.74

Table 7.2: Quality indicators derived for the synthetic tomography solution

At the beginning χ^2 was smaller than '1', i.e. the accuracy of the observations and therewith the weights were defined too pessimistic. This was corrected for the second iteration by giving more weights to the observations and less weights to the a priori information ($\sigma^2_{0,1} = 0.51$ and $\sigma^2_{0,2} = 1.62$). After two iterations χ^2 reached 1 and after ten iterations also the variances converged slowly to 1.

The last two columns in Table 7.2 show the norm $\|res\|_2$ and the root mean square error (Res_{RMS}) of the **weighted residuals.**

$$Res_{RMS} = \sqrt{\frac{Res^T \cdot P \cdot Res}{n_{obs}}} \tag{7.58}$$

It is interesting to see that the norm reaches its minimum after five iterations, while the root mean square error increases continuously. The smallest norm of the residuals is obtained when χ^2 is closest to '1', i.e. when the inverse solution fits the data best. The Res_{RMS} of the weighted residuals increases since more weight is given to the observations, in consequence artefacts due to ill-posedness become more rigorous. In addition a larger Res_{RMS} is influenced by the a priori variance-covariance matrices which does not accurately reflect the relative precision and possible correlations between the observations. Unit weights would yield better results for the synthetic data, nevertheless, it is expected that the defined relative weights fit better to real observations as analysed in Chapter 8.

Besides, also the **standard deviation** s_{ZTD} of the estimated parameters was computed after each iteration. It can be recovered from the variance-covariance matrix a posteriori as follows:

$$s_{ZTD} = \hat{\sigma}_0 \cdot \sqrt{diag\left(Cov_{\hat{X}\hat{X}}\right)} \tag{7.59}$$

After the variance component analysis was applied the standard deviation increased approximately by a factor of five. In case the parameter was resolved by observations the resulting standard deviation becomes more realistic since it reflects approximately the magnitude of the differences between reference and estimated refractivity field. In case the parameter is resolved by a priori information, larger standard deviations are not realistic anymore, since in the synthetic solution the differences between a priori and reference field are zero.

In consequence the variance component analysis shall be handled with care. Certain benefits might be gained if the accuracy of the observations is not known a priori. Whether the solution after applying variance component analysis converges to a better solution could not be confirmed so far . Hence in the following $\chi^2 \sim 1$ is used as stop criteria since it is related to the smallest residuals.

Nevertheless, the provided measures of quality give less information about the ill-posedness of the equation system. By regularisation an approximate solution for the ill-posed problem is obtained but the impact of the assumptions made on A and N_w are therewith not specified. Natterer (2001) provides some measures of ill-posedness which allow to judge the degree of ill-posedness and to specify the incomplete data problem.

In GNSS tomography ill-posedness is mainly caused by **limited observation angles** and **restricted sources**. So in principle they are related to geometrical effects. Natterer (2001) shows that limited angles lead to small eigenvalues. Since TSVD (see Section 7.1.3) was applied for solving the equation system it is expected that the most critical linear combinations are already removed. Nevertheless, correlation between the differences in refractivity and the observation geometry is still expected, hence it was tested for the synthetic dataset.

Correlation coefficients were computed for the differences in refractivity on the one hand and the observation angles, the path lengths and the number of stations involved on the other hand. Unfortunately only correlation coefficients < 0.1 could be obtained. In consequence no new quality measures could be derived for evaluation of the accuracy of the estimated refractivity field. Hence for the following validation test cases the conventional measures (residuals, variance-covariance matrix, χ^2 and resolution matrix, ...) and external datasources (radionsondes, radiometer data) are used for validation of the tomography results.

Chapter 8

Tomography test cases in alpine environment

The tomography processing strategies and models described in Chapter 7 and tested against simulated slant wet delays are hereinafter applied to slant wet delays derived from GNSS observations of a network of reference stations in Western Austria.

Initially the study period is defined and meteorologically characterised. Further, the software package 'ATom' for Atmospheric TOMography is introduced since it was used for the reconstruction of the refractivity fields and for testing of specific parameter settings. Finally the results are validated against radiometer and radiosonde profiles retrieved in the Inn Valley.

8.1   Study period and atmospheric conditions

May 2013 was selected as study period since it was in a meteorological sense a very interesting period. INCA[1] precipitation analysis (see Möller *et al.*, 2015) revealed heavy precipitation events in May, especially end of May, with up to $300\,mm$ accumulated precipitation in $72\,h$ over South-East Germany and Austria. A series of extratropical cyclones of type 'Vb' (Grams *et al.*, 2014) with origin in the Mediterranean and South-East Europe brought very moist and warm air around the Alps which finally caused a century flood event affecting the Danube and Elbe catchment areas.

---

[1]Integrated Nowcasting through Comprehensive Analysis (INCA) is the operational analysis and nowcasting tool, developed and operated at ZAMG.

Usually cyclones coming from the South-East move over Central Europe further north but end of May 2013 two anticyclones over North Atlantic and Scandinavia were blocking the movement. Cyclone 'Frederik' was forced to form an equatorward ascending warm conveyor belt (Grams *et al.*, 2014) which was characterised by advecting warm air, large gradients in potential temperature (see Section 2.3.1.3) and high accumulated rainfall.

8.2   Reconstruction of wet refractivity fields

For the selected test cases in alpine environment a tomography solution was demanded which allows for describing the weather situation in May 2013. Thereby the models and strategies as described in previous chapters were applied in order to define an optimal tomography solution. In particular the impact of atmospheric bending, remaining hydrostatic effects in slant wet delays, post-fit residuals and of various tomography processing strategies on the estimated refractivity fields were further analysed and are presented in the following.

8.2.1   ATom software package

The algorithms and mathematic relations behind the 'ATom' software package were compiled within the research project 'GNSS-ATom'[2] in the years 2013 to 2015 and further refined during this PhD studies. The program code was mainly written from scratch (except for the basic ray-tracer, mapping and time-conversion functions) in MATLAB. In its current version the ATom software package contains all functionalities necessary for the analysis of GNSS tropospheric parameters and the derivation of advanced tropospheric products like slant delays, a priori or improved wet refractivity fields. Its graphical user interface is structured in panels; each panel is assigned to a specific task. Figure 8.1 shows a screenshot of the panel '3D Tomography', which should give an impression about the possible input data, setting options and visualisation tools for GNSS tomography. In principle all relations and models described in Chapter 7 can be applied and tested within this software package.

In addition further panels allow for the conversion of double difference residuals into zero-difference residuals (Section 4.6.4), the conversion of ZTDs into ZWDs (Section 6.1), and of broadcast ephemerides into elevation and azimuth angles (Section 7.2.1).

---

[2]The research project 'GNSS-ATom' was funded by the Austrian Research Promotion Agency (FFG, project ID: 840098).
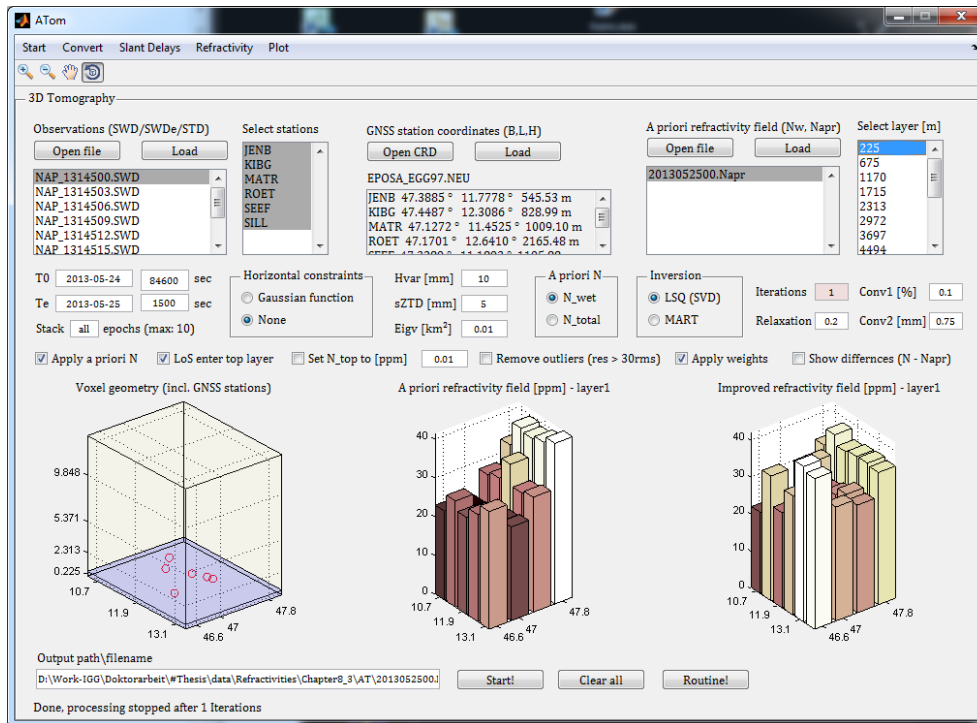
Figure 8.1: Screenshot of the '3D Tomography' panel provided with software 'ATom'

Another panel is dedicated to the mapping of zenith delays into various directions, taking different mapping functions and possible observation residuals into account (Chapter 6).

The ATom software package reads also numerical weather model data in grib1 format for the computation of a priori refractivities (Section 5.2), zenith delays or ray-traced delays (Chaper 6.5). Finally the various parameters can be plotted against each other for visual comparisons or read out in common data formats.

Recently a 'routine' function has been added which opens possibilities for automated processing. It can be seen as a primary stage for the operational near real-time processing scheme, which is foreseen to be realised in a future step.

8.2.2 GNSS slant wet delays

From the Austrian GNSS reference network EPOSA (www.eposa.at) six sites in the mountainous West of Austria (see Figure 8.2) were selected and their GPS and GLONASS observations were processed with the PPP software package Napeos v3.3.1 for estimating ZTD and gradient parameters (G_N and G_E). The main processing options and input

data are summarised in Table 8.1. More details to the processing strategy are provided in Section 4.6.2.
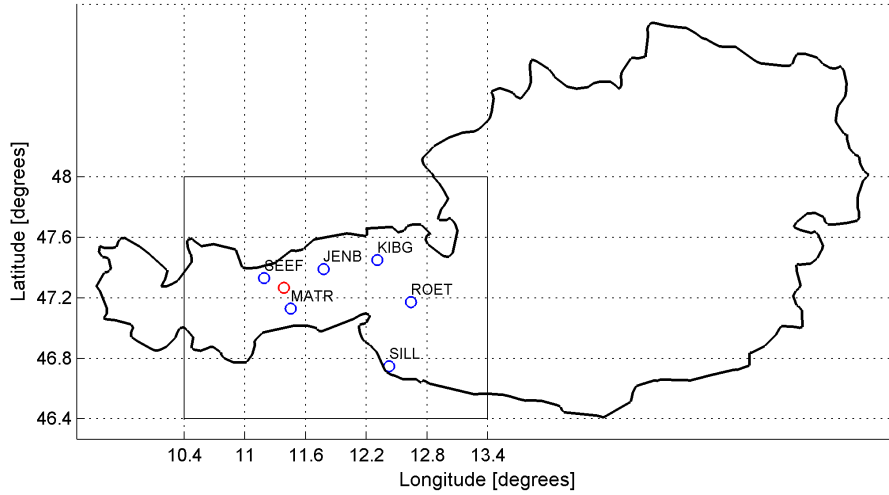
Figure 8.2: Voxel model and station distribution in Western Austria. The black rectangle describes the area of the voxel model, GNSS stations are represented by blue dots and the radiometer location at University of Innsbruck is highlighted in red

Parameter	Settings
Observation period / rate	May 2013 / 30 sec
Satellite systems	GPS and GLONASS
Satellite positions and clock corrections	ESA final products (high rate)
Station coordinates	ITRF2008 (2013.34), constrained
Antenna phase centre corrections	Individual antenna calibration files
Cut-off angle	3 degrees
Tropospheric model / mapping	Saastamoinen + GPT / GMF
Estimated parameters and spacing	1h ZTD and 2h gradients (G_N and G_E)

Table 8.1: GNSS processing options and data used in Napeos for the estimation of tropospheric parameters

After parameter estimation the hydrostatic part of the ZTD was reduced using measurements of the TAWES network (see Section 6.1). The remaining ZWD and the gradients were mapped to the elevation and azimuth angles of the satellites observed using the VMF1 wet mapping function (Böhm *et al.*, 2006a) and the Chen & Herring (1997) gradient mapping function. Beforehand the temporal resolution was increased to $5\,min$ by linear interpolation between the nodal points. Finally, the interpolated SWDs were stored together with post-fit residuals in observation files.

8.2.3 Initial tomography settings

The lower atmosphere above the area of interest (see Figure 8.2) was block parameterised, i.e. divided into 20 x 15 **voxels** with a side length of about $45\,km$ which corresponds to an horizontal resolution of 0.6° x 0.4° in mid latitudes. The vertical spacing, i.e. the heights of the 15 voxels were defined by Eq.7.17 with the input parameters as already used in Chapter 7 ($dh(0) = 450\,m$, $q_h = 1.1$). The resulting voxel boundaries are listed in Table 7.1.

The tomography processing was started with the definition of the **eigenvalue threshold**. Therefore the slant wet delays were processed without a priori information but with different eigenvalue thresholds. The optimal value was selected by means of the L-curve technique (see Section 7.1.3.1). Dependent on the observation geometry the optimal threshold varied between $0.01\,km^2$ and $0.1\,km^2$. As consequence $0.05\,km^2$ was set as trade-off for the entire study period.

For the bended ray-tracer but also as a priori information for the tomography solution **a priori refractivity fields** had to be computed. Therefore, in particular for the study period, ALARO analysis data (see Section 5.2.2) were utilised. The meteorological parameters (pressure, temperature and specific humidity) provided by ALARO were interpolated to the voxel centre points and converted into hydrostatic and wet refractivity.

8.2.4 Impact studies

In order to identify the impact of specific parameter settings like atmospheric bending or observation weights on the alpine test cases, in the following difference plots of wet refractivity with respect to a reference solution are shown and further analysed.

8.2.4.1 Reference solution

For the period May 2013 a tomography solution was computed using the input data and settings as listed below:

- A priori wet refractivity fields derived from ALARO analysis data at 0, 3, 6, 9, 12, 15, 18 and 21 UTC

- SWDs as observed at the epoch of interest (no stacking)

- Elevation-dependent weighting was applied for the SWDs with $\sigma_{ZTD} = 5\,mm$.

- The model presented by Steiner *et al.* (2006) was used to compute weights for the a priori refractivity fields.

- The eigenvalue threshold was set to $0.05\,km^2$.

- Straight line ray-tracing was applied for the reconstruction of the path lengths in each voxel.

- Observations ($<2\,\%$) which enter the voxel model through a lateral surface were discarded.

The obtained wet refractivity fields are visualised in Figure 8.3, exemplary for the atmospheric column above Innsbruck. In the following this tomography solution is denoted as reference solution.
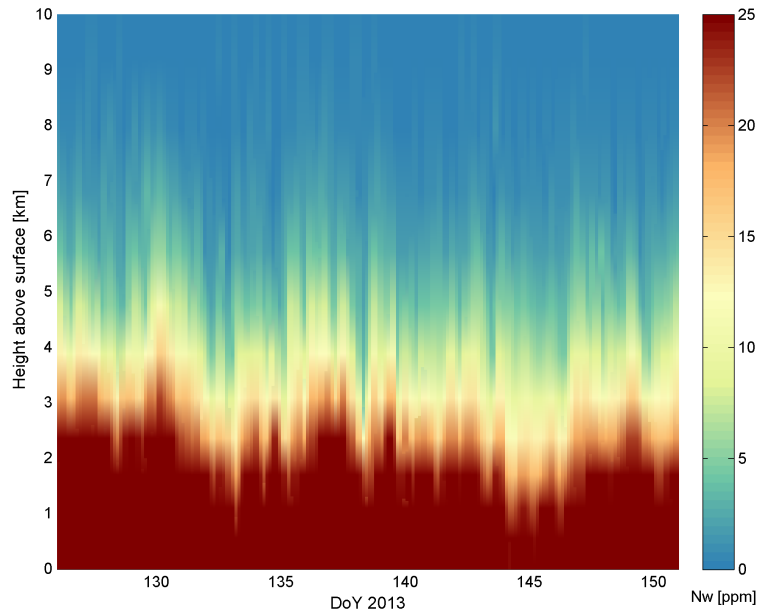
Figure 8.3: Three-hourly vertical profiles of wet refractivity above Innsbruck as obtained from the reference tomography solution. Period: 6th of May until 31st of May 2013

8.2.4.2 Atmospheric bending

The impact of atmospheric bending increases with decreasing elevation angle (see Section 7.2.3). Thus bended ray-tracing was carried out for all observations below 15° elevation angle through a priori refractivity fields derived from ALARO analysis data (1

133

iteration). Afterwards the obtained refractivity fields were compared to the reference so-
lution. Figure 8.4 shows the differences in wet refractivity for one epoch, whereby voxel
number '1' is dedicated to the South-West column and number '20' to the North-East col-
umn of the voxel model. Between the voxels a bilinear interpolation method was applied.
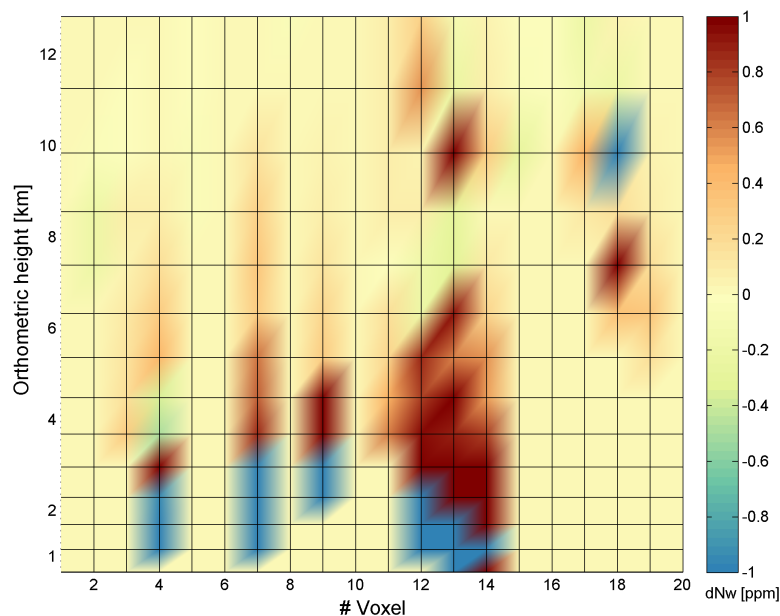
Figure 8.4: Differences in wet refractivity (reference minus bended ray-tracer solution) as
observed at the 4th of May 2013 15 UTC

Even though on average over all voxels no bias in wet refractivity is observed, specific
voxels show differences in wet refractivity of up to $12\,ppm$, particularly if due to bending
different voxels than in the reference case are traversed.

From all differences in wet refractivity (reference minus bended) and over all 248 epochs
in May 2013 a maximum value of $15.6\,ppm$, a bias of $0.08\,ppm$ and a standard deviation
of $0.20\,ppm$ were obtained. Although the bias and standard deviation over all voxels is
small, differences of about $1\,ppm$ were observed on average at each epoch, whereby largest
values appear when observations below 10° elevation enter the tomography solution.

In a second step the processing was repeated but the path lengths were computed iter-
atively, i.e. after each iteration the a priori wet refractivity field was replaced by the
estimated wet refractivity field[3]. After the first iteration differences in wet refractivity

---

[3]The estimated wet refractivity field is used only for the computation of the paths geometry, the a priori
information for the inversion is not replaced.

of up to $0.5\,ppm$ were observed (see Figure 8.5), after the second iteration no differences larger than $10^{-4}\,ppm$ appear. Thus, a strict use of the iterative non-linear solution in atmospheric tomography is not recommended if adequate a priori refractivity fields can be made available. Usually a processing of the path lengths once in the beginning is sufficient, only in very raw cases a second iteration provides further significant corrections.
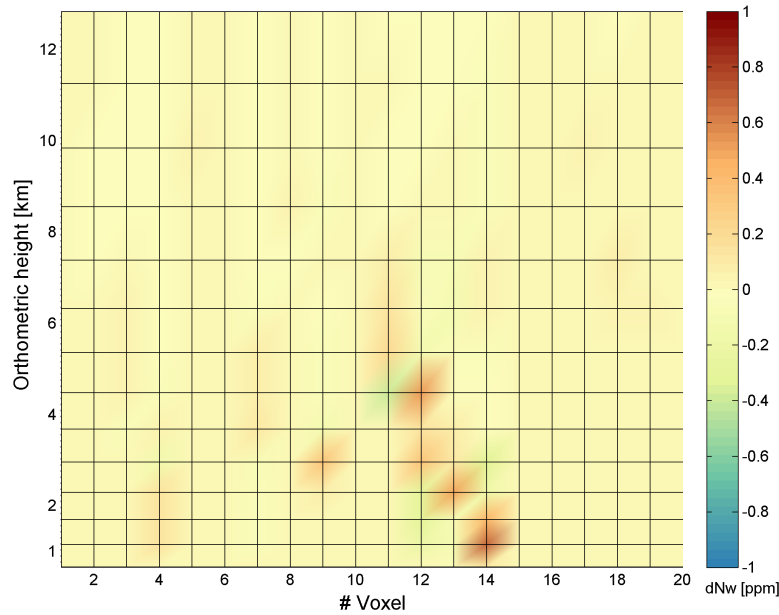
Figure 8.5: Differences in wet refractivity between two solutions based on bended ray-tracing. For the first solution ray-tracing was carried out once in the beginning, for the second solution the path geometry was computed iteratively by replacing the a priori model by the improved wet refractivity field obtained in first iteration

8.2.4.3 Observation weighting

In the following the impact of the two weighting models as presented in Section 7.2.4.6 on the tomography solution is analysed. For the first solution the weighting model presented by Steiner *et al.* (2006) was replaced by refractivity-dependent weighting, for the second solution variance component analysis (see Section 7.2.4.7) was applied.

For each solution the differences in wet refractivity were computed with respect to the a priori model. The statistic over all affected voxels and epochs in May 2013 is summarised in Table 8.2.

The statistical analysis revealed that all solutions are rather close to the a priori refractivity field. Nevertheless, differences in the statistical parameters of the first two solutions are mainly caused by different weighting of specific atmospheric layers. The model by Steiner *et al.* (2006) gives more weight to the a priori refractivities in the lower $1\,km$ of the atmosphere where largest variations of wet refractivity are expected. This leads in total to smaller deviations from the a priori refractivity field.

	$\overline{dN_w}$	$stddev(dN_w)$	$max(dN_w)$
Steiner *et al.* (2006)	$-0.33\,ppm$	$1.45\,ppm$	$7.32\,ppm$
$0.10 \cdot N_w$	$-0.48\,ppm$	$2.11\,ppm$	$9.97\,ppm$
VCA	$-0.33\,ppm$	$1.59\,ppm$	$7.75\,ppm$

Table 8.2: Impact of two different a priori refractivity weighting models and Variance Component Analysis (VCA) on the tomography solution; shown for the differences in wet refractivity with respect to the a priori refractivity field. Analysed period: May 2013

For a more detailed analysis the differences in refractivity were visualised epoch-wise for the entire voxel model (not shown). Thereby a clear systematic was observed between the two weighting models. Refractivity-dependent weighting seems to be too 'tight' in the upper troposphere. In consequence no variation to the a priori model $>1\,ppm$ is observed at $6\,km$ height or above. Possible variations in this part are wrongly allocated to the lower troposphere. In return, the model presented by Steiner *et al.* (2006) allows variation in almost every part of the atmosphere; hence priority is given to this model over refractivity-dependent weighting.

In addition to the statistical parameters as presented in Table 8.2 also the χ^2 distribution, the norm of the residuals and the RMS error of the residuals were computed and are summarised in Table 8.3.

	$\overline{\chi^2}$	$stddev(\chi^2)$	$\|res\|_2$	Res_{RMS}
Steiner *et al.* (2006)	0.35	0.29	$22.18\,ppm$	$0.35\,ppm$
$0.10 \cdot N_w$	2.18	2.44	$38.41\,ppm$	$0.78\,ppm$
VAC	0.71	0.06	$21.45\,ppm$	$0.47\,ppm$

Table 8.3: Summary of quality parameters derived from various tomography solutions. For each solution a different weighting approach was applied. Analysed period: May 2013

If the model by Steiner *et al.* (2006) is used significantly smaller residuals are obtained than for refractivity-dependent weighting. However, even though the misfit function χ^2 is closer to 1, the weighting model cannot compensate for epoch-wise accuracy variations between different observation types. Changes in the observation geometry or in accuracy lead to variations in the misfit function which is expressed in Table 8.3 as standard deviation ($stddev(\chi^2)$).

Variance Component Analysis (VCA) allows for compensation of relative weighting deficiency between observations and a priori refractivities, in consequence χ^2 becomes closer to 1 and its variation decreases significantly (by a factor of 5 to 0.06). Largest corrections were obtained at the day boundaries which is related to highest formal errors of the GNSS tropospheric parameters, processed in daily batches.

In terms of bias, standard deviation and maximum deviation relative to the a priori refractivity field, slightly larger values were obtained by VCA as for the reference solution (see Table 8.2) which means that by VCA more weight was given to the observations. Whether this goes along with absolute improvements in wet refractivity is further analysed in Section 8.3 by comparison with radiometer and radiosonde data.

8.2.4.4 Unmodelled tropospheric effects in slant wet delays

Slant wet delays reconstructed from GNSS tropospheric parameters using Eq.6.1 are not free from hydrostatic effects since the gradients obtained from GNSS processing describe the total effect, a separation into hydrostatic and wet components is not possible unless external information is introduced. In addition unmodelled tropospheric effects as stored in the post-fit residuals were so far not considered, however whether they are a valuable data source in GNSS tomography is analysed in the following.

Hydrostatic azimuthal asymmetry

For the analysis of hydrostatic asymmetry ray-tracing through HRES weather model data[4] was carried out, as described in Section 6.3, to obtain asymmetric delay correction for the slant wet delays at 0, 6, 12, and 18 UTC. Over the first seven days in May 2013 corrections between $-32\,mm$ and $31\,mm$ were received and removed from the observations. Mostly negative values were obtained in North direction and positive ones in South direction (similar as shown in Figure 6.3). This is widely related to systematic differences

---

[4]ALARO data, as used in previous studies, could not be applied since the model domain is too limited. Especially at low elevation angles GNSS rays travel through areas of the neutral atmosphere which are not described anymore by the regional weather model.

in tropospheric height as already described in Section 6.3. Since the magnitude of the hydrostatic corrections decreases rapidly with elevation angle, an angle of 20° was set as upper limit for the ray-tracer, i.e. for slant wet delays observed at higher elevation angles no corrections were applied.

	$\overline{\chi^2}$	$stddev(\chi^2)$	$\|res\|_2$	res_{RMS}
reference	0.41	0.34	$25.91\,ppm$	$0.40\,ppm$
hydr. asymmetry	0.39	0.31	$25.47\,ppm$	$0.39\,ppm$

Table 8.4: Summary of quality parameters to highlight the impact of hydrostatic asymmetry on the tomography solution. Analysed period: 1st to 7th of May 2013

The 'corrected' slant wet delays introduced in the tomography approach lead to variations in wet refractivity of up to $2\,ppm$. In $75\,\%$ of the cases a smaller Res_{RMS} and $\|res\|_2$ than for the reference solution was obtained (see Table 8.4). On average the norm of the residuals decreases by $2\,\%$, in some cases also by $7\,\%$. Hence a correction of hydrostatic asymmetry is generally recommended.
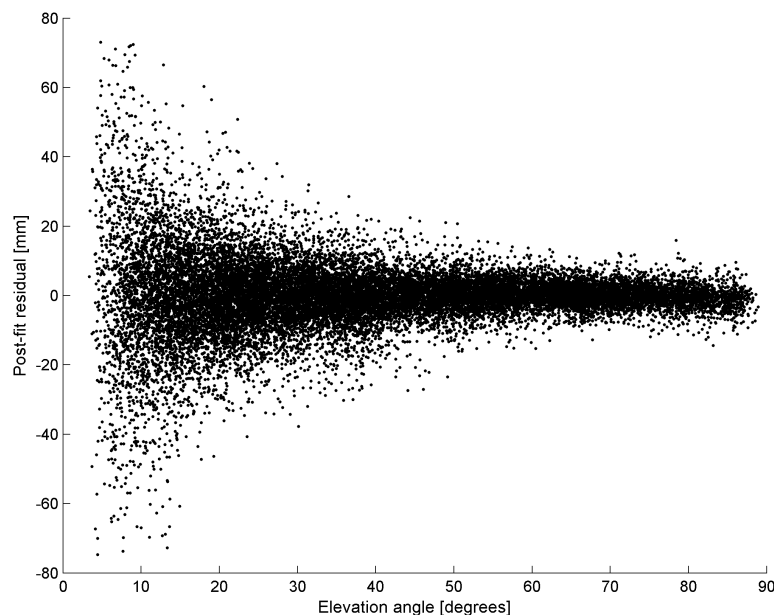
Figure 8.6: Elevation-dependent distribution of GNSS post-fit phase residuals

GNSS post-fit residuals

In fact raw GNSS post-fit residuals contain unmodelled tropospheric effects but unfortunately they are superimposed by other signals, caused by satellite clock errors, multipath, unmodelled antenna phase variations or observation noise. Common cleaning methods as described in Section 6.4 allow for removing constant terms at specific elevation angles and epochs but have in general less impact on the variation pattern. Figure 8.6 shows the residual distribution for all observations used within the study period, 'outliers' larger than $75\,mm$ were removed beforehand.

The 'corrected' slant wet delays (with post-fit residuals) introduced into the tomography solution have a significant impact on the estimated refractivity field. Within the study period and in specific voxels wet refractivity variations of up to $21.5\,ppm$ were observed, caused by the GNSS post-fit residuals. On average differences of $4.8\,ppm$ appear at least in one voxel at each epoch, whereby largest values are related to observations at low elevation angles.

	$\overline{\chi^2}$	$stddev(\chi^2)$	$\|res\|_2$	Res_{RMS}
reference	0.35	0.29	$22.18\,ppm$	$0.35\,ppm$
residuals	2.88	1.58	$55.70\,ppm$	$0.87\,ppm$

Table 8.5: Summary of quality parameters to highlight the impact of GNSS post-fit residuals on the tomography solution. Analysed period: May 2013

The statistical parameters as listed in Table 8.5 reveal a strong degraded tomography solution. Quality indicators like χ^2 or the norm of the post-fit residuals (of the tomography solution) increased by a multiple and the tomography solution with GNSS post-fit phase residuals became significantly noisier than the reference tomography solution. Hence adding GNSS post-fit phase residuals to the slant wet delays is generally not recommended.

8.2.4.5   Observation stacking

Observation stacking denotes the combined processing of observations within a predefined observation arc (see Section 4.6.1). Thereby a trade-off has to be found between stacking period and smoothing effects since during each processing run the refractivity field is assumed as constant. In the following an observation window of $60\,min$ ($30\,min$ before and $30\,min$ after the epoch of interest) was assumed and its impact on the tomography solution was further analysed.

	$\overline{\chi^2}$	$stddev(\chi^2)$	$\|res\|_2$	res_{RMS}
reference	0.22	0.18	$18.31\,ppm$	$0.29\,ppm$
stacked	1.19	0.89	$80.78\,ppm$	$0.74\,ppm$

Table 8.6: Summary of quality parameters to highlight the impact of observation stacking on the tomography solution. Analysed period: 25th to 31st of May 2013

It is obvious that the norm of the residuals of the stacked solution increases since the slant wet delays observed under different atmospheric conditions were stacked together. However, it is interesting to see that the residuals of the stacked solution vary much more than the residuals of the reference solution. Figure 8.7 shows that especially on the 31st of May (DoY 151) the residual norm of the stacked solution increases while the norm of the reference solution remains rather constant. During this day the ascending warm conveyor belt as described in Section 8.1 reaches the voxel area from the North and causes large advection of warm air and heavy rain fall. In consequence the residuals of the stacked tomography solution increased significantly, with largest values observed at station Jenbach and Kirchberg, located in the North-East of Tyrol, Austria.
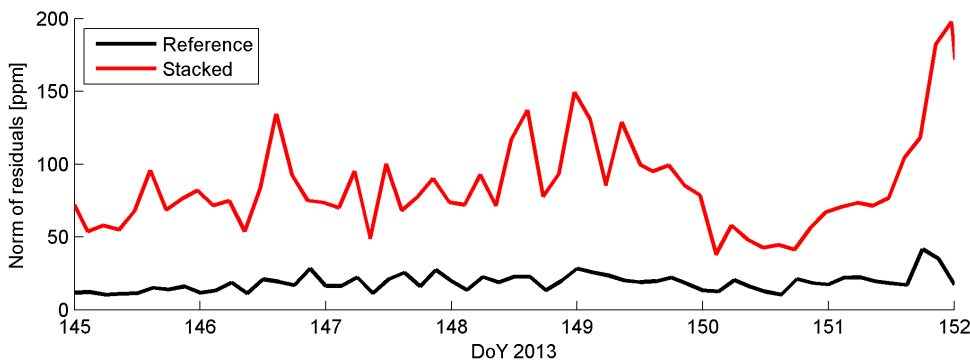
Figure 8.7: Residual norm of the reference and stacked tomography solution. Analysed period: 25th to 31st of May 2013

In consequence the defined quality parameters serve not only as good quality indicator for single solutions but also for the evaluation of changes in atmospheric conditions.

However, taking these findings into account it is expected that the constant observation window of $60\,min$ could improve the tomography solution under calm atmospheric conditions but probably smoothes the wet refractivity too much under convection or in high advective systems. More precise findings are expected from the comparison with ZWDs and radiosonde data (see Section 8.2.5 and 8.4).

8.2.4.6 Outer delay

So far observations were discarded if they enter the voxel model through a lateral surface and not through the top layer. It is expected that these observations introduced into the equation system would lead to an overestimation of wet refractivity in the voxel model by misallocation of the outer delay to voxels along the ray path. In order to get rid of this effect and to return these observations (particularly at low elevation angles) into the equation system, the outer delay has to be estimated or removed from the observations beforehand.

Therefore the voxel model could be extended by an outer voxel model for estimation of the additional delays (Rohm *et al.*, 2014). Alternatively the additional **path delay outside the voxel model** could be computed e.g. by ray-tracing through NWM data and subtracted from the observations. Latter might be promising since therewith the number of observations can be further increased without adding additional parameters to the equation system. Nevertheless the approach is only of practical relevance if the outer delay is significant and whether it can be determined with adequate accuracy.

Within the alpine test cases 1.2% of the observations are affected, i.e. they enter the voxel model not through the top layer, whereat most of them (about 70%) were detected at station Seefeld (SEEF). Thus, major differences in the estimated refractivity field are expected in the Eastern part of the voxel model.

The absolute value of the outer delay depends on the height at which the ray enters the voxel model and the outer atmospheric conditions. Within the analysed test cases in May 2013 outer delays between $0.1\,mm$ and $23\,mm$ were determined and removed from the affected observations. The corrected observations introduced into the equation system caused changes in wet refractivity of up to $10.5\,ppm$. On average differences of $1.0\,ppm$ appear at least in one voxel at each epoch.

If the observations would be introduced without correcting the outer delay beforehand, a positive offset in wet refractivity of up to $0.4\,ppm$, on average of $0.05\,ppm$, would be introduced. Since this offset is small, a correction of the outer delay in the alpine test cases is not mandatory. In consequence the additional observations were introduced directly into the equation system without further corrections. Its impact on the estimated refractivity field is evaluated in the following chapter.

8.2.5   Time series of integrated ZWDs

From the a priori and estimated refractivity fields *ZWD*s were computed by vertical integration using Eq.8.1

$$ZWD = 10^{-6} \int_{H_0}^{H_t} N_w \cdot dh = 10^{-6} \sum_{H_0}^{H_t} N_w \cdot dh \tag{8.1}$$

where H_0 is the height of the GNSS station and H_t the height of the voxel top ($H_t \approx$ $13.7\,km$). Beforehand N_w was horizontally interpolated from adjacent voxel centre points to the position of the GNSS stations, and the vertical resolution was further increased to $20\,m$.
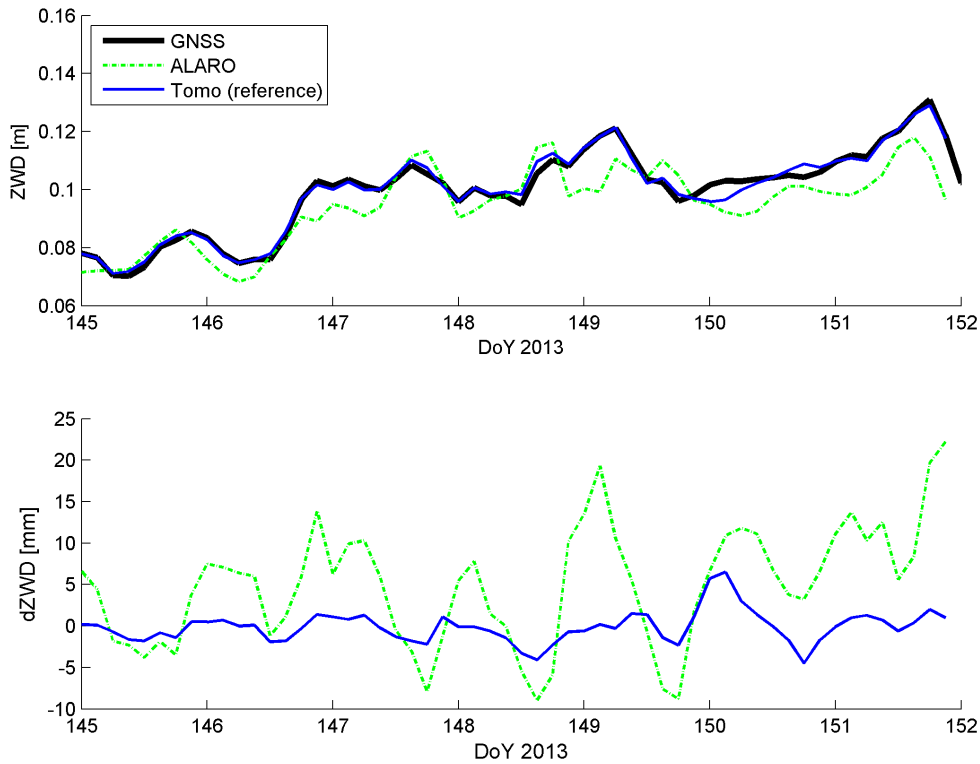
Figure 8.8: Comparison of integrated *ZWD*s with *ZWD*s estimated from GNSS observations at station Jenbach (JENB). The (top) plot shows the absolute values and the (bottom) plot highlights the differences with respect to the GNSS derived *ZWD*s

For comparison *ZWD* time series were derived for the last seven days in May 2013 with a temporal resolution of three hours. Figure 8.8 shows the resulting *ZWD*s as obtained for the a priori refractivity fields (ALARO) and the reference tomography solution, together with the GNSS derived *ZWD*s.

142

Between the various time series clear differences in *ZWD* can be observed. The tomography solution is more consistent with the GNSS solution while the *ZWD*s derived from ALARO are occasionally biased, a few hours 'ahead' or 'behind' the GNSS derived *ZWD*s.

	GNSS minus ALARO		GNSS minus Tomo	
	$\overline{dZWD}$	$stddev(dZWD)$	$\overline{dZWD}$	$stddev(dZWD)$
JENB	4.8 mm	7.2 mm	-0.1 mm	1.9 mm
KIBG	7.3 mm	6.9 mm	2.4 mm	1.7 mm
MATR	4.9 mm	6.7 mm	0.8 mm	2.0 mm
ROET	2.7 mm	6.2 mm	-0.4 mm	1.8 mm
SEEF	5.8 mm	4.8 mm	0.6 mm	1.0 mm
SILL	4.7 mm	5.7 mm	0.9 mm	2.8 mm
Total	**5.02 mm**	**6.25 mm**	**0.70 mm**	**1.88 mm**

Table 8.7: Station-wise statistic of the differences in *ZWD* between three different solutions. The GNSS solution was obtained by parameter estimation using GNSS phase observations at site, the ALARO and the Tomo solutions were computed by vertical integration through the ALARO model and the improved tomography (reference) refractivity fields, respectively. Analysed period: 25th to 31st of May 2013

A statistic of the *ZWD* differences is provided with Table 8.7. The tomography solution corrects for errors in the ALARO model, in consequence the statistical parameters improves by a multiple. However slightly larger bias and standard deviation is obtained at remote stations like Kirchberg (KIBG) and Sillian (SILL) since they are located at the boundaries of the network.

	$\overline{dZWD}$	$stddev(dZWD)$
reference (ref)	0.70 mm	1.88 mm
ref + bending	0.61 mm	1.87 mm
ref + stacking	0.33 mm	1.99 mm
ref + outer delay	0.71 mm	1.88 mm
ref + VCA	0.57 mm	1.89 mm

Table 8.8: Statistic of the differences in *ZWD* between GNSS and various tomography solutions. Analysed period: 25th to 31st of May 2013

Additional 'improvements' were observed after **atmospheric bending** was considered (see Table 8.8). At each station the standard deviation decreased slightly and the bias

could be further reduced at four of the six GNSS stations. Almost identical improvements were observed after **hydrostatic gradients** were applied (not shown).

At stations located at the voxel model boundaries **observation stacking** helps to further reduce the bias but leads to slightly larger standard deviations (see Table 8.8). Larger smoothing effects by observation stacking as assumed in the previous chapter could not be observed for the selected stacking period of $60\,min$. In general stacking provides rather reasonable results, especially in terms of bias and in case of data gaps it helps in addition to make the tomography solution more robust.

Almost no impact on the ZWD ($dZWD < 0.1\,mm$) was observed after observations were added which enter the voxel model through any lateral surface of the voxel model. The main reason is that for the alpine test cases the voxel model was already defined larger as necessary to cover the GNSS stations. In consequence the number of additional observations and the **outer delay** of the few affected observations became less relevant. A much larger impact is expected when the voxel model would be defined more closely around the GNSS stations or whether a lower cut-off angle would be set.
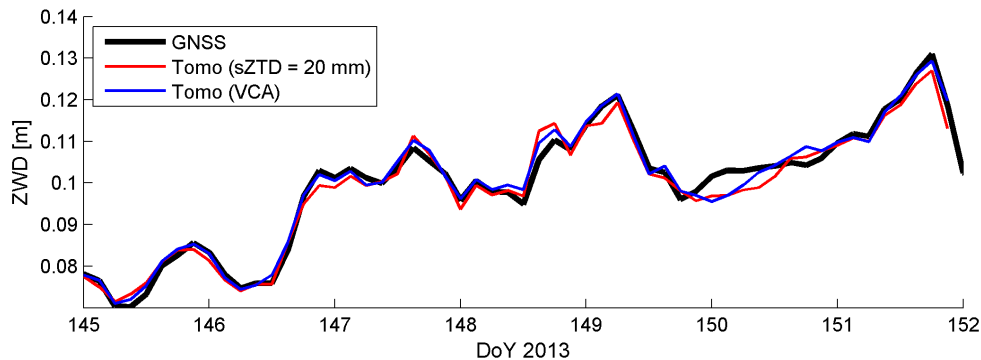
Figure 8.9: Impact of variance component analysis on the ZWD time series at station Kirchberg, Tyrol

Finally, also the impact of **variance component analysis** on the ZWD was analysed. Within the last seven days in May 2013 the standard deviation increased slightly but the offsets introduced by 'overweighting' of the a priori refractivity field could be widely corrected. Figure 8.9 shows this exemplary for station Kirchberg, Tyrol. For testing σ_{ZWD} was set to $\pm20\,mm$, i.e. the accuracy of the slant wet delays was assumed too pessimistic. After VCA was applied the impact of insufficient weighting on the $ZWDs$ was widely corrected. The bias in ZWD with respect to GNSS ZWDs reduced from $2.4\,mm$ to $0.7\,mm$. However, if the relative accuracy between the different observation

types is known a priori and whether it does not vary significantly over time VCA is not recommended since it tends to amplify the noisy behaviour of the tomography solution.

8.3   Comparison with passive radiometer data

The Institute of Atmospheric and Cryospheric Sciences of the University of Innsbruck installed under the lead of Prof. Mathias Rotach an observing system in the Inn Valley to study the "characteristics of turbulence structure and exchange processes in truly complex topography" (University of Innsbruck, 2017). For comparison and validation of the GNSS tomography results especially temperature and water vapour profiles provided by the passive radiometer (HATPRO, see Section 5.3) are of interest since they are available with high temporal resolution and since they can be converted into wet refractivity profiles. Latter allows a direct evaluation of the estimated wet refractivity fields. More details about the specifications of the HATPRO radiometer, operated at the University of Innsbruck, are given in Massaro *et al.* (2015).
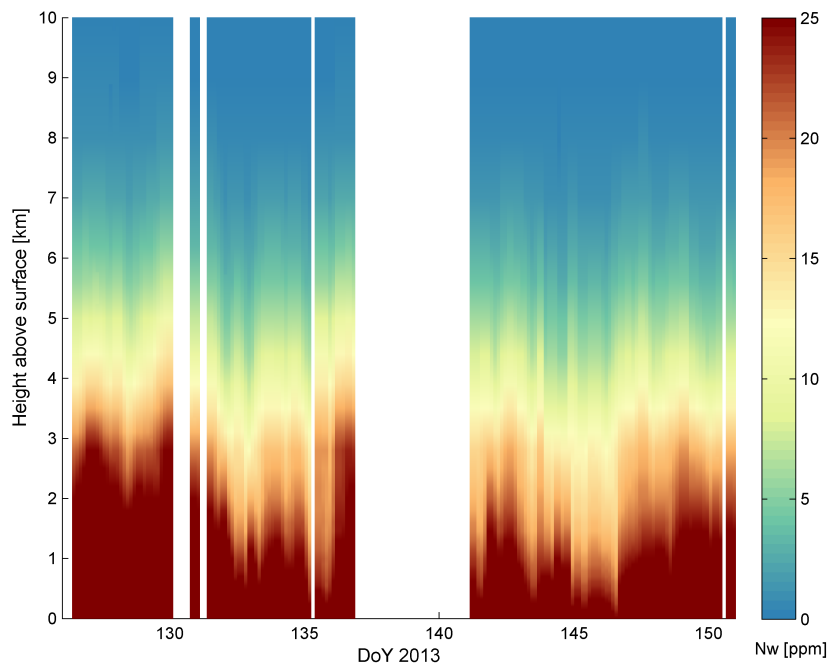
Figure 8.10: Three-hourly vertical profiles of wet refractivity above Innsbruck as derived from radiometer temperature and humidity profiles. The white stripes indicate data gaps or rain periods in which no meaningful radiometer observations could be obtained.

8.3.1 Preprocessing of radiometer data

For the period May and June 2013 profiles of temperature $T\,[K]$ and absolute humidity $ah\,[g/m^3]$ were provided with a temporal resolution of about $5\,min$ and one second, respectively. The set of measurements was complemented by a list of rain flags.

First the dataset was screened and epochs with rain flag '1' were deleted. From the remaining records common epochs of temperature and absolute humidity were identified. For each temperature profile all humidity profiles observed within a $5\,min$ search window were averaged. Finally absolute humidity was converted into water vapour pressure using Eq.2.11 and combined with temperature to wet refractivity using Eq.3.18. Therewith wet refractivity profiles are obtained with $5\,min$ temporal resolution for 38 height levels, covering the height range from surface (the radiometer is installed at the roof of the university building at $H = 612\,m$) up to $10\,km$ above surface. Figure 8.10 shows the refractivity distribution for the period May 2013.
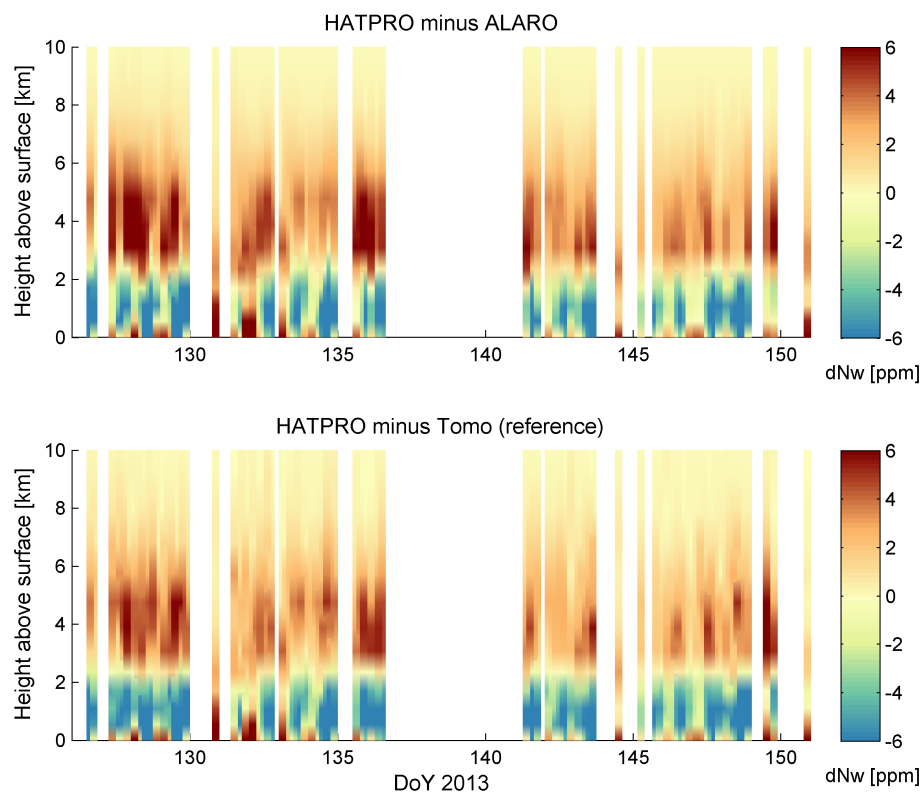
Figure 8.11: Difference plots of wet refractivity between radiometer data (HATPRO), ALARO and the reference tomography solution for May 2013

8.3.2 Difference plots of wet refractivity

Refractivity profiles derived from the radiometer data were used to evaluate the tomography solutions. Figure 8.11 shows the differences in wet refractivity (HATPRO minus Tomo reference) for each height level. In contrast to the ALARO data the reference tomography solution shows slightly higher variations but reduces significantly the bias in the atmospheric window from $2.5\,km$ to $6\,km$ height above surface.

From the comparison of integrated ZWDs with GNSS derived ZWDs in previous chapter is was assumed that the tomography profiles are in a better agreement with the radiometer profiles than ALARO analysis data. This is widely confirmed by Figure 8.11 but still larger negative and positive values appear which cancel each other out only during vertical integration. The whole amount of water vapour seems to be corrected in an integral sense but not always allocated correctly to the individual height layers.
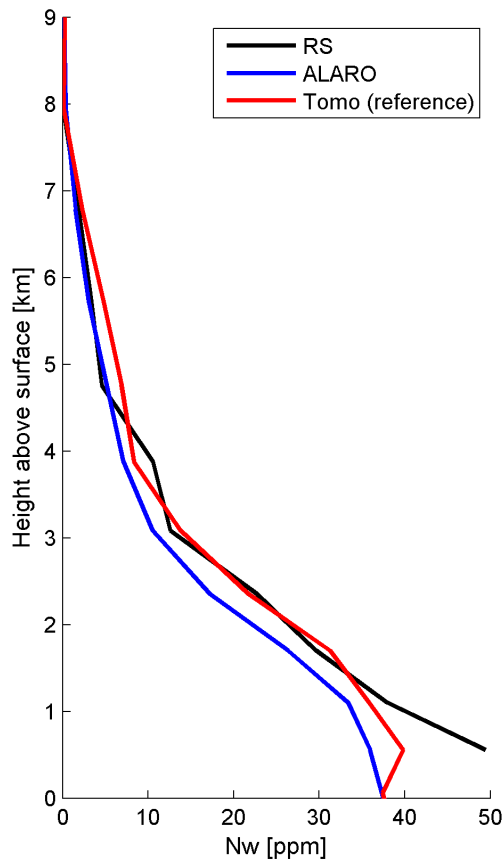
Figure 8.12: Profile of wet refractivity as derived for the 1st of May 2013, 3 UTC from radiosonde measurements, ALARO data and tomography estimates in the Inn Valley

8.4   Comparison with radiosonde data

At the airport of Innsbruck [lat: 47.26°, lon: 11.35°, $H = 579\,m$] a radiosonde of type RS92 (see Section 5.4) is launched once a day between 2 and 3 UTC. The linear distance between airport and the University of Innsbruck is about $3\,km$, hence from both instruments (radiometer and radiosonde) comparable profiles of wet refractivity are expected.

First, the radiosonde data were pre-processed, i.e. outliers in temperature were removed, dew point temperature was converted to water vapour pressure using Eq.2.10 and further to wet refractivity using the last two terms of Eq.3.18. Finally, the obtained wet refractivity profiles were linearly interpolated to the height of the voxel centre points.

For evaluation the refractivity fields were horizontally interpolated to the ground-position of the radiosonde and from the resulting vertical profiles at 3 UTC differences in wet refractivity were computed to each radiosonde profile. Figure 8.12 shows the obtained profile for the 1st of May 2013 (DoY 121).
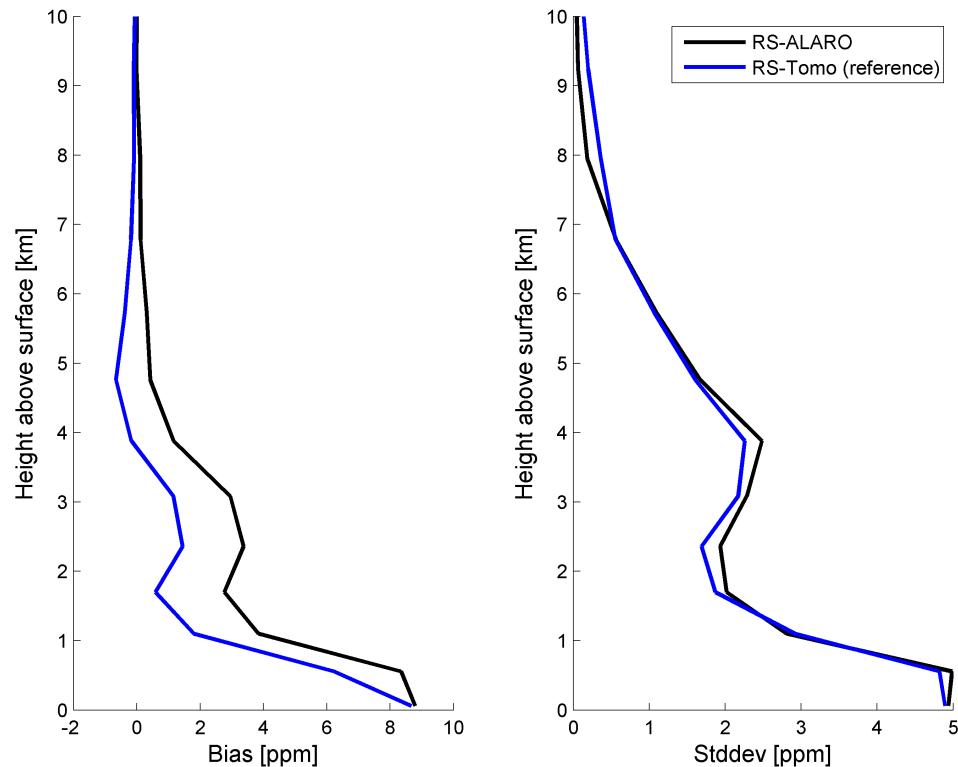
Figure 8.13: Statistics of the comparison of ALARO and tomography derived wet refractivities with radiosonde profiles. Analysed period: May 2013

The tomography (reference) solution corrects the offset of the ALARO data in the middle atmosphere between $1\,km$ and $4\,km$ height above surface. This widely confirms the finding from the comparison with radiometer data. However, the negative bias with respect to radiometer data as shown in Figure 8.11 was not found. In contrast at the analysed epoch both, ALARO and the tomography solution underestimate the wet refractivity in the lower atmosphere below $2\,km$. A similar characteristic was obtained after all epochs in May were analysed, see Figure 8.13. It demonstrates indirectly that both, radiometer and radiosonde data are not consistent. Especially in the lower atmosphere up to $2\,km$ the radiometer underestimates the water vapour content significantly (see Figure 8.11).

Nevertheless, the comparison with radiosonde data reveals that the tomography solution can clearly reduce the bias in the ALARO model data at almost all layers. Largest improvements are obtained in the range from $1\,km$ to $6\,km$ height above surface, which goes along with small improvements also in standard deviation.

	$\overline{dN_w}$	$stddev(dN_w)$
ALARO	2.30 ppm	1.79 ppm
reference (ref)	1.31 ppm	1.75 ppm
ref + bending	1.29 ppm	1.75 ppm
ref + stacking	1.27 ppm	1.92 ppm
ref + outer delay	1.30 ppm	1.78 ppm
ref + VCA	1.53 ppm	1.81 ppm

Table 8.9: Statistic of the differences in N_w between radiosonde measurements in the Inn Valley and various tomography solutions. Analysed period: May 2013

Further improvements, especially in bias can be obtained if atmospheric bending is considered, hydrostatic gradients are removed (not shown) or if observations within a predefined observation window (e.g. $60\,min$) are processed together. Latter leads to a stabilisation of the tomography solution but also to an increase in standard deviation of about $10\,\%$, see Table 8.9.

8.5   Interpretation of results

Within the analysed test cases in alpine environment a clear picture became apparent: GNSS tomography can provide significant improvement with respect to a priori refractivities derived from ALARO analysis data in several ways. First, GNSS tomography can

correct wet refractivity in an integral sense. ALARO tends to underestimate the wet re-fractivity content in the lower and middle atmosphere which leads on average to $5\,mm$ smaller *ZWD*s than expected from GNSS estimates. This negative bias is widely corrected in the tomography solution. Comparisons with radiosonde data reveal that largest improvements are visible in the middle atmosphere between $1\,km$ and $6\,km$ height above surface. In this part of the atmosphere GNSS tomography shows its highest potential, assuming GNSS station distances of about $50\,km$ as commonly targeted in commercial reference networks.

Secondly, GNSS tomography allows to correct for time-shifts whether they appear in the a priori field. In consequence weather phenomena forecasted with a time shift of a few hours can be widely corrected with GNSS tomography as highlighted in the following in more detail.
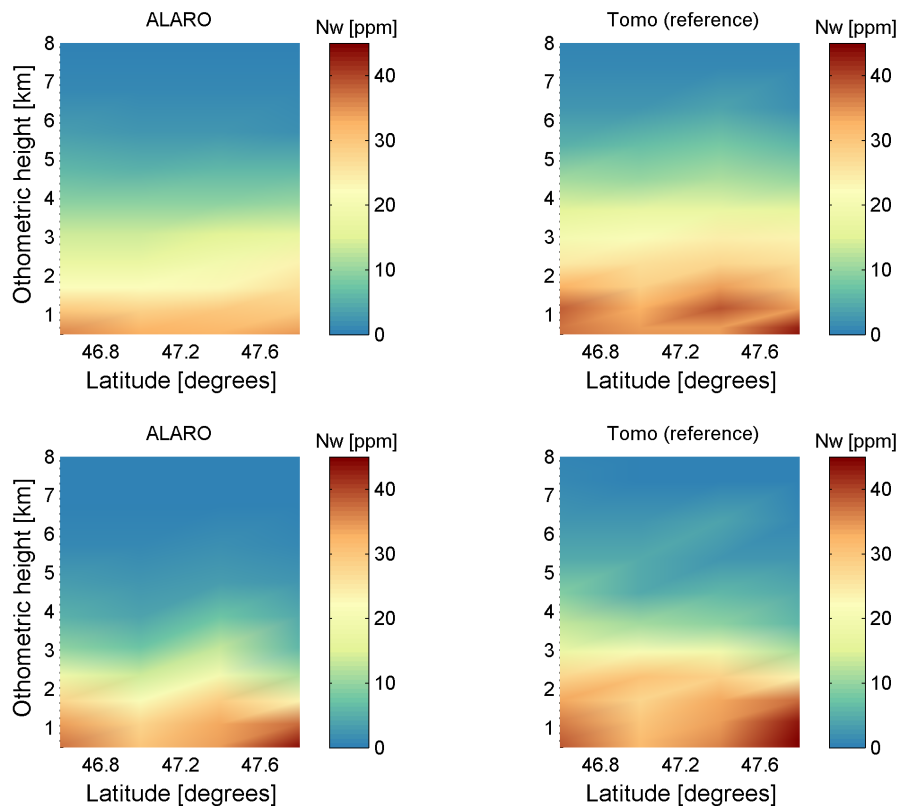
Figure 8.14: Wet refractivity profiles as obtained from ALARO (left) and the reference tomography solution (right) along the 12.5° E meridian for the 31st of May 2013, 9 UTC (top) and 21 UTC (bottom)

Figure 8.14 shows the wet refractivity profile along the 12.5° E meridian. The profile starts in the South near Cortina d'Ampezzo, Italy (46.6° latitude), is scraping the Grossglockner, Austria at 47.0° latitude on the East and ends near the Chiemsee in Germany (47.8° latitude). On the 31st of May 9 UTC the tomography solution shows already a significant increase in wet refractivity in the lower atmosphere with largest values in the lower right corner, at the foothills of the Alps near Chiemsee. In sequel this increase in wet refractivity is identified as first trough of the warm conveyor belt, as described in Section 8.1.

At 21 UTC (15 hours later) the increase is now visible in the ALARO data but still with smaller amplitude and lower extend as in the tomography solution.

This example illustrates that the tomography solution allows for significant variations from the a priori refractivity field. In consequence large-scale weather phenomena can be identified and corrected in time. This is a major step since common arguments against GNSS tomography claim that the tomography solution is too closely aligned with the a priori field.

Besides, comparison with radiometer and radiosonde profiles confirmed that GNSS tomography has also potential for correcting the bias of NMW also on longer time scales. In conclusion GNSS tomography can be seen as valuable technique for describing the atmospheric conditions area-wide and with high temporal resolution. This makes it to an interesting weather analysis tool.

A recent study highlighted that improved wet refractivity fields assimilated into the weather forecast model AROME operated at ZAMG helps to further improve the amplitude score of humidity related parameters, e.g. of precipitation on very short time scales (<8 hours). For further details the reader is referred to Möller *et al.* (2015).

Chapter 9

Summary and Conclusions

Earth´s atmosphere is well approximated by a two-component gaseous system formed by dry air and water vapour. Thus, according to Gibb´s rule, three variables, namely pressure, temperature and water vapour pressure, are sufficient to define its thermodynamic state. While the concentration of the dominant dry atmospheric constituents is rather stable over time it can be modelled accurately from surface measurements assuming hydrostatic equilibrium. Short-lived constituents like water vapour are much more erratic and therewith difficult to predict.

Empirical models like GPT2w (see Böhm *et al.* 2015) provide pressure, temperature, specific humidity and other related atmospheric parameters on global grids as mean value, and annual and semi-annual amplitudes, and allow therewith the capturing of macro-scale features driven particularly by global differences in net solar radiation. On the meso-scale level and short time scales, classical observing systems like surface-based sensor networks, including weather stations or radiosondes, can provide more accurate information about the actual state of the atmosphere at specific points and epochs. However, with these measurements, the complex water vapour distribution in the lower atmosphere can only be partly described. A holistic description requires new, more complex observation technologies.

Satellite systems like GNSS transmit signals in the microwave frequency L-band ($1 - 2GHz$) and allow therewith for continuous operation during all weather conditions. According to Maxwell´s equations, the signal propagation is dependent on the electric and magnetic properties of the propagation medium, and the signal phase velocity is directly connected with the index of refraction n, which expresses the state of the atmosphere and varies like its describing parameters in time and space.

The GNSS signal phase excess in the atmosphere can be retrieved from phase measurements by applying advanced processing strategies. They allow for separation of atmospheric propagation effects from a series of other effects like clock errors or multipath. Usually longer observation arcs are required for decorrelating the atmospheric delay from the station coordinates and also for ambiguity resolution.

Unfortunately for each GNSS observation the slant total delay (STD) cannot be estimated directly but rather its components, the zenith total delay (ZTD) and horizontal gradient parameters are estimated as piece-wise linear functions.

First order gradient parameters (G_E and G_N) describe the dominant part of horizontal asymmetry, i.e. azimuthal-dependent delay variations particularly caused by the heterogeneous distribution of water vapour in the lower atmosphere. Although gradients are small, it was shown that a gradient of $2\,mm$ can cause a ZTD estimation error of up to $35\,mm$ if it remains unattended. By estimating first order gradients together with ZTDs, the phase excess in the neutral atmosphere can be reconstructed from GNSS measurements with mm- to cm-accuracy, dependent on the elevation angle of the satellite and actual weather conditions.

Analysis of the GNSS phase residuals reveal that even if first order gradient parameters are estimated short-term variations of refractivity and small-scale effects like turbulences remain unmodelled, especially during severe weather events, as was exemplarily shown for cyclone 'Fredrik' at the end of May 2013. In consequence, more advanced asymmetry models have to be developed and applied in GNSS data processing for retrieving more structural information from GNSS phase measurements[1].

The hydrostatic component of the STD can be precisely determined from measurements of air pressure. Comparisons based on three different pressure sources, namely in-situ measurements taken from the Austrian TAWES network, global ECMWF and regional ALARO numerical weather model data, reveal that all three sources are well suited for describing the pressure variations at the GNSS site. Over the period of two months - May and June 2013 - and at 43 Austrian GNSS sites, the highest consistency was observed between TAWES and ECMWF data ($-0.06 \pm 0.42\,hPa$) with the smallest scatter in the rather flat East of Austria. A similar bias but a slightly larger standard deviation was found between TAWES and ALARO data ($0.09 \pm 0.67\,hPa$).

Since the pressure values are usually not provided directly at the GNSS site the measurements have to be extrapolated, e.g. by means of the hypsometric equation. Dependent on

---

[1]By taking current GNSS developments into account such models might be applicable in a couple of years when about 120 GNSS navigation satellites are observable on three frequencies.

the extrapolation-distance ($dist$) a scatter of $\pm 0.0068\,hPa \cdot dist\,[km]$ is introduced, related to local pressure variations (e.g. alpine pumping). In contrast the height difference usually has less impact on the extrapolation accuracy since the atmosphere is almost in a state of hydrostatic equilibrium.

By making use of numerical weather model (NWM) data, hydrostatic asymmetric effects can also be determined. Therefore ray-tracing methods have to be applied to the model data. Assuming a constant elevation angle but different azimuth angles, azimuth-dependent variations in hydrostatic delay can be detected. Within the analysed period in summer 2013 and at 13 selected GNSS sites in Austria, hydrostatic delay variations of up to $7\,cm$ at 3° elevation angle were found. These variations are caused by differences in tropospheric height but also by local pressure variations. While the effect increases with decreasing elevation angle, hydrostatic asymmetry should be taken into account for observations below 15° elevation angle.

After removing hydrostatic effects from the slant total delay, the Slant Wet Delay (SWD) remains. It describes the integral effect of water vapour along the signal path through the lower atmosphere. By taking into account all GPS and GLONASS satellites in view above a 3° elevation angle, currently 13 to 22 SWDs can be obtained per epoch and GNSS site.

However, structural information about the water vapour distribution can only be retrieved if the SWDs of a network of GNSS receivers are processed together within a tomography approach. Based on Fermat´s principle the functional relation $SWD = A \cdot N_w$ can be solved for wet refractivity (N_w), whereby matrix A describes the geometry of the signal paths.

For obtaining structural information, the lower atmosphere (up to $\sim 12\,km$ in mid-latitudes) has to be divided into volume elements, short: voxels. If the signal path length in each voxel is known, the wet refractivity in each voxel can be estimated from the slant wet delays.

The path length in each voxel can be obtained by means of ray-tracing techniques. For elevation angles larger than 15° the ray path can be assumed as a straight line and the intersection points between the ray paths and the voxel surfaces in ellipsoidal coordinates are determined by spherical trigonometrical relations. Below 15° elevation angle, signal bending becomes effective and the true signal path deviates significantly from a straight line. Since the bended ray travels generally 'above' the straight line, it enters the top layer of the voxel model always 'later' than its straight equivalent. Consequently, by ignoring atmospheric bending, the signal path in the voxel model is determined systematically too large, approximately by about $3\,km$ at 3° elevation angle.

The exact ray path depends on the actual atmospheric conditions. Hence for highest accuracy the bended ray-tracer should be applied iteratively. The number of iterations can be significantly reduced if a priori refractivity fields, e.g. from NWM forecast data, are introduced.

If the path geometry is known, the tomography equation can be solved for wet refractivity ($N_w = A^{-1} \cdot SWD$). Unfortunately matrix A is singular in GNSS tomography, i.e. not uniquely solvable. Nevertheless, a solution can be obtained e.g. by applying iterative algebraic reconstruction techniques or Singular Value Decomposition (SVD) methods. The challenge in SVD is to define an optimal threshold for the eigenvalues in order to reduce reconstruction artefacts without losing too much structural information due to smoothing effects. Within this disseration it was shown that the L-curve technique as commonly used in seismic processing is well applicable to GNSS tomography and allows for finding an optimised solution by comparing the norm of the estimates with the norm of the residuals.

The tomography solution further benefits from observation-dependent weighting. Especially between the a priori refractivity field and the slant wet delays relative weighting helps to further improve the tomography solution, in particular if the a priori field is less accurate. By proper weighting an improved refractivity field can be obtained which is stabilised by the a priori field without being too dependent on it.

In addition also relative weights between the slant wet delays might be beneficial since therefore the impact of less accurate observations on the tomography solution can be further reduced. Since the accuracy of the slant wet delays and also of the a priori model is usually not known, a weighting model has to be defined. For the slant wet delays typically the formal error of the *ZTD* multiplied with the sine of the elevation angle is a good indicator for the accuracy of the observations. For the a priori data, a height-dependent accuracy model is proposed. Nevertheless, more advanced quality information about the a priori refractivity fields could be derived from ensemble forecast data.

If no accuracy information is made available, Variance Component Analysis (VCA) can also be applied to find a realistic weighting scenario for the different observation types. However VCA should be handled with care since it can also amplify the scatter of the tomography solution. In any case the normalised misfit function and also the norm of the weighted residuals should be checked since they are good indicators of proper weighting.

The developed tomography approach was applied to slant wet delays obtained from a network of GNSS stations in the mountainous area of Austria by considering all GPS and GLONASS satellites in view above 3° elevation angle. Especially by taking observations at

low elevation angles into account - but also due to proper handling of hydrostatic gradients, atmospheric bending and observation-dependent weighting - the quality and the stability of the tomography solution could be further increased. Moreover, its sensibility to changes in the observation geometry could also be significantly reduced.

Accordingly, a set of improved wet refractivity fields was derived that was competitive with wet refractivity profiles derived from radiometer measurements in the Inn Valley, Austria. Based on the outcome, the following statements can be derived: GNSS tomography has great potential for improving existing weather models in several ways. First, the improved wet refractivity fields are mostly closer to radiosonde profiles. Especially in the range from $1\,km$ to $6\,km$ height above the surface, GNSS tomography clearly reduces the bias in wet refractivity compared to ALARO model data. Therewith GNSS tomography has potential as a weather analysis tool, either for evaluation of numerical weather models or as an additional observation technique for water vapour distribution, which can be assimilated into operational weather forecast systems. First assimilation tests revealed that the improved wet refractivity fields help to further reduce the amplitude score of humidity related parameters and therefore to improve short-term precipitation forecasts (see Möller *et al.*, 2015).

Further, GNSS tomography is a precise sensor for the total amount of water vapour in the lower atmosphere. As a result, by vertical integration through the improved wet refractivity fields, the bias and standard deviation with respect to GNSS estimated *ZWD*s can be significantly reduced from $5.0\,mm \pm 6.3\,mm$ as obtained from the ALARO data to $0.7\,mm \pm 1.9\,mm$. This makes GNSS tomography derived wet refractivity fields interesting as input for ground-based observing techniques like GNSS or VLBI which rely on precise modelling of the water vapour content in the atmosphere.

Chapter 10

Outlook: Inter-satellite ranging

Simulations have pointed out that GNSS tomography solutions can be further improved when vertical profiles of wet refractivity are introduced (see Section 7.2.4.4). Even a single profile reduces misallocations due to glancing intersections of the GNSS signals. Thereby not only the voxels along the vertical profile benefit from the additional information but rather the entire voxel model is positively affected.

In order to obtain such profiles either radiosonde or radio occultation data can be utilised. Within the ISR-Atmosphere project[1] it was demonstrated that also GNSS inter-satellite ranging (ISR) can be a potential source of information about the vertical distribution of refractivity in the lower atmosphere, see Weber *et al.* (2016).

In the following a geometrical contemplation for the Galileo constellation is carried to identify possible ISR events through the atmosphere. Based on this a series of requirements was defined which have to be fulfilled before detailed information about the atmospheric state can be retrieved from ISR measurements.

10.1   Geometrical contemplation

Many GNSS constellations consider already the possibility to incorporate inter-satellite ranging capabilities to further improve the overall system capability concerning orbit and clock prediction accuracy and to further reduce the dependency on the ground infrastructure. Aside, if the inter-satellite ray enters the Earth´s atmosphere additional information about the ionosphere and the neutral atmosphere can be derived.

---

[1]The ISR-Atmosphere project was funded within the European GNSS Evolution Programme. Project number: EGEP-ID89-1.15.

In order to identify such events a GNSS constellation of 24 (27 and 30) Medium Earth Orbit (MEO) satellites, 4 Inclined Geosynchronous Orbit (IGSO) satellites and 1 MEO spare satellite was simulated over the year 2014 taking precise orbit information of the active Galileo satellite E19 (IOV-3) into account. The positions of the missing MEO satellites were computed with respect to E19 in order to fill the gaps in the 3/1 Walker constellation. The 4 IGSO satellites were placed 10° West and 10° East of the Greenwich meridian with the same inclination as the MEO satellites ($i = 56°$) to guarantee a good visibility over Europe. For each IGSO satellite a set of Keplarian elements was generated and assumed as constant for the entire study period. Since the MEO spare satellite is designed for fast replacement in case of failure of one of the regular satellites it was set in one of three existing orbital planes of the Walker constellation but in a special orbital longitude (mean anomaly). Thereby a permanent link to one of the regular satellites in the same orbital plane could be installed which allows for permanently scanning a specific layer of the atmosphere. Figure 10.1 shows the resulting observation geometry. In contrast to a nominal 27/3/1 constellation the MEO spare satellite had to be shifted in orbit by 5° in mean anomaly.
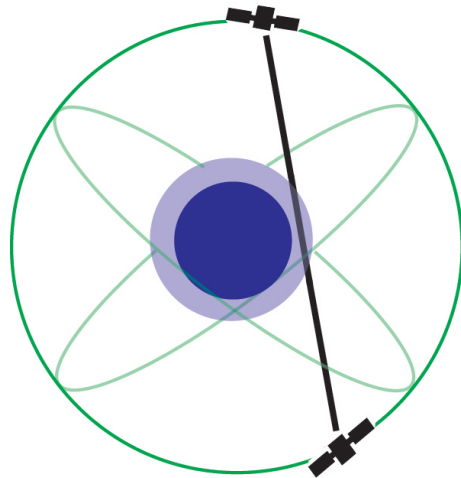
Figure 10.1: Observation geometry between a regular MEO and a MEO spare satellite in the same orbital plane

In Figure 10.2 the resulting ground track of the inter-satellite ray between a MEO and a **MEO spare** satellite in the same orbital plane is visualised. The ground track of the inter-satellite ray moves parallel to the ground track of the MEO satellites and covers thereby the entire longitude range during its ten day repeat cycle. In latitudinal direction the ground track is limited by the inclination angle of the satellites, which was set to 56°.
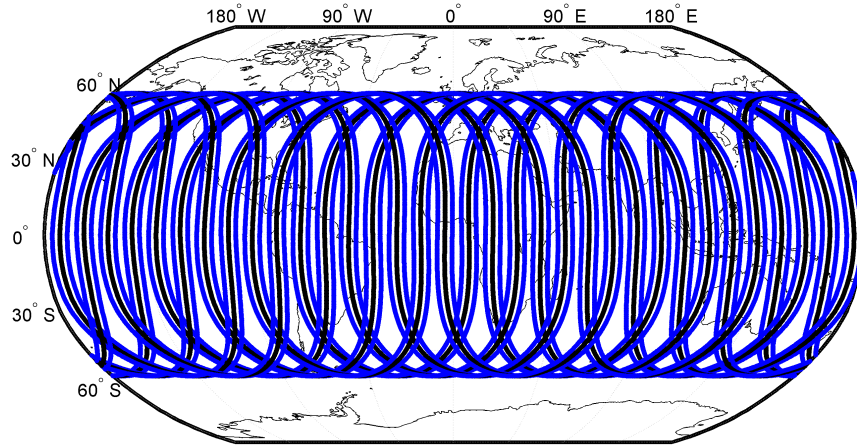
Figure 10.2: Ground track of the inter-satellite ray passing the neutral atmosphere between a regular MEO and a MEO spare satellite in the same orbital plane. The entry points into the neutral atmosphere ($h < 40\,km$) are marked as blue dots, the centre point is highlighted in black. Analysed period: 4th to 13th of May 2014
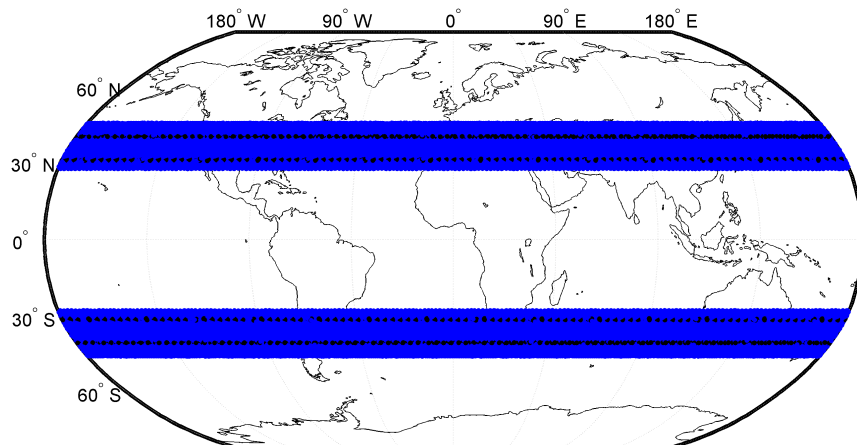
Figure 10.3: Ground tracks of the inter-satellite rays passing the neutral atmosphere between 24 regular MEO satellites in a 24/3/1 Walker constellation. The entry points into the neutral atmosphere ($h < 40\,km$) are marked as blue dots, the centre point is highlighted in black. Analysed period: 4th to 8th of May 2014

Figure 10.3 shows the resulting ground track between 24 **MEO** satellites assuming a 24/3/1 Walker constellation. Each MEO satellite has four choices to build inter-satellite

links which enter the atmosphere[2], whereby no events are possible between MEO satellites within the same orbital plane.

Within the repeat cycle of five days two latitude bands are covered by about 320 events per day. Within each event the entire atmosphere is vertically scanned. Assuming the neutral atmosphere by $h < 40\,km$ and the ray paths as straight lines the inter-satellite events can be divided into four classes. All events cover the latitude range from 25° to 50° latitude on both hemispheres but differ significantly with respect to event duration (16 sec vs. 29 sec) and repetition rate (80 min vs 340 min).

For the 27/3/1 and 30/3/1 constellation similar classes of events were detected as for the 24/3/1 constellation with comparable event durations and repetition rates. Due to the increasing number of satellites also the number of events increases to 400 events per day for 30 satellites but not for the 27 satellite constellation. Hereby only 270 events per day were obtained. However, by increasing the upper rim of the atmosphere to $h < 1100\,km$ for the 27/3/1 constellation in addition a fifth class of events was detected whereby the ray enters the ionosphere but not the neutral atmosphere.
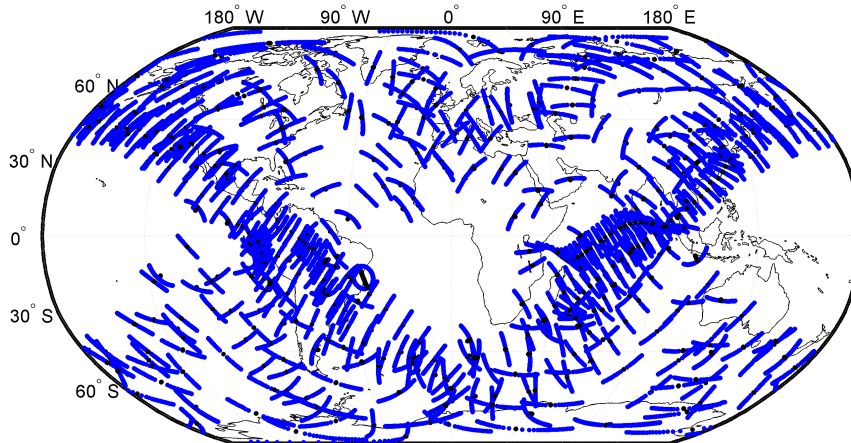
Figure 10.4: Ground tracks of the inter-satellite rays passing the neutral atmosphere between 4 IGSO and 24 MEO satellites in a 24/3/1 Walker constellation. The entry points into the neutral atmosphere ($h < 40\,km$) are marked as blue dots, the centre point is highlighted in black. Analysed period: 4th to 8th of May 2014

In contrast Figure 10.4 shows the resulting ground tracks between 4 **IGSO** and 24 MEO satellites. Due to the different orbital planes also the number, duration and distribution

---

[2]One MEO satellite in orbital plane one can connect to two specific MEO satellites on orbital plane two and two specific MEO satellites on orbital plane three.

of events becomes more complex than for the MEO-only case. In principle any IGSO-MEO satellite link can enter the neutral atmosphere. Therefore a global coverage can be obtained with highest density of events East and West of the IGSO ground tracks but also with observation gaps over the Pacific Ocean and over East Africa. Within the repeat cycle of five days the majority of events, about 105 per day, last less than $25\,min$. About 12 events per day last longer than $25\,min$, up to one hour. While the IGSO orbit is less affected by temporal varations, the ascending node of the MEO orbit drifts about $-10°$/year eastwards (assuming $i = 56°$ and $a = 29600\,km$). In consequence the number and duration of events changes slightly over time.

10.2 ISR requirements and processing options

Based on the geometrical examinations a series of requirements can be defined which have to be fulfilled before the potential of ISR for sensing the neutral atmosphere can be fully exploit.

- Cross-plane ranging is required except for MEO to MEO spare links.

- The frequency of the ranging signal should allow continuous signal reception, independent from the actual weather conditions and of the atmospheric penetration depth; preferable in L-band $(1-2\,GHz)$, S-band $(2-4\,GHz)$ or C-band $(4-8\,GHz)$.

- The ionospheric delay should be reducible, either by dual-frequency techniques or ionospheric models. In case of ionospheric models higher frequency measurements in C-band or K-band $(18 - 27\,GHz)$ are prefereable since the ionospheric delay is less pronounced at higher frequencies (in K-band less than $1\,m$).

- Inter-satellite range measurements should be provided with high sampling rate (preferable with sub-sec rate) and with dm range-accuracy or better.

- The free-space satellite distance should be known with dm-accuracy or better.

If these requirements can be fulfilled signal delays in the neutral atmosphere can be derived from ISR measurements with dm-accuracy. These delays can be either processed like radio occultation delays on longer baselines or introduced together with ground-based GNSS derived slant delays within a tomography approach for estimating refractivity fields. Latter was tested within the ISR-Atmosphere project. For further details the reader is referred to Weber *et al.* (2016).

Appendix A

Formulas and settings

A.1   Acronyms

ALADIN	Aire Limitée Adaptation Dynamique Développement International
ALARO	Combined model of ALADIN and AROME
AROME	Application de la Recherche à l'Opérationnel à Meso-Echelle
ART	Algebraic Reconstruction Technique
CDMA	Code Division Multiple Access
COSMIC	Constellation Observing System for Meteorology, Ionosphere and Climate
DDR	Double-Difference Residuals
ECMWF	European Centre for Medium-Range Weather Forecasts
EGG97	Europäisches Gravimetrisches Geoid 1997
EPOSA	Echtzeit POSitionierung Austria
ERA-Interim	ECMWF Re-Analysis product
ESA	European Space Agency
ESOC	European Space Operations Centre
ESRL	NOAA's Earth System Research Laboratory
FDMA	Frequency Division Multiple Access
GCRF	Geocentric Celestial Reference Frame

GLONASS	GLObalnaja NAwigazionnaja Sputnikowaja Sistema
GMF	Global Mapping Function
GMSP	Global Mean Surface Pressure
GMSR	Global Mean Surface Refractivity
GMST	Global Mean Surface Temperature
GNSS	Global Navigation Satellite Systems
GPS	Global Positioning System
GPT	Global Pressure and Temperature model
GPT2w	Global Pressure and Temperature model 2 Wet
HATPRO	Humidity And Temperature PROfiling microwave radiometer
HRES	High RESolution atmospheric forecast model
IEEE	Institute for Electrical and Electronic Engineers
IERS	International Earth Rotation and Reference System Service
IFS	Integrated Forecast System
IGS	International GNSS Service
IGSO	Inclined GeoSynchronous Orbit
INCA	Integrated Nowcasting through Comprehensive Analysis
ISR	Inter-Satellite Ranging
ITRF	International Terrestrial Reference Frame
ITRS	International Terrestrial Reference System
LEO	Low Earth Orbit
LSQ	Least Squares Adjustment
MART	Multiplicative Algebraic Reconstruction Technique
MEO	Medium Earth Orbit
METOP	METeorological OPerational satellite
MOPS	Minimum Operational Performance Standards
NASA	National Aeronautics and Space Administration
NCAR	National Center for Atmospheric Research

NCEP	National Centers for Atmospheric Prediction
NOAA	National Oceanic and Atmospheric Administration
NWM	Numerical Weather Model
PPP	Precise Point Positioning
PRN	Pseudo Random Noise
QBO	Quasi-Biennial Oscillations
RINEX	Receiver Independent Exchange Format
RMS	Root Mean Square
RO	Radio Occultation
RS	RadioSonde
RTCA	Radio Technical Commission for Aeronautics
SDR	Single-Difference Residuals
SINEX	Solution (Software) INdependent EXchange format
STD	Slant Total Delay
SWD	Slant Wet Delay
TAWES	Teilautomatisches-Wetter-Erfassungs-System
TSVD	Truncated Singular Value Decomposition
UTC	Coordinated Universal Time
VCA	Variance Component Analysis
VLBI	Very Long Baseline Interferometry
VMF1	Vienna Mapping Function 1
WGS84	World Geodetic System 1984
WMO	World Meteorological Organization
ZAMG	Zentralanstalt für Meteorologie und Geodynamik
ZDR	Zero-Difference Residuals
ZHD	Zenith Hydrostatic Delay
ZTD	Zenith Total Delay
ZWD	Zenith Wet Delay

A.2 Normal gravity above the ellipsoid

According to (Somigliana, 1929) the normal gravity g_0 on the ellipsoid at geodetic latitude φ is defined as follows

$$g_0 = \frac{a \cdot g_{eq} \cdot cos^2\varphi + b \cdot g_p \cdot sin^2\varphi}{\sqrt{a^2 \cdot cos^2\varphi + b^2 \cdot sin^2\varphi}} \tag{A.1}$$

where $g_{eq} = 9.78032677\,m/s^2$ is the normal gravity at the equator, $g_p = 9.83218637\,m/s^2$ is the normal gravity at the pole, a and b are the semi-major and semi-minor axes of the ellipsoid, respectively. Assuming WGS84 ellipsoid (semi-major axis $a = 6378137\,m$, flattening $f_E = 0.003352811$ and gravity ratio $m = 0.003449787$, see Mahoney, 2001) and ignoring higher order terms Eq.A.1 is well approximated by

$$g_0 = g_{eq} \cdot (1 + 0.00530244 \cdot sin^2\varphi + 0.00000582 \cdot sin^2 2\varphi). \tag{A.2}$$

In order to obtain normal gravity g at any height h above the ellipsoid, g_0 is expanded into series in terms of h.

$$g = g_0 + \frac{\partial g_0}{\partial h}h + \frac{1}{2}\frac{\partial^2 g_0}{\partial h^2}h^2 + ... \tag{A.3}$$

By spherical approximation Eq.A.3 reads

$$g = g_0 \cdot \left(1 - \frac{2 \cdot h}{R_E} + \frac{3}{a^2}h^2\right) \tag{A.4}$$

with R_E as the effective Earth radius.

$$R_E = a/(1 + f_E + m - 2 \cdot f_E \cdot sin^2\varphi) \tag{A.5}$$

In case of WGS84 and $\varphi = 45°$ EqA.4 simplifies to

$$g = g_0 - 0.308769 \cdot h\,mGal \tag{A.6}$$

also known as 'free-air' correction. Assuming the Hayford-ellipsoid ($a = 6378388\,m$ and and $f_E = 1/297$) and by ignoring the second-order term the well-known value of $-0.3086 \cdot h$ is obtained.

For further simplification Eq.A.4 can be approximated by

$$g = \frac{g_0}{(1 + h/R_E)^2}. \tag{A.7}$$

The resulting error in g increases with height but remains less than $1\,mGal$ for $h < 55\,km$.

A.3   Simulated GNSS observations

In order to study the information content in differenced post-fit residuals a set of dual-frequency GPS observations was simulated for 12 stations in Austria. Table A.2 summarises the main settings and files used for the generation of the pseudorange (C1, C2) and phase observations (L1, L2).

Parameter	Setting
Observation period / rate	01.10.2013, 00:00 - 23:59:30 GPS time / 30 sec
Satellite position	IGS final orbits
Satellite clock	IGs final clocks (high rate)
Earth Rotation Parameters	IGS final ERPs
Station coordinates	ITRF2008 coordinates, fixed
Troposphere model	dry Saastamoinen + GPT + GMF + 2 mm East-West gradients
Ionosphere model	none
Observation noise, Multipath	none

Table A.2: Settings for the simulation of GPS observations using software package Bernese v5.2 (GPSSIM)

The tropospheric delay was computed by means of the following equation

$$ZTD = 0.002277 \cdot sec(90°\text{-}\varepsilon) \cdot \left[p + (1255/T + 0.05) \cdot e - 1.16 \cdot tan^2(90° - \varepsilon) \right] \tag{A.8}$$

whereby water vapour pressure e was set to zero and elevation angle ε to 90°. Pressure p and temperature T at each station was computed by means of GPT (Böhm *et al.*, 2007). The resulting *ZTD* was mapped to the elevation angle of the satellite by means of GMF (Böhm *et al.*, 2006b). In addition gradients were added to the six stations in the East of Austria (Baden, Leopoldau, Mattersburg, Mistelbach, Traisen and Ziersdorf). Therefore

the gradient model of Chen & Herring (1997) as given by Eq.4.25 was applied, whereby G_E was set to $2\,mm$ and G_N to $0\,mm$, i.e. only a East-West gradient is assumed.

A.4   Least squares adjustment

The least squares adjustment can be applied to observations if they are normally distributed, i.e. free of gross errors or systematic effects. Further, the linear relation between the unknowns and the observations has to be correctly known. If these conditions are fulfilled, the linear (or linearised) system of observation equations is defined by

$$Res = A \cdot \delta\hat{x} - l \qquad (A.9)$$

where l is the vector of reduced observations, $\delta\hat{x}$ is the vector of the adjusted corrections to the unknowns x, matrix A is the so-called design matrix and Res is the vector of observation residuals.

In case of GNSS, the observation equations (Eq.4.1 and 4.2) describe the functional relation between observations and unknowns. Since the observation equations are not linear, they have to be linearised around a point of approximation using a Taylor series expansion (function $L(x)$, one unknown x):

$$L(x) = L(x_0) + \frac{\partial L(x)}{\partial x} \cdot (x - x_0) + ... \qquad (A.10)$$

The zero-order term $L(x_0)$ is an approximation of $L(x)$, whereby the unknown has been replaced by an a priori value x_0. The first-order term describes the slope of the linearised function. It results from the deviation of $L(x)$ with respect to x, multiplied by the correction $\delta x = x - x_0$. The second and higher-order terms of the Taylor expansion are non-linear, hence for the purpose of adjustment they are neglected. The resulting linearised model for one observation and j unknowns reads:

$$Res = L(x_0) + \sum_j \frac{\partial L(x)}{\partial x_j} \cdot \delta x_j - L(x) \qquad (A.11)$$

where $l = L(x) - L(x_0)$ defines the vector of reduced observations.

In case of tropospheric parameters the partial deviations of $L(x)$ with respect to the unknowns (ZWD, G_E, G_N) as piece-wise linear offset function are defined as follows

$$\frac{\partial L(x)}{\partial ZWD} = \gamma \cdot mf_w \qquad (A.12)$$

$$\frac{\partial L(x)}{\partial G_E} = \gamma \cdot \frac{\partial mf_g}{\partial z} \cdot sin(\alpha) \tag{A.13}$$

$$\frac{\partial L(x)}{\partial G_N} = \gamma \cdot \frac{\partial mf_g}{\partial z} \cdot cos(\alpha) \tag{A.14}$$

where z is the zenith angle, α is the azimuth angle and γ represents the derivation of the piece-wise linear function with respect to the unknowns (x_i and x_{i+1}) at epoch i and $i+1$. By limiting the range of t to $t_i < t < t_{i+1}$ the partial derivatives of the piece-wise linear offset function read

$$\gamma_i = 1 - \frac{t - t_i}{\Delta t} \tag{A.15}$$

$$\gamma_{i+1} = \frac{t - t_i}{\Delta t} \tag{A.16}$$

whereby $\Delta t = t_{i+1} - t_i$ defines the temporal spacing between the nodal points. The resulting design matrix A for the estimation of the tropospheric parameters follows to:

$$A = \left[\begin{array}{cccccc} \frac{\partial L(x)}{\partial ZWD_i} & \frac{\partial L(x)}{\partial ZWD_{i+1}} & \frac{\partial L(x)}{\partial G_{E,i}} & \frac{\partial L(x)}{\partial G_{E,i+1}} & \frac{\partial L(x)}{\partial G_{N,i}} & \frac{\partial L(x)}{\partial G_{N,i+1}} \end{array} \right] \tag{A.17}$$

The size of A is defined by the unknowns (number of columns) and the observations (number of rows). To solve the adjustment problem an optimisation strategy has to be defined. For the least squares method, the L2-norm is minimised. This is achieved by minimising the squared sum of the observation residuals.

$$\left[Res^T \cdot Res \right] \rightarrow min \tag{A.18}$$

This condition is fulfilled when $\hat{x}$ is determined as follows:

$$\hat{x} = x_0 + \delta\hat{x} = x_0 + \left(A^T \cdot A \right)^{-1} \cdot A^T \cdot l \tag{A.19}$$

thereby it is assumed that all observations are uncorrelated and equally weighted.

A.5 Satellite positions from GPS broadcast ephemerides

The GPS navigation message as modulated on top of the ranging codes contains the Keplerian orbit elements and additional perturbation parameters for computing the **satellite position** in an Earth-Centred, Earth-Fixed (ECEF) coordinate system with m-accuracy. Table A.4 gives an overview about the minimum input data required for the computation.

t_{oe}	Time of ephemeris	*sec* of GPS week
t_k	Time difference to t_{oe}	*sec*
a	Semi-major axis	*m*
M	Mean anomaly	*rad*
e	Eccentricity	[ ]
ω	Argument of perigee	*rad*
i	Inclination angle	*rad*
Ω	Right ascension	*rad*
dn	Correction for mean motion	[ ]
$\dot{\Omega}$	Rate of change of right ascension	*rad*
$\dot{i}$	Rate of change of inclination	*rad*
C_{us}, C_{uc}	Correction terms for the argument of latitude	*rad*
C_{is}, C_{ic}	Correction terms for the inclination	*rad*
C_{rs}, C_{rc}	Correction terms for the orbit radius	*m*

Tabelle A.4: Overview about the input data required for the computation of satellite positions from GPS broadcast ephemerides

The parameter $t_k = t - t_{oe}$ describes the time difference between the time of interest t and the time of ephemeris t_{oe}. During this period the satellite moves further in orbit, thus the mean anomaly M_k has to be corrected as follows

$$M_k = M + n \cdot t_k \tag{A.20}$$

where n is the mean motion with $GM = 3.986005 \, m^3/s^2$ as the geocentric gravitational constant.

$$n = \sqrt{GM/a^3} + dn \tag{A.21}$$

The eccentric anomaly E_k is computed iteratively using the following equation.

$$E_k = M_k + e \cdot sin\, M_k \tag{A.22}$$

E_k is needed for computation of the true anomaly ν_k.

$$v_k = 2 \cdot atan \left(\sqrt{\frac{1+e}{1-e}} \cdot tan\, \frac{E_k}{2} \right) \tag{A.23}$$

The argument of latitude Φ_k follows to

$$\Phi_k = v_k + \omega \tag{A.24}$$

Due to perturbations position corrections have to be applied for latitude (δu_k), radius (δr_k) and inclination (δi_k).

$$\delta u_k = C_{uc} \cdot cos2\Phi_k + C_{us}sin2\Phi_k \tag{A.25}$$

$$\delta r_k = C_{rc} \cdot cos2\Phi_k + C_{rs}sin2\Phi_k \tag{A.26}$$

$$\delta i_k = C_{ic} \cdot cos2\Phi_k + C_{is}sin2\Phi_k \tag{A.27}$$

The corrected argument of latitude u_k, orbit radius r_k and inclination i_k read:

$$u_k = \Phi_k + \delta u_k \tag{A.28}$$

$$r_k = a \cdot (1 - e \cdot cos\, E_k) + \delta r_k \tag{A.29}$$

$$i_k = i + i \cdot t_k + \delta i_k \tag{A.30}$$

The satellite position in the orbital plane (x'_k, y'_k) follows to:

$$x'_k = r_k \cdot cos\, u_k \tag{A.31}$$

$$x'_k = r_k \cdot sin\, u_k \tag{A.32}$$

In order to obtain the position vector $X^s = [x_k,\, y_k,\, z_k]$ in ECEF coordinates, the orbit position vector has to be corrected for Earth rotation Ω_k and rotated into the equatorial plane.

$$x_k = x'_k \cdot cos\, \Omega_k - y'_k \cdot sin\, \Omega_k \cdot cos\, i_k \tag{A.33}$$

$$y_k = x'_k \cdot sin\, \Omega_k + y'_k \cdot cos\, \Omega_k \cdot cos\, i_k \tag{A.34}$$

$$z_k = y'_k \cdot sin\, i_k \tag{A.35}$$

with

$$\Omega_k = \Omega + (\dot{\Omega} - \dot{\Omega}_e) \cdot t_k - \dot{\Omega}_e \cdot t_{oe} \tag{A.36}$$

where $\dot{\Omega}_e = 7.2921151467 \cdot 10^{-5} rad/s$ is the Earth rotation rate.

The satellite position can be further converted into **ellipsoidal coordinates**. Therefore the distance r between z-axis and satellite is derived.

$$r = \sqrt{x_k^2 + y_k^2} \tag{A.37}$$

The reduced latitude β is computed iteratively by making use of the following equation

$$\beta = atan\,(m + n \cdot sin\,\beta) \tag{A.38}$$

with

$$\tilde{\beta} = atan\left(\frac{z_k}{r}\right), \tag{A.39}$$

$$m = \frac{b \cdot z_k}{a \cdot r} \quad and \quad n = \frac{a^2 - b^2}{a \cdot r} \tag{A.40}$$

Semi axes a and b depend on the selected reference ellipsoid (e.g. WGS84). The ellispodial latitude φ^s, longitude λ^s and height h^s follow to:

$$\varphi^s = atan\left(\frac{a}{b} \cdot tan\,\beta\right) \tag{A.41}$$

$$\lambda^s = atan2\left(\frac{y_k}{x_k}\right) \tag{A.42}$$

$$h^s = \frac{z_k}{sin\,\varphi^s} - \left(1 - \frac{a^2 - b^2}{a^2}\right) \cdot \left(\frac{a}{\sqrt{1 - e \cdot sin^2\varphi^s}}\right) \tag{A.43}$$

From the satellite position vector X^s and a user position vector X_r also the **elevation angle and azimuth** can be computed under which the satellite is observed. Therefore the direction vector $R_r^s = X^s - X_r$ is transformed into the local coordinate system.

$$r_r^s = \begin{bmatrix} r_x \\ r_y \\ r_z \end{bmatrix} = \begin{bmatrix} -sin\,\lambda_r & cos\,\lambda_r & 0 \\ -sin\,\varphi_r \cdot cos\,\lambda_r & -sin\,\varphi_r \cdot sin\,\lambda_r & cos\,\varphi_r \\ cos\,\varphi_r \cdot cos\,\lambda_r & cos\,\varphi_r \cdot sin\,\lambda_r & sin\,\lambda_r \end{bmatrix} \cdot R_r^s \tag{A.44}$$

where λ_r and φ_r are the ellipsoidal coordinates of the user position. Finally elevation angle ε and azimuth α follows to:

$$\varepsilon = asin\left(\frac{r_z}{\sqrt{r_x^2 + r_y^2 + r_z^2}}\right) \quad and \quad \alpha = atan2\left(\frac{r_x}{r_y}\right) \tag{A.45}$$

Appendix B

Tables

B.1 TAWES site coordinates

The Zentralanstalt für Meteorologie und Geodynamik (ZAMG) operates more than 250 automated weather stations (as of June 2013), well distributed over the domain of Austria. The measurements are transferred to ZAMG every $10\,min$ via Ethernet or GPRS. Dependent on the sensors installed, two different types of stations can be distinguished. Sensor station A provides air temperature, relative humidity or dew point temperature, soil temperature, pressure and precipitation. Sensor station B is equipped with wind and radiation sensors. Details about the installed sensors for pressure, temperature and humidity together with their accuracy information are provided in Section 5.1.

In the following site coordinates are listed for selected TAWES sites, either mentioned in previous chapters or co-located with GNSS sites. All of them are sensor stations of type A, at least.

SiteNr	Name	Lat	Lon	H_site	H_baro
11004	REICHERSBERG	48° 19' 52"	13° 22' 34"	351 m	351 m
11018	AMSTETTEN	48° 06' 29"	14° 53' 55"	266 m	264 m
11019	ALLENTSTEIG	48° 41' 27"	15° 22' 01"	599 m	607 m
11021	LITSCHAU	48° 57' 17"	15° 02' 18"	558 m	557 m
11025	WEITRA	48° 42' 08"	14° 53' 55"	572 m	570 m
11050	REICHENAU/MÜHLKREIS	48° 27' 33"	14° 20' 44"	689 m	693 m
11056	VÖCKLABRUCK	48° 00' 24"	13° 38' 44"	432 m	431 m
11082	GUMPOLDSKIRCHEN	48° 02' 25"	16° 16' 56"	219 m	221 m
11090	WIEN-DONAUFELD	48° 15' 26"	16° 25' 53"	160 m	163 m

SiteNr	Name	Lat	Lon	H_site	H_baro
11112	LANDECK	47° 08' 25"	10° 33' 49"	796 m	809 m
11121	INNSBRUCK-FLUGPLATZ	47° 15' 27"	11° 21' 13"	578 m	593 m
11136	KRIMML	47° 13' 45"	12° 10' 55"	1009 m	1011 m
11138	RUDOLFSHÜTTE	47° 08' 06"	12° 37' 33"	2317 m	2320 m
11157	AIGEN/ENNSTAL	47° 31' 58"	14° 08' 18"	641 m	652 m
11166	SECKAU	47° 16' 15"	14° 46' 43"	872 m	872 m
11175	BRUCK/MUR	47° 24' 20"	15° 14' 59"	482 m	484 m
11190	EISENSTADT-NORDOST	47° 51' 14"	16° 32' 19"	184 m	182 m
11198	GÜSSING	47° 03' 45"	16° 19' 19"	215 m	217 m
11218	BAD BLEIBERG	46° 37' 31"	13° 41' 04"	909 m	917 m
11234	BAD EISENKAPPEL	46° 29' 26"	14° 35' 36"	623 m	616 m
11235	FERLACH	46° 31' 52"	14° 18' 51"	459 m	459 m
11238	GRAZ-STRASSGANG	47° 02' 46"	15° 24' 37"	357 m	356 m
11244	BAD GLEICHENBERG	46° 52' 20"	15° 54' 13"	269 m	271 m
11255	KÖTSCHACH-MAUTHEN	46° 40' 39"	12° 59' 54"	714 m	711 m
11290	GRAZ-UNIVERSITT	47° 04' 40"	15° 26' 56"	367 m	379 m
11296	WAGNA-LEIBNITZ	46° 46' 03"	15° 33' 10"	268 m	266 m
11307	LANGEN AM ARLBERG	47° 07' 54"	10° 07' 24"	1221 m	1218 m
11325	JENBACH	47° 23' 20"	11° 45' 29"	530 m	531 m
11330	MAYRHOFEN	47° 09' 45"	11° 51' 05"	640 m	641 m
11344	KOLM SAIGURN	47° 04' 10"	12° 59' 05"	1626 m	1622 m
11347	MICHELDORF	47° 52' 59"	14° 08' 04"	459 m	459 m
11361	BAD ISCHL	47° 42' 22"	13° 38' 50"	507 m	509 m
11374	WACHTBERG BEI STEYR	48° 02' 51"	14° 27' 40"	384 m	385 m
11386	KRUMBACH	47° 31' 41"	16° 11' 12"	545 m	542 m
11390	HARTBERG	47° 16' 50"	15° 58' 43"	330 m	337 m
11394	BRUCKNEUDORF	48° 00' 46"	16° 50' 42"	166 m	166 m
11395	ANDAU	47° 46' 21"	17° 02' 00"	118 m	121 m

Table B.1: Ellipsoidal coordinates of selected TAWES sites, where H_site is the orthometric height of the site and H_baro of the pressure sensor, respectively

For pressure reduction to GNSS site the heights were converted to ellipsoidal heights by adding EGG97 undulations (Denker & Torge, 1998) which vary in Austria between $42.9\,m$ and $51.6\,m$.

B.2 GNSS site coordinates

Site	Name	Lat	Lon	H_ell	H_ortho
ALST	ALLENTSTEIG	48.71577°	15.32971°	589.7 m	543.1 m
AMST	AMSTETTEN	48.12119°	14.89018°	334.1 m	288.2 m
ANDA	ANDAU	47.81582°	17.04222°	172.1 m	128.0 m
ANDF	ANDORF	48.36936°	13.56597°	406.3 m	361.3 m
ATPU	ATTNANG/PUCHHEIM	48.01576°	13.72299°	488.5 m	443.5 m
BADE	BADEN	48.00094°	16.24761°	281.7 m	236.4 m
DALA	DALAAS	47.12740°	9.99147°	992.5 m	943.4 m
GRAZ	GRAZ	47.07359°	15.41657°	444.2 m	396.9 m
GUES	GÜSSING	47.07417°	16.31912°	281.9 m	236.0 m
GUMM	GUMMERN	46.65685°	13.76680°	557.5 m	508.9 m
JENB	JENBACH	47.38851°	11.77781°	593.7 m	545.5 m
KIBG	KIRCHBERG	47.44870°	12.30863°	876.6 m	828.9 m
KLAG	KLAGENFURT	46.61527°	14.30915°	526.1 m	478.2 m
LAND	LANDECK	47.14833°	10.57803°	844.8 m	794.6 m
LEIB	LEIBNITZ	46.77983°	15.54704°	333.6 m	286.7 m
LEOB	LEOBEN	47.38695°	15.09063°	610.1 m	562.5 m
LEOP	LEOPOLDAU	48.27193°	16.41985°	222.5 m	178.2 m
LIEZ	LIEZEN	47.56278°	14.24218°	709.1 m	661.6 m
LINZ	LINZ	48.28982°	14.29282°	333.5 m	288.1 m
MATR	MATREI	47.12719°	11.45253°	1059.0 m	1009.1 m
MATT	MATTERSBURG	47.72239°	16.38272°	317.6 m	272.1 m
MIST	MISTELBACH	48.56599°	16.56529°	265.4 m	221.6 m
MURZ	MÜRZZUSCHLAG	47.60764°	15.67693°	745.4 m	698.0 m
OBER	OBERPULLENDORF	47.50623°	16.50506°	308.3 m	262.7 m
OCHS	OCHENIG SÜD	46.93710°	13.21210°	1078.4 m	1028.9 m
PAMA	PAMA	48.03943°	17.02617°	185.6 m	141.8 m
ROET	RÖTENKOGEL	47.17013°	12.64099°	2214.7 m	2165.4 m
SAAL	SAALFELDEN	47.42591°	12.83160°	796.4 m	748.7 m
SALZ	SALZBURG	47.81539°	13.04785°	492.9 m	447.6 m
SEEF	SEEFELD	47.32894°	11.18929°	1244.9 m	1195.8 m
SHEI	SCHEIFLING	47.14773°	14.41899°	857.5 m	808.8 m
SHLA	SCHLADMING	47.39352°	13.67801°	802.2 m	754.0 m
SILL	SILLIAN	46.74572°	12.42502°	1146.2 m	1095.2 m
TRAI	TRAISEN	48.05662°	15.61241°	407.7 m	361.2 m
WEYE	WEYER	47.86150°	14.66734°	462.5 m	416.3 m
WOBG	WOLFSBERG	46.84202°	14.83876°	523.9 m	475.6 m
WOFU	WOLFURT	47.45647°	9.74068°	481.0 m	434.2 m
ZIDF	ZIERSDORF	48.52842°	15.92157°	305.5 m	259.9 m
0145	BAD ELSTER	50.28104°	12.23395°	572.2 m	525.6 m

Table B.2: Ellipsoidal coordinates of selected GNSS sites in Austria and Germany

List of Figures

177

List of Tables

Bibliography

ADAVI, Z., & MASHHADI-HOSSAINALI, M. 2014. 4D-tomographic reconstruction of water vapor using the hybrid regularization technique with application to the North West of Iran. *Adv. Space Res.*, 55(7), 1845–1854.

AHN, Y. W. 2016. *De-correlation of tropospheric error and height component on GNSS using combined zenith-dependent parameters.* Ph.D. thesis, University of New Brunswick, Department of Geodesy and Geomatics Engineering. http://www2.unb.ca/gge/Pubs/TR306.pdf.

AKI, K., CHRISTOFFERSSON, A., & HUSEBYE, E. S. 1977. Determination of the three-dimensional seismic structure of the lithosphere. *J. Geophys. Res.*, 82(2), 277–296.

ALBER, C., RANDOLPH, W., ROCKEN, C., & BRAUN, J. 2000. Obtaining single path phase delays from GPS double differences. *Geophys. Res. Lett.*, 27(17), 1944–8007.

ANDERSSON, E. 2015. *User guide to ECMWF forecast products.* European Centre for Medium-Range Weather Forecasts. Manual.

ANDREWS, D. G. 2000. *An introduction to atmospheric physics.* 2nd edn. Cambridge Univ. Press. ISBN: 9780521693189.

APARICIO, J. M., DEBLONDE, G., GARAND, L., & LAROCHE, S. 2009. Signature of the atmospheric compressibility factor in COSMIC, CHAMP, and GRACE radio occultation data. *J. Geophys. Res.*, 114(D16), 2156–2202.

AXELRAD, P., COMP, C. J., & MACDORAN, P. F. 1996. SNR-based multipath error correction for GPS differential phase. *IEEE Trans. Aerosp. Electron. Syst.*, 32(2), 650–660.

BALDWIN, M. P., GRAY, L. J., DUNKERTON, T. J., HAMILTON, K., HAYNES, P. H., RANDEL, W. J., HOLTON, J. R., ALEXANDER, M. J., HIROTA, I., HORINOUCHI, T.,

JONES, D. B. A., KINNERSLEY, J. S., MARQUARDT, C., SATO, K., & TAKAHASHI, M. 2001. The quasi-biennial oscillation. *Rev. Geophys.*, 39(2), 179–229.

BANNISTER, R. N. 2007. *Elementary 4D-Var: DARC*. Tech. rept. 2. Data Assimilation Research Centre, University of Reading.

BAUER, P., THORPE, A., & BRUNET, G. 2015. The quiet revolution of numerical weather prediction. *Nature*, 525(7567), 47–55.

BEAN, B. R., & DUTTON, E. J. 1966. *Radio meteorology*. National Bureau of Standards. doi: http://dx.doi.org/10.5962/bhl.title.38144.

BENDER, M., & RAABE, A. 2007. Preconditions to ground based GPS water vapour tomography. *Ann. Geophys.*, 25(8), 1727–1734.

BENDER, M., DICK, G., GE, M., DENG, Z., WICKERT, J., KAHLE, H.-G., RAABE, A., & TETZLAFF, G. 2011. Development of a GNSS water vapour tomography system using algebraic reconstruction techniques. *Adv. Space Res.*, 47(10), 1704–1720.

BENEVIDES, P., NICO, G., CATALAO, J., & MIRANDA, P. M. A. 2017. Analysis of Galileo and GPS integration for GNSS tomography. *IEEE Trans. Geosci. Remote Sens.*, 55(4), 1936–1943.

BESSON, L., BOUDJABI, C., CAUMONT, O., & DU CHATELET, J. PARENT. 2012. Links between weather phenomena and characteristics of refractivity measured by precipitation radar. *Boundary-Layer Meteorol.*, 143(1), 77–95.

BEVIS, M., BUSINGER, S., HERRING, T A., ROCKEN, C., ANTHES, R. A., & WARE, R. H. 1992. GPS meteorology: Remote sensing of atmospheric water vapor using the Global Positioning System. *J. Geophys. Res.*, 97(D14), 15787–15801.

BEVIS, M., BUSINGER, S., & CHISWELL, S. 1994. GPS meteorology: Mapping zenith wet delays onto precipitable water. *J. Appl. Meteor.*, 33(3), 379–386.

BEYERLE, G., SCHMIDT, T., WICKERT, J., HEISE, S., ROTHACHER, M., KÖNIG-LANGLO, G., & LAURITSEN, K. B. 2006. Observations and simulations of receiver-induced refractivity biases in GPS radio occultation. *J. Geophys. Res.*, 111(D12101), 1–13.

Böhm, J., Werl, B., & Schuh, H. 2006a. Troposphere mapping functions for GPS and Very Long Baseline Interferometry from European Centre for Medium-Range Weather Forecasts operational analysis data. *J. Geophys. Res.*, 111(B02406), 1–9.

Böhm, J., Niell, A., Tregoning, P., & Schuh, H. 2006b. Global Mapping Function (GMF): A new empirical mapping function based on numerical weather model data. *Geophys. Res. Lett.*, 33(L07304), 1–4.

Böhm, J., Heinkelmann, R., & Schuh, H. 2007. Short note: A global model of pressure and temperature for geodetic applications. *J. Geod.*, 81, 679–683.

Böhm, J., Möller, G., Schindelegger, M., Pain, G., & Weber, R. 2015. Development of an improved empirical model for slant delays in the troposphere (GPT2w). *GPS Solut.*, 19(3), 433–441.

Boisits, J. 2014. *Prozessierung eines globalen GNSS Netzwerkes zur Ableitung von troposphärischen Delay-Zeitserien.* BSc thesis, TU Wien, Department of Geodesy and Geoinformation.

Bos, M.S., & Scherneck, H. G. 2017 (April). http://holt.oso.chalmers.se/loading/.

Brenot, H. 2006. *Potentiel de la mesure GPS sol pour l'etude des pluies intenses mediterranneennes.* Ph.D. thesis, Universite Joseph Fourier, Grenoble. https://tel.archives-ouvertes.fr/tel-00012085/file/TheseHB.pdf.

Brenot, H., Caumont, O., Bosser, P., Biondi, R., Bock, O., Ducrocq, V., & Roozendael, M. Van. 2017. Interest of GNSS tomography for nowcasting in the frame of HyMeX. *In: Proceedings of the European Geosciences Union General Assembly 2017, Vienna, Austria, 23-28 April 2017 (Poster).*

Channon, T. 2016 (July). https://tallbloke.wordpress.com/2012/01/31/back-to-basics-2-lapse-rates-and-atmospheric-stability/.

Chen, G., & Herring, T. A. 1997. Effects of atmospheric azimuthal asymmetry on the analysis of space geodetic data. *J. Geophys. Res.*, 102(B9), 20489–20502.

Cormack, A. M. 1963. Representation of a function by its line integrals, with some radiological applications. *J. Appl. Phys.*, 34(9), 2722–2727.

Dach, R., Lutz, S., Walser, P., & Fridez, P. (eds). 2015. *Bernese GNSS software version 5.2.* University of Bern, Astronomical Institute. ISBN: 9783906813059.

DAVIS, J. L., HERRING, T. A., SHAPIRO, I. I., ROGERS, A. E. E., & ELGERED, G. 1985. Geodesy by radio interferometry: Effects of atmospheric modeling errors on estimates of baseline length. *Radio Sci.*, 20(6), 1593–1607.

DENG, Z., BENDER, M., ZUS, F., GE, M., DICK, G., RAMATSCHI, M., WICKERT, J., LÖHNERT, U., & SCHÖN, S. 2011. Validation of tropospheric slant path delays derived from single and dual frequency GPS receivers. *Radio Sci.*, 46(6), 1–11.

DENKER, H., & TORGE, W. 1998. *Geodesy on the move: Gravity, geoid, geodynamics and Antarctica.* Springer Berlin Heidelberg. ISBN: 978-3-642-72245-5. Chap. The European gravimetric quasigeoid EGG97 - An IAG supported continental enterprise. 249-254.

DESSLER, A. E., ZHANG, Z., & YANG, P. 2008. Water-vapor climate feedback inferred from climate fluctuations, 2003-2008. *Geophys. Res. Lett.*, 35(20), 1–4.

DOUŠA, J., DICK, G., KAČMAŘÍK, M., BROŽKOVÁ, R., ZUS, F., BRENOT, H., STOY-CHEVA, A., MÖLLER, G., & KAPLON, J. 2016. Benchmark campaign and case study episode in central Europe for development and assessment of advanced GNSS tropospheric models and products. *Atmos. Meas. Tech.*, 9(7), 2989–3008.

ECMWF. 2017 (January). http://www.ecmwf.int/en/forecasts/datasets/.

E+E ELEKTRONIK. 2016. *EE33 Feuchte / Temperatur Messumformer für Hochfeuchte-und Chemieanwendungen.* Manual.

ELDEN, L. 1977. Algorithms for the regularization of ill-conditioned least squares problems. *BIT*, 17(2), 134–145.

ELGERED, G., DAVIS, J. L., HERRING, T. A., & SHAPIRO, I. I. 1991. Water vapor radiometry for estimation of the wet delay. *J. Geophys. Res.*, 96(B4), 6541–6555.

ESA. 2012. *Galileo reference troposphere model for the user receiver.* Tech. rept. ESA. ESA-APPNG-REF/00621-AM.

ESOC. 2017 (April). ftp://dgn6.esoc.esa.int/products.

ESSEN, L., & FROOME, K.D. 1951. The refractive indices and dielectric constants of air and its principal constituents at 24,000 Mc/s. *Proc. of the Physical Society*, 64(10), 862–875.

FABRY, F. 2006. The spatial variability of moisture in the boundary layer and its effect on convection initiation: Project-long characterization. *Mon. Wea. Rev.*, 134(1), 79–91.

FLORES, A. 1999. *Atmospheric tomography using satellite radio signals.* Ph.D. thesis, Universitat Politecnica de Catalunya, Departament de Teoria del Senyal i Comunicacions. http://www.tdx.cat/handle/10803/6881.

GHOSH, S. N. 2002. *Electromagnetic theory and wave propagation.* Narosa Publishing. ISBN: 9780849324307.

GLANER, M. 2017. *Eigenschaften und Einsatzmöglichkeiten von GPS und Galileo Signal-Linearkombinationen.* MA thesis, TU Wien, Department of Geodesy and Geoinformation.

GRAMS, C. M., BINDER, H., PFAHL, S., PIAGET, N., & WERNLI, H. 2014. Atmospheric processes triggering the central European floods in June 2013. *Nat. Hazards Earth Syst. Sci.*, 14(7), 1691–1702.

GRAY, L. J., BEER, J., GELLER, M., HAIGH, J. D., LOCKWOOD, M., MATTHES, K., CUBASCH, U., FLEITMANN, D., HARRISON, G., HOOD, L., LUTERBACHER, J., MEEHL, G. A., SHINDELL, D., VAN GEEL, B., & WHITE, W. 2010. Solar influences on climate. *Rev. Geophys.*, 48(4), 2–53.

GURTNER, W., & ESTEY, L. 2007. *RINEX - The Receiver Independent Exchange Format - version 3.00.* University of Bern, Astronomical Institute, and UNAVCO, Boulder, Colorado.

HAIDEN, T., JANOUSEK, M., BAUER, P., BIDLOT, J., DAHOUI, M., FERRANTI, L., PRATES, F., RICHARDSON, D. S., & VITART, F. 2015. *Evaluation of ECMWF forecasts, including 2014-2015 upgrades.* Tech. rept. ECMWF.

HÅKANSSON, M., JENSEN, A. B. O., HOREMUZ, M., & HEDLING, G. 2017. Review of code and phase biases in multi-GNSS positioning. *GPS Solut.*, 21(3), 849–860.

HALLIDAY, D., RESNICK, R., & WALKER, J. 1981. *Fundamentals of physics.* 10th edn. John Wiley & Sons Inc. ISBN: 9781118230718.

HALLORAN, G. 2014. *Assimilation of GNSS delay observations at the UK Met Office.* Presentation. Proc. of the International Symposium on Data Assimilation 2014, Munich, Germany, 24-28 February 2014.

HAN, Y., & WESTWATER, E. R. 2000. Analysis and improvement of tipping calibration for ground-based microwave radiometers. *IEEE Trans. Geosci. Remote Sens.*, 38(3), 1260–1276.

HANSEN, P. C. 2000. *Computational inverse problems in electrocardiology.* WIT Press. Chap. The L-curve and its use in the numerical treatment of inverse problems. 119-142.

HAUSER, J. P. 1989. Effects of deviations from hydrostatic equilibrium on atmospheric corrections to satellite and lunar laser range measurements. *J. Geophys. Res.*, 94(B8), 10182–10186.

HERRING, T. A. 1992. Modelling atmospheric delays in the analysis of space geodetic data. *In:* DEMUNK, J.C., & SPOELSTRA, T.A. (eds), *Proc. of the symposium on Refraction of Transatmospheric Signals in Geodesy. 157-164.*

HERTZ, H. 1887. Über einen Einfluss des ultravioletten Lichtes auf die elektrische Entladung. *Ann. Phys.*, 267(8), 983–1000.

HILL, R. J., R. S. LAWRENCE, J. T., & PRIESTLEY. 1982. Theoretical and calculational aspects of the radio refractive index of water vapor. *Radio Sci.*, 17(5), 1251–1257.

HINTERBERGER, F. 2016. *Influence of GPS satellite orbits and clock corrections on the estimation of single difference uncalibrated phase delays.* Ph.D. thesis, TU Wien, Department of Geodesy and Geoinformation. http://katalog.ub.tuwien.ac.at/AC13382775.

HOBIGER, T., ICHIKAWA, R., KOYAMA, Y., & KONDO, T. 2008a. Fast and accurate ray-tracing algorithms for real-time space geodetic applications using numerical weather models. *J. Geophys. Res.*, 113(D20302), 1–14.

HOFMEISTER, A. 2016. *Determination of path delays in the atmosphere for geodetic VLBI by means of ray-tracing.* Ph.D. thesis, TU Wien, Department of Geodesy and Geoinformation. http://katalog.ub.tuwien.ac.at/AC13248753.

HOPFIELD, H. S. 1969. Two-quartic tropospheric refractivity profile for correcting satellite data. *J. Geophys. Res.*, 74(18), 4487–4499.

HOUNSFIELD, G. N. 1973. Computerized transverse axial scanning tomography: Part I. Description of the system. *Br. J. Radiol.*, 46(552), 1016–1022.

HOUZE, R. A. 2004. Mesoscale convective systems. *Rev. Geophys.*, 42(RG4003), 1–43.

IEEE. 1990. The (1990) IEEE standard definitions of terms for radio wave propagation. *IEEE Std*, 211-1990, 1–24.

IEEE. 2003. IEEE standard letter designations for radar-frequency bands. *IEEE Std*, 521-2002, 1–10.

INTERNATIONAL GNSS SERVICE. 2017 (April). https://igscb.jpl.nasa.gov/igscb/data/format/ sinex_tropo.txt.

IYER, H.M., & HIRAHARA, K. 1993. *Seismic tomography: Theory and practice.* Springer Netherlands. ISBN: 9780412371905.

JACKSON, J. D. 1998. *Classical electrodynamics.* Wiley and Sons, New York. ISBN: 9780471309321.

JIN, S., ESTEL, C., & FEIQIN, X. 2014. *GNSS remote sensing.* Springer Netherlands. ISBN: 9789400774827.

KACZMARZ, S. 1937. Angenäherte Auflösung von Systemen linearer Gleichungen. *Bull. Int. Acad. Pol. Sci. Let.*, 35, 355–357.

KAPLON, J. 2017. *Analysis of systematic effects in slant total delay estimation.* Presentation. COST Action ES1206 - GNSS4SWEC, Final Workshop, Noordwijk, Netherlands, 21-23 February 2017.

KARABATIC, A., WEBER, R., & HAIDEN, T. 2011. Near real-time estimation of tropospheric water vapour content from ground based GNSS data and its potential contribution to weather now-casting in Austria. *Advances in Space Research*, 47(10), 1691–1703.

KAČMAŘÍK, M., DOUŠA, J., DICK, G., ZUS, F., BRENOT, H., MÖLLER, G., POTTIAUX, E., KAPŁON, J., HORDYNIEC, P., VÁCLAVOVIC, P., & MOREL, L. 2017. Inter-technique validation of tropospheric slant total delays. *Atmos. Meas. Tech.*, 10(6), 2183–2208.

KNÖPFLER, A. 2015. *Korrektur stationsabhängiger Fehler bei GNSS.* Ph.D. thesis, Karlsruher Institute of Technology, Department of Civil Engineering, Geo and Environmental Sciences. https://www.ksp.kit.edu/download/1000045959.

KOCH, K. R. 1996. Robuste Parameterschätzung. *Allg. Verm. Nachr.*, 103, 1–18.

KOUBA, J. 2015. *A guide to using International GNSS Service (IGS) products.* Tech. rept. Natural Resources Canada.

KRAUS, H. 2001. *Die Atmosphäre der Erde.* Springer Berlin Heidelberg. ISBN: 9783540418443.

KURSINSKI, E. R., HAJJ, G. A., SCHOFIELD, J. T., LINFIELD, R. P., & HARDY, K. R. 1997. Observing Earth's atmosphere with radio occultation measurements using the Global Positioning System. *J. Geophys. Res.*, 102(D19), 23429–23465.

LANDSKRON, D. 2017. *Modeling tropospheric delays for space geodetic techniques*. Ph.D. thesis, TU Wien, Department of Geodesy and Geoinformation. http://katalog.ub.tuwien.ac.at/AC13733035.

LI, H., LIAN, Y., WANG, X., MA, W., & ZHAO, L. 2011. Solar constant values for estimating solar radiation. *Energy*, 36(3), 1785–1789.

LIEBE, H. J. 1985. An updated model for millimeter wave propagation in moist air. *Radio Sci.*, 20(5), 1069–1089.

LIEBE, H. J., HUFFORD, G. A., & MANABE, T. 1991. A model for the complex permittivity of water at frequencies below 1 THz. *Int. J. Infrared. Milli. Waves.*, 12(7), 659–675.

LOGOTRONIC. 2016. *Gealog NTC temperature sensors*. Manual.

LORENZ, L. 1880. Über die Refractionsconstante. *Ann. Phys.*, 247(9), 70–103.

LUO, X., MAYER, M., & HECK, B. 2009. *Observing our changing Earth*. Springer Berlin Heidelberg. Chap. Improving the stochastic model of GNSS observations by means of SNR-based weighting. 725-734.

MACMILLAN, D. S. 1995. Atmospheric gradients from Very Long Baseline Interferometry observations. *Geophys. Res. Lett.*, 22(9), 1041–1044.

MAHONEY, M. J. 2001. *A discussion of various measures of altitude*. http://archive.li/b9viL.

MANNING, T. 2013. *Sensing the dynamics of severe weather using 4D GPS tomography in the Australien region*. Ph.D. thesis, Royal Melbourne Institute of Technology, School of Mathematical and Geospatial Sciences. http://researchbank.rmit.edu.au/eserv/rmit:160752/Manning.pdf.

MARSH, K.N. 1987. *Recommended reference materials for the realization of physicochemical properties*. Blackwell Scientific Publications. ISBN: 9780632017188.

MARZANO, F. S., & VISCONTI, G. 2003. *Remote sensing of atmosphere and ocean from space: Models, instruments and techniques.* Kluwer Academic Publishers. ISBN: 9780306481505.

MASOUMI, S., MCCLUSKY, S., KOULALI, A., & TREGONING, P. 2016. A new model of tropospheric directional gradients in global positioning system and its application to investigate extreme weather events. *In: Proc. of the IGS workshop 2016, Sydney, Australia, 8-12 February 2016 (Poster).*

MASSARO, G., STIPERSKI, I., POSPICHAL, B., & ROTACH, M. W. 2015. Accuracy of retrieving temperature and humidity profiles by ground-based microwave radiometry in truly complex terrain. *Atmos. Meas. Tech.,* 8(8), 3355–3367.

MELBOURNE, W. G. 2004. *Radio occultations using Earth satellites: A wave theory treatment.* Jet Propulsion Laboratory. ISBN: 9780471712220.

MENDES, V. B. 1999. *Modeling the neutral-atmospheric propagation delay in radiometric space techniques.* Ph.D. thesis, University of New Brunswick, Department of Geodesy and Geomatics Engineering. http://www2.unb.ca/gge/Pubs/TR199.pdf.

METEOLABOR AG. 2005. *Barometer BM35.* Manual.

MILLER, C. 2010. *Practical consideration of temporal correlation in RTK GPS surveying using a modified Kalman filter.* MA thesis, University of Calgary, Department of Geomatics Engineering.

MILLER, S. 1953. A production of amino acids under possible primative earth conditions. *Science,* 117(3046), 528–529.

MLYNCZAK, P. E., SMITH, G. L., & DOELLING, D. R. 2011. The annual cycle of Earth radiation budget from clouds and the Earth Radiant Energy System (CERES) data. *J. Appl. Meteor. Climatol.,* 50(12), 2490–2503.

MÖLLER, G. 2015. *EPOSA antennen tests 2015.* Presentation. EPOSA Technik Meeting - GNSS, Vienna, Austrian, 16th of November 2015.

MÖLLER, G. 2016. *Bended ray-tracer for GNSS tomography applications.* Tech. rept. TU Wien, Department of Geodesy and Geoinformation.

MÖLLER, G., WEBER, R., & BÖHM, J. 2014. Improved troposphere blind models based on numerical weather data. *Navigation,* 61(3), 203–211.

MÖLLER, G., WITTMANN, C., YAN, X., UMNIG, E., JOLDZIC, N., & WEBER, R. 2015. 3D ground based GNSS atmospheric tomography. *Final report, FFG project GNSS-ATom (ID:840098)*.

MOORE, E. H. 1920. On the reciprocal of the general algebraic matrix. *Bull. Amer. Math. Soc.*, 26, 394–395.

MORAN, G. M. 2014. Future GNSS: Improved signals and constellations. *In: Proc. of the 34th European Telemetry and Test Conference, Nürnberg, Germany, 3-5 July 2014*. 166-171.

MOREL, L., POTTIAU, E., DURAND, F., & BAELEN, J. VAN. 2015. Validity and behaviour of tropospheric gradients estimated by GPS in Corsica. *Adv. Space Res.*, 55(1), 135–149.

NAFISI, V., URQUHART, L., SANTOS, M. C., NIEVINSKI, F. G., BÖHM, J., WIJAYA, D. D., SCHUH, H., ARDALAN, A. A., HOBIGER, T., ICHIKAWA, R., ZUS, F., WICKERT, J., & GEGOUT, P. 2012. Comparison of ray-tracing packages for troposphere delays. *IEEE Trans. Geosci. Remote Sens.*, 50(2), 469–481.

NASA. 2016 (July). http://climate.nasa.gov/vital-signs/global-temperature/.

NATTERER, F. 2001. *The mathematics of computerized tomography*. SIAM. ISBN: 9780898714937.

NIEMEIER, W. 2002. *Ausgleichungsrechnung*. Walter de Gruyter, Berlin. ISBN: 9783110190557.

NOAA. 2017 (April). https://www.ngdc.noaa.gov/mgg/global/global.html.

OGAJA, C. A. 2011. *Applied GPS for engineers and project managers*. American Society of Civil Engineers. ISBN: 9780784411506.

OWENS, J. C. 1967. Optical refractive index of air: Dependence on pressure, temperature and composition. *Appl. Optics*, 6(1), 51–59.

PEIXOTO, J. P., & OORT, A. H. 1992. *Physics of climate*. American Institute of Physics. ISBN: 9780883187128.

PENROSE, R. 1955. A generalized inverse for matrices. *Proc. of the Cambridge Philosophical Society*, 51(3), 406–413.

PERLER, D. 2011. *Water vapor tomography using Global Navigation Satellite Systems.* Ph.D. thesis, ETH Zurich, Department of Civil, Environmental and Geomatic Engineering. https://www.sgc.ethz.ch/sgc-volumes/sgk-84.pdf.

PETIT, G., & LUZUM, B. 2010. *IERS conventions (2010).* Verlag des Bundesamts für Kartographie und Geodäsie. ISBN: 3898889896.

PEVNY, G., & MAIR, M. 2008. TAWES - The new Austrian meteorological measuring network. *In: Lakeside conference proceeding, 2008. 1-16.*

PHINNEY, R. A., & ANDERSON, D. L. 1968. On the radio occultation method for studying planetary atmospheres. *J. Geophys. Res.*, 73(5), 1819–1827.

RADON, J. 1917. *Berichte über die Verhandlungen der Sächsischen Gesellschaft der Wissenschaften zu Leipzig.* Vol. 69. Akad. Wiss. Chap. Über die Bestimmung von Funktionen durch ihre Integralwerte längs gewisser Mannigfaltigkeiten. 262-277.

RAMASWAMY, V., HURRELL, J. W., MEEHL, G. A., PHILLIPS, A., SANTER, B. D., SCHWARZKOPF, M. D., SEIDEL, D. J., SHERWOOD, S. C., & THORNE, P. W. 2006. *Temperature trends in the lower atmosphere: Steps for understanding and reconciling differences.* U.S. Climate Change Science Program. Chap. Why do temperatures vary vertically and what do we understand about why they might vary and change over time? 15-28.

RAWLINSON, N., & SAMBRIDGE, M. 2003. Seismic traveltime tomography of the crust and lithosphere. *Adv. Geophys.*, 46, 81–197.

REICHLER, T., DAMERIS, M., & SAUSEN, R. 2003. Determining the tropopause height from gridded data. *Geophys. Res. Lett.*, 30(20), 1–5.

RICHERT, T., & EL-SHEIMY, N. 2007. Optimal linear combinations of triple frequency carrier phase data from future global navigation satellite systems. *GPS Solut.*, 11(1), 11–19.

RIECKH, T., SCHERLLIN-PIRSCHER, B., LADSTÄDTER, F., & FOELSCHE, U. 2014. Characteristics of tropopause parameters as observed with GPS radio occultation. *Atmos. Meas. Tech.*, 7(11), 3947–3958.

ROCKEN, C., SOKOLOVSKIY, S., JOHNSON, J. M., & HUNT, D. 2001. Improved mapping of tropospheric delays. *J. Atmos. Oceanic Technol.*, 18(7), 1205–1213.

RODRIQUEZ, G. 2005. An algorithm for estimating the optimal regularization parameter by the L-curve. *Rend. Mat.*, 25, 69–84.

ROHM, W., ZHANG, K., & BOSY, J. 2014. Limited constraint, robust Kalman filtering for GNSS troposphere tomography. *Atmos. Meas. Tech.*, 7(5), 1475–1486.

ROSE, T. 2011a. *Measurement and deployment examples*. Tech. rept. Radiometer Physics.

ROSE, T. 2011b. *Technical instrument manual, description of instrument technology, applicable for HATPRO*. Radiometer Physics. Manual.

ROTHACHER, M., BEUTLER, G., WEBER, R., & HEFTY, J. 1998. High-frequency variations in Earth rotation from Global Positioning System data. *J. Geophys. Res.: Solid Earth*, 105(B7), 13711–13738.

RTCA. 1999. *Minimum operational performance standards for Global Positioning System / Wide area augmentation system airborne equipment*. Tech. rept.

RÜEGER, J. 2002. Refractive index formulae for electronic distance measurements with radio and millimetre waves. *Unisurv. Rep.*, 109, 758–766.

SAASTAMOINEN, J. 1972. *The use of artificial satellites for geodesy*. American Geophysical Union. Chap. Atmospheric correction for the troposphere and stratosphere in radio ranging satellites. 247-251.

SAMMER, J. 2017. *Einfluss regionaler Klimatologie auf die Genauigkeit von troposphärischen Laufzeitverzögerungen*. BSc thesis, TU Wien, Department of Geodesy and Geoinformation.

SANTER, B. D., WEHNER, M. F., WIGLEY, T. M. L., SAUSEN, R., MEEHL, G. A., TAYLOR, K. E., AMMANN, C., ARBLASTER, J., WASHINGTON, W. M., BOYLE, J. S., & BRÜGGEMANN, W. 2003. Contributions of anthropogenic and natural forcing to recent tropopause height changes. *Science*, 301(5632), 479–483.

SCHILLER, C., GROOSS, J.-U., KONOPKA, P., PLÖGER, F., SILVA DOS SANTOS, F. H., & SPELTEN, N. 2009. Hydration and dehydration at the tropical tropopause. *Atmos. Chem. Phys.*, 9(24), 9647–9660.

SCHMID, R., DACH, R., COLLILIEUX, X., JÄGGI, A., SCHMITZ, M, & DILSSNER, F. 2015. Absolute IGS antenna phase center model igs08.atx: status and potential improvements. *J. Geod.*, 90(4), 343–364.

SCHÜLER, T. 2001. *On ground-based tropospheric delay estimation.* Ph.D. thesis, Universität der Bundeswehr München, Fakultät für Bauingenieur- und Vermessungswesen. https://www.unibw.de/IfG/Org/schriftenreihe/pdf-ordner/heft-73/heft-73.pdf.

SCHÜLER, T. 2006. GNSS meteorology on moving platforms. *InsideGNSS*, 1(3), 56–60.

SHANGGUAN, M., HEISE, S., BENDER, M., DICK, G., RAMATSCHI, M., & WICKERT, J. 2015. Validation of GPS atmospheric water vapor with WVR data in satellite tracking mode. *Ann. Geophys.*, 33(1), 55–61.

SHOJI, Y., NAKAMURA, H., IWABUCHI, T., AONASHI, K., SEKO, H., MISHIMA, K., ITAGAKI, A., ICHIKAWA, R., & OHTANI, R. 2004. Tsukuba GPS dense net campaign observation: Improvement in GPS analysis of slant path delay by stacking one-way postfit phase residuals. *J. Meteor. Soc. Japan. Ser. II*, 82(1B), 301–314.

SMIT, H., KIVI, R., VÖMEL, H., & PAUKKUNEN, A. 2013. *Monitoring atmospheric water vapour.* Springer New York. Chap. Thin film capacitive sensors. 11-38.

SMITH, E. K., & WEINTRAUB, S. 1953. The constants in the equation for atmospheric refractive index at radio frequencies. *J. Res. Natl. Bur. Stand.*, 50(1), 39–41.

SOMIGLIANA, C. 1929. *Teoria generale del campo gravitazionale dell ellissoide di rotazione.* Libr. Editr. Politecnica.

SPEKTRUM. 2016 (May). http://www.spektrum.de/lexikon/geowissenschaften/atmosphaere.

SPRINGER, T. A. 2009. *NAPEOS mathematical models and algorithms.* Tech. rept. ESA. DOPS-SYS-TN-0100-OPS-GN.

STEINER, A. K., LÖSCHER, A., & KIRCHENGAST, G. 2006. *Error characteristics of refractivity profiles retrieved from CHAMP radio occultation data.* Springer Berlin Heidelberg. Chap. Atmosphere and climate. 27-36.

STENSRUD, D.J. 2009. *Parameterization schemes: Keys to understanding numerical weather prediction models.* Cambridge University Press. ISBN: 9780521126762.

STRANG, G., & BORRE, K. 1997. *Linear algebra, geodesy, and GPS.* Wellesley-Cambridge Press. ISBN: 0961408863.

TAPLEY, B. D. 1973. *Statistical orbit determination theory.* Springer Netherlands. Chap. Recent advances in dynamical astronomy. 396-425.

TARANTOLA, A. 2005. *Inverse problem theory.* SIAM. ISBN: 0898715725.

TEKE, K. 2011. *Sub-daily parameter estimation in VLBI data analysis.* Ph.D. thesis, TU Wien, Department of Geodesy and Geoinformation. http://katalog.ub.tuwien.ac.at/AC08908993.

TEUNISSEN, P. J. G. 1994. A new method for fast carrier phase ambiguity estimation. *In: Position Location and Navigation Symposium, 1994. 562-573.*

THAYER, D. G. 1974. An improved equation for the radio refractive index of air. *Radio Sci.*, 9(10), 803–807.

THIDE, B. 2011. *Electromagnetic field theory.* 2nd edn. Upsilon Books. ISBN: 978048647732.

TIKHONOV, N. 1963. Solution of incorrectly formulated problems and the regularization method. *Soviet Math. Dokl.*, 4, 1035–1038.

TRENBERTH, K. E., FASULLO, J. T., & KIEHL, J. 2009. Earth's global energy budget. *Bull. Amer. Meteor. Soc.*, 90(3), 311–323.

UNIVERSITY OF INNSBRUCK. 2017 (March). http://acinn.uibk.ac.at/research/atmospheric-dynamics/projects/i-box.

URLICHICH, Y., SUBBOTIN, V., STUPAK, G., DVORKIN, V., POVALYAEV, A., & KARUTIN, S. 2011. GLONASS modernization. *In: Proc. of the 24th International Technical Meeting of The Satellite Division of the Institute of Navigation, September 20 - 23, 2011. 3125-3128.*

URQUHART, L. 2011. *Assessment of tropospheric slant factor models: Comparison with three dimensional ray-tracking and impact on geodetic positioning.* Ph.D. thesis, University of New Brunswick, Department of Geodesy and Geomatics Engineering. http://www2.unb.ca/gge/Pubs/TR275.pdf.

VAISALA. 2010. *Vaisala Radion RS92-D datasheet.* Manual.

VAISALA. 2013. *GPS-based measurement of height and pressure with Vaisala RS41.* Manual.

VARAH, J. M. 1979. A practical examination of some numerical methods for linear discrete ill-posed problems. *SIAM Rev.*, 21(1), 100–111.

VASIN, V. V. 2011. *Optimization and regularization for computational inverse problems and applications.* Springer Berlin Heidelberg. Chap. Inverse problems with a priori information. 35-64.

VON ENGELN, A., ANDERS, Y., MARQUARDT, C., & SANCHO, F. 2009. GRAS radio occultation on-board of Metop. *Adv. Space Res.*, 47(2), 1–22.

VYAS, M., LIM, S., RIZOS, C., ZHANG, K., & MÖLLER, G. 2011. Analysis of zenith path delay in dynamically changing environment. *In: Conference Paper IGNSS 2011, Sydney, Australia, 15-17 November 2011. 1-8.*

WALLACE, J. M., & HOBBS, P. V. 2006. *Atmospheric science - An introductory survey.* 2nd edn. Academic Press Inc. ISBN: 9780127329512.

WANG, Y., & PRATT, R. G. 1997. Sensitivities of seismic traveltimes and amplitudes in reflection tomography. *Geophys. J. Int.*, 131(3), 618–642.

WANG, Y., HAIDEN, T., & KANN, A. 2006. The operational limited area modelling system at ZAMG. *Österreichische Beiträge zu Meteorologie und Geophysik*, 37, 33 pp.

WEBER, R., MÖLLER, G., HINTERBERGER, F., BERGLEZ, P., VIJAYAKUMAR, L. S., HINTEREGGER, S., & BÖHM, J. 2016. Use of inter-satellite ranging for troposphere tomography and ionosphere monitoring. *Final report, ESA project ISR-Atmosphere (ID:EGEP-ID89-1.15).*

WICKERT, J., BEYERLE, G., HAJJ, G. A., SCHWIEGER, V., & REIGBER, C. 2002. GPS radio occultation with CHAMP: Atmospheric profiling utilizing the space-based single difference technique. *Geophys. Res. Lett.*, 29(8), 28.1–28.4.

WINKLER, P., LUGAUER, M., & REITEBUCH, O. 2006. Alpines Pumpen. *promet*, 32(1), 34–42.

WMO. 1957. Meteorology: A three dimensional science. *WMO Bull.*, 6, 134–138.

WMO. 2008. *Guide to meteorological instruments and methods of observation.* 7th edn. Vol. 8. Secretariat of the World Meteorological Organization.

WOO, K. T. 2000. Optimum semicodeless carrier-phase tracking of L2. *Navigation*, 47(2), 82–99.

XIA, P., CAI, C., & LIU, Z. 2013. GNSS troposphere tomography based on two-step reconstructions using GPS observations and COSMIC profiles. *Ann. Geophys.*, 31(10), 1805–1815.

XU, G. 2007. *GPS: Theory, algorithms and applications.* Springer-Verlag Berlin. ISBN: 9783540727156.

YAO, Y. B., ZHAO, Q. Z., & ZHANG, B. 2016. A method to improve the utilization of GNSS observation for water vapor tomography. *Ann. Geophys.*, 34(1), 143–152.

Curriculum Vitae

Name	**Dipl.-Ing. Gregor Möller BSc**
Date of Birth	28.01.1984
Place of Birth	Saalfeld/Saale
Nationality	German
Address	Heinzelmanngasse 6/4
	1200 Vienna
	Austria
Email	Gregor.Moeller@gmx.at

ACADEMIC EDUCATION

10/2012 - 08/2017	Doctoral Programme in Technical Sciences, TU Wien Specialisation "Surveying and Geoinformation"
03/2008 - 11/2010	Dipl.-Ing., Specialisation "Geodesy and Geophysics", TU Wien Thesis title: Analysis of the GNSS reference station network EPOSA
10/2005 - 02/2008	BSc., Specialisation "Surveying and Geoinformation", TU Wien Thesis title: Determination of forest parameters from full-waveform airborne laser scanning data
10/2003 - 09/2005	Pre-degree, Specialisation "Geodesy", Dresden Technical University
09/1994 - 06/2002	Grammar school, Staatliches Heinrich-Böll-Gymnasium Saalfeld

WORK EXPERIENCE

04/2014 - present	Univ.Ass., Department of Geodesy and Geoinformation, TU Wien
05/2011 - 03/2014	Project assistent, Department of Geodesy and Geoinformation, TU Wien
11/2010 - 04/2011	Scientific exchange, School of Surveying and Spatial Systems The University of New South Wales, Sydney
07/2009 - 10/2010	Project assistant, Institute of Geodesy and Geophysics, TU Wien
11/2006 - 03/2009	Survey assistant, ÖBB Infrastruktur Bau AG
05/2006 - 10/2006	Survey assistant, Land Surveyors office Franziska Silwester
09/2005 - 10/2005	Student assistant, Institute of Photogrammetry and Remote Sensing, TU Wien